

# **Luminescence Investigations of CaS:Eu<sup>2+</sup> Powder and Pulsed Laser Deposited Thin Films for Application in Light Emitting Diodes**

By

**Raphael Lavu Nyenge**

**(MSc)**

*A thesis submitted in fulfillment of the requirements for the degree*

**PHILOSOPHIAE DOCTOR**

*in the*

**Department of Physics**

**Faculty of Natural and Agricultural Sciences**

*at the*

**University of the Free State**

**Republic of South Africa**

**Promoter: Prof. O. M. Ntwaeaborwa**

**Co-promoter: Prof. H. C. Swart**

**June 2015**

**Declaration**

This thesis is my original work and has not been presented for the award of a degree at the University of the Free State or any other University. I have acknowledged other people's work by referencing adequately.

**Raphael L. Nyenge**

(2011173107)

Signed.....on the .....day of ..... 2015

This thesis is submitted with our approval as University supervisors:

**Prof O. M. Ntwaeaborwa**

.....

Signature

.....

Date

**Prof H. C. Swart**

.....

Signature

.....

Date

## **Dedication**

In memory of my late mother, Ann Kalondu Nyenge

## Acknowledgments

*The thankful receiver bears a plentiful harvest. -William Blake*

To the **Almighty God**, my heavenly Father above, with eyes full of mercy and a heart full of love. He touched hearts to provide, He watched as the laser pulsed and layer upon layer formed, the beautiful colors springing up. Though new many were, He gave me skill and understanding; He really cares for I am more than the lilly of the valley. When I felt like giving up, he carried me by His arms and whispered: photons, phonons, electrons, and ions are still in transition; fear not, **I AM** with you. And now behold, every electron sits where it is supposed to be, Glory be to His Name!

Special thanks to my employer, Kenyatta University for granting me a study leave, and the chairman, Physics Department for his support during my period of study.

My colleagues at Kenyatta University: Dr. Bem and Dr. Munji for introducing me to Profs Ntwaeaborwa and Swart; I will remain eternally indebted to them.

I am indebted to Prof O. M. Ntwaeaborwa, my supervisor and my friend, for having faith in me; you guided, encouraged and inspired me; I have learnt a lot from you *Ntate* Ntwaeaborwa.

I am deeply grateful to my co-supervisor, Prof H.C. Swart for his guidance and securing funds for my study program. Prof, if only you could listen to my heart for words are not enough!

I wish to express my gratitude to Prof J.J. Terblans for opening the gates of the University of the Free State and accepting me as a student in the Department of Physics.

Thank you Prof Kroon: for your insightful, thought stimulating and exciting questions during group meetings. You were always ready to give advice and assistance.

I express my gratitude to Dr Liza Coetsee-Hugo and Dr Mart-Mari Duvenhage for assistance and guidance during the surface characterization.

Prof Roos: Thank you for your valuable advice on X-ray Photoelectron Spectroscopy. To Prof Petrus Meintjes, thank you for being a friend.

My gratitude to the administrative staff: K. Cronje and Y. Fick for their support and kindness during my research.

To the technical staff Dr. S. Cronje and Dr. P. Heerden; I appreciate your support.

I am grateful to Professor Pieter Van Wyk, and Ms. Hanlie Grobler, of the Microscopy center, University of the Free State for assisting with SEM measurements.

I appreciate Steven Nkosi and Bathusile Masina both of the National Laser Center, CSIR for their assistance with the pulsed laser deposition system.

I am thankful to my fellow researchers: A. Abbass, Dr. A.Yousif, R. Jafer, Dr.W. Tabaza, Mubarak, X.Yan, Winfred M. Mulwa, Ali Wako, Dr.Vijay Kumar, Dr.Vinod Kumar Papnai, Dr. S. Somo and Dr. Pandaye for their assistance, encouragement and support during my research. A. Abbass, who was also my office mate, requires special mention: thank you for very constructive discussions and the loads of assistance you accorded me.

To my fellow research group members: Dr. P.S. Mbule, Dr. Sammy Shaat, M.A. Tshabalala, P.P. Mokoena, and Simon Ogugua; you were wonderful people to work with.

To Dr. Luyanda Noto: for invaluable assistance in different experimental techniques and for being a true friend; for that I am eternally grateful.

Dr. Munene Mwaniki, of the Department of Linguistics and Language Practice of the University of the Free State for thought provoking conversations, and his conviction that revolutionary ideas are hidden in simplicity; I say *Asante sana*.

To Pastor Maina and the brethren in Kenya, Pastor George Sheneke and the brethren in the church at Bloemfontein, thank you for your spiritual support, brotherly love and prayers during my stay in South Africa. My sincere gratitude to Brother Marimane and his family for taking me as a member of their family; may the Lord richly bless them.

To the many friends out there, thank you for your encouragement and your silent prayers.

I greatly appreciate my brothers and sisters for their support and encouragement during my study.

Special appreciation to my family: my wife Jane, my daughters Ndanu, Nthoki, and Mwendu for their sacrifice, love, patience and prayers during my study. You have a special place in my heart.

## Abstract

The main objective of this thesis was to investigate the luminescent properties of commercial CaS:Eu<sup>2+</sup> powder and pulsed laser deposited thin films for application in light emitting diodes. X-ray diffraction (XRD), X-ray photoelectron spectroscopy, and photoluminescence (PL) spectroscopy data suggest that the CaS:Eu<sup>2+</sup> phosphors contain secondary phases that were possibly formed during the preparation or due to unintended contamination. An intense red PL broad band with a maximum at 650 nm was observed when the powder was excited at 484 nm using a monochromatized xenon lamp. When the powder was excited using a 325 nm He-Cd laser an additional PL emission peak was observed at 384 nm. The origin of this emission is discussed. Auger electron spectroscopy and Cathodoluminescence (CL) spectroscopy were used to monitor the changes in the surface chemical composition and CL intensity when the phosphor was irradiated with a 2 keV electron beam in vacuum. Possible mechanism for the degradation of CL intensity is presented.

Thermal quenching in CaS:Eu<sup>2+</sup> occurred at a relatively low temperature of 304 K. The kinetic parameters, namely activation energy and order of kinetics of  $\gamma$ -irradiated CaS:Eu<sup>2+</sup> were determined using initial rise and peak shape methods, respectively. An Edinburgh Instruments FS920 fluorescence spectrometer equipped with a Xe lamp as the excitation source was used to collect emission and excitation spectra at low temperature. The samples were exposed to  $\gamma$ -radiation ranging from 10 to 50 Gy for thermoluminescence studies, from a <sup>60</sup>Co source. The thermoluminescence data were obtained using a Harshaw thermoluminescence Reader (Harshaw 3500 TLD Reader). The possible mechanism leading to the decay of luminescence is explored.

Pulsed laser deposited thin films of CaS:Eu<sup>2+</sup> phosphor were grown on Si (100) or Si (111) substrates using the Q-switched Nd: YAG laser. For the purpose of this work, the deposition parameters which were varied during the film deposition are: laser wavelength, working atmosphere, number of laser pulses, deposition pressure, and substrate temperature. The film thickness, crystalline structure, surface morphology, and the photoluminescent properties of the thin films were found to be a function of the laser wavelength. The results from XRD showed that the as-deposited CaS:Eu<sup>2+</sup> thin films were amorphous, except for the (200) diffraction peak observed from the films deposited at the wavelengths of 266 and 355 nm.

The Rutherford backscattering (RBS) results indicate that film thickness depends on the laser wavelength used during deposition. Atomic force microscopy and scanning electron microscopy results show that the roughness of the samples is determined by the laser wavelength. The interaction of laser with matter is discussed, and the best wavelength for ablating this material is proposed. With RBS, it was possible to look at the variation of composition with depth as well as to determine the thickness of the thin films. Compositional analysis carried out using the energy dispersive X-ray spectroscopy showed that the films contained oxygen as an impurity.

The films prepared in an oxygen atmosphere were amorphous while those prepared in a vacuum and argon atmosphere showed a degree of crystallinity. The roughness of the films has a strong influence on the PL intensity. The PL intensity was better for films in the argon atmosphere; showing bigger surface structures with respect to the other films. The emission detected at around 650 nm for all the films was attributed to  $4f^6 5d^1 \rightarrow 4f^7$  transitions of the  $\text{Eu}^{2+}$  ion. An emission at around 618 nm was observed, and was attributed to  ${}^5D_0 \rightarrow {}^7F_2$  transitions in  $\text{Eu}^{3+}$ , suggesting that  $\text{Eu}^{2+}$  was unintentionally oxidized to  $\text{Eu}^{3+}$ . Results from time-of-flight secondary ion mass spectroscopy study show that all the films contain oxygen although the film prepared in oxygen contain more oxygen.

The PL intensity of the  $\text{CaS:Eu}^{2+}$  films was found to depend on the pulse rate, with PL intensity increasing as the number of pulses is increased. XRD studies showed that there was an improvement in crystallinity of  $\text{CaS:Eu}^{2+}$  thin films upon post-deposition annealing, and subsequently an improvement on the PL intensity. PL intensity also improved significantly at a substrate temperature of  $650^\circ\text{C}$ . The best PL intensity as a function of deposition pressure was obtained at an argon pressure of 80 mTorr.

## **Keywords**

$\text{CaS:Eu}^{2+}$ , Pulsed laser deposition, Light emitting diode, Photoluminescence, X-ray photoelectron spectroscopy, Scanning electron microscopy, Atomic force microscopy, Cathodoluminescence, thermoluminescence, Auger electron spectroscopy, TOF SIMS,

Absorption, Wavelength, Thermal quenching, Glow curve, Pulses, Substrate temperature, Deposition pressure.

## Acronyms

▪ AES	Auger electron spectroscopy
▪ AFM	Atomic force microscopy
▪ APPHs	Auger peak-to-peak heights
▪ CL	Cathodoluminescence
▪ CRI	Color rendering index
▪ EDS	Energy dispersive spectroscopy
▪ FWHM	Full width at half maximum
▪ He-Cd	Helium cadmium
▪ JCPDS	Joint committee on powder diffraction standards
▪ LED	Light emitting diode
▪ pc-WLEDs	phosphor-converted WLEDs
▪ PL	Photoluminescence
▪ PLD	Pulsed laser deposition
▪ PLE	Photoluminescence excitation
▪ RBS	Rutherford backscattering spectrometry
▪ RE	Rare earth
▪ SEM	Scanning electron microscopy
▪ TEM	Transmission electron microscopy
▪ TL	Thermoluminescence
▪ TOF-SIMS	Time of flight secondary ion spectrometry
▪ UV	Ultraviolet
▪ WLEDs	White light-emitting diodes
▪ XPS	X-ray photoelectron spectroscopy
▪ XRD	X-ray diffractometer



## Table of Contents

Title and Affiliation.....	i
Declaration.....	ii
Dedication.....	iii
Acknowledgements.....	iv
.	
Abstract.....	vi
Keywords.....	vii
Acronyms.....	viii
Table of Contents.....	ix
List of Figures.....	xv
List of Tables.....	xxi
<b>Chapter 1 Introduction</b>	
1.1 Overview.....	1
1.2 Rationale and Motivation .....	2
1.2.1 Statement of the Research Problem.....	2
1.2.2 Research Objectives.....	3
1.3 Lay Out of the Thesis.....	3
References.....	4
<b>Chapter 2 Theoretical Background</b>	
2.1 Introduction.....	6
2.2 Luminescent Materials.....	6
2.2.1 Types of Luminescence.....	6
2.3 Photoluminescence.....	7
2.3.1 Fluorescence and Phosphorescence.....	8
2.3.2 Excitation mechanism.....	9
2.4 The Cathodoluminescence Process.....	9
2.5 Mechanism of Thermoluminescence.....	11
2.5.1 The Thermoluminescence Process.....	11
2.5.2 A general Model to Explain the TL Mechanism.....	12

2.5.3	Methods of Analysis.....	14
2.6	Calcium Sulfide as a Host Lattice.....	15
2.7	Luminescent Centres.....	16
2.7.1	The Eu <sup>2+</sup> Ion as The Activator.....	17
2.7.2	The Eu <sup>3+</sup> Ion.....	18
2.8	Basic Principles of Inorganic Light Emitting Diodes.....	19
2.8.1	The Structure of a Light Emitting Diode.....	19
2.8.2	Luminous Efficiency and Color Rendering Index.....	21
2.8.3	Common LED Materials.....	22
2.8.4	White Light LEDs.....	22
2.8.5	Phosphor-based LEDs.....	22
2.8.6	UV- pumped Phosphor-based White LEDs Using a Single Host.....	24
2.8.7	Advantages and Applications of LEDs.....	24
2.9	The Pulsed Laser Deposition Process.....	25
2.9.1	Laser-material Interaction .....	26
2.9.2	Ablation and Plume Formation.....	27
2.9.3	Film Growth.....	28
2.9.4	Advantages of PLD and Draw Back.....	29
2.9.5	Origin of Particulates and Methods of Overcoming Particulates.....	29
	References.....	30

### **Chapter 3 Research Techniques**

3.1	Introduction.....	34
3.2	Photoluminescence Spectroscopy.....	34
3.3	Atomic Force Microscopy.....	36
3.4	Pulsed Laser Deposition.....	39
3.5	Scanning Electron Microscope and Energy Dispersive X-ray Spectrometry.....	40
3.5.1	SEM.....	40
3.5.2	Energy Dispersive X-ray Spectrometry .....	42
3.6	Transmission Electron Microscopy.....	43

3.7	X-Ray Diffraction.....	45
3.7.1	Diffractometer.....	45
3.7.2	Applications.....	46
3.8	X-ray Photoelectron Spectroscopy.....	48
3.9	Secondary Ion Mass Spectrometry.....	51
3.10	Auger Electron Spectroscopy.....	53
3.10.1	The Auger Process.....	53
3.11	Rutherford Backscattering Spectrometry.....	56
3.11.1	Basic Principle.....	57
3.11.2	Instrumentation.....	58
3.12	Thermoluminescence Spectroscopy.....	59
	References.....	60

#### **Chapter 4 Luminescent Properties, Intensity Degradation and X-Ray Photoelectron Spectroscopy Analysis of CaS:Eu<sup>2+</sup> Powder**

4.1	Introduction.....	63
4.2	Experimental.....	65
4.3	Results and Discussion.....	66
4.3.1	XRD, SEM and TEM Analyzes.....	66
4.3.2	Surface Characterization by X-ray Photoelectron Spectroscopy .....	69
4.3.3	Photoluminescence and Cathodoluminescence Properties of CaS:Eu <sup>2+</sup> .....	74
4.3.3.1	The Excitation Spectrum of the Eu <sup>2+</sup> Ion in CaS.....	74
4.3.3.2	The Emission Spectra of the Eu <sup>2+</sup> Ion in CaS.....	74
4.3.3.3	AES and APPHs Results.....	78
4.3.3.4	CL Results.....	80
4.4	Conclusion.....	82
	References.....	83

**Chapter 5 Thermal Quenching, Cathodoluminescence and Thermoluminescence Study of Eu<sup>2+</sup> Doped CaS Powder**

5.1	Introduction.....	86
5.2	Experimental.....	88
5.3	Results and Discussion.....	89
5.3.1	SEM, EDX, CL Images, Cathodoluminescence and Photoluminescence.....	89
5.3.2	Temperature Dependent Decay Times of CaS:Eu <sup>2+</sup> .....	92
5.3.3	Thermal Quenching of Luminescence.....	94
5.3.4	5.3.4. Thermoluminescence Studies.....	96
5.4	5.4. Conclusion.....	98
	References.....	98

**Chapter 6 The Influence of Laser Wavelength on the Structure, Morphology and Photoluminescence Properties of Pulsed Laser Deposited CaS:Eu<sup>2+</sup> Thin Films**

6.1	Introduction.....	101
6.1.1	The Interaction of Laser radiation and target: A theoretical perspective.....	102
6.2	Experimental.....	104
6.3	Characterization.....	106
6.4	Results and Discussion.....	106
6.4.1	XRD Results.....	106
6.4.2	Rutherford Backscattering Results.....	107
6.4.3	AFM SEM and EDS Results.....	110
6.4.3.1	AFM Results.....	110
6.4.3.2	SEM and EDS Results.....	111
6.4.4	Photoluminescence Results.....	114
6.5	Conclusion.....	115
	References.....	116

**Chapter 7 TOF SIMS Analysis, Structure and Photoluminescence Properties of Pulsed Laser Deposited CaS:Eu<sup>2+</sup> Thin Films**

7.1	Introduction.....	118
7.2	Experimental.....	119
7.3	Characterization Methods.....	120
7.4	Results and Discussion.....	120
7.4.1	XRD Results.....	120
7.4.2	AFM and SEM Results.....	122
7.4.2.1	AFM Results.....	122
7.4.2.2	SEM and EDS results.....	123
7.4.3	Photoluminescence Results.....	126
7.4.4	TOF-SIMS Analysis.....	128
7.5	Conclusion.....	131
	References.....	131

**Chapter 8 The Influence of the Number of Pulses and Post-Deposition Annealing on the Morphology and Photoluminescence Properties of CaS:Eu<sup>2+</sup> Pulsed Laser Deposited Thin Films**

8.1	Introduction.....	134
8.2	Experimental.....	135
8.3	Results and Discussion.....	136
8.3.1	XRD Results.....	136
8.3.2	AFM and SEM Results.....	139
8.3.2.1	AFM Results.....	139
8.3.2.2	SEM Results.....	141
8.4	Photoluminescence Results.....	142
8.5	Conclusion.....	144
	References.....	145

<b>Chapter 9 Influence of Substrate Temperature and Deposition pressure on the Pulsed Laser Deposited Thin Films of CaS:Eu<sup>2+</sup> Phosphors</b>		
9.1	Introduction.....	146
9.2	Experimental.....	147
9.3	Characterization.....	147
9.4	Results and Discussion.....	148
9.4.1	XRD Results.....	148
9.4.2	AFM Results.....	150
9.4.3	Photoluminescence Results.....	152
9.5	Conclusion.....	154
	References.....	155
<b>Chapter 10 Summary and Suggestions for Future Work</b>		
10.1	Thesis Summary.....	157
10.2	Recommendations for Future Work.....	159
<b>Appendix A: Publications and Conferences/Workshops</b> .....		161

## List of Figures

<b>Fig 2.1</b>	Schematic illustration of photoluminescence.....	7
<b>Fig 2.2</b>	A schematic representation of (a) fluorescence, and (b) phosphorescence emissions.....	8
<b>Fig 2.3</b>	(a) Schematic representation showing energy absorption by an activator (A) doped in a host (H) lattice, and (b) energy transfer by a sensitizer (S).....	9
<b>Fig 2.4</b>	Schematic representation of the processes that cause CL generation in a phosphor.....	10
<b>Fig 2.5</b>	Schematic illustration of the effects produced by electron-beam interaction with a specimen to produce cathodoluminescence.....	11
<b>Fig 2.6</b>	A general energy band model showing the electronic transitions in thermoluminescence material.....	12
<b>Fig 2.7</b>	The initial rise part of a thermoluminescence glow curve.....	15
<b>Fig 2.8</b>	Schematic view of the face centered cubic structure of CaS.....	16
<b>Fig 2.9</b>	Schematic diagram for $\text{Eu}^{2+}$ 5d energy levels.....	18
<b>Fig 2.10</b>	The principle of operation and structure of an LED.....	19
<b>Fig 2.11</b>	Parabolic electron and hole dispersion relations showing “vertical” electron-hole recombination and photon emission [30].....	21
<b>Fig 2.12</b>	Principle of color conversion in a LED.....	23
<b>Fig 2.13</b>	Some applications of LEDs.....	25
<b>Fig 2.14</b>	Schematic illustration and photograph, showing: (a) absorption of laser radiation by a target and the plume. (b) an image of $\text{CaS:Eu}^{2+}$ plume formed by a 266 nm laser.....	27
<b>Fig 2.15</b>	Film growth modes.....	28
<b>Fig 3.1</b>	Schematic diagram of fluorescence spectrometer instrumentation.....	35
<b>Fig 3.2</b>	(a) The Cary Eclipse Fluorescence spectrometer (b) the He-Cd laser photoluminescence units, both at the Physics Department, University of the Free State. ....	36
<b>Fig 3.3</b>	Simplified Schematic of an atomic force microscope system.....	37

<b>Fig 3.4</b>	Photo of a desktop AFM, the Shimadzu SPM-9600 atomic force microscopy, showing the control unit, data processing system, optical microscope, and SPM unit at the Department of Physics, University of the Free State .....	38
<b>Fig 3.5</b>	Schematic diagram of a laser deposition set up.....	39
<b>Fig 3.6</b>	The pulsed laser deposition (PLD) system at the National Laser Centre (NLC, CSIR), Pretoria .....	40
<b>Fig 3.7</b>	Schematic diagram of a scanning electron microscope column.....	41
<b>Fig 3.8</b>	(a) The Shimadzu Superscan SSX-550 (Kyoto, Japan) and (b) JEOL JSM-7800F scanning electron microscopes (SEM) at the Microscopy Center, University of Free State .....	42
<b>Fig 3.9</b>	(a) Schematic of X-ray emission from an atom (b) energy level diagram for an atom (c) EDS spectrum of CaS:Eu <sup>2+</sup> .....	43
<b>Fig 3.10</b>	Schematic diagram of a transmission electron microscope.....	44
<b>Fig 3.11</b>	Philips (FEI, The Netherlands) CM100 Transmission electron microscope at the Microscopy Center, University of Free State .....	45
<b>Fig 3.12</b>	A schematic of an X-ray diffractometer.....	46
<b>Fig 3.13</b>	Schematic diagram of diffraction of X-rays at crystal planes.....	47
<b>Fig 3.14</b>	The Bruker AXS D8 ADVANCE X-ray diffractometer at the Department of Physics of the University of the Free State .....	48
<b>Fig 3.15</b>	Schematic diagram of the XPS process, showing the ejection of a 1s electron from shell K of an atom, adapted from Ref. [17].....	49
<b>Fig 3.16</b>	Schematic diagram of an XPS system.....	50
<b>Fig 3.17</b>	PHI 5000 Versaprobe scanning X-ray photoelectron spectrometer unit at the Department of Physics of the University of the Free State .....	51
<b>Fig 3.18</b>	A schematic of the basic components of a modern SIMS instrument.....	52
<b>Fig 3.19</b>	Photograph of the SIMS equipment, the IONTOF TOF-SIMS5 imaging mass spectrometer in the Department of Physics at the University of the Free State .....	53
<b>Fig 3.20</b>	The basic steps of the AES process, showing the relaxation of the ionized atom by the emission of a KL <sub>1</sub> L <sub>2</sub> Auger electron.....	54



<b>Fig 3.21</b>	A Schematic of an AES experimental setup using a cylindrical mirror analyzer	55
<b>Fig 3.22</b>	The PHI, model 545 Auger electron spectroscopy (AES) unit combined with a CL unit at the Physics Department, University of the Free State .....	56
<b>Fig 3.23</b>	A collision between two positively charged particles, before, and after the collision .....	57
<b>Fig 3.24</b>	Layout of a typical ion beam scattering setup including a tandem accelerator and scattering chamber in backscattering configuration.....	58
<b>Fig 3.25</b>	Photograph of the RBS system at the Ithemba Labs, Cape Town, South Africa .....	59
<b>Fig 3.26</b>	Schematic representation of the TL spectroscopy system, adapted.....	60
<b>Fig 4.1</b>	XRD diffraction patterns of CaS:Eu <sup>2+</sup> powder.....	67
<b>Fig 4.2</b>	SEM images of the CaS:Eu <sup>2+</sup> powder with field of view of (a) 120 and (b) 39..	69
<b>Fig 4.3</b>	(a) TEM image. (b) Particle size distribution for CaS:Eu <sup>2+</sup> powder.....	69
<b>Fig 4.4</b>	XPS survey scan spectrum of the undegraded CaS:Eu <sup>2+</sup> (a) before sputtering. (b) after sputtering .....	71
<b>Fig 4.5</b>	XPS Spectra of Ca 2p (a) before and (b) after degradation.....	72
<b>Fig 4.6</b>	XPS spectra of sulfur (S 2p) (a) before and (b) after degradation.....	72
<b>Fig 4.7</b>	XPS spectra of O 1s (a) before and (b) after degradation.....	73
<b>Fig 4.8</b>	(a) Energy level diagram for Eu <sup>2+</sup> in CaS. (b) PL excitation spectrum ( $\lambda_{em} = 650nm$ ) of CaS:Eu <sup>2+</sup> at room temperature (300 K).....	76
<b>Fig 4.9</b>	Graphs showing CaS:Eu <sup>2+</sup> powder: (a) PL excitation and emission spectrum using Cary Eclipse. (b) Emission spectrum using 325 nm He-Cd PL laser .....	77
<b>Fig 4.10</b>	Energy level diagram for Eu <sup>2+</sup> in CaS and CaSO <sub>4</sub> (impurity in the powder) showing $4f^6[{}^7F_0]5d^1(t_{2g}) \rightarrow 4f^7({}^8S_{7/2})$ transitions, which give rise to the broad band emission .....	77
<b>Fig 4.11</b>	AES spectra from CaS:Eu <sup>2+</sup> phosphor before and after degradation .....	78
<b>Fig 4.12</b>	The relative CL intensity and Auger peak-to-peak heights (APPHs) change with electron dose of the CaS:Eu <sup>2+</sup> surface during electron bombardment .....	79

<b>Fig 4.13</b>	The variation of Auger peak-to-peak heights (APPHs) ratios of Ca: C, O: C and S: C with electron dose of the CaS:Eu <sup>2+</sup> surface during electron bombardment .....	80
<b>Fig 4.14</b>	CL spectra of CaS:Eu <sup>2+</sup> before and after degradation at 1 x 10 <sup>-8</sup> Torr vacuum .....	81
<b>Fig 4.15</b>	Variation of CL spectra of the CaS:Eu <sup>2+</sup> powder with different emission current under a constant 2 keV electron-beam excitation in a 1x 10 <sup>-8</sup> Torr vacuum .....	82
<b>Fig 5.1</b>	(a) Backscattered electron image and chemical maps for (b) Ca-K, (c) S-K, (d) O-K EDX in false colors .....	90
<b>Fig 5.2</b>	CL maps of CaS: Eu <sup>2+</sup> showing (a) emission barycenter in nm and (b) total intensity on the scanned area .....	91
<b>Fig 5.3</b>	(a) PL Excitation and emission spectra (b) CL intensity (both at room temperature) .....	92
<b>Fig 5.4</b>	(a) Luminescence decay curves of CaS: Eu <sup>2+</sup> at 10 K (■) and at 300 K (■), (b) Decay curve of persistent luminescence for the powder measured at room temperature .....	94
<b>Fig 5.5</b>	(a) PL integrated intensity between -50°C and 200°C. (b) Temperature dependence of the FWHM and the peak wavelength of the emission band for the CaS:Eu <sup>2+</sup> .....	95
<b>Fig 5.6</b>	(a) Thermoluminescence glow curves of CaS:Eu <sup>2+</sup> phosphors after excitation by different doses of 10, 20 30, 40, and 50 Gy, recorded at a heating rate of 5°C/s. (b) The initial rise method used to obtain the activation energy, E. The slope of the linear fit is an approximation of the activation energy of the traps .....	97
<b>Fig 6.1</b>	Schematic illustrations of target absorption: (a) 266 nm laser absorbed near the surface (b) 355 nm laser absorbed deeper into the target, (c) 532 nm laser passing through with little absorption .....	104
<b>Fig 6.2</b>	Formation of a plume by (a) weak plume for the long-wavelength (532 nm), (b) well-defined plume for short-wavelength (266 nm) pulsed laser .....	105

<b>Fig 6.3</b>	X-ray diffraction patterns of CaS:Eu <sup>2+</sup> thin films deposited at different laser wavelengths: (a) 532 nm, (b) 355 nm, and (c) 266 nm .....	107
<b>Fig 6.4</b>	RBS spectra showing experimental (black) and simulated (red) spectra of the CaS:Eu <sup>2+</sup> thin films deposited at laser wavelengths of 266 nm, 355 nm, and 532 nm .....	109
<b>Fig 6.5</b>	AFM images of the films deposited using the a) 266 nm, b) 355 nm, and c) 532 nm laser .....	110
<b>Fig 6.6</b>	SEM photographs of films deposited at different laser wavelengths; (a) 266 nm, (b) 355 nm and 532 nm .....	112
<b>Fig 6.7</b>	EDS spectra of CaS:Eu <sup>2+</sup> PLD thin films deposited at laser wavelengths of 532 nm. EDS was performed in positions S5 and S7 (inset) .....	113
<b>Fig 6.8</b>	PL (a) excitation and (b) emission spectra at laser wavelength 266, 355, and 532 nm and inset, variation of PL intensity with wavelength .....	115
<b>Fig 7.1</b>	The XRD spectra of the CaS:Eu <sup>2+</sup> thin films deposited in different atmospheres .....	121
<b>Fig 7.2</b>	The AFM images of the PLD CaS:Eu <sup>2+</sup> thin films in a) Ar, b) vacuum, and c) O <sub>2</sub> atmospheres .....	123
<b>Fig 7.3</b>	SEM images of films deposited in different atmospheres (a) argon (b) vacuum and (c) oxygen .....	124
<b>Fig 7.4</b>	EDS spectra of CaS:Eu <sup>2+</sup> PLD thin films deposited in an argon atmosphere. EDS was performed in positions S3 and S4 (inset) .....	125
<b>Fig 7.5</b>	PL (a) excitation spectra and (b) the emission spectra of the CaS: Eu <sup>2+</sup> thin films deposited in different atmospheres.....	127
<b>Fig 7.6</b>	Deconvoluted PL emission ( $\lambda_{exc} = 250$ nm) spectrum of the film prepared in O <sub>2</sub> atmosphere.....	128
<b>Fig 7.7</b>	PL emission spectra ( $\lambda_{exc} = 470$ nm) for the film deposited in different atmospheres.....	128
<b>Fig 7.8</b>	TOF-SIMS depth profile of a CaS:Eu <sup>2+</sup> PLD thin film (on a Si (100) substrate) in positive spectroscopy mode deposited in a) a vacuum, b) an argon atmosphere, and c) an oxygen atmosphere.....	129

<b>Fig 7.9</b>	TOF-SIMS spectra of CaS:Eu <sup>2+</sup> PLD thin films obtained in a) argon, b) vacuum, c) oxygen and grown on Si (100) substrates.....	130
<b>Fig 8.1</b>	XRD diffractograms of the CaS:Eu <sup>2+</sup> thin films deposited at 18000, 12000 and 6000 pulses.....	137
<b>Fig 8.2</b>	XRD spectra for annealed CaS:Eu <sup>2+</sup> thin films .....	139
<b>Fig 8.3</b>	AFM images of PLD CaS:Eu <sup>2+</sup> thin films deposited at a) 18000,b) 12000, c) 6000 pulses, and (d) the variation of CaS: Eu <sup>2+</sup> thin films rms roughness with number of pulses .....	140
<b>Fig 8.4</b>	AFM pictures for thin films annealed at, (a) 400°C, (b) 600°C, and 800°C in H <sub>2</sub> /Ar atmosphere .....	141
<b>Fig 8.5</b>	The SEM images of CaS:Eu <sup>2+</sup> films deposited at (a) 18000, (b) 12000, and (c) 6000 pulses .....	141
<b>Fig 8.6</b>	SEM images for thin films annealed at, (a) 400°C, (b) 600°C, and (c) 800°C ...	142
<b>Fig 8.7</b>	Emission spectra for PLD CaS:Eu <sup>2+</sup> thin films at different number of pulses ...	143
<b>Fig 8.8</b>	PL results for the 18000-pulses CaS:Eu <sup>2+</sup> thin films annealed at 400°C, 600°C, and 800°C in a H <sub>2</sub> /Ar atmosphere .....	144
<b>Fig 9.1</b>	(i) X-ray diffraction patterns for CaS:Eu <sup>2+</sup> films deposited at various temperatures: (a) 200°C, (b) 400°C, (c) 550°C, (d) 650°C. (ii) Variation of FWHM of (200) peak with substrate temperature .....	149
<b>Fig 9.2</b>	XRD patterns for films deposited at different argon pressures. S is due to the Substrate .....	150
<b>Fig 9.3</b>	AFM images for CaS:Eu <sup>2+</sup> for substrate temperatures of (a) 200°C, (b) 400°C, (c) 550°C, and (d) 650°C .....	151
<b>Fig 9.4</b>	AFM images of CaS:Eu <sup>2+</sup> thin films deposited in argon pressure of (a) 40 mTorr, (b) 80 mTorr, (c) 160 mTorr, (d) 350 mTorr .....	152
<b>Fig 9.5</b>	(a) The excitation and (b) emission spectra for CaS:Eu <sup>2+</sup> PLD thin films at various substrate temperatures; (i) 200°C, (ii) 400°C, (iii) 550°C, (iv) 650°C ...	153
<b>Fig 9.6</b>	Variation of (i) PL intensity and (ii) PL peak with chamber deposition pressure	154

## List of Tables

<b>Table 4.1</b>	The calculated structural parameters for CaS:Eu <sup>2+</sup> powder sample. Secondary phases marked with asterisk (*) are ascribed to CaSO <sub>4</sub> .....	68
<b>Table 4.2</b>	XPS peak position, and chemical bonding for CaS:Eu <sup>2+</sup> powder before (B) and after (A) degradation.....	73
<b>Table 4.3</b>	Peak energy values of the $4f^6(^7F_J)5d^1$ states in CaS:Eu <sup>2+</sup> .....	76
<b>Table 5.1</b>	Decay times of the phosphorescence of CaS:Eu <sup>2+</sup> at different temperatures.....	93
<b>Table 6.1</b>	Stoichiometry (ratios of Ca: S) and thickness of the films deposited at different laser wavelengths.....	109
<b>Table 7.1</b>	Approximate elemental concentration by % weight and % atomic in regions S3 and S4 (see Fig. 7.4).....	126
<b>Table 8.1</b>	Variation of crystal size with number of pulses.....	138
<b>Table 8.2</b>	Change of crystallite size with annealing temperature.....	138
<b>Table 9.1</b>	Variation of crystallite size with substrate temperature.....	149

# Chapter 1

## Introduction

### 1.1. Overview

The application of white light emitting diode (wLED) as the next generation light source will change the lighting industry in a fundamental way. This is so because LEDs have many advantages over incandescent light sources such as lower energy consumption, longer lifetime, improved physical robustness, smaller size, faster switching, safety and its environmental-friendly characteristics [1-3]. The common wLED device is composed of chips that emit blue and phosphors that can be excited by the blue to emit red or green [4-6]. Therefore, phosphors such as  $\text{CaS:Ce}^{3+}$  (green) and  $\text{CaS:Eu}^{2+}$  (red), with strong blue absorption are needed.

Our major focus in this study is CaS, which is a wideband semiconductor with a rock salt cubic structure. In the crystal, each  $\text{S}^{2-}$  ion is surrounded by an octahedron of six  $\text{Ca}^{2+}$  ions, and complementarily, each  $\text{Ca}^{2+}$  ion is surrounded by six  $\text{S}^{2-}$  ions to make  $\text{O}_h$  symmetry [7]. The  $\text{Ca}^{2+}$  and  $\text{Eu}^{2+}$  have ionic radii of 114 and 131 pm, respectively. Consequently, the local symmetry of the  $\text{Ca}^{2+}$  site will not deviate much from that in the pure material upon  $\text{Eu}^{2+}$  doping. The broad band PL emission centered at around 650 nm arises from the transition from the lower  $4f^6 5d^1(t_{2g})$  state to the  $4f^7(^8S_{7/2})$  ground state of the  $\text{Eu}^{2+}$  ions in the CaS matrix.

In most of the reported works [8-10], the  $\text{CaS:Eu}^{2+}$  has been prepared as and investigated in the form of powders. However, for various technological applications such as device fabrication and surface coatings, it is important to investigate the performance of these phosphors in the form of thin films as well. Moreover, it is well documented that thin film phosphors have several advantages over powders, such as higher lateral resolution from smaller grains, better thermal stability, reduced out gassing, and better adhesion to solid substrates [11].

Amongst the techniques used to prepare luminescent thin films, the pulsed laser deposition (PLD) technique has gained popularity due to its ability to transfer the material stoichiometry from a multi-component ablation target to a growing film [12 - 14]. In order to get films with the desired properties using the PLD technique, different deposition parameters need to be optimized. The parameters are such as partial pressure [15], laser fluence [16], substrate temperature [17], and pulse duration [18]. Another important parameter is the laser wavelength chosen for ablation. The absorption of the laser by the material depends on the wavelength of the laser used. A laser wavelength whose laser photon energy is less than the material's optical band gap is poorly absorbed and gives a thin film with a large population of particulate. This in turn affects the quality of the film produced. It is therefore important to choose the right laser wavelength for a given material.

In this work, luminescent properties of the powder and thin film forms of  $\text{CaS:Eu}^{2+}$  were investigated.

## **1.2. Rationale and Motivation**

Driven by the rising demand for energy, researchers are looking for more efficient and low-energy consuming devices. One such area of interest is better sources of light. The consumer market for white-light-emitting LEDs is expanding rapidly. From specialized applications, such as flashlights, back lighting for mobile and display devices, white light LEDs are now finding their way into general lighting applications and are expected to be found in every home and office soon. The combination of blue light from the LED and the yellow emission from the most widely applied YAG:Ce phosphor gives a relatively cool white light. For general lighting applications, it is essential to make pc-LEDs that emit a warmer white light [19]. A shift to the red spectral region is needed to realize this, and hence our focus on the red-emitting  $\text{CaS:Eu}^{2+}$  phosphor.

### **1.2.1 Statement of the Research Problem**

$\text{CaS:Eu}^{2+}$  phosphor is a potential candidate for applications in light emitting diodes (LEDs) owing to its ability to convert the blue light emitted from a blue LED chip into red light. Due

to this great potential for application of  $\text{CaS:Eu}^{2+}$ , there is need to understand its science for large scale production and the suitability of the PLD process for preparing  $\text{CaS:Eu}^{2+}$  thin films. The powder and the thin films were characterized by various techniques such as atomic force microscopy (AFM), time of flight secondary ion mass spectrometry (TOF-SIMS), X-ray photoelectron spectroscopy (XPS), Rutherford backscattering spectrometry (RBS), and Energy Dispersive X-ray Spectrometry (EDS), and many others as presented in chapter 3.

### 1.2.2. Research Objectives

- Characterize  $\text{CaS:Eu}^{2+}$  powder phosphor using various experimental techniques.
- Prepare  $\text{CaS:Eu}^{2+}$  thin films using the pulsed laser deposition technique.
- Using different experimental techniques, study the variations on the thin film's properties with the PLD deposition parameters.
- Compare the results of characterized  $\text{CaS:Eu}^{2+}$  powder phosphor and the characterized  $\text{CaS:Eu}^{2+}$  thin films.
- Investigate the elemental composition of pulsed laser deposited thin films using the AES, TOF SIMS, XPS, RBS, and EDS.

### 1.3. Lay Out of the Thesis

**Chapter 1** includes the introduction, the research problem and the objectives of this study.

In **Chapter 2** a short introduction to luminescence, and especially cathodoluminescence, thermoluminescence and photoluminescence has been given a fair amount of space. A detailed account on the structure of CaS, the excitation and emission mechanism of the  $\text{Eu}^{2+}$  ion are discussed. An overview of LEDs, a brief description of the interaction of matter and laser energy, ablation and the eventual formation of a thin film has been presented.

**Chapter 3** is devoted to the description of the research techniques used in this work, which include the film preparation technique and film characterization techniques.



**Chapter 4** reports the structure, particle morphology, surface chemical states, photoluminescent properties and cathodoluminescence intensity degradation of the CaS:Eu<sup>2+</sup> powder phosphors.

**Chapter 5** studies photoluminescence thermoluminescence and thermal quenching of CaS:Eu<sup>2+</sup>; to examine the suitability of this phosphor for white light emitting diodes.

**Chapter 6** focuses on the influence of laser wavelength on the film thickness, structure, morphology, and photoluminescent (PL) properties of PLD-grown thin films of CaS:Eu<sup>2+</sup>.

**Chapter 7** reports the influence of Ar, O<sub>2</sub>, and vacuum atmospheres on the structure, surface morphology and photoluminescence properties of the deposited thin films.

In **Chapter 8** we examine the influence of number of laser pulses on the photoluminescence properties of CaS:Eu<sup>2+</sup>. This chapter also discusses the effect of post deposition annealing on the thin films.

**Chapter 9** takes a look at the influence of substrate temperature and deposition pressure on the structural and photoluminescence properties of the PLD CaS:Eu<sup>2+</sup> thin films.

**Chapter 10** presents the summary of the work of this thesis and recommendations for future work. A list of publications resulting from this work and the conference/workshop presentations forms the last part of the thesis.

## References

1. M. S. Shur, A. Zukauskas, Solid state lighting: toward superior illumination, Proc. IEEE **93** (10) (2005) 1073–1691.
2. M. J. Bowers II, J.R. McBride, S.J. Rosenthal, J. Am. Chem. Soc. **127** (2005) 15378–15379.
3. [www.nobelprize.org/nobel\\_prizes/physics/laureates/2014/advanced-physicsprize2014.pdf](http://www.nobelprize.org/nobel_prizes/physics/laureates/2014/advanced-physicsprize2014.pdf), accessed on 7/10/2014.
4. J. Yum, S. Seo, S. Lee, Y. Sung, J. Electrochem. Soc. **150** (2003) H47-H52.
5. F. S. Shahedipour, M.P. Ulmer, B.W. Wessels, C.L. Joseph, T. Nishashi, IEEE J. Quantum Electro. **38** (2002) 333-335.

6. J. K. Sheu, S.J. Chang, C.H. Kuo, Y.K. Su, L.W. Wu, Y.C. Lin, W.C. Lai, J.M. Tsai, G.C. Chi, R.K. Wu, IEEE Photonics. Technol. Lett. **15** (2003) 18-20.
7. D. Jia, J. Zhu, B. Wu, J. Electrochem. Soc. **147** (2000) 3948-3952.
8. D. Jia , X.-J. Wang, Opt. Mater. **30** (2007) 375-379.
9. C. Guo, D. Huang, Q. Su, Mater. Sci. Eng., B **130** (2006)189-193.
10. M. Nazarov, C. Yoon, J. Solid State Chem. **179** (2006) 2529–2533.
11. D. P. Norton, Mater. Sci. Eng., R **43** (2004) 139-247
12. G. A. Hirata, O. A. Lopez, L. E. Shea, J. Y. Yi, T. Cheeks, J. McKittrick, J. Siqueiros, M. Avalos-Borja, A. Esparza, C. Falcony, J. Vac. Sci. and Tech. A **14** (1996) 1694.
13. M. S. Hegde, J. Indian Acad. Sci. **113**(2001) 445 - 458.
14. C. B. Arnold, M. J. Aziz, Appl. Phys. A **69** (1999) S23-S27.
15. T. Haugan , P. N. Barnes, L. Brunke, I. Maartense, J. Murphy, Physica C **397** (2003) 47- 57.
16. L. Fang, M. Shen, J. Cryst. Growth **310** (2008) 3470-3473.
17. M. Suche , S. Christoulakis, , N. Katsarikis, E. Koudoumas, Appl. Surf. Sci. **253** (2007) 8141- 8145.
18. L.V. Zhigilei, B. J. Garrison, Appl. Phys. A **69** (1999) S75- S80.
19. V. Bachmann, C. Ronda, O. Oeckler, W. Schnick, A. Meijerink, Chem. Mater. **21**(2009) 316-325.

# Chapter 2

## Theoretical Background

### 2.1. Introduction

In this chapter a brief introduction to luminescence is presented; especially cathodoluminescence, photoluminescence and thermoluminescence have been given a fair amount of space. We give an account on the structure of CaS, the excitation and emission mechanism of the  $\text{Eu}^{2+}$  ion. An overview of LEDs, a brief description of the interaction of matter and laser energy, ablation and the eventual formation of a thin film has been presented.

### 2.2. Luminescent Materials

The word phosphor originating from the Greek word phosphoros, translating into ‘light bearer’, was used to describe a complex preter-natural solid, made by Casciarolo of Bologna, Italy, about 1603. This solid had the property of glowing in the dark after exposure to daylight [1]. Such a material is also called luminescent material. Luminescent materials, thus, are substances which convert energy incident on the material into the emission of electromagnetic waves in the ultraviolet (UV), visible or infrared (IR) regions of the electromagnetic spectrum. Examples of metal ion activator-based luminescent materials are  $\text{CaS}:\text{Eu}^{2+}$ ,  $\text{Y}_3\text{Al}_5\text{O}_{12}:\text{Nd}$ , and  $\text{SrAl}_2\text{O}_4:\text{Eu}^{2+}$ ,  $\text{Dy}^{3+}$

#### 2.2.1. Types of Luminescence

Luminescence describes spontaneous emission from atoms or molecules of a substance excited by some means. These atoms then release the excess energy in the form of ultraviolet, visible, or infrared radiation. Each type of luminescence may be referred to by a

name according to the method of excitation. For example: Luminescence excited by photons is called photoluminescence (PL), electroluminescence (EL) refers to excitation caused by the passage of an electric current through a specimen, and when excited by bombardment of high energy electrons, it is called cathodoluminescence (CL), when excited by chemical reactions it is called chemiluminescence. Thermoluminescence (TL) is the emission of light from an insulator or a semiconductor when it is heated, following the previous absorption of energy from ionizing radiations such as charged particles, ultraviolet, X-rays, and  $\gamma$ -rays [2, 3]. It must be pointed out here that heat is not an exciting source in TL, but it acts only as a stimulant. We give a more detailed treatment of PL, CL and TL in the sections which follow (2.3, 2.4, and 2.5, respectively).

### 2.3. Photoluminescence

Luminescence in solids, i.e. inorganic insulators and semiconductors, is classified in terms of the nature of the electronic transitions producing it. It can either be intrinsic or extrinsic. In the intrinsic photoluminescence process, the luminescence results from the inherent defects present in the crystal structure [4]. This type of luminescence does not involve impurity atoms. Extrinsic photoluminescence on the other hand, results from the intentionally incorporated impurities in the crystal structure [5]. Fig. 2.1 schematically illustrates the absorption of a high energy photon and the subsequent emission of a low energy photon, which is the photoluminescence process.

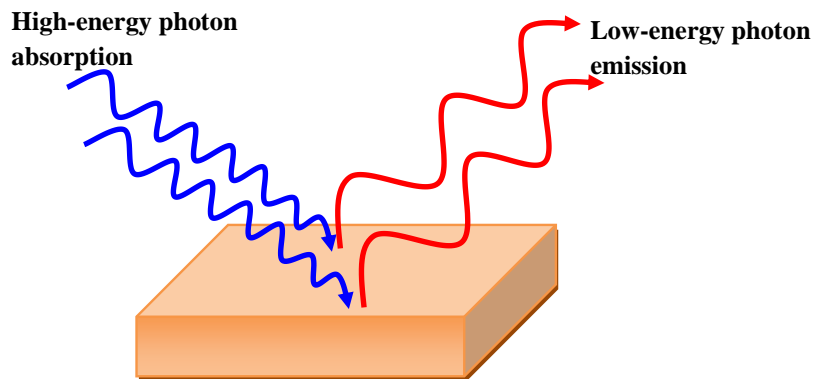


**Figure 2.1:** Schematic illustration of photoluminescence.

### 2.3.1. Fluorescence and Phosphorescence

Depending on the duration of the decay lifetime (the average time an electron stays in its excited state before returning to ground state), PL can be divided into two types: fluorescence and phosphorescence. Light emission from a substance during the time when it is exposed to exciting radiation is called fluorescence, while the after-glow if detectable by the human eye after the cessation of excitation is called phosphorescence [6], thus in fluorescence the emission of photons stops almost immediately when excitation is cut off [7]. Fluorescence processes normally have decay times lower than 10 ns, while phosphorescence processes have decay times of more than 100 ns [8]. Simply put, fluorescence refers to spontaneous emission from an excited state produced by the absorption of light, while phosphorescence describes the situation in which the emission persists long after the exciting light is turned off. Another difference between phosphorescence and fluorescence is that the former is temperature dependent, while the latter is essentially independent of temperature; phosphorescence being associated with shallowly trapped charge carriers [9]. In Fig. 2.2, absorbed energy excites electrons from ground state (gs) to excited state (es). Fluorescence takes place when the electron returns to ground state through transition (2). However, if the excited electron makes a transition (3) to a metastable state (ms), which may be a defect, it can remain there until it receives enough energy to return to es through (4). Upon its relaxation to ground state, it displays a delayed emission, which is phosphorescence.

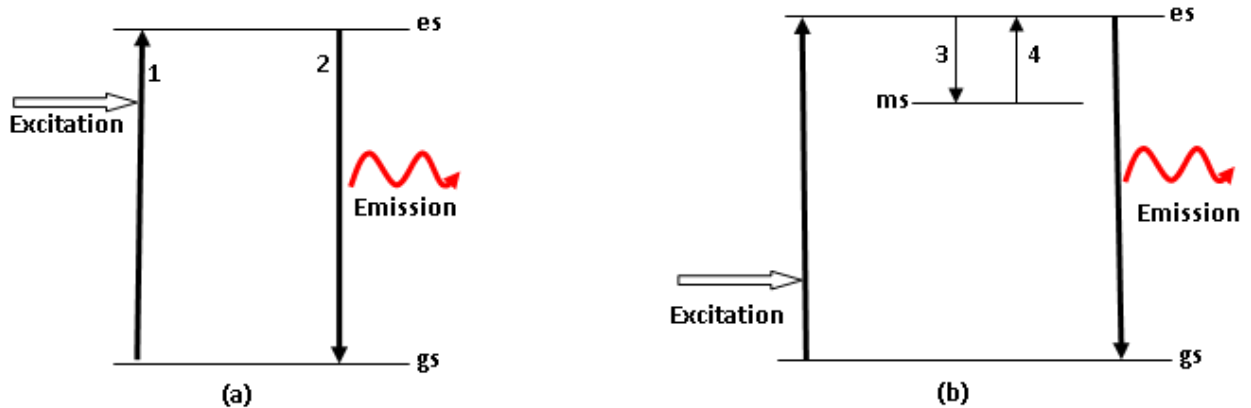


**Figure 2.2:** A schematic representation of (a) fluorescence, and (b) phosphorescence emissions.

### 2.3.2. Excitation Mechanism

The absorption of energy, which is used to excite the luminescence, takes place by either the host lattice or by intentionally doped impurities. In most cases, the emission takes place on the impurity ions, which, when they also generate the desired emission, are called activator ions. When the activator ions show too weak an absorption, a second kind of impurity known as sensitizer can be added, which absorb the energy and subsequently transfer the energy to the activators, thus inducing luminescence [10]. Fig 2.3 is a schematic representation of the role in the luminescence process of an activator (A) and a sensitizer (S) doped into a host (H) lattice [11]. In the present study, calcium sulfide (CaS) was used as the host, while  $\text{Eu}^{2+}$  was used as the activator.

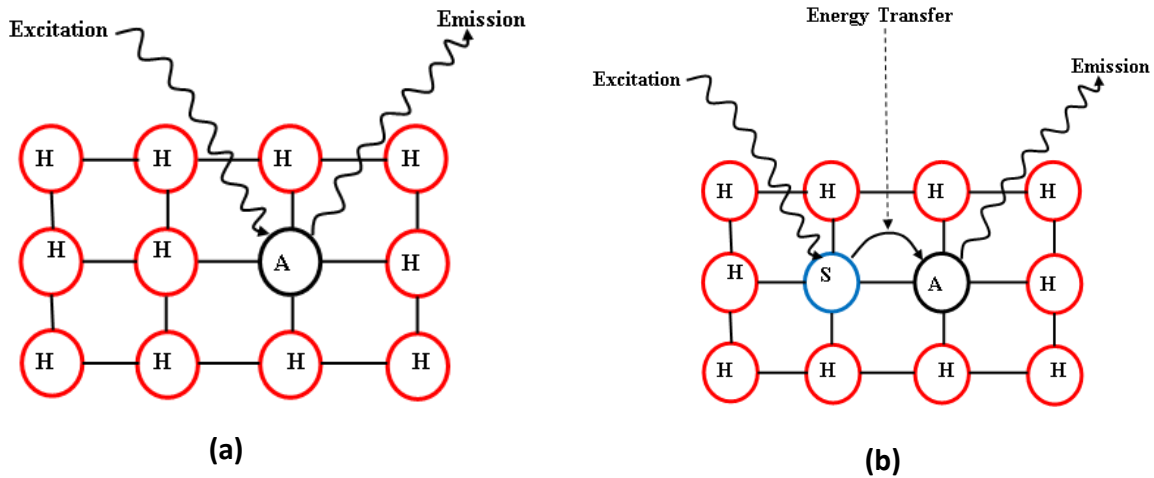


**Figure 2.3:** (a) Schematic representation showing energy absorption by an activator (A) doped in a host (H) lattice, and (b) energy transfer by a sensitizer (S) to an activator (A) and the subsequent emission in both cases.

### 2.4. The Cathodoluminescence Process

When an electron beam impinges on a crystal, a number of physical processes take place, which include emission of X-rays, back-scattered electrons, Auger electrons etc. A little of the total energy carried in the beam acts to promote nonlocalized electrons from the valence band to the conduction band, as schematically indicated in Fig. 2.4(b), leaving holes behind

in the valence band. That is, the electrons go from the ground state to an excited state. After a short time, these promoted electrons undergo de-excitation and return to a lower-energy state, moving randomly through the crystal structure until they encounter a trap that momentarily intercept and hold electrons as they move through the band gap to the valance band, as shown schematically in Fig. 2.4(c). As indicated in Fig. 2.4, electrons may encounter a single trap or multiple traps as they move through the band gap. Those traps that empty promptly, producing photons with energies in the near-UV and visible portions of the electromagnetic spectrum, are the basis for cathodoluminescence (CL). The intensity of the CL is generally a function of the density of the traps. If no traps are present, electrons fall directly back to the valence band and emit photons with wavelengths in the near ultraviolet. Fig.2.5 shows a schematic representation of the cathodoluminescence process.

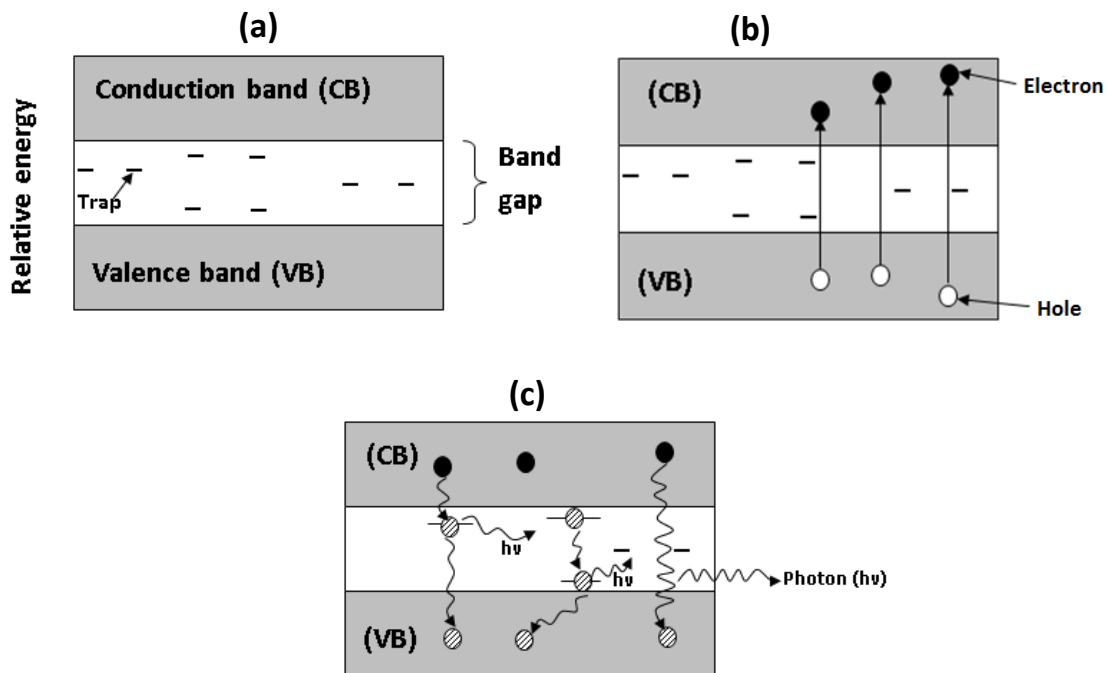


**Figure 2.4:** Schematic representation of the processes that cause CL generation in a phosphor, (a) the traps within the band gap (b) electrons promoted from valence to conduction band (c) emission of photons from traps and band to band [12].

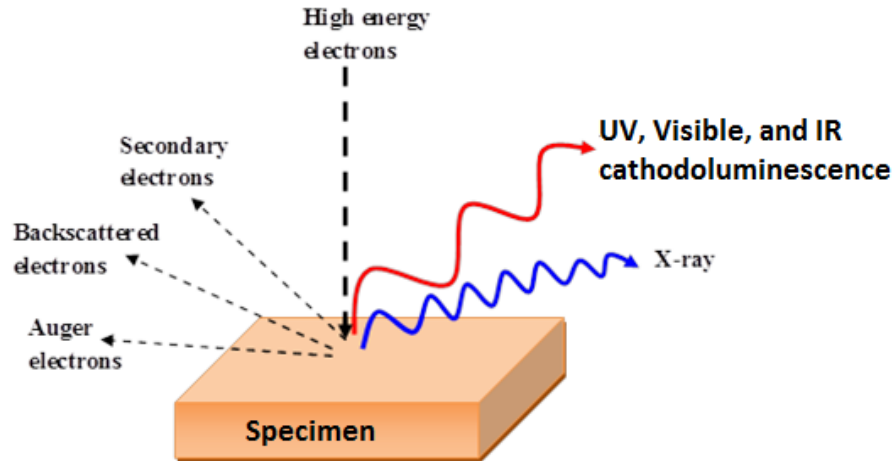


**Figure 2.5:** Schematic illustration of the effects produced by electron-beam interaction with a specimen to produce cathodoluminescence.

## 2.5. Mechanism of Thermoluminescence

### 2.5.1. The Thermoluminescence Process

Imperfections in a crystal, associated with impurities and /or lattice defects may create new localized energy levels in the forbidden gap. On irradiation, an electron (or hole) from the valence band can be trapped at these sites. Some electrons can also be trapped when they de-excite from the conduction band. Thermoluminescence (TL) measurements are useful in defects and impurities related studies in phosphors in that we are able to explain phenomena like persistence of luminescence. In these experiments, a phosphor is excited with some radiations for a desired period of time after which the exciting radiation is removed. The exciting source may be UV light, X-rays, gamma rays, alpha particles, electrons, ion beam, neutrons, etc. The material is then stimulated by heating at a constant rate and the light intensity output is measured as a function of temperature of the phosphor. The results are plotted to give a graph known as TL glow curve. A glow curve may exhibit one or more peaks depending upon the number of electron/hole traps present in the lattice. The position of the peaks on the temperature scale is a measure of the energy depth of the trapped electrons in the solid, while area under the peak often indicates the number of electrons transferred into



these traps by exciting radiations [13]. These peaks may be well resolved or may not be well separated. The position, shape and intensity of the glow peaks therefore are characteristic of the specific material and the impurities and defects present. Thus, the nature of the TL glow peaks gives information about the luminescent centers present in the material.

### 2.5.2. A General Model to Explain the TL Mechanism

The production of TL in a sample by exposure to ionizing radiation may be divided into two stages:

- i) Electron and/or hole trapping,
- ii) electron and hole recombination with photon emission.

The energy band configuration shown in Fig. 2.6 is a simplified model used to explain the TL process.

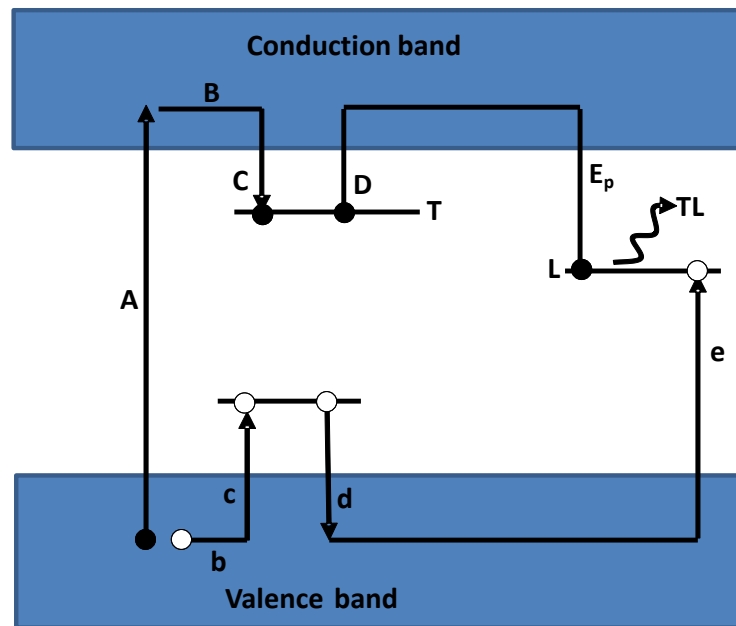


**Figure 2.6:** A general energy band model showing the electronic transitions in thermoluminescence material.

When an ionizing radiation is absorbed by the phosphor material, free electrons are produced, which is equivalent to transferring electrons from the valence band to the

conduction band (A). These electrons are free to move through the crystal (B), but if trapping levels such as (T) are present, the electrons may be trapped. The production of free electrons is associated with the production of free holes which may also migrate via the valence band (b) and may also be trapped (c). Majority of hole centres are thermally unstable and may decay rapidly at room temperature (d). Provided they do not acquire sufficient energy, the trapped electrons remain in the traps. This will be determined by the trap depth and temperature of a particular material. If the temperature of the material is raised, trapped electrons may acquire sufficient thermal energy to escape, indicated by D. Released electrons may recombine with holes at the luminescent centre (L) and emit visible or UV photons ( $E_p$ ). The TL mechanism is thus the capture of an electron, and delayed recombination with a hole at a luminescent centre (L).

As the phosphor is heated, the probability of releasing any particular electron is increased and at some temperature there is virtual certainty of its release. The emission (TL) will thus start to increase, go through a maximum and then decrease again to zero [14].

The equations governing the thermoluminescence processes have been given by Randall-Wilkins [15], Garlick-Gibson [16] and May-Partridge [17] for first, second, and general orders, respectively:

$$I(t) = -\frac{dn}{dt} = nse^{-E/kT} \quad (2.1)$$

$$I(t) = -\frac{dn}{dt} = \frac{n^2}{N} se^{-E/kT} \quad (2.2)$$

$$I(t) = -\frac{dn}{dt} = n^b s' e^{-E/kT} \quad (2.3)$$

Where  $E$ ,  $b$ , and  $s$ , referred to as kinetic parameters are the activation energy or trap depth, the kinetic order, and frequency factor, respectively.  $T$  is the absolute temperature, and  $k$  is the Boltzmann constant, while  $N$  is the total trap concentration,  $n$  is the concentration of trapped electrons at a time  $t$ , and  $s'$  is the effective preexponential factor for general order kinetics. First order kinetics assume that every charge carrier released from a trap recombines in a luminescent center, while second order kinetics proposes 'retrapping' and recombination of charge carriers.

### 2.5.3. Methods of Analysis

Various techniques have been developed over time to derive the kinetic parameters from the TL glow curve. Some of them are the initial rise methods, whole glow curve, peak position, peak shape methods, methods of various heating rates, curve fitting methods, etc. [9, 18]. A detailed treatment of these methods has been presented in [18]. However, we will delve a bit more on the theoretical background of the initial rise (IR) method.

The initial rise method of analysis first suggested by Garlick and Gibson [16], applies to any order of kinetics. It is based on the analysis of the low temperature interval of the peak up to a temperature ( $T_c$ ) corresponding to TL intensity ( $I_c$ ) below 15% of the maximum intensity ( $I_M$ ) as illustrated in Fig. 2.7 [18]. Assuming that the amount of trapped electrons in the low temperature tail of a TL glow peak to be approximately constant, they described the thermoluminescence emission by the expression of Eq. (2.4).

$$I(T) \propto \exp\left(\frac{-E}{kT}\right) \quad (2.4)$$

where  $E$  is the activation energy of the electrons within the trap centre and  $k$  is Boltzmann constant. A graph of  $\ln(I)$  vs  $1/kT$ , gives a straight line whose slope is  $-E$  [18], thus allowing us to evaluate the activation energy.

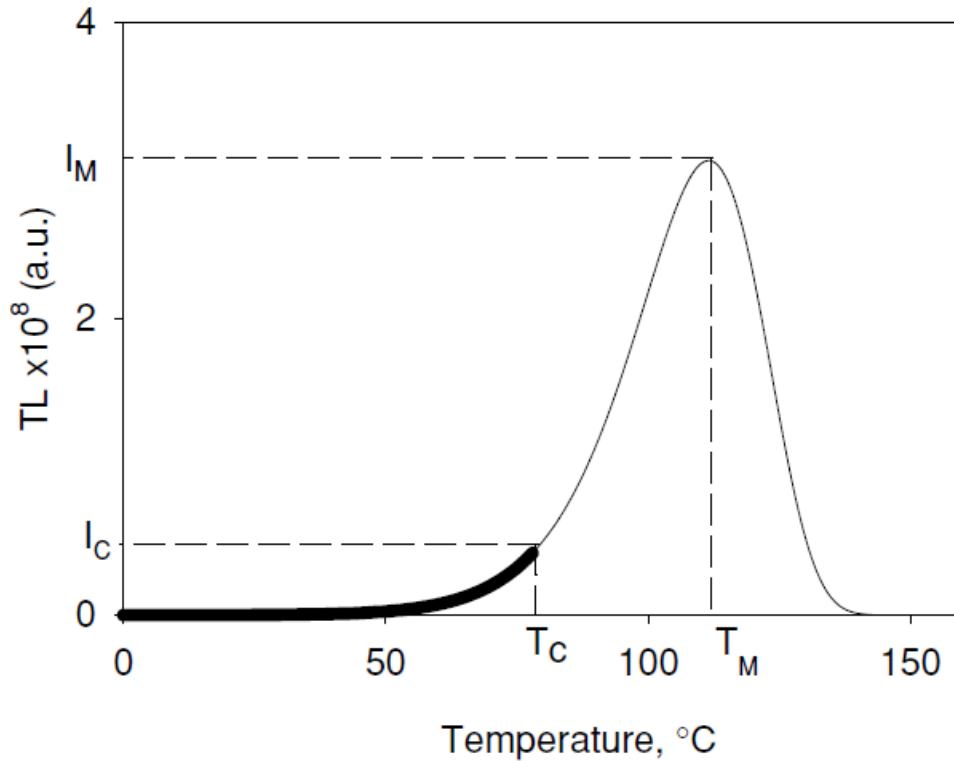


**Figure 2.7:** The initial rise part of a thermoluminescence glow curve [18].

## 2.6. Calcium Sulfide as a Host Lattice

The CaS host is a group II-VI wideband semiconductor whose band gap is 4.43 eV, with a lattice constant of 5.697 Å [19]. It crystallizes into a rock salt (sodium chloride) cubic type structure as shown in Fig. 2.8. In the crystal, each  $S^{2-}$  ion is surrounded by an octahedron of six  $Ca^{2+}$  ions, and complementarily, each  $Ca^{2+}$  ion is surrounded by six  $S^{2-}$  ions to make  $O_h$  symmetry [20]. When doped, for example with  $Eu^{2+}$ , the  $Eu^{2+}$  ion sits in the site of  $Ca^{2+}$ . Since the  $Ca^{2+}$  and  $Eu^{2+}$  ions have similar ionic radii of 114 and 131 pm, respectively, the local symmetry of the  $Ca^{2+}$  site will not deviate much from that in the pure material upon  $Eu^{2+}$  doping.

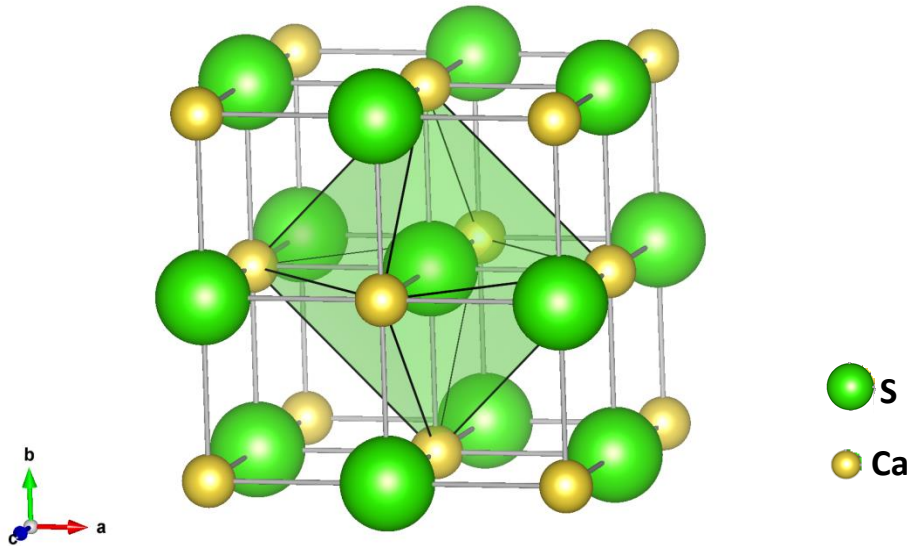


**Figure 2.8:** Schematic view of the face centered cubic structure of CaS.

## 2.7. Luminescent Centres

An impurity (dopant) atom or defects responsible for the luminescence of a phosphor form a luminescent or emitting centre. A wide variety of centres give rise to luminescence in semiconductors and insulating materials, including rare-earth ions such as europium. Some luminescence spectra consist of broad emission bands arising from the interaction between the electronic system of the luminescent centre and the vibrations of the atoms or ions, which surround it; the broad bands arise from simultaneous transitions of both electronic and vibrational systems. The other type of spectra comprises sharp lines arising from purely electronic transitions, and the effect of the environment is felt mainly through their effects on the lifetimes of the states.

Europium (Eu) is a member of the lanthanide series of elements with atomic numbers 57 through 71, from lanthanum (La) through lutetium (Lu), respectively. Together with scandium and yttrium, these fifteen lanthanides are known as rare-earth (RE) elements. They are characterized by a partially filled 4f-electron shell. The numerous optical transitions between the 4f states have made the lanthanides the most popular activator ions for lightning

and display applications [21]. The Eu ion, our lanthanide of interest, has two stable oxidation states, namely  $\text{Eu}^{2+}$  and  $\text{Eu}^{3+}$ .

### 2.7.1. The $\text{Eu}^{2+}$ Ion as the Activator

In the divalent state, the  $\text{Eu}^{2+}$  is coordinated as  $[\text{Xe}]4f^7$  having a ground state of  $4f^7 ({}^8S_{7/2})$ . Thus, the  $\text{Eu}^{2+}$  ion has seven  $f$  electrons which form a stable half-filled  $4f$  valence shell. These seven  $4f$  electrons do not strongly interact with the environment of the host material because they are effectively shielded by filled  $5s^2$  and  $5p^6$  shell and thus are affected weakly by changes in the environment. The first excited state is the  $[\text{Xe}]4f^6 5d^1$  after one of the  $4f$  electrons is excited to the  $5d$  level. This electron is strongly influenced by the crystal field, leading to broad, host dependent  $5d \rightarrow 4f$  emission bands. The five  $4f^6 5d^1$  orbitals are split by the octahedral crystal field into the  $t_{2g}$  band with the triple degenerate  $xy$ ,  $yz$ , and  $zx$  orbitals and the  $e_g$  band with the doubly degenerate  $x^2-y^2$  and  $z^2$  orbitals [22]. These bands give rise to an absorption or excitation spectrum comprising of two broad bands. As the position of the band corresponding to the  $4f^6 5d^1$  configuration is strongly influenced by the host, the emission can be anywhere from ultraviolet (UV) to visible [23]. For instance,  $\text{SrS}:\text{Eu}^{2+}$  and  $\text{CaS}:\text{Eu}^{2+}$  have emissions at 615 and 652 nm, respectively [23, 24], arising from the transition from the lower  $4f^6 5d^1 (t_{2g})$  state to the  $4f^7 ({}^8S_{7/2})$  ground state of  $\text{Eu}^{2+}$ . The  $\text{Sr}^{2+}$  and  $\text{Eu}^{2+}$  have similar sizes, but  $\text{Ca}^{2+}$  is notably smaller therefore, it exerts higher crystal field strength on its surroundings. Crystal field splitting of 1.49 and 1.86 eV, have been reported in [25] for  $\text{SrS}:\text{Eu}^{2+}$  and  $\text{CaS}:\text{Eu}^{2+}$ , respectively. The schematic diagram for crystal-field splitting of  $\text{Eu}^{2+}$   $5d$  energy levels is shown in Fig. 2.9. Sharp line spectra due to  $4f^7 \rightarrow 4f^7$  transitions are observed from  $\text{Eu}^{2+}$  in cases where the lowest excited state,  $4f^7 ({}^6P_{7/2})$  is lower than  $4f^6 5d^1$ .

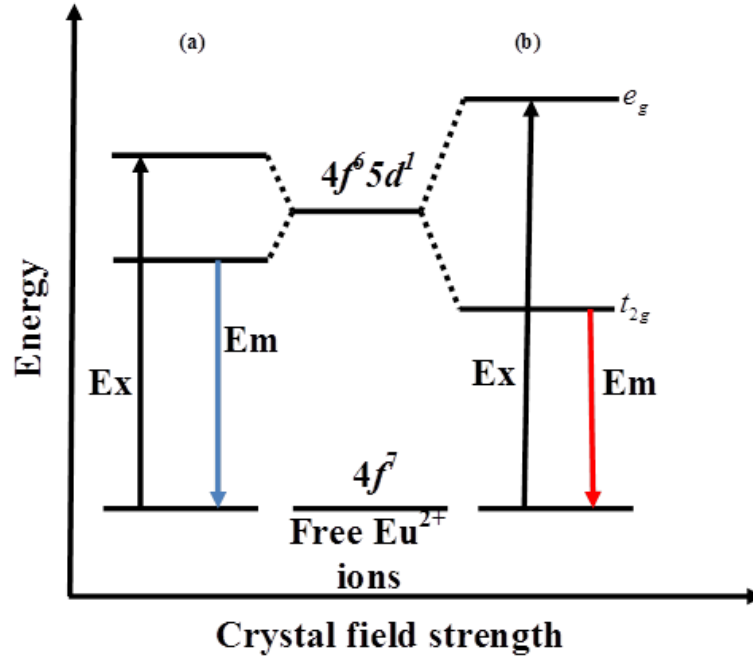


**Figure 2.9:** Schematic diagram for  $\text{Eu}^{2+}$  5d energy levels in (a) weak and (b) strong crystal fields.

### 2.7.2. The $\text{Eu}^{3+}$ Ion

On the other hand, the trivalent ( $\text{Eu}^{3+}$ ) rare earth ion has an outer electronic configuration  $5s^2 5p^6 4f^6$ , with the  $4f^6$  electrons shielded by the completely filled  $5s^2$  and  $5p^6$  subshells; thus, they are strongly isolated from the lattice environment. As a result, the transition energies among the  $^{2S+1}L_J$  manifolds within the  $4f^n$  configuration of a rare earth ion are hardly influenced by the type of host material [26]. The luminescence due to  $\text{Eu}^{3+}$  originates from  $4f^6 \rightarrow 4f^6$  transitions characterized by narrow emission bands in the red spectral range. Majority of the lines belong to transitions from the  $^5D_0$  level to the  $^7F_J$  ( $J = 0, 1, 2, 3, 4, 5, 6$ ) levels, although transitions from other 5D-levels are also observed [27].

## 2.8. Basic Principles of Inorganic Light Emitting Diodes

### 2.8.1. The Structure of a Light Emitting Diode

Light-emitting diodes (LEDs) are solid-state devices that can generate light having a peak wavelength in a specific region of the light spectrum [28]. The basic structure of an LED is a p-n junction. Under forward bias of a p-n junction, electrons injected from n-side recombine with holes injected from p-side. This recombination may result in the emission of a photon, depending on whether the recombination is radiative or non-radiative. The operation and structure of a light emitting diode is shown in Fig.2.10 [29].

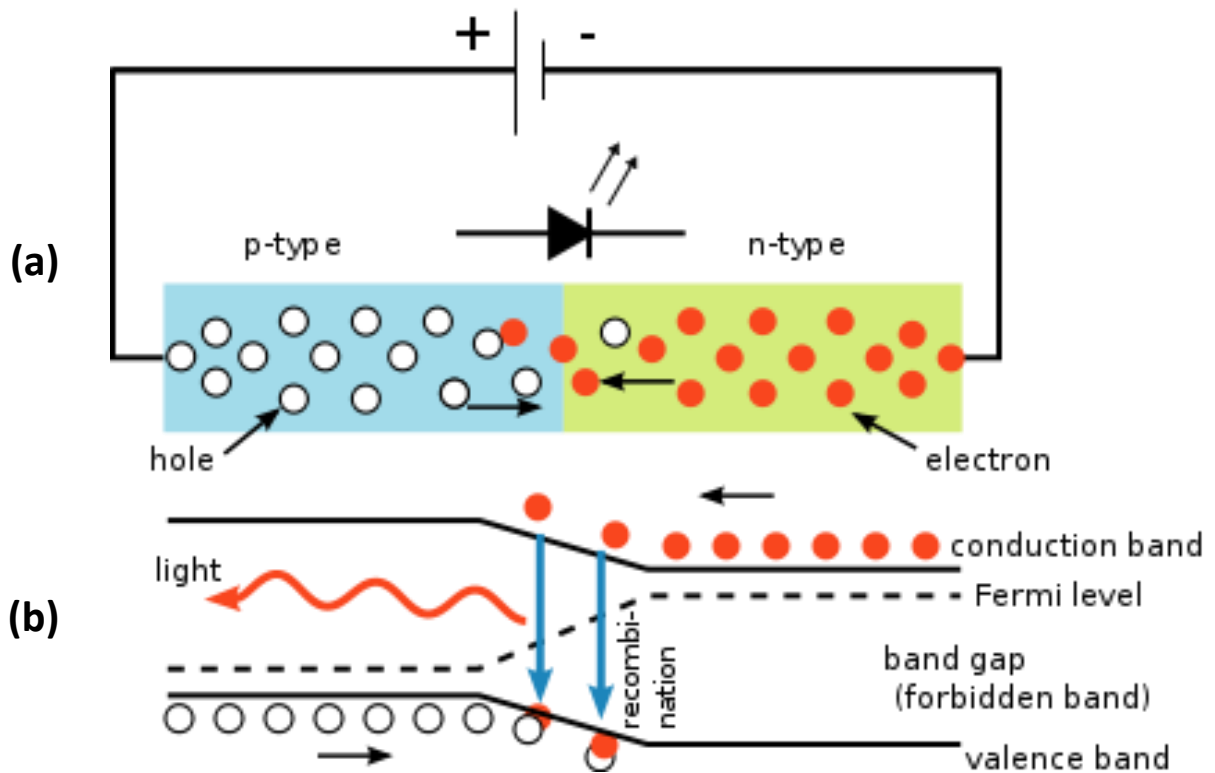


**Figure 2.10:** The principle of operation and structure of an LED, showing (a) circuit (a) and (b) band diagram.



The requirement of energy and momentum conservation leads to further insight into the radiative recombination mechanism. It follows from the Boltzmann distribution that electrons and holes have an average kinetic energy of  $kT$ . Energy conservation requires that the photon energy is given by the difference between the electron energy,  $E_e$ , and the hole energy,  $E_h$ , i.e.

$$h\nu = E_e - E_h \approx E_g \quad (2.5)$$

The photon energy is approximately equal to the band gap energy,  $E_g$ , if the thermal energy is small compared with the band gap energy, that is,  $kT \ll E_g$ . Thus, the desired emission wavelength of an LED can be attained by choosing a semiconductor material with an appropriate band gap energy.

It is helpful to compare the average carrier momentum with the photon momentum. A carrier with kinetic energy  $kT$  and effective mass  $m^*$  has the momentum

$$p = m^* v = \sqrt{2m^* \frac{1}{2} m \times v^2} = \sqrt{2m^* kT} \quad (2.6)$$

The momentum of a photon with energy  $E_g$  can be obtained from the de Broglie relation

$$p = \frac{h\nu}{c} = \frac{E_g}{c} \quad (2.7)$$

Calculation of the carrier momentum (using Eq. (2.6)) and the photon momentum (Using Eq. (2.7)) yields that the carrier momentum is orders of magnitude larger than the photon momentum. Therefore the electron momentum must not change significantly during the transition. The transitions are therefore “vertical” as shown in Fig. 2.11; i. e. electrons recombine with only those holes that have the same momentum or  $k$  value. [30].

Thus, efficient recombination occurs in direct-gap semiconductors. The recombination probability is much lower in indirect-gap semiconductors because a phonon-assisted recombination is required to satisfy momentum conservation.

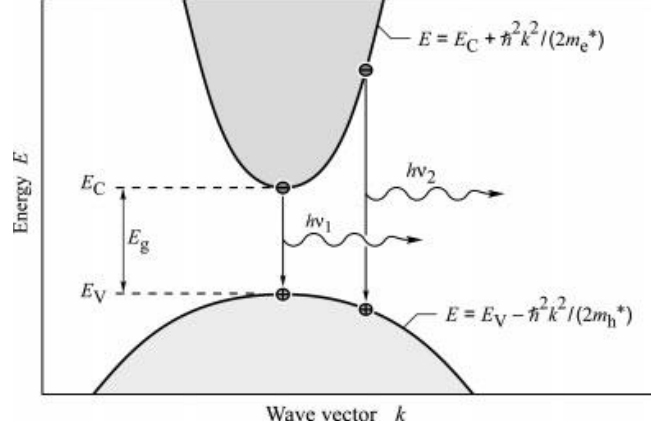


**Figure 2.11:** Parabolic electron and hole dispersion relations showing “vertical” electron-hole recombination and photon emission [30].

### 2.8.2. Luminous Efficiency and Color Rendering Index

Luminous efficiency and color rendering index (CRI) are important parameters in the design of white LEDs for general lighting. Color rendering is a property of a light source that shows how natural the colors of objects look under a given illumination.

For LED applications in display and illumination, the luminous efficiency is an important parameter. The brightness of light output is measured by the luminous flux (in lumens),

$$\text{Luminous flux} = L_0 \int V(\lambda) P_{op}(\lambda) d\lambda \text{ lm} \quad (2.8)$$

where  $L_0$  is a constant with a value of 683 lm/W,  $V(\lambda)$  the relative eye sensitivity, and  $P_{op}(\lambda)$  the power spectrum of the radiation output. The eye sensitivity function  $V(\lambda)$  is normalized to unity for the peak at  $\lambda = 555$  nm.

The luminous efficiency is then given by Eq. 2.9 from Ref. [31]:

$$\eta_{lu} = \frac{\text{luminous flux}}{\text{electrical power in}} = \frac{683 \int V(\lambda) P_{op} d\lambda}{VI} \text{ lm/W} \quad (2.9)$$

The maximum luminous efficiency has a value of 683 lm/W.

### 2.8.3. Common LED Materials

Some common inorganic semiconductor materials for producing LEDs given in Ref. [29] are:

**a) AlGaAs (Aluminium gallium arsenide):** The  $\text{Al}_x\text{Ga}_{1-x}\text{As}$  systems cover a wide range of wavelengths from red to infrared.

**b) InAlGaP (Indium aluminium gallium phosphide).** This material system emits in higher energies than AlGaAs, covering a wide range of the visible spectrum, i.e., red, orange, yellow, and green.

**c) InGaN (Indium gallium arsenide).** This material has a wide spectrum covering green, blue, and violet. More importantly, it is an important provider for blue and violet which had been difficult from a material point of view.

### 2.8.4. White Light LEDs

There are two primary ways of producing white light-emitting diodes (wLEDs) that generate high-intensity white light. In the first method, individual LEDs, each emitting one of the three primary colors; red, green, or blue, are combined to form white light. The second method involves using a phosphor material to convert monochromatic light from a blue or UV LED to produce broad-spectrum white light, much in the same way a fluorescent light bulb works. For purpose of our work, we only focus on phosphor-based LEDs.

### 2.8.5. Phosphor-based LEDs

Phosphor-based LEDs use a wavelength converter coated on a LED of one color to form white light; the resultant LED is called phosphor-based or phosphor-converted white LED (pcwLED).

A wavelength converter is a material that absorbs the original LED light and emits light of different frequency. The converter material can be a phosphor, organic dye, or another semiconductor [32]. For a phosphor conversion, white light can be obtained by coating a blue

light LED, emitting at 460 nm with YAG:Ce<sup>3+</sup>, a yellow emitting phosphor [33], as illustrated in Fig. 2.12. The mixture of the unabsorbed blue light from the blue LED and the yellow from the down-conversion phosphor results in a white light emission. A disadvantage of the application of a single yellow phosphor is that low color temperatures (warm white light) cannot be achieved with a high color rendering because of the lack of red light in the LED spectrum. In addition, the color rendering of cool white LEDs depends on the driving conditions. These problems are solved by trichromatic white LEDs comprising two phosphors [34], such as CaS:Eu<sup>2+</sup> (red) and CaS:Ce<sup>3+</sup> (green) because they have strong absorption in the blue region [19].

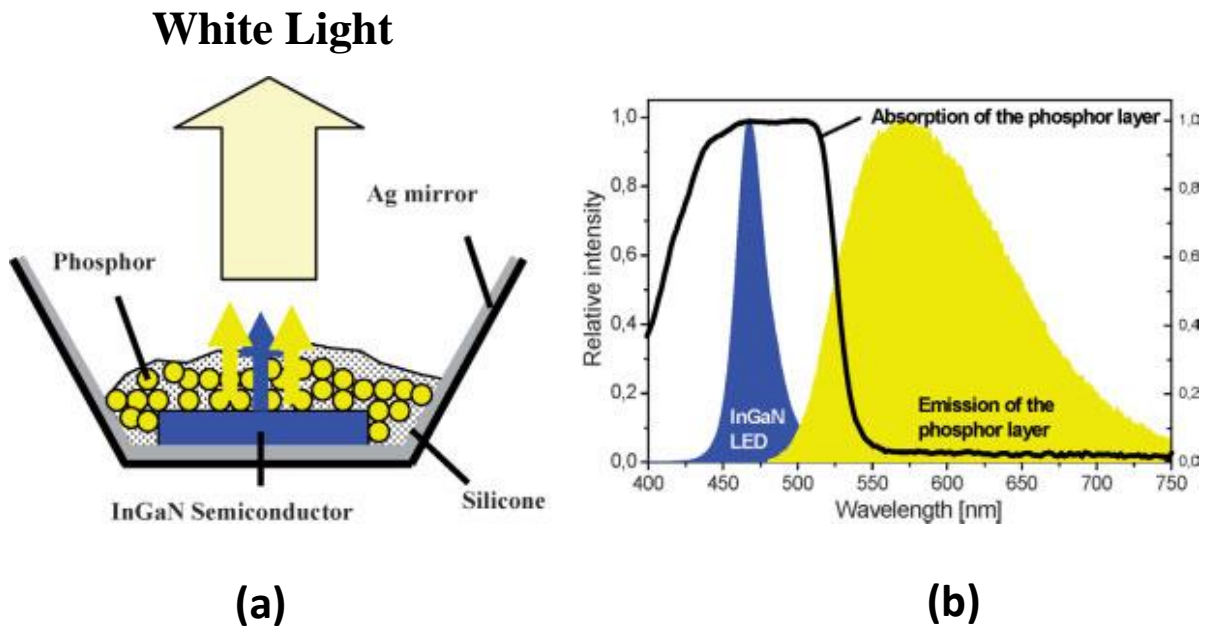


**Figure 2.12:** Principle of color conversion in a LED, (a) InGaN phosphor-converted pcLED, (b) spectrum of a white LED showing blue light directly emitted by InGaN-based LED and the more broadband stokes-shifted light emitted by a phosphor e.g. YAG:Ce<sup>3+</sup> [33, 34].

The host lattice must show high chemical and thermal stability in order to survive the LED lifetime of more than 10 000 h [35]. Moreover, the phosphor should have a short decay time to avoid saturation at high drive levels, since this will result in a change, i.e. a blue-shift, of the LED spectrum with driving conditions. A broad emission band is necessary in order to achieve high color rendering index. Most prominent LED converter materials are thus

activated by those ions relying on allowed  $4f \rightarrow 5d$  transitions, i.e.  $\text{Eu}^{2+}$  and  $\text{Ce}^{3+}$ , which are doped into rigid host lattices (oxides, nitrides, and sulfides).

### 2.8.6. UV- pumped Phosphor-based White LEDs Using a Single Host

White light LEDs can also be fabricated by optical excitation of phosphor in the ultraviolet (UV) wavelength range [36]. LEDs emitting in the UV are required for such white LEDs. In UV-pumped white LEDs, the entire visible emission originates in the phosphor.

Recently several workers have demonstrated that white light can be generated from a single host doped with one or more rare-earth ions or transition metal ions. For example, Shaat et al., [37] Kim et al., [38] and Lee et al. [39] have, respectively, observed white light from  $\text{Ca}_x\text{Sr}_{1-x}\text{Al}_2\text{O}_4:\text{Tb}^{3+}$ ,  $\text{Eu}^{3+}$ ,  $\text{Ba}_3\text{MgSi}_2\text{O}_8:\text{Eu}^{2+}$ ,  $\text{Mn}^{2+}$  and  $\text{CaMgSi}_2\text{O}_6:\text{Eu}^{2+}$ ,  $\text{Mn}^{2+}$  phosphors.

A fundamental disadvantage of UV-pumped white LEDs is the relatively high energy loss incurred when converting UV light to white light. The luminous efficiency of UV-pumped white LEDs is therefore markedly lower than white LEDs with excitation in the blue wavelength range [30].

### 2.8.7. Advantages and Applications of LEDs

LEDs have many advantages over incandescent light sources including lower energy consumption, longer lifetime, improved physical robustness, smaller size, faster switching, safety and its environmental-friendly characteristics [40-45].

Light-emitting diodes are now used in applications as diverse as aviation lighting, automotive headlamps, traffic signals, advertising, general lighting, and camera flashes, back-illuminated liquid crystal displays in mobile phones, tablets, laptops, etc. Fig.2.13 shows some applications of LEDs. An exciting development is the use of LEDs in street lighting [46]. This smart, 'green' option for outdoor LED lighting has emerged on the green scene due to the recent technological advancements of LED illumination.

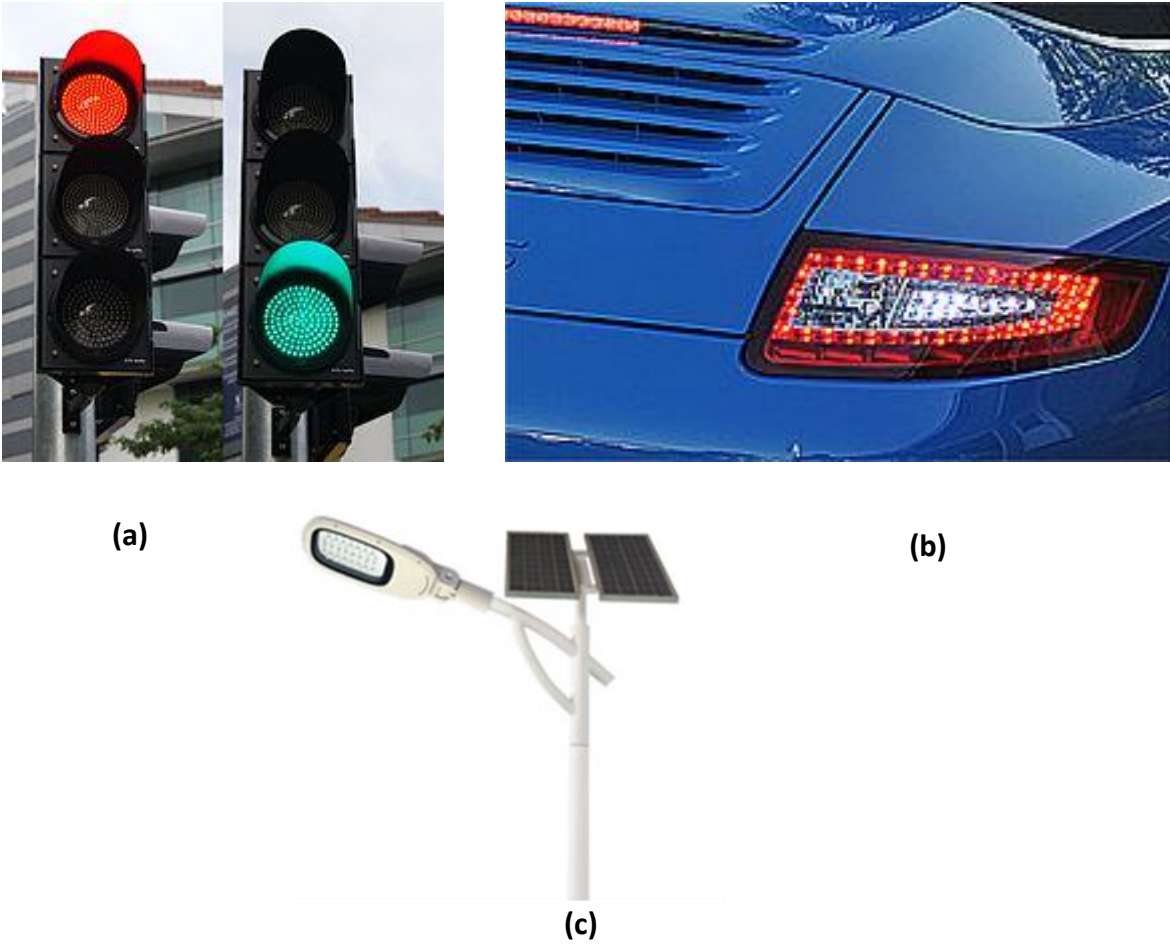


**Figure 2.13:** Some applications of LEDs; (a) red and green traffic signals, (b) red and white-emitting LEDs in an automobile, (c) solar street light using LEDs.

## 2.9. The Pulsed Laser Deposition Process

Pulsed laser deposition (PLD) can be described as a four-step process:

- Absorption of the laser radiation
- Ablation of the target material
- Formation of a highly energetic plume
- Growth of the film on the substrate

### 2.9.1. Laser-material Interaction

Laser systems which have found wide use in the PLD process are the Nd: YAG (1064 nm, 532 nm, 355 nm, 266 nm), operable in Q-switched mode, ruby (694 nm), and excimers (XeCl at 308 nm, KrF at 248 nm, and ArF at 193 nm) [47]. Laser-material interaction involves both thermal and photochemical (electronic) mechanisms. Photochemical contribution is most evident when using very short (sub-picosecond) pulse duration while thermal contributions dominate when using longer (nanosecond) duration laser pulses [48]. Inside the target material, the laser intensity  $I$  of the radiation decays exponentially with the depth  $x$  according to the Beer–Lambert law [49]:

$$I(x) = I(x_0)e^{-\alpha(x-x_0)} \quad (2.10)$$

where  $I(x)$  is the intensity at a point  $x$  below the surface of the target material,  $I(x_0)$  is the intensity at a surface point  $x_0$  and  $\alpha$  is the absorption coefficient, which determines the depth at which light energy of a certain wavelength penetrates the target material. The optical penetration or absorption depth,  $\delta$ , which is the depth at which the intensity of the transmitted light drops to  $\frac{1}{e}$  of its initial value at the interface has been defined in Ref. [50]

as:

$$\delta = \frac{1}{\alpha} \quad (2.11)$$

$\alpha$  is defined in [51] as:

$$\alpha = \frac{4\pi\kappa_a}{\lambda} = \frac{2\omega\kappa_a}{c} = \frac{4\pi n\kappa_0}{\lambda} \quad (2.12)$$

where  $\kappa_a = n\kappa_0$  is the absorption index,  $\kappa_0$  the attenuation index, and  $n$  is the refractive index of the material, respectively. Thus, the depth of penetration depends on the absorption coefficient for a given laser wavelength.

### 2.9.2. Ablation and Plume Formation

The extremely short laser pulses, each lasting less than 50 ns, cause the temperature of the surface to rise rapidly to thousands of degrees Celsius, but the bottom of the target remains virtually unheated; close to room temperature. Such non-equilibrium heating produces a flash of evaporants directed towards the substrate. Fig. 2.14 shows a schematic of the absorption of laser radiation by the target, and the formation of a plume, which also absorbs the later part of the incident laser pulse. The excitation and ionization of species in the plume leads to the formation of a plasma plume which expands along the direction normal to the target surface. When it reaches the substrate, placed in front of the target, part of the evaporated material will form a thin film with composition identical to that of the target surface on this substrate.

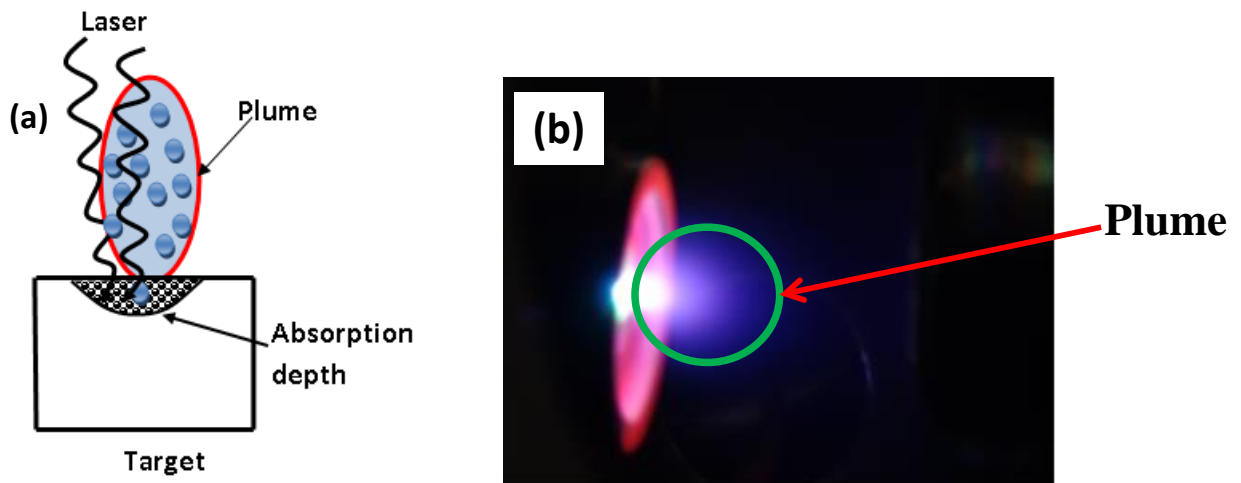


**Figure 2.14:** Schematic illustration and photograph, showing: (a) absorption of laser radiation by a target and the plume (b) an image of CaS:Eu<sup>2+</sup> plume formed by a 266-nm laser.



### 2.9.3. Film Growth

The amount of film growth per laser pulse will depend on multiple factors, including target–substrate separation, background gas pressure, and laser energy density. Once on the surface, adsorbed particles may move on the surface, diffuse or nucleate with pre-existing surface atoms and clusters. Three different growth modes, schematically depicted in Fig. 2.15, as suggested in [52] are distinguished:

- The Volmer–Weber growth mode takes place when there is no bonding between film and substrate, leading to three-dimensional islands.
- In a case where the adhesive energy between atoms and substrate exceeds the cohesive energy between ablated atoms, then a smooth monolayer is encouraged subsequent to which further layer by layer (Frank-Van de Merwe) or
- Island-layer (Stranski- Krastanov) deposition on the monolayer may occur.

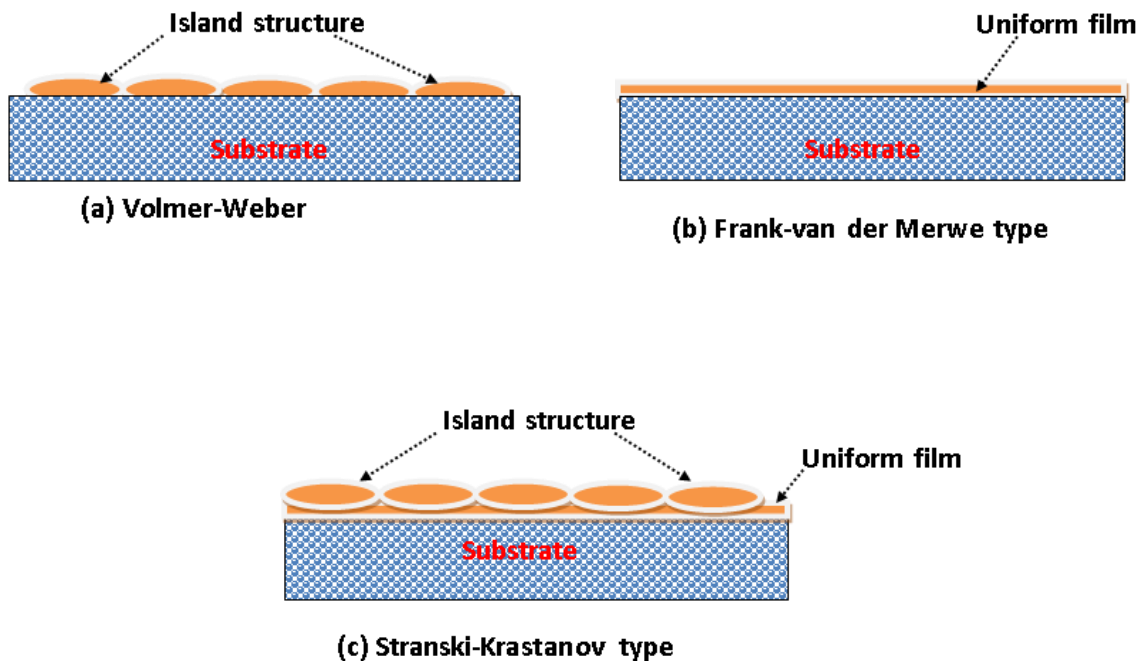


**Figure 2.15:** Film growth modes. Adapted from [53] (a) Volmer-Weber (Island) (b) Frank-van der Merwe (layer-by-layer) (c) Stranski-Krastanov

#### **2.9.4. Advantages of PLD and Draw Back**

The PLD technique has a number of advantages over conventional thin-film deposition techniques (e.g. spray pyrolysis, molecular beam epitaxy, thermal evaporation, etc.), which include cost-effectiveness, inherent simplicity for the growth of multilayered structures, small size target size, clean deposition due to the absence of atmospheric gases, and a film surface identical to that of the target [54- 56]. Apart from the stoichiometric transfer of material from the target, the PLD method is versatile in that many experimental parameters can be changed, which then have a strong influence on the film properties, and almost all materials can be ablated.

One of the major drawbacks of the PLD technique is related to the presence of various types of particulates, both on the surface of the films as well as embedded into the bulk. This is often observed when the penetration depth of the laser pulse into the target material is large [57].

#### **2.9.5. Origin of Particulates and Methods of Overcoming Particulates**

- material dislocation caused by the sub surface superheating of the target,
- liquid phase expulsion under the action of the recoil pressure of the ablated substance (vapour and plasma),
- Condensation (clustering) of the evaporated material in the expanding plumes, blast-wave explosion at the liquid (melt)–solid interface, and/or Hydrodynamic instabilities at the molten target surface [56].

Several strategies for particulate reduction have been demonstrated, though these usually require some redesign of the deposition chamber.

- One involves the introduction of one or more appropriately synchronized mechanical velocity filters designed so as to transmit fast moving atoms and ions but to block the much more slowly moving particulates [59].
- The use of highly dense ablation targets and ablation wavelengths that are strongly absorbed by the target tends to reduce or eliminate particle formation [57].

- Gyorgy et al. [58] applied a two-laser system in order to withdraw the particulates in cases of Ta and TaO<sub>x</sub> thin films. The targets were irradiated by the first UV laser, while the second IR laser was directed parallel to the target surface, aiming to heat and evaporate the particulates.
- A great reduction of particulates in PLD of Ag-Co using a shaded off-axis geometry was observed by [60]. Lackner et al. [61] obtained nearly droplet free silicon and SiO<sub>x</sub> PLD thin films with the substrates in shaded off-axis geometry.

## References

1. H.W. Leverenz, *An Introduction to Luminescence of Solids*, Wiley: New York, NY, USA, 1950.
2. S. O. Pillai, *solid state physics*, 6/ed, New Age International (P),Ltd,New Dehli, 2010.
3. G. Sharma, S.P. Lochab, N. Singh, *Current Appl. Phys.* **11** (2011) 921-925.
4. S. Boggs, D. Krinsley, *Applications of Cathodoluminescence imaging to the study of sedimentary rocks*, Cambridge University Press, England, 2006.
5. R. D. Blackledge, *Forensic analysis on the cutting edge*, John Wiley & Sons Publications, USA, 2007.
6. S. Shionoya, Introduction to the Handbook, In: *Phosphors Handbook*, Yen, W.M. Shionoya, S. Yamamoto, H. (Eds), Chap.1 CRC Press, USA, 2007.
7. J. Ball, A.D. Moore, *Essential Physics for Radiographers*, Blackwell Publishing, First edition, Oxford, 1979.
8. C. Feldmann, T. Jüstel, C. R. Ronda, P. J. Schmidt, *Adv. Funct. Mater.* **13** (2003)511-516.
9. R. Chen, S.W.S. McKeever, *Theory of Thermoluminescence and Related Phenomena*, World Scientific Publishers, Singapore, London, Hong Kong, 1997.
10. C. Ronda, *Luminescence: from theory to Applications*, WILEY-VCH verlag GmbH & co.KGaA,Weinheim, 2008.
11. J. A. Deluca, *J. Chem. Educ.* **57** (1980) 541-545.
12. S. Boggs, D. Krinsley, *Application of cathodoluminescence imaging, to the study of sedimentary rocks*, Cambridge University Press, 2006, p.10.

13. A. Vij, S.P. Lochab, S. Singh, R. Kumar, N. Singh, J. Alloys Comps. **486** (2009) 554–558.
14. R. P. RAO, Mater. Sci. **21** (1986) 3357-3386.
15. J. T. Randall, M.H.F. Wilkins, Proc. Roy. Soc. A **184** (1945) 366-389.
16. G. F. J. Garlick, A.F. Gibson, Proc. Phys. Soc. **60** (1948) 574-590.
17. C. E. May, J.A. Partridge, J. Chem. Soc. **40** (1964) 1401-1409.
18. V. Pagonis, G. Kitis, C. Furetta, *Numerical and Practical Exercises in Thermoluminescence*, Springer Science+Business Media, New York, 2006.
19. D. Jia, X. Wang, J. Opt. Mater. **30** (2007) 375–379.
20. D. Jia, J. Zhu, B. Wu, J. Electrochem. Soc. **147** (2000) 3948-3952.
21. G. Blasse, B.C. Grabmaier, *Luminescent Materials*, Springer, Berlin, 1994.
22. A. M. Srivastava , H. A. Comanzo , S. Camardello , S. B. Chaney, M. Aycibin , U. Happek. J. Lumin. **129** (2009) 919–925.
23. C. R. Ronda, *Emission and Excitation Mechanisms of Phosphors*. In: *Luminescence: From Theory to Applications*, Cees Ronda (Ed) WILEY-VCH Verlag GmbH & Co. KGaA, Weinheim, (2008), p. 28.
24. P. Dorenbos, J. Lumin. **104** (2003) 239-260.
25. P. Dorenbos, J. Phys.: Condens. Matter **15** (2003) 4797-4807.
26. B. Henderson, G.F. Imbusch, *Optical Spectroscopy of Inorganic Solid*, Clarendon Press, Oxford, 1989.
27. T. Kano, *Principal phosphor Materials and their optical Properties*. In: *Phosphor Handbook*, W. M. Yen, S. Shionoya, H. Yamamoto (Eds), CRC Press, New York, Chap 3, (2007).
28. Y. Hu, W. Zhuang, H. Ye, S. Zhang, Y. Fanga, X. Huang, J. Lumin. **111** (2005) 139–145.
29. S. M. Ze, K. N. Kwok, *Physics of semiconductor devices*, 3<sup>rd</sup> ed, John Wiley & Sons, Inc., 2007.
30. E. F. Schubert, *Light-emitting Diodes*, Cambridge University press, New York, 2003, p86.
31. C. H. Gooch, *Injection Electroluminescent Devices*, Wiley, New York, 1973.
32. L. S. Rohwer, A.M. Srivastava, The Electrochem. Interface, **12** (2003) 36-39.

33. S. Lee, S.Y. Seo, J. Electrochem. Soc. **149** (2002) J85-J88.
34. T. Justel, *Luminescence*, in: *From theory to Applications*, Cees Ronda (ed), Wiley-VCH, 2008, p 184.
35. K.Scott, The Lighting Journal, **34** (May/June 2002).
36. R.F. Karliceck Jr., personal communication (1999).
37. S. K. K. Shaat, H. C. Swart, O. M. Ntwaeaborwa, Opt. Mater. Express **2** (2012) 962.
38. J. S. Kim, P. E. Jeon, J. C. Choi, H. L. Park, S. I. Mho, G. C. Kim, J. Appl. Phys. **84** (2004) 2931.
39. S. H. Lee, J. H. Park, S. M. Son, J. S. Kim, H. L. Park, Appl. Phys. Lett. **89** (2006) 221916.
40. A. H. Mueller, M.A. Petruska, M. Achermann, D.J. Werder, E.A. Akhador, D.D. Koleske, M. A. Hoffbauer, V.I. Klimov, Nanoletters **5** (6) (2005) 1039–1044.
41. N. Narendran, Y. Gu, J. P. Freyssonier-Nova, Y. Zhu, Phys. Stat. Sol. (a) **202** (6) (2005) R60–R62.
42. Y.Q. Li, A.C. Delsing, G. de With, H. T. Hintzen, Chem. Mater. **17** (2005) 3242–3248.
43. M. S. Shur, A. Zukauskas, Solid state lighting: toward superior illumination, Proc. IEEE **93** (10) (2005) 1073–1691.
44. M. J. Bowers II, J.R. McBride, S.J. Rosenthal, J. Am. Chem. Soc. **127** (2005) 15378–15379.
45. [www.nobelprize.org/nobel\\_prizes/physics/laureates/2014/advanced-physicsprize2014.pdf](http://www.nobelprize.org/nobel_prizes/physics/laureates/2014/advanced-physicsprize2014.pdf), accessed on 7/10/2014.
46. [www.spark-oe.com/solar-led-street-lights/solar-street-lighting-led.html?gclid=CI2fgN\\_kmsQCFVDHtAodnQ8ACA-](http://www.spark-oe.com/solar-led-street-lights/solar-street-lighting-led.html?gclid=CI2fgN_kmsQCFVDHtAodnQ8ACA-) accessed 09/03/2015
47. I. W. Boyd, Ceram. Int. **22** (1996) 429-434.
48. M. N. R. Ashfold, F. Claeysens, G. M. Fuge, S. J. Henley, Chem. Soc. Rev. **33**(2004) 23-31.
49. M. S. Brown, C. B. Arnold, Fundamentals of Laser-Material Interaction. In: *Laser Precision Microfabrication*, Koji Sugioka, Michel Meunier', Alberto Piqu'e (Editors), Springer-Verlag Berlin Heidelberg, 2010, pp. 91-120.
50. D. Bauerle, *Laser Processing and Chemistry*, Springer-Verlag Berlin Heidelberg, 2011.

51. A. Kitai, *Principles of Solar Cells, LEDs and Diodes: the role of the PN junction*, John Wiley & Sons, Ltd, 2011.
52. J. A. Venebles, *Introduction to Surface and thin film Processes*, Cambridge University Press, New York, 2003, pg 146.
53. K. Wasa, M. Kitabatake, H. Adachi, *Thin film Materials Technology: Sputtering of Compound Materials*, William Andrew, Inc. 2004.
54. Tong X.L, Jiang D.S, Hu W.B, Liu Z.M, Luo M.Z, *Appl. Phys.*, **A 84** (2006) 143-148.
55. O. M.Ntwaeaborwa, PhD., dissertation, University of the Free State, South Africa (2006).
56. T. Yoshitake, G. Shiraishi, K. Nagayama, *Appl. Surf. Sci.* **197-198** (2002) 379-383.
57. D. P. Norton, pulsed laser deposition of complex materials: progress toward applications, In: *Pulsed laser deposition of thin films*, Robert Eason (Ed), Jon Wiley & Sons, Inc., Hoboken, New Jersey, 2007.
58. E. Gyorgy, I.N. Mihailescua, M. Kompitsasb,, A. Giannoudakos, *Thin Solid Films* **446** (2004) 178–183.
59. A. Anders, *Surf. Coat. Technol.* **121** (1999)319-330.
60. E. Agostinelli, S. Kaciulis , M. Vittori-Antisari, *Appl. Surf. Sci.* **156** (2000) 143–148.
61. J. M. Lackner, W. Waldhauser, R. Ebner, W. Lenz, C. Suess, G. Jakopic, G. Leising, H. Hutter, *Surf. Coat. Technol.* **163 –164** (2003) 300–305.

# Chapter 3

## Research Techniques

### 3.1. Introduction

The characterization techniques used to prepare or investigate the properties of the phosphor used in this study are presented. The pulsed laser deposition technique was used to grow thin films on Si (100/111) substrates under different conditions. The Auger electron spectroscopy (AES) and the X-ray photoelectron spectroscopy (XPS) were used to obtain elemental composition on the surfaces of the powder phosphors, while energy dispersive X-ray spectroscopy (EDS) gave the composition of the thin films. Rutherford backscattering spectroscopy (RBS) was used for elemental composition analysis and thickness determination of thin films. Secondary ion mass spectrometry (SIMs) with Time-of-Flight mass analysis (TOF) was used to characterize the surface and sub-surface region of the thin films. SEM and AFM were used to obtain morphological and topographical information of thin film samples. XRD was used to identify crystalline structure and phases of both powder and thin film samples. Luminescence investigations were done using fluorescence spectrometry, cathodoluminescence spectroscopy and thermoluminescence reader.

### 3.2. Photoluminescence Spectroscopy

The excitation source in a Photoluminescence Spectroscopy (PL) system can be a UV light or a laser beam. In this study, the two systems used for PL characterization are the KIMON IK series He-Cd laser ( $\lambda = 325$  nm) and a Cary Eclipse fluorescence spectrometer (Model: LS 55). In the Cary Eclipse, fluorescence is measured using an excitation source placed at  $90^\circ$  to the emission detector. Excitation radiation is provided by a monochromatized xenon flash lamp whose wavelength can be varied [1]. The emission is detected with a photomultiplier tube (PMT). The PL Spectrum provides the transition energies, which can be used to

determine the electronic energy levels [2]. On the other hand, the laser PL system measures emission spectra for samples using an excitation wavelength of 325 nm from a He-Cd laser and uses a PMT and lock-in amplifier for detection. The output of the detector gives a luminescence emission spectrum representing the luminescence intensity measured over a range of emission wavelengths (or energy) at a fixed excitation wavelength. A generalized schematic of a PL system is shown in Fig. 3.1.

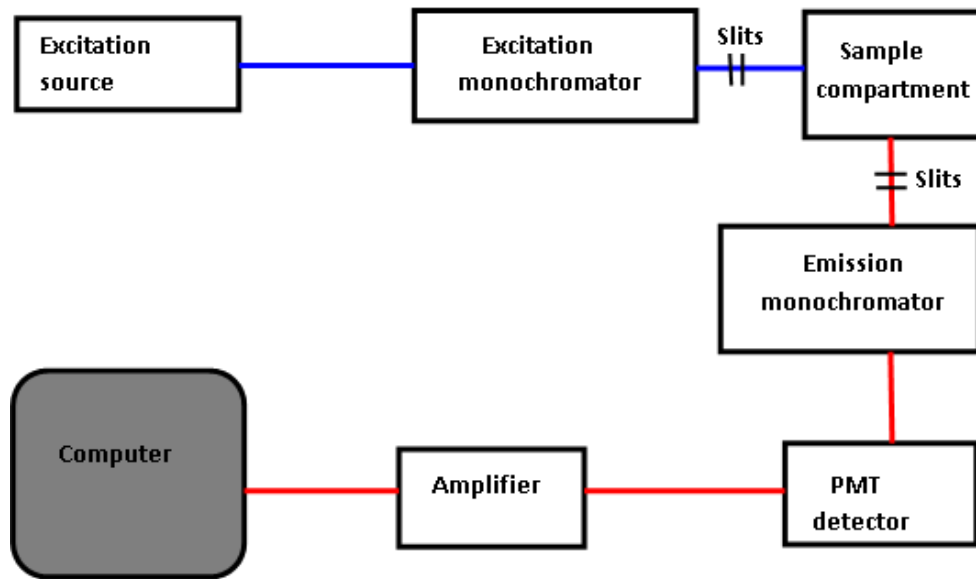


**Figure 3.1:** Schematic diagram of a generic fluorescence spectrometer instrumentation, adapted from Ref [1].



The photographs of the two systems used for this study are shown in Figure 3.2 (a) and (b).



**Figure 3.2:** (a) The Cary Eclipse fluorescence spectrometer (b) the He-Cd laser photoluminescence units, both at the physics Department, University of the Free State.

### 3.3. Atomic Force Microscopy

The atomic force microscope (AFM) is a Scanning Probe Microscope (SPM) that makes high magnification observations by scanning a microscopic probe over the surface of a sample. The probe builds up a map of the height or topography of the surface as it goes along [3]. The AFM, invented in the 1980s finds use in materials science, nanotechnology, physics, chemistry, and biology [3].

The AFM consists of a cantilever with a sharp tip (probe) at its end that is used to scan the specimen surface, shown in Fig 3.3. The cantilever is typically silicon or silicon nitride with a tip radius of curvature in the order of nanometers. The cantilever behaves like a spring, so that any forces acting between the AFM tip and the sample surface causes the cantilever to deflect. The force  $F$ , the van der Waals-type force acting upon the tip is related to the cantilever deflection value  $x$  under Hooke's law:

$$F = -kx \tag{3.1}$$

where  $k$  is cantilever spring constant.

Basically the AFM consists of piezoelectric transducers, force transducers, and feedback control. The piezoelectric transducer moves the tip over the sample surface, the force transducer senses the force between the tip and the surface, and the feedback control feeds the signal from the force transducer back in to the piezoelectric, to maintain a fixed force between the tip and the sample [4]. A laser beam is transmitted to and reflected from the cantilever for measuring the cantilever orientation. The reflected laser beam is detected with a position-sensitive detector, preferably a photodiode. During scanning the output of the photodiode is provided to a computer which is used to read the amount of Z-axis feedback (voltage output to scanner) of each XY position and then processes this information to generate a topographic (3D) image of the sample surface.

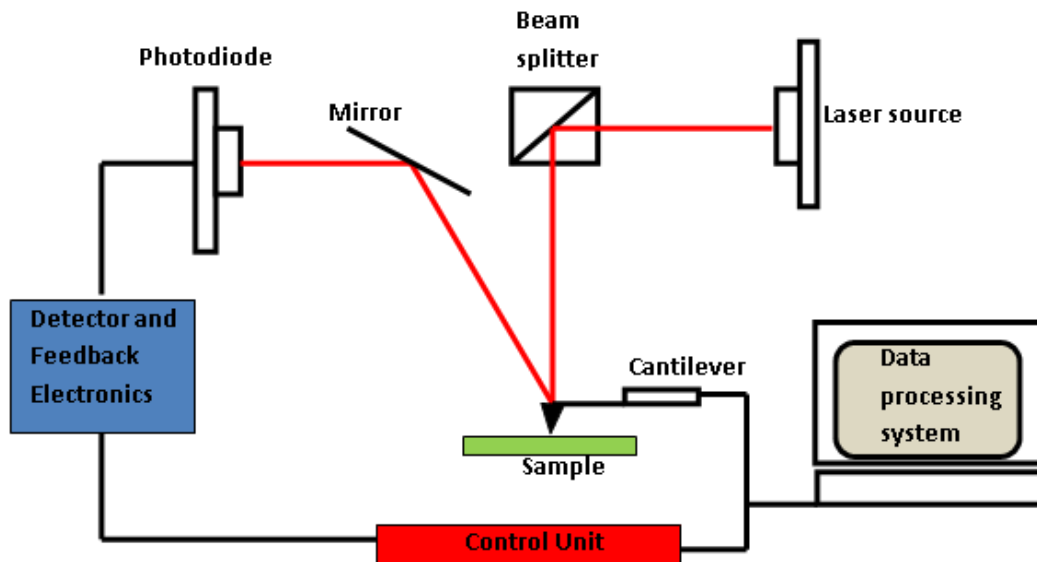


**Figure 3.3:** Simplified schematic of an atomic force microscope system.

The AFM can be operated in a number of modes, depending on the application. In general, possible imaging modes are divided into static (also called contact) modes and a variety of dynamic (non-contact or "tapping") modes where the cantilever is vibrated.

Roughness is a very important surface property widely used as a quantitative measurement of surface changes in a wide range of samples. Roughness, measured by the root-mean-squared roughness ( $R_q$  or  $R_{rms}$ ), is one of the most commonly used statistical parameters for

describing AFM images. It gives useful information about the sample surface, and can be correlated with results from other techniques [2].

The root-mean-squared roughness ( $R_q$  or  $R_{rms}$ ) of the surface is defined as:

$$R_q = \sqrt{\frac{1}{n} \sum_{i=1}^n (z_i - z_{ave})^2} \quad (3.2)$$

where  $Z_i$  is the current value of  $Z$ ,  $Z_{ave}$  the mean value of  $z$  in the scan area and  $n$  is the number of points.

In this work, surface topography and roughness were studied from images captured in contact mode using the Shimadzu SPM-9600 atomic force microscopy, shown in Fig 3.4.

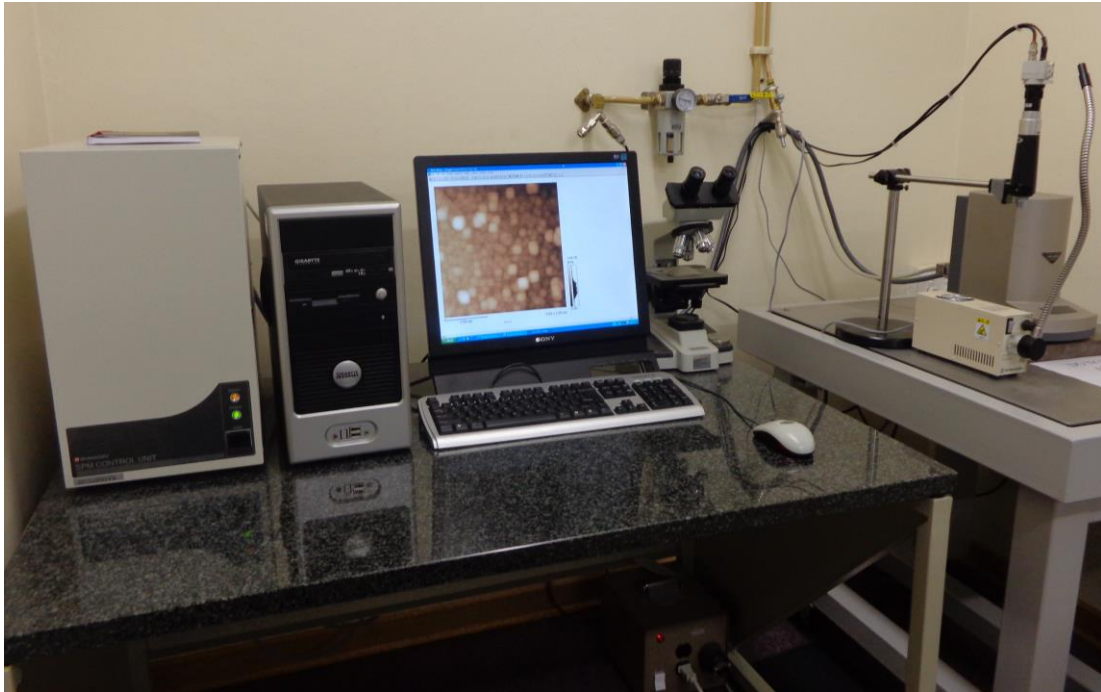


**Figure 3.4:** Photo of a desktop AFM, the Shimadzu SPM-9600 atomic force microscopy, showing the control unit, data processing system, optical microscope, and SPM unit at the Department of Physics, University of the Free State.

### 3.4. Pulsed Laser Deposition

Pulsed laser deposition (PLD) is a thin-film deposition technique which involves ablation of solid target in a high vacuum chamber; either in vacuum or in the presence of some background gas (e.g. O<sub>2</sub>, Ar, N<sub>2</sub> etc) by means of laser pulses [5]. The vaporized material (in a plasma plume) is deposited as a thin film on a substrate, such as a silicon wafer facing the target. The first thin film, which was grown utilizing a ruby laser, was deposited in 1965 by Smith and Turner [6].

A typical set-up for PLD using Nd: YAG laser is schematically shown in Fig.3.5.

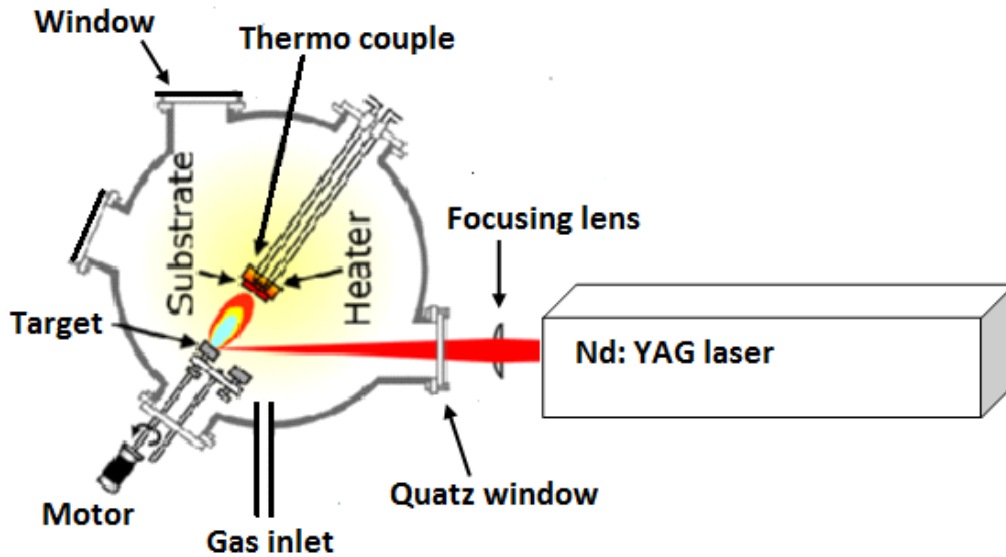


**Figure 3.5:** Schematic diagram of a laser deposition set up, adapted from Ref. [7].

The pulsed laser system consists of a laser and a vacuum system. From the laser system parameters such as laser fluence, wavelength, pulse duration, and repetition rate can be altered. Conditions in the vacuum system including target-to-substrate distance, substrate temperature, background gas and pressure, can also be varied. All these parameters influence the growth of the film [8, 9]. The basic principles explaining laser-matter interaction, formation of a plume and the subsequent film growth are discussed in greater detail in section 2.9 of chapter 2.

A Spectra Physics Quanta-Ray Pro-270 Nd: YAG operable in laser of wavelengths of 1064 nm, 532 nm, 355 nm, and 266 nm was used for the current work. Fig. 3.6 shows a photograph of the PLD system.

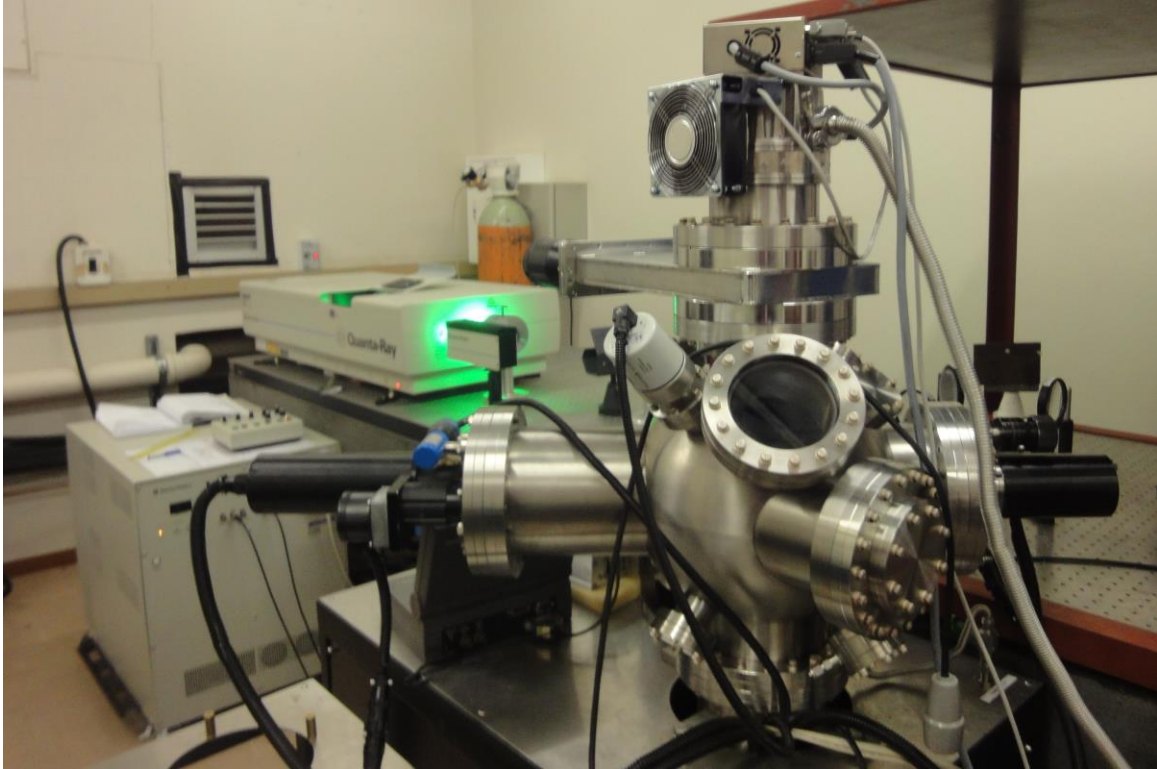


**Figure 3.6:** The pulsed laser deposition (PLD) system at the National Laser Centre (NLC, CSIR), Pretoria.

### **3.5. Scanning Electron Microscope and Energy Dispersive X-ray Spectrometry**

#### **3.5.1. SEM**

In 1937, Manfred Von Ardenne invented [10] a microscope with high magnification by scanning a very small raster with a demagnified and finely focused electron beam. This was the beginning of the scanning electron microscope (SEM) which is a type of electron microscope that produces high resolution images of a sample surface by scanning it with a focused beam of electrons. The electrons interact with atoms in the sample, producing

various signals that can be detected and that contain information about the sample's surface topography and composition [11]. The types of signals produced from the interaction of the electron beam with the sample include secondary electrons (SE), back-scattered electrons (BSE), characteristic X-rays, and other photons of various energies [12]. The signal from SE or BSE in a SEM is utilized for imaging, while the characteristic X-rays (see section 3.4.2) are useful in elemental composition analysis. The electron beam also yields cathodoluminescence (CL), which can be analyzed to produce CL spectra and CL maps [13, 14]. A more detailed description of these signals can be found in [15]. Due to the very narrow electron beam, SEM micrographs have a large depth of field yielding a characteristic three-dimensional appearance useful for understanding the surface structure of a sample. The imaging signals of greatest interest are the secondary and BSE because these vary primarily as a result of differences in surface topography. The backscattering coefficient  $\eta$  (the fraction of primary electrons that escape as BSE) increases with atomic number, and BSE images can show contrast due to variations in chemical composition of a specimen (higher atomic number elements will appear brighter in the image). On the other hand, SE images reflect mainly the surface topography of the specimen [15, 16]. Fig. 3.7 shows a schematic diagram of a SEM.

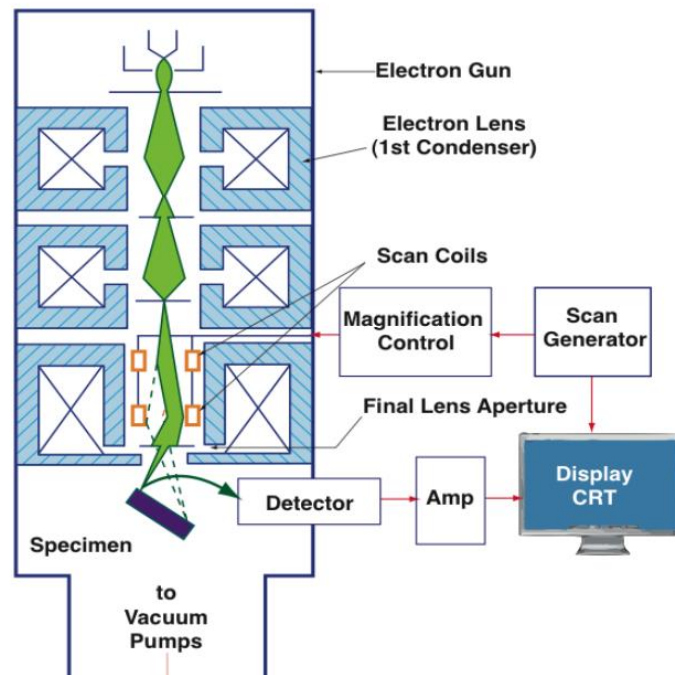


**Figure 3.7:** Schematic diagram of a scanning electron microscope column [12].

The Shimadzu Superscan SSX-550 and JEOL JSM-7800F are the SEM used in the present study and their photographs are shown in Fig. 3.8.



**Figure 3.8:** (a) The Shimadzu Superscan SSX-550 (Kyoto, Japan) and (b) JEOL JSM-7800F scanning electron microscopes (SEM) at the Microscopy Center, University of Free State.

### 3.5.2. Energy Dispersive X-ray Spectrometry

Energy Dispersive X-ray Spectrometry (EDS) makes use of the X-ray spectrum emitted by a solid sample bombarded with a focused beam of electrons to obtain a localized chemical analysis. The incident beam of electrons creates secondary electrons as it bounces through the sample. It leaves thousands of the sample atoms with holes in the electron shells where the secondary electrons used to be. If these "holes" are in inner shells, the atoms are not in a stable state. To stabilize the atoms, electrons from outer shells will drop into the inner shells, see Fig. 3.9. However, because the outer shells are at a higher energy state, to do this the atom must lose some energy. It does this in the form of X-rays. The X-rays emitted from the sample atoms are characteristic in energy and wavelength to, not only the element of the parent atom, but also to which shells lost electrons and which shells replaced them [12]. For instance, if the innermost shell (the K shell) electron of an atom is replaced by an L shell electron, a K alpha ( $K\alpha$ ) X-ray is emitted from the sample. Or, if the innermost shell (the K shell) electron of the atom is replaced by an M shell electron, a K beta ( $K\beta$ ) X-ray is emitted from the sample. The X-rays are emitted from a depth equivalent to how deep the secondary electrons are formed.

Depending on the sample atomic number, density and accelerating voltage of the incident beam, this is usually from 1/2 to 2 microns in depth [12].

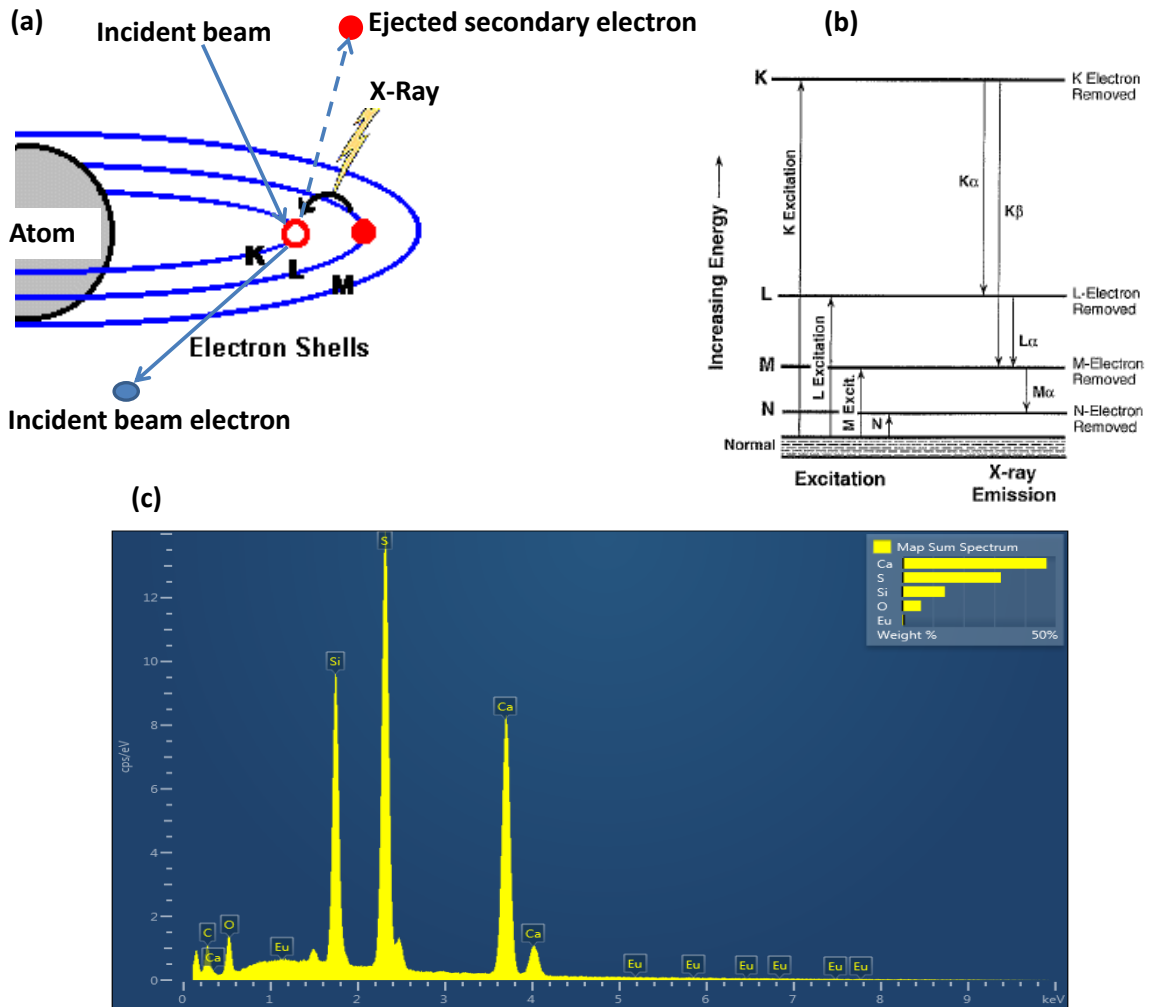


**Figure 3.9:** (a) schematic of X-ray emission from an atom (b) energy level diagram for an atom (c) EDS spectrum of CaS:Eu<sup>2+</sup>

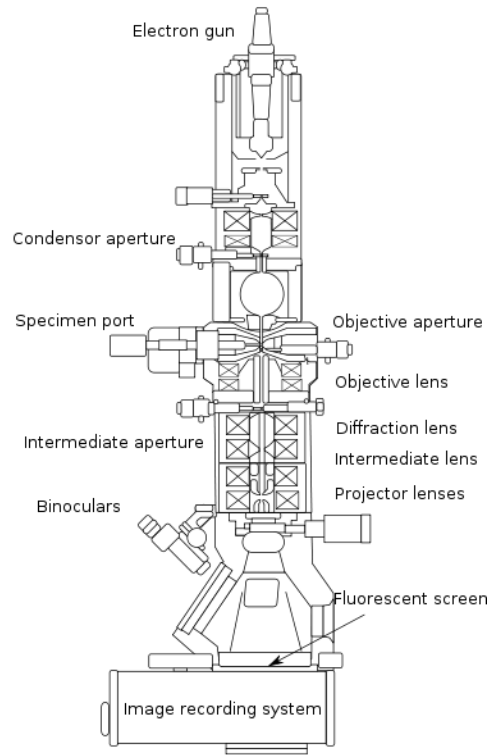
### 3.6. Transmission Electron Microscopy

Transmission electron microscopy (TEM) is a microscopy technique whereby a beam of electrons is transmitted through an ultra-thin specimen, interacting with the specimen as it passes through. An image is formed from the interaction of the electrons transmitted through the specimen; the image is magnified and focused onto an imaging device, such as a



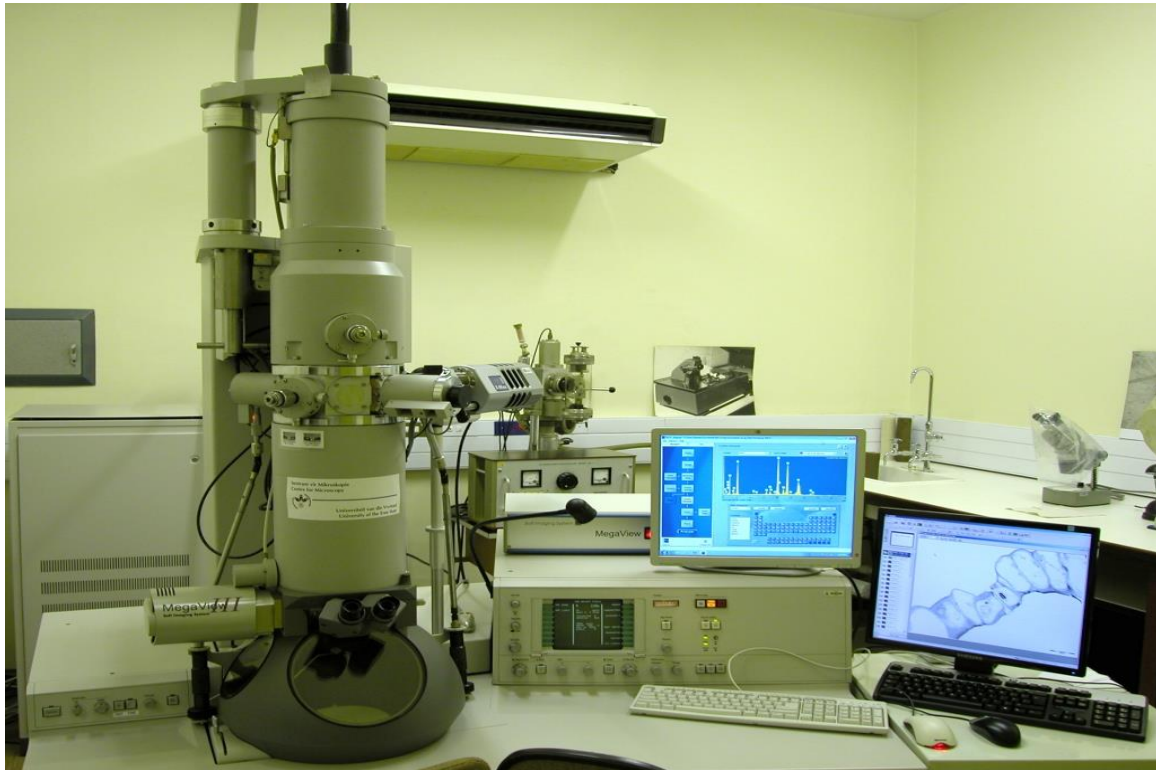
fluorescent screen, on a layer of photographic film, or to be detected by a sensor such as a CCD camera [15].

Fig 3.10 shows the basic construction of a transmission electron



**Figure 3.10:** Schematic diagram of a transmission electron microscope [16].

A TEM is composed of several components; which include a vacuum system in which the electrons travel, an electron emission source for generation of the electron stream, a series of electromagnetic lenses, as well as electrostatic plates. The latter two allow the operator to guide and manipulate the beam as required. Also required is a device to allow the insertion into, motion within, and removal of specimens from the beam path. Imaging devices are subsequently used to create an image from the electrons that exit the system. The TEM results in this project were obtained using a Philips (FEI, The Netherlands) CM100 transmission electron microscope, available at the Microscopy Center, University of Free State (Fig. 3.11).



**Figure 3.11:** Philips (FEI, The Netherlands) CM100 transmission electron microscope at the Microscopy Center, University of Free State.

### **3.7. X-Ray Diffraction**

#### **3.7.1. Diffractometer**

An X-ray diffractometer consists of three basic elements: an X-ray tube, a sample holder, and an X-ray detector (Fig. 3.12). X-rays are generated in a cathode ray tube by heating a filament to produce electrons, which are accelerated toward a target by applying a voltage, and bombarding the target material with the electrons. Characteristic X-ray spectra are produced following the ejection of an inner orbital electron and subsequent transition of atomic orbital electrons from high energy states to low energy states. These spectra consist of several components, the most common being  $K_{\alpha}$  and  $K_{\beta}$ . The specific wavelengths are

characteristic of the target material (Cu, Fe, Mo, Cr). Copper is the most common target material for single-crystal diffraction, with  $\text{CuK}_\alpha$  radiation  $\sim 1.54 \text{ \AA}$ . Filtering, by foils or a crystal monochromator, is required to produce monochromatic X-rays needed for diffraction.

The geometry of an X-ray diffractometer is such that the sample rotates in the path of the collimated X-ray beam at an angle  $\theta$  while the X-ray detector is mounted on an arm to collect the diffracted X-rays and rotates at an angle of  $2\theta$ .

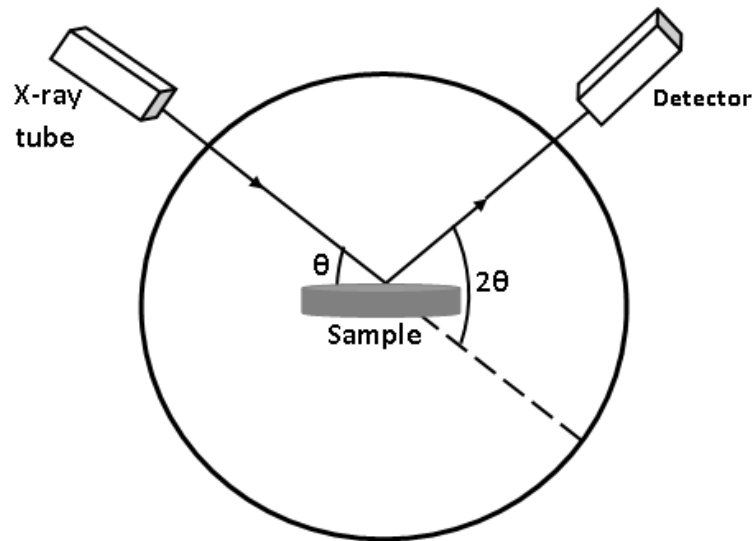


**Figure 3.12:** A schematic of an X-ray diffractometer.

### 3.7.2. Application

X-ray diffraction (XRD) is a powerful nondestructive technique for characterizing crystalline materials. X-ray diffraction peaks are produced by constructive interference of a monochromatic beam of X-rays scattered at specific angles from each set of lattice planes in a sample. Fig. 3.13 shows the schematic diagram of two adjacent crystal planes with X-rays being reflected from each. If the distance between the planes is  $d$  then the difference in the path length is  $2d \sin \theta$ . If this distance is equal to an integral number of wave lengths, then the X-rays interfere constructively, if not, destructive interference takes place. The X-rays are

diffracted when conditions satisfy Eq. (3.3), known as Bragg's law [17], developed by W. L. Bragg in 1912 -1913 [18, 19].

$$n\lambda = 2d \sin\theta \quad (3.3)$$

where  $n$  is an integer,  $\lambda$  is the wavelength of the X-rays,  $d$  is the interplanar spacing generating the diffraction, and  $\theta$  is the diffraction angle.

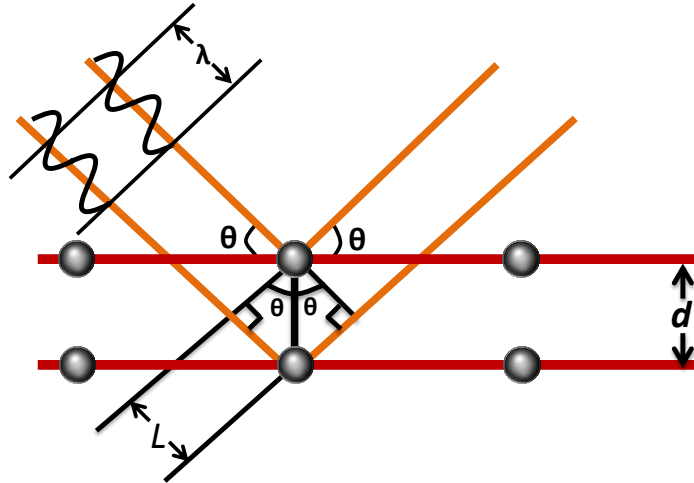


**Figure 3.13:** Schematic diagram of diffraction of X-rays at crystal planes, adapted [20].

For most samples, the aim of analysis is to get information on structures, preferred crystal orientation (texture), identify the crystalline phases present and purity of samples prepared under various conditions [21, 22]. Phase identification is accomplished by comparing the data (peaks and relative intensities) from the sample with peaks and relative intensities from a very large set of “standard” data provided by the International Center for Diffraction Data (ICDD).

The XRD technique can also be used in the determination of grain size, strain, crystal defects, lattice constants, and degree of crystallinity in a mixture of amorphous and crystalline substances [23]. It is possible to determine an average crystallite size by the Scherrer equation:

$$D = \frac{k\lambda}{\cos\theta\sqrt{\beta^2 - \beta_0}} \quad (3.4)$$

Where  $D$  denotes the average size of the crystallites,  $k$  is a factor which is usually set to 0.9,  $\theta$  is the Bragg angle,  $\beta$  is the broadening of the diffraction line measured at half of its

maximum intensity (in radians) ,  $\beta_0$  represents the scan aperture of the diffractometer, and  $\lambda$  is the X-ray radiation wavelength. An error for crystallite size by this formula can be up to 50% [22].

In this study, the Bruker AXS D8 ADVANCE (Bruker Corporation of Germany) X-ray diffractometer with a Cu anode producing X-rays of a wavelength ( $\lambda$ ) of 1.5406 Å was used and is shown in Fig. 3.14.



**Figure 3.14:** The Bruker AXS D8 ADVANCE X-ray diffractometer at the Department of Physics of the University of the Free State.

### **3.8. X-ray Photoelectron Spectroscopy**

X-ray photoelectron spectroscopy (XPS), also known as Electron Spectroscopy for Chemical Analysis (ESCA) is a widely used technique to investigate the chemical composition of surfaces. The first commercial monochromatic XPS instrument was produced in the USA, at Hewlett-Packard by Kai Siegbahn and co-workers [24] in 1969.

Surface analysis by XPS is accomplished by irradiating a sample with monoenergetic soft X-rays, and analyzing the energy of the detected electrons [25]. The most commonly used X-ray sources are  $\text{AlK}\alpha$  (1486.6 eV) and  $\text{MgK}\alpha$  (1253.6 eV) [17]. The X-rays interact with atoms in the surface regions, causing electrons to be emitted by the photoelectric effect [26]. Fig. 3.15 shows the process of photoemission where a 1s photoelectron is ejected from the K shell by an X-ray photon of energy  $h\nu$ . The ionized atom will relax by possibly ejecting an Auger electron (see section 3.10.1)

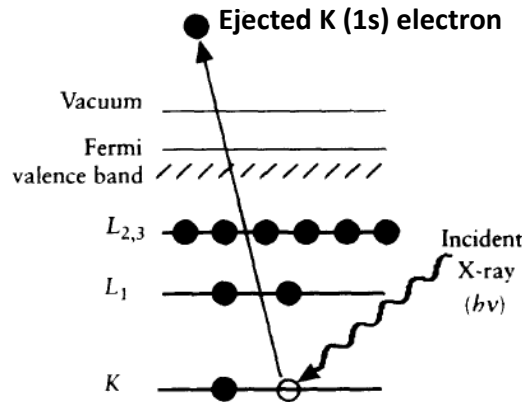


**Figure 3.15:** Schematic diagram of the XPS process, showing the ejection of a 1s electron from shell K of an atom, adapted from Ref. [17].

The emitted photoelectrons have measured kinetic energies given by Eq. 3.5 [27]

$$E_K = h\nu - BE - \phi_s \quad (3.5)$$

where  $h\nu$  is the energy of the photon,  $BE$  is the binding energy of the atomic orbital from which the electron originates, and  $\phi_s$  is the spectrometer work function. The work function term,  $\phi_s$  is an adjustable instrumental correction factor that accounts for the few eV of kinetic energy given up by the photoelectron as it becomes absorbed by the instrument's detector. It is a constant that rarely needs to be adjusted in practice.

The binding energy of the electron ( $BE$ ) is the parameter which identifies the electron specifically, both in terms of its parent element and atomic energy level [17]. Eq. (3.5) can then be re-written as:

$$BE = h\nu - (E_K + \phi_s) \quad (3.6)$$

A typical XPS spectrum is a plot of the number of electrons detected (sometimes per unit time) versus the binding energy of the electrons detected. Each element produces a characteristic set of XPS peaks at characteristic binding energy values that directly identify each element that exist in or on the surface of the material being analyzed[25]. These characteristic peaks correspond to the electron configuration of the electrons within the atoms, e.g., 1s, 2s, 2p, 3s, etc. The number of detected electrons in each of the characteristic peaks is directly related to the amount of element within the area (volume) irradiated.

An XPS system includes an X-ray source, a sample stage, a lens, an analyzer, a detector, and a data processing system [26], as seen in Fig. 3.16.

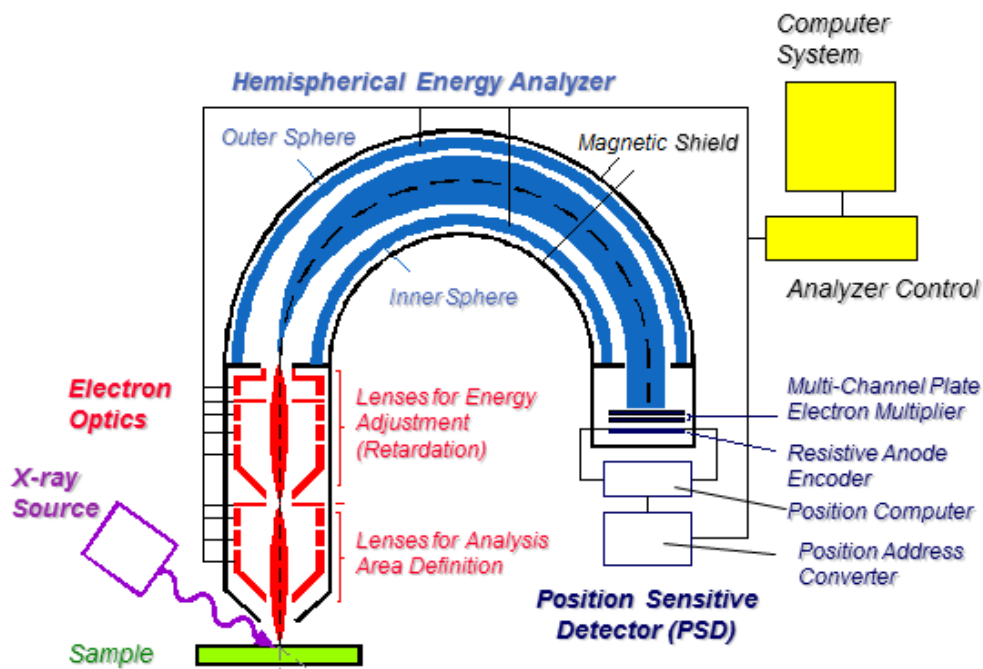


**Figure 3.16:** Schematic diagram of an XPS system [26].

The XPS measurements in this study were performed using a PHI 5000 Versaprobe scanning X-ray photoelectron spectrometer (Fig. 3.17).

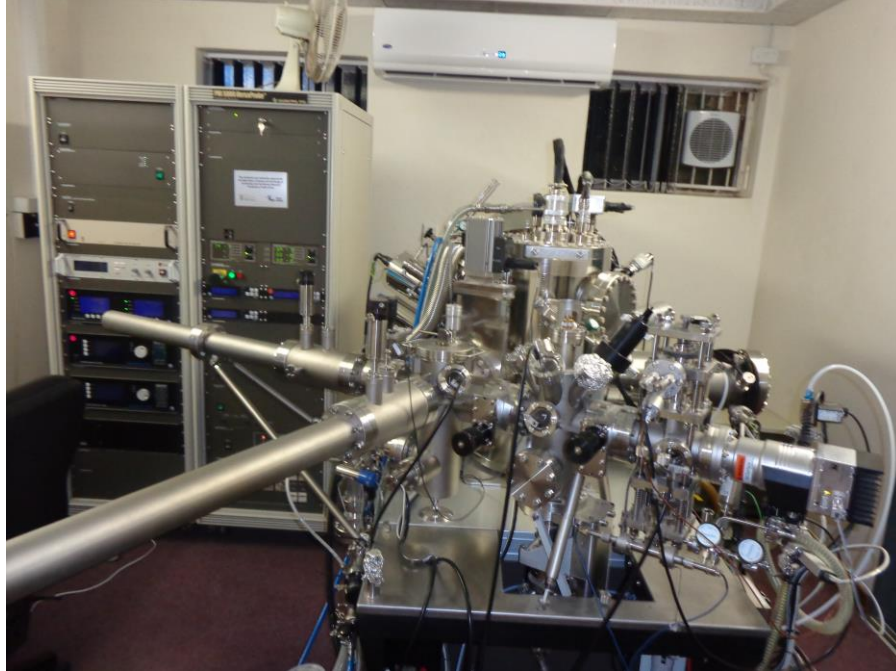


**Figure 3.17:** PHI 5000 Versaprobe scanning X-ray photoelectron spectrometer unit at the Department of Physics of the University of the Free State.

### 3.9. Secondary Ion Mass Spectrometry

Secondary ion mass spectrometry (SIMS) with Time-of-flight mass analysis (TOF) is a surface analysis technique used to characterize the surface and sub-surface region of materials. The surface of a solid sample is subjected to the bombardment by high energy ions, called the primary beam. The bombarding ions eject secondary ions from the surface of the sample. The subsequent mass analysis of the emitted ions provides detailed information on the elemental and molecular composition of the surface [28]. The first prototype experiment on SIMs was performed by Herzog and Viehbock [29] in 1949, at the University of Vienna, Austria. In 1910, J.J Thomson had already observed a release of positive ions and neutral atoms from a solid surface induced by ion bombardment [30].

The basic components of a SIMS shown in Fig. 3.18 [31] are:

- i) A primary beam source (e.g.  $Ar^+$ ,  $O_2^+$ ,  $Cs^+$ )
- ii) Sample



- iii) Method of collecting the ejected secondary ions
- iv) A mass analyser to isolate the ion of interest (e.g. Quadrupole, or TOF)
- v) An ion detection system to record the magnitude of the secondary ion signal (e.g. Faraday cup)

The common modes of analysis of the SIMS are [28]:

- a) Mass spectrum mode; Surface Spectroscopy provides detailed elemental and molecular information from the outer monolayers.
- b) Ion image: by rastering a fine-focused ion beam over the surface, mass resolved secondary ion images (chemical maps) can be obtained simultaneously.
- c) Depth profile mode: is used to measure the concentration of specific preselected elements as a function of depth from the surface. Two ion beams operate in the Dual Beam Mode, where the first beam sputters a crater, while the second beam progressively analyses the crater bottom.
- d) 3D image: a 3D visualisation sample structures is achieved by combining spectral, imaging and depth information

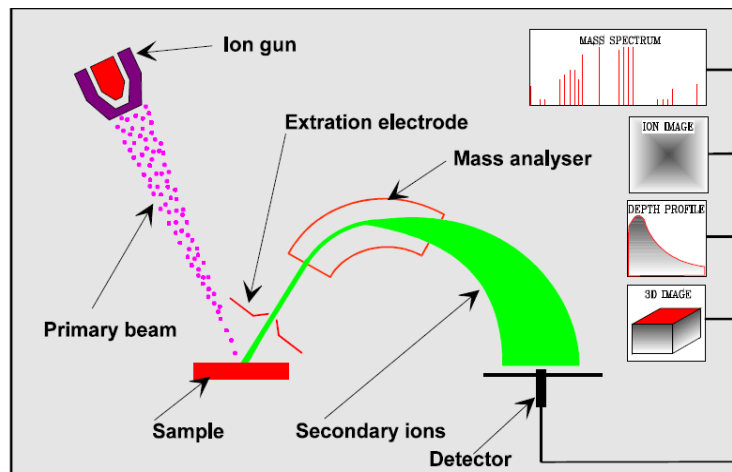


**Figure 3.18:** A schematic of the basic components of a modern SIMS instrument [32].

Mass analyzers based on TOF operate in static and dynamic modes. Static SIMS uses a low dose of incident particles and thus obtains surface chemical information, while dynamic SIMS uses a much higher energy primary beam. The higher ion flux takes the beam steadily

deeper into the sample, thus generating secondary ions that characterize the composition at varying depths [33]. Fig. 3.19 shows the photograph of the system used in the present study.

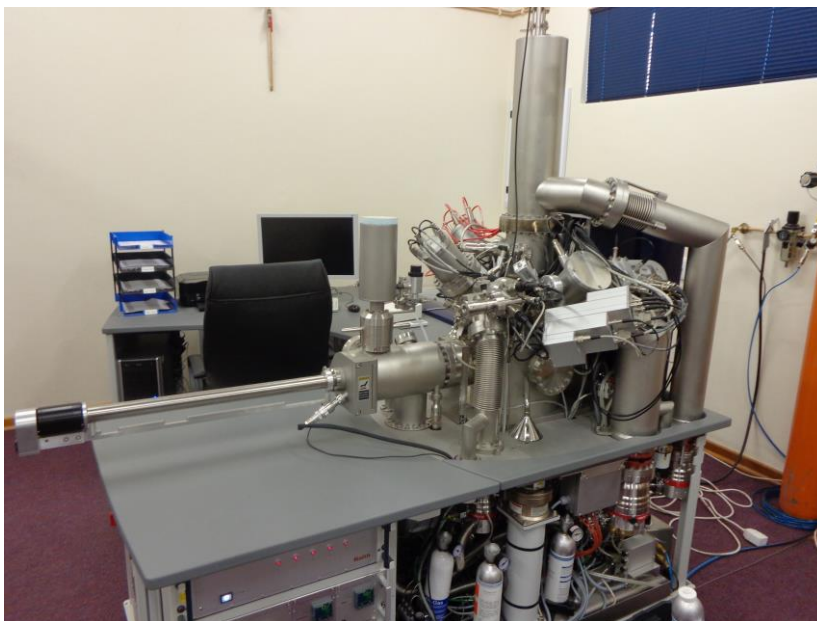


**Figure 3.19:** Photograph of the SIMS equipment, the IONTOF TOF-SIMS5 imaging mass spectrometer in the Department of Physics at the University of the Free State.

### **3.10. Auger Electron Spectroscopy**

The Auger effect was discovered by Pierre Auger [34] in 1925 while the Auger Electron Spectroscopy (AES) was developed in the 1960s [35].

The AES is an analytical technique that uses a primary electron beam to probe the outermost layers of a material surface. The technique is therefore particularly suited for surface analysis and is capable of identifying individual elements in a sample.

#### **3.10.1. The Auger Process**

The Auger process can be explained by considering the ionization process of an isolated atom under electron bombardment. The incident electron with sufficient primary energy,  $E_p$ ,

irradiates the specimen, and a core electron is ejected. The ionized atom relaxes by filling the hole with an electron coming from an outer level, e.g. L<sub>1</sub>.

As a result, the energy difference (E<sub>K</sub> - E<sub>L1</sub>) becomes available as excess energy, which can be given to another electron, as in the L<sub>2</sub> level. This electron is ejected from the atom as an Auger electron [17]. This whole process is shown in Fig.3.20.

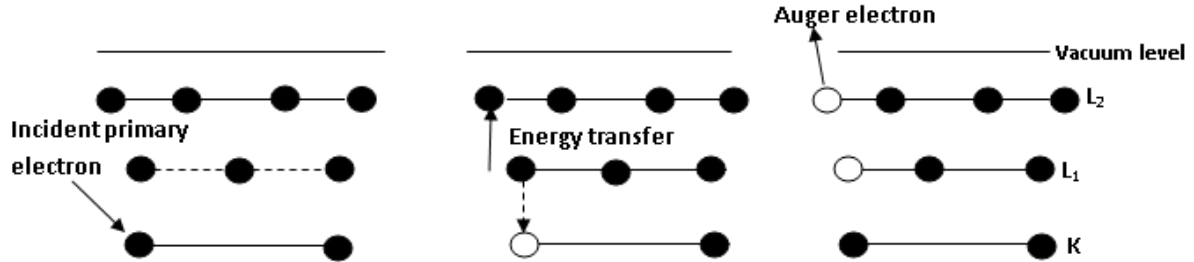


**Figure 3.20:** The basic steps of the AES process, showing the relaxation of the ionized atom by the emission of a KL<sub>1</sub>L<sub>2</sub> Auger electron.

The Auger electron will have energy estimated by Eq. 3.7:

$$E_{KLL} \approx E_K - E_{L_1} - E_{L_2} \quad (3.7)$$

where E<sub>K</sub>, E<sub>L1</sub>, and E<sub>L2</sub> are the energies associated with levels K, L<sub>1</sub>, and L<sub>2</sub>, respectively.

The energy of this electron is characteristic of the atom from which it was emitted and the number of electrons emitted is dependent on the concentration of that element in the sample [36]. Lithium represents the lower limit for AES sensitivity since the Auger effect is a "three state" event necessitating at least three electrons.

The essential components of an AES spectrometer are:

- Ultra high vacuum (UHV) environment
- Electron gun
- Electron energy analyzer
- Electron detector
- Data recording, processing, and output system

Fig.3.21 depicts a schematic for a basic configuration, used in AES, containing a cylindrical mirror analyzer (CMA). The sample is irradiated with electrons from an electron gun. The emitted secondary electrons are analyzed for energy by an electron spectrometer. The AES spectra (either direct spectrum or differentiated spectrum) thus obtained are plotted on a kinetic energy scale. By combining Auger analysis with ion etching of the surface, a composition profile of elements as a function of depth may be achieved.

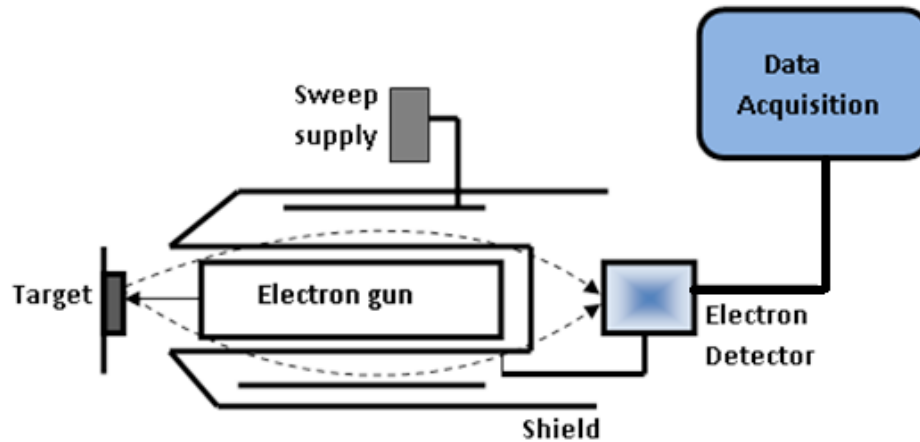


**Figure 3.21:** A Schematic of an AES experimental setup using a cylindrical mirror analyzer.

Fig.3.22 shows the photo of a Physical Electronics (PHI) model 545 Auger electron spectrometer (AES) combined with a CL system. This system allowed for simultaneous measurement of AES surface and CL emission data used for the current work.



**Figure 3.22:** The PHI, model 545 Auger electron spectroscopy (AES) unit combined with a CL unit at the Physics Department, University of the Free State.

### **3.11. Rutherford Backscattering Spectrometry**

Rutherford backscattering spectrometry (RBS) is named after Lord Ernest Rutherford, who between 1909 and 1914 supervised a study carried out by Hans Geiger and Ernest Marsden concerning the scattering of alpha particles by metal foils [37]. RBS is a non-destructive technique that allows the quantitative determination of the composition of a material and depth profiling of individual elements in thin films. The analyzed depth is typically about 2  $\mu\text{m}$  for incident He-ions and about 20  $\mu\text{m}$  for incident protons.

### 3.11.1. Basic Principle

The basic principle is contained in the kinematics for binary collisions. A beam of known particles (ions) with mass  $M_1$  is given the energy  $E_0$  and directed onto the sample containing the particles  $M_2$  that are to be investigated (see Fig. 3.23).

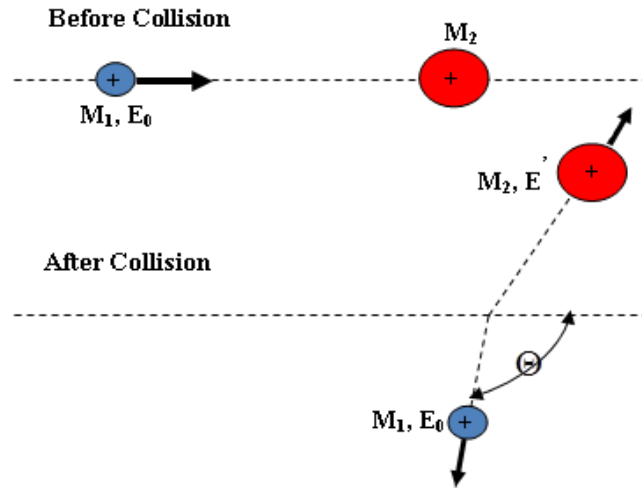


**Figure 3.23:** A collision between two positively charged particles, before, and after the collision.

The energy  $E_1$  and the scattering angle  $\Theta$  of the particle  $M_1$  are detected, with  $E_1$  related to  $E_0$  as:

$$E_1 = k.E_0$$

where  $k$  is known as the kinematical factor, given as:

$$k = \left( \frac{M_1 \cos\Theta \pm \sqrt{M_2^2 \pm M_1^2 (\sin\Theta)^2}}{M_1 + M_2} \right)^2 \quad (3.8)$$

$M_1$  is the projectile,  $M_2$  is the target nucleus, and  $\Theta$  is the scattering angle of the projectile. From the conservation laws of energy and momentum, it is then possible to deduce the mass of the target particles  $M_2$ . The abundance of  $M_2$  particles in the sample is estimated by counting the yield of scattered particles  $M_1$  in a certain solid angle covered by the detector [38].

By analyzing the energy spectrum from the scattered ions, the elements contained in a sample can be determined from the positions of peaks in the energy spectrum. Depth can be determined from the width and shifted position of these peaks, and relative concentration from the peak heights.

### 3.11.2. Instrumentation

A typical Rutherford backscattering setup consists (see Fig. 3.24) of:

- An ion source, usually alpha particles ( ${}^4\text{He}^+$  ions)
- A linear particle accelerator capable of accelerating incident ions to high energies, usually in the range 1-3 MeV.
- A detector capable of measuring the energies of backscattered ions over some range of angles.
- Data processing system

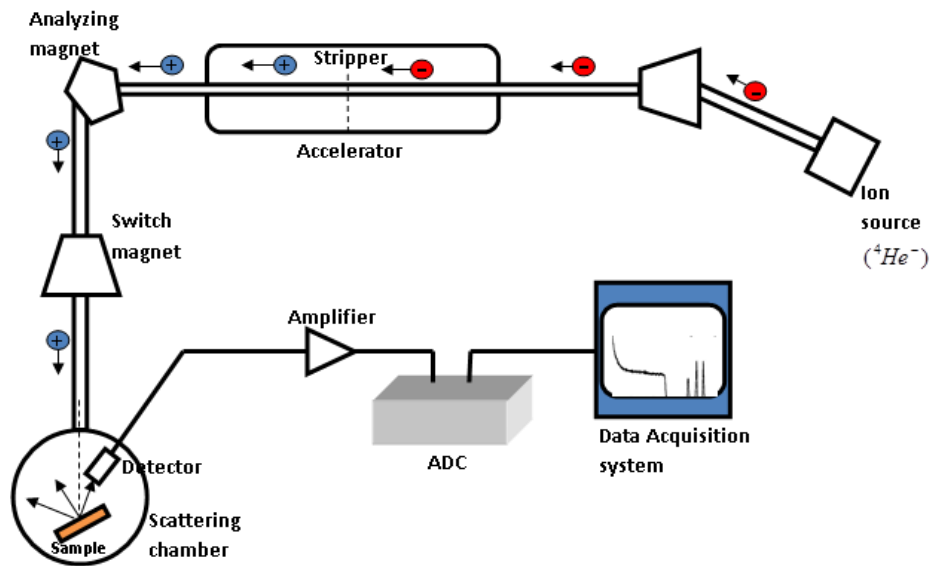


**Figure 3.24:** Layout of a typical ion beam scattering setup including a tandem accelerator and scattering chamber in backscattering configuration.

Fig.3.25 shows a photograph of the RBS system used to analyze thin films in this study.



**Figure 3.25:** Photograph of the RBS system at the Ithemba Labs, Cape Town, South Africa.

### 3.12. Thermoluminescence Spectroscopy

An ionizing radiation creates electronic excited states in crystalline materials. In some materials, these states are trapped, for extended periods of time by localized defects, or imperfections in the crystal lattice. Heating the crystal causes the electrons to drop back to their ground state, releasing a photon of energy equal to the energy difference between the trap state and the ground state. The resulting thermoluminescence is used to approximate the number of trapped electrons and the depth of the trap levels within the forbidden region, and a thermoluminescence spectroscopy is used to reveal such information [39].

The thermoluminescence spectroscopy system which was used in this study was the Harshaw 3500 TLD Reader that is equipped with a  $^{60}\text{Co}$   $\gamma$ -radiation source. The Harshaw includes a sample drawer for a single element TLD dosimeter, a linear, programmable



heating system and a cooled photomultiplier tube with associated electronics to measure the TL light output. It has a heating temperature capability up to 600 °C, a 7 decade glow curve acquisition range, and an optional neutral density filter to extend the high measurement range. Fig.3.26 is a schematic of a typical setup of the 3500 TLD spectroscopy system.

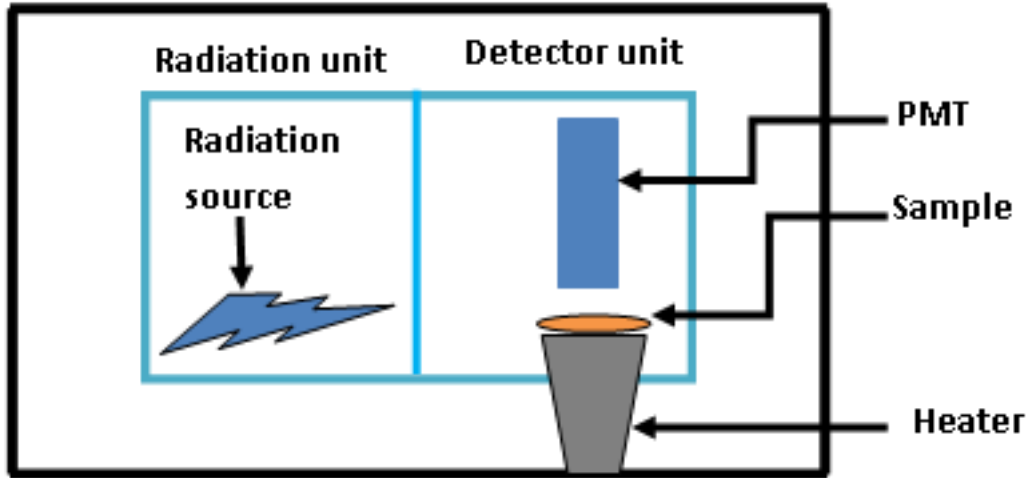


**Figure 3.26:** Schematic representation of the TL spectroscopy system, adapted [37].

## References

1. [http://www.wlu.ca/documents/25789/Cary\\_Eclipse.pdf](http://www.wlu.ca/documents/25789/Cary_Eclipse.pdf) -accessed on 14/11/2013.
2. T. H. Gfroerer, Photoluminescence in Analysis of surfaces and Interfaces. In *Encyclopedia of Analytical chemistry*. R.A. Meyers (Ed.) 9209-9231, John Wiley & Sons Ltd, Chichester, 2000.
3. [www.antteknik.com/documents/catalogs/SPM-9600\\_C147-E010.pdf](http://www.antteknik.com/documents/catalogs/SPM-9600_C147-E010.pdf), Date accessed 02/08/2013.
4. P. Eaton, P. West, *Atomic Force Microscopy*, Oxford University Press Inc. New York, 2010.
5. J. T. Cheung, *Method of laser ablation for uniform thin film deposition*, US Patent (1995).
6. [http://en.wikipedia.org/wiki/Pulsed\\_laser\\_deposition](http://en.wikipedia.org/wiki/Pulsed_laser_deposition)-visted on 3/3/2015.
7. [http://www.en.wikipedia.org/wiki/pulsed\\_laser\\_deposition](http://www.en.wikipedia.org/wiki/pulsed_laser_deposition), accessed on 10/02/ 2015.

8. M. S. Hegde, J. Indian Acad. Sci. **113** (2001) 445-458.
9. T. Haugan, P. N. Barnes, L. Brunke, I. Maartense, J. Murphy, Physica C **397** (2003) 47-57.
10. M. von Ardenne, Improvements in electron microscopes, convention date (Germany) 18 February 1937.
11. University of Nebraska-Lincoln: [www.unl.edu/CMRAcfem/semoptic.html](http://www.unl.edu/CMRAcfem/semoptic.html)
12. J. I. Goldstein, D.E. Newbury, D.C. Joy, *Scanning Electron Microscopy and X-ray Microanalysis*, Kluwer Academic, New York, 2003.
13. D. Poelman, P. F. Smet, Physica B **439**(2014)35–40.
14. P. F. Smet, J. Botterman, A. B. Parmentier, D. Poelman, Opt. Mater. **35** (2013) 1970–1975.
15. R. F. Egerton, *Physical Principles of Electron Microscopy: An Introduction to TEM, SEM, and AEM*, Springer, 2005.
16. [http://www.charfac.umn.edu/instruments/sem\\_primer.pdf](http://www.charfac.umn.edu/instruments/sem_primer.pdf) accessed 31/08/2013.
17. J. F. Watts, J. Wolstenholme ‘*An Introduction to Surface Analysis by XPS and AES*’, John Wiley & Sons, West Sussex, England, 2003.
18. W. L. Bragg, "The Specular Reflexion of X-rays". *Nature* **90** (2250) (1912) 410.
19. W. L. Bragg, "The Diffraction of Short Electromagnetic Waves by a Crystal". *Proceedings of the Cambridge Philosophical Society* **17** (1913) 43.
20. J. D. Rachwal, "*X-ray diffraction applications in thin films and (100) silicon substrate stress analysis*" (2010). Graduate School Theses and Dissertations, 2010.  
<http://scholarcommons.usf.edu/etd/1745-> accessed on 16/11/2013.
21. <http://www.eag.com/mc/x-ray-diffraction.html> accessed on 10/03/2014.
22. B. D. Cullity, S. R. Stock, *Elements of X-Ray Diffraction, 3<sup>rd</sup> Edition*, Prentice Hall Inc. New Jersey, 2001.
23. Hong Kong Baptist University: [www.hkbu.edu.hk/~csa/fesem.html](http://www.hkbu.edu.hk/~csa/fesem.html), accessed 16/11/2013.
24. [http://en.wikipedia.org/wiki/X-ray\\_photoelectron\\_spectroscopy](http://en.wikipedia.org/wiki/X-ray_photoelectron_spectroscopy)-accessed on 3/3/2015.
25. J. F. Moulder, W. F. Stickle, P.E. Sobol, K.D. Bomben, Handbook of X-ray Photoelectron Spectroscopy, ULVAC-PHI, Inc. 370 Enzo, Chigasaki 253-8522 Japan.

26. UK Surface Analysis Forum: XPS: <http://www.uksaf.org/tech/xps.html> accessed 02/09/2013.
27. G. C. Smith, *Surface Analysis by Electron Spectroscopy*, Plenum Press, New York, 1994.
28. <http://www.iontof.com/technique-surfacespectroscopy>, accessed 24/02/2014.
29. R. F. K. Herzog, F. Viehboeck, "Ion source for mass spectrography". *Phys. Rev.* **76** (6) (1949) 855–856.
30. J. J. Thomson, "Rays of positive electricity". *Phil. Mag.* **20** (1910) 752–767.
31. <http://www.geos.ed.ac.uk/facilities/ionprobe/SIMS4.pdf> accessed 18/09/2013.
32. <http://www.geos.ed.ac.uk/facilities/ionprobe/SIMS4.pdf> accessed 18/09/2013.
33. [http://www.chem.qmul.ac.uk/surfaces/scc/scat5\\_5.htm](http://www.chem.qmul.ac.uk/surfaces/scc/scat5_5.htm) accessed 18/09/2013.
34. J. T. Grant, D. Briggs, *Surface Analysis by Auger and X-ray Photoelectron Spectroscopy*. IM Publications, Chichester: 2003.
35. L. A. Harris, *J. Appl. Phys.* **39** (1968)1419-1427.
36. O. M. Ntwaeaborwa, PhD., dissertation, University of the Free State, South Africa (2006).
37. [http://en.wikipedia.org/wiki/Rutherford\\_backscattering\\_spectrometry](http://en.wikipedia.org/wiki/Rutherford_backscattering_spectrometry)-accessed on 3/3/2015.
38. W. Chu, J. W. Mayer, M. Nicolet, *Backscattering spectrometry*, Academic press, Inc, San Diego, California, 1978.
39. L. L. Noto, PhD., dissertation, University of the Free State, South Africa (2015).

## Chapter 4

### Luminescent Properties, Intensity Degradation and X-Ray Photoelectron Spectroscopy Analysis of CaS:Eu<sup>2+</sup> Powder

#### 4.1. Introduction

Alkaline earth sulfides such as zinc sulfide (ZnS), calcium sulfide (CaS), strontium sulfide (SrS), and barium sulfide are wide bandgap semiconducting materials that have been used as phosphor materials for a long time [1]. Some of the applications of these phosphors are in light emitting devices such as field emission displays (FEDs) [2], wavelength converters in light emitting diodes (LEDs) for solid-state lighting [3, 4], cathode ray tubes [5], and thermoluminescent dosimeters [6]. In particular, europium (Eu<sup>2+</sup>) doped CaS phosphor has emerged as a preferred source of red light in three-band phosphor-converted white LEDs pumped by blue LEDs, since this phosphor has a strong absorption between 450-500 nm associated with the  $4f \rightarrow 5d$  transitions of the Eu<sup>2+</sup> dopant ion. A popular blue-emitting LED is the highly efficient InGaN semiconductor which emits in the range 420 – 480 nm [7]. This blue radiation can partially be absorbed by green and red-emitting phosphors to achieve white emission from the LED.

The CaS host is a wide band semiconductor whose band gap is 4.43 eV [8]. It has a rock salt (sodium chloride) cubic structure. Its melting point is 2525 °C, while its density is 2.59 g/cm<sup>3</sup>. In the crystal, each S<sup>2-</sup> ion is surrounded by an octahedron of six Ca<sup>2+</sup> ions, and complementarily, each Ca<sup>2+</sup> ion is surrounded by S<sup>2-</sup> ions. Thus, the Eu<sup>2+</sup> activator ion sits in a six-fold Ca<sup>2+</sup> site surrounded by S<sup>2-</sup> ions to make an O<sub>h</sub> symmetry [9]. The Eu<sup>2+</sup> ion has seven  $f$  electrons which form a stable half-filled  $4f$  valence shell. These seven  $4f$  electrons do not strongly interact with the environment of the host material because they are effectively shielded by filled  $5s^2$  and  $5p^6$  shell and thus are affected weakly by changes in the environment. After one of the  $4f$  electrons is excited to the  $5d$  level, this electron is

strongly influenced by the crystal field, leading to broad, host dependent  $5d \rightarrow 4f$  emission bands. The five  $4f^6 5d^1$  orbitals are split by the octahedral crystal field into the  $t_{2g}$  band with the triple degenerate  $xy$ ,  $yz$ , and  $zx$  orbitals and the  $e_g$  band with the doubly degenerate  $x^2-y^2$  and  $z^2$  orbitals [10]. These bands give rise to an absorption or excitation spectrum comprising of two broad bands. The host lattice dependence of the emission is mainly connected with covalency (the nephelauxetic effect), and the strength of the crystal field [11]. As the position of the band corresponding to the  $4f^6 5d^1$  configuration is strongly influenced by the host, the emission can be anywhere from ultraviolet (UV) to visible [12]. The emission peaks of  $\text{Eu}^{2+}$  in a CaS host are located in the wavelength range of 600-750 nm, with a maximum at 650 nm corresponding to the transition from the lower  $4f^6 5d^1(t_{2g})$  state to the  $4f^7(^8S_{7/2})$  ground state of  $\text{Eu}^{2+}$ .

Furthermore,  $\text{CaS:Eu}^{2+}$  phosphor has the potential application as a source of red light in low voltage field emission displays (FEDs). Generally, sulfide based phosphors are still attracting the attention of various investigators [13-15] for applications in FEDs due to their high luminous efficiencies [16, 17]. However, one set back of sulfides in FED applications is their cathodoluminescence (CL) intensity degradation [18, 19]. Various mechanisms that affect the CL of sulfide-based phosphors in a FED environment have been reported [20-23]. In particular, based on electron interaction with residual gases, Swart et al. [21] proposed the electron stimulated surface chemical reaction (ESSCR) model of the degradation of the CL intensity of different phosphor materials. This model relates the CL intensity degradation to chemical reactions occurring on the surface during the interaction of electrons with the phosphors.

In the present study, we investigated the surface chemical states, photoluminescent (PL) and structural properties of the commercially available CaS doped with  $\text{Eu}^{2+}$ . The CL of the phosphor bombarded by an electron beam in a vacuum and the effects of beam current on the CL intensity are reported. Using two different primary excitation sources, namely a monochromatized xenon lamp and a 325 nm He-Cd laser to excite the powder, we investigated the absorption and emission mechanism of the  $\text{Eu}^{2+}$  ion in CaS. The unintended impurities in the  $\text{CaS:Eu}^{2+}$  powder, have been used to demonstrate the dependence of the

emission of the  $\text{Eu}^{2+}$  ion on the host lattice. The phosphor was evaluated for applications in low voltage FEDs and in phosphor down-converted white emitting LEDs.

## 4.2. Experimental

The commercial  $\text{CaS:Eu}^{2+}$  powder phosphor was purchased from Phosphor Technology in the United Kingdom. The crystal structure of the phosphor was studied using the X-ray diffractometer; Bruker AXS D8, with  $\text{CuK}\alpha$  radiation of wavelength 1.5406 Å. The diffraction patterns were recorded over the range  $20^\circ \leq 2\theta \leq 80^\circ$ . The morphology of the powder was studied using a Scanning Electron Microscope (SEM), and the Philips (FEI, the Netherlands) CM 100 transmission electron microscope (TEM). The Shimadzu Superscan SSX-550 system was used to record the SEM images. The SEM system was set at an operating voltage of 5.00 kV, a probe diameter of 1.8 nm, and a working distance (WD) of 17 mm. The X-ray photoelectron spectroscopy (XPS) data were collected using the XPS-PHI 5000 Versa probe equipped with a monochromatic  $\text{AlK}\alpha$  with energy of 1486.6 eV. The survey scans were performed in the binding energy range of 0-1400 eV with a pass energy of 11.8 eV in order to analyze the chemical composition of the material. High resolution scans for O 1s, Ca 2p, and S 2p XPS peaks were recorded with a pass energy of 11.8 eV and were fitted using MULTIPACK [25] version 8.2c data analysis software. The fitting procedure was done using the Shirley background and the peak shapes were 100 % Gaussian. The full width at half maximum (FWHM) for all the deconvoluted peaks in each high resolution spectrum was kept the same. All the binding energies of the photoelectron spectra were corrected with C 1s signal at 284.6 eV. The degradation study of  $\text{CaS:Eu}^{2+}$  was carried in situ using a PHI Model 545 Auger Electron Spectroscopy (AES). The chamber was evacuated to  $1 \times 10^{-8}$  Torr. The phosphor powder was excited for CL measurements by the same primary electron beam of energy 2 keV, which was used for Auger excitation. AES spectra and CL intensity were measured simultaneously and continuously over a eighteen-hour period. The diameter of the electron beam was 300  $\mu\text{m}$ , as determined according to the procedure outlined in [26]. The corresponding current density was 14.1  $\text{mA/cm}^2$ . The CL data was collected via an optical fiber attached to the quartz view port of the UHV chamber and a

computer. CL intensity was monitored at a constant accelerating voltage and different beam currents. The ocean optics S2000 spectrometer using OOIBase32 computer software was used for CL data acquisition. PL spectra were recorded using the PL system and the Cary Eclipse fluorescence spectrometer using a 325 nm He-Cd laser and a monochromatized xenon lamp as excitation sources, respectively. While a fixed wavelength of 325 nm was used when using the PL laser system, the excitation wavelengths for the xenon lamp were varied from 200 nm - 600 nm and the respective emissions were observed in the wavelength ranges of 400 to 800 nm at room temperature.

### 4.3. Results and Discussion

#### 4.3.1. XRD, SEM and TEM Analyzes

The XRD pattern of the CaS:Eu<sup>2+</sup> powder is illustrated in Fig. 4.1. The lattice parameters for the face-centered cubic Eu<sup>2+</sup> doped CaS was determined by using the relation given in Eq. (4.1) [27] and the parameter values are listed in Table 4.1.

$$\frac{1}{d^2} = \frac{h^2 + l^2 + k^2}{a^2} \quad (4.1)$$

Eq. (4.1) was used to calculate the lattice constant, (*a*) of the CaS:Eu<sup>2+</sup>, and an average value of 5.707 Å was obtained. This is consistent with the lattice constant of 5.686 Å, for standard face-centred cubic CaS referenced in JCPDS file number 08-0464. Secondary phases marked with asterisk (\*) are ascribed to CaSO<sub>4</sub> as referenced in JCPDS file number 80-0787 and this is probably coming from the starting materials used in the preparation and/or incidental contamination, as explained in section 4.3.3., or owing to interaction of the surface with atmospheric gases due to chemical stimulated interactions with X-ray beam. Holloway et al. [13, 23] and Kumar et al. [20] have shown that ZnS and other phosphors are very reactive under electron beam irradiation. The effects of X-rays (and laser radiation), however, still need to be determined. The XRD peak at around  $2\theta = 31^\circ$  (Fig. 4.1), was used to calculate the crystallite size (*D*), using Scherer's equation [28].

$$D = \frac{k\lambda}{\beta \cos\theta}, \quad (4.2)$$

where  $\beta$  is the FWHM of the peak in radians, and  $k$  is a constant which is usually set as 0.9, and  $\lambda$  is the X-ray radiation wavelength (0.154056 nm) and  $\theta$  is the peak position, also known as Bragg angle. The estimated crystallite size was found to be 0.15  $\mu\text{m}$ . The actual crystallite size could be greater than 0.15  $\mu\text{m}$  if other factors such as peak broadening resulting from instrumental resolution and/or residual strain effect are taken into account.

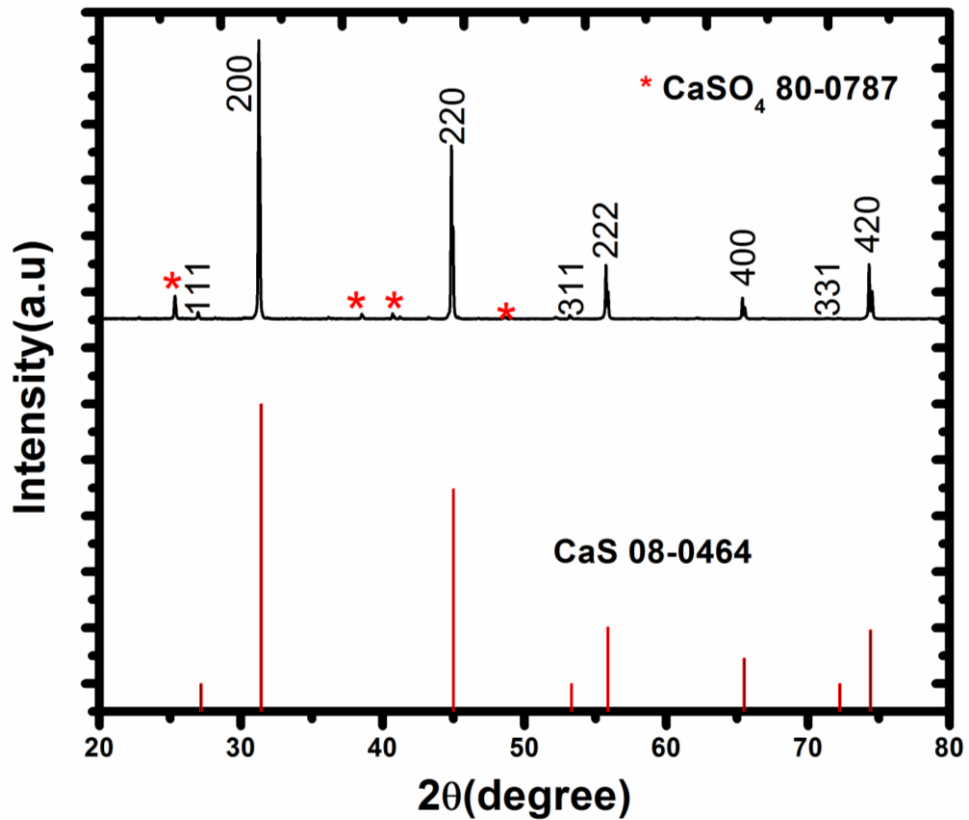


**Figure 4.1:** XRD diffraction patterns of CaS:Eu<sup>2+</sup> powder.



**Table 4.1:** The calculated structural parameters for CaS:Eu<sup>2+</sup> powder sample. Secondary phases marked with asterisk (\*) are ascribed to CaSO<sub>4</sub>.

(h k l)	2θ(°)	FWHM(°)	d(Å)	a(Å)	Area
*	25.3485	0.1181	.....		299.52
<b>1 1 1</b>	26.9512	0.1378	3.29491	5.70695	99.90
<b>2 0 0</b>	31.2605	0.0840	2.85347	5.70694	4596.44
*	38.5393	0.1920	.....		121.58
*	40.7153	0.1920	.....		113.19
<b>2 2 0</b>	44.8415	0.0780	2.01771	5.70695	2948.33
*	48.6175	0.2880	.....		76.53
<b>3 1 1</b>	53.2222	0.2880	1.72071	5.70695	89.42
<b>2 2 2</b>	55.7349	0.0960	1.64745	5.70693	1048.11
<b>4 0 0</b>	65.3809	0.0960	1.42674	5.70696	462.25
<b>4 2 0</b>	74.3089	0.0780	1.27611	5.70694	981.70

The SEM and TEM images are shown in Figs. 4.2 and 4.3, respectively. Most of the particles are spherical in shape with some degree of faceting. It is also clear from the images that some of the larger particles were made up of an agglomeration of the smaller particles. The average diameter of the powder particles as estimated from Fig. 4.3 (a) is 3.64 μm and the size distribution is ranging from 1- 7 μm as shown in Fig. 4.3(b).

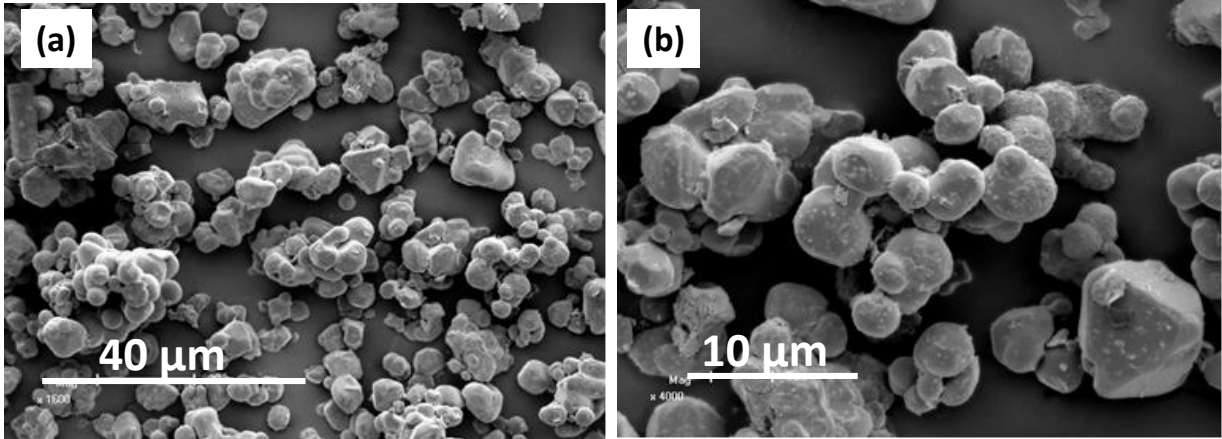


**Figure 4.2:** SEM images of the CaS:Eu<sup>2+</sup> powder with field of view of (a) 120 and (b) 39.

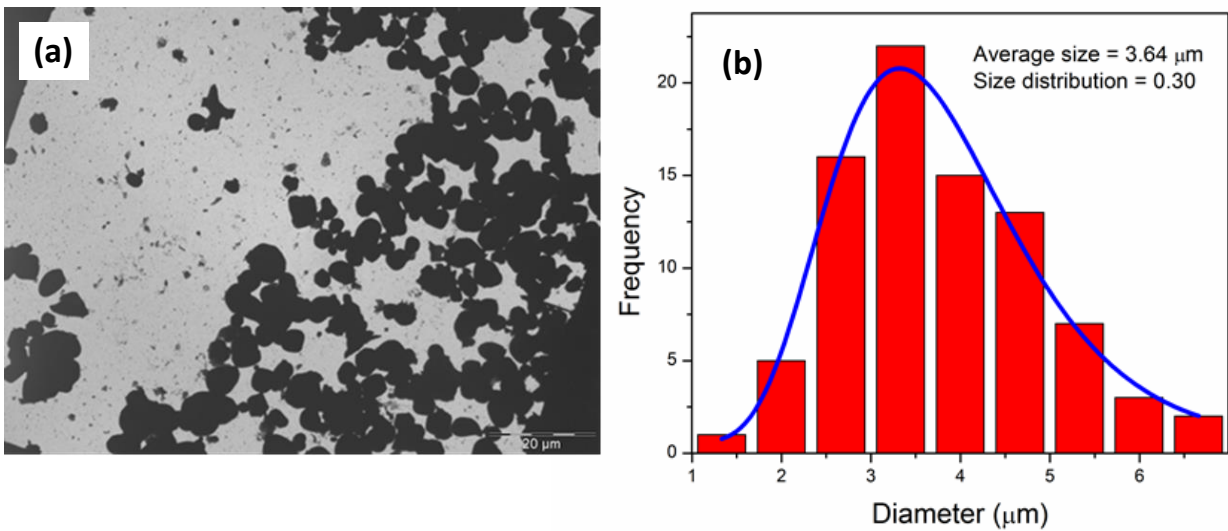
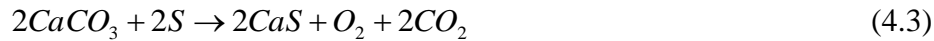


**Figure 4.3:** (a) TEM image. (b) Particle size distribution for CaS:Eu<sup>2+</sup> powder.

#### 4.3.2. Surface Characterization by X-ray Photoelectron Spectroscopy

The chemical states of the undegraded and degraded CaS:Eu<sup>2+</sup> were analyzed using XPS. Fig. 4.4 shows the XPS survey scans of the CaS:Eu<sup>2+</sup> powder before and after sputtering with Ar<sup>+</sup> ions for the undegraded powder. The scan before sputtering reveals that the sample

contains Ca, S, O, and C, as expected. After sputtering the amount of C was reduced considerably while O remains on the surface and there was significant increase in the Ca XPS peak intensity. The small amount of C is probably due to surface contamination from atmospheric hydrocarbons and from the tape on which the powder was mounted. The presence of O and the increase in the Ca XPS peak intensity can be explained by considering the following equations proposed by several investigators [8, 29] especially when CaS was prepared using CaCO<sub>3</sub> as one of the precursors



As shown in Eq. (4.3) above, CaS is formed from the reaction of CaCO<sub>3</sub> with S, and O<sub>2</sub> and CO<sub>2</sub> are released as by-products. Qui et al. [30] and Anthony et al. [31] have shown that CO<sub>2</sub> can convert CaS, under pressurized and/or atmospheric conditions over a wide range of temperatures, to CaSO<sub>4</sub>, as shown by Eq. (4.4).



CaO and CaSO<sub>4</sub> could also be formed as reported by Marban et al. [32] and Torres et al. [33] when CaS reacts with O<sub>2</sub> as in Eq. (4.5) and (4.6), respectively. It is therefore most likely that, the presence of O and the increase in the Ca XPS peak intensity was due to the formation of oxygen and calcium containing CaO/CaSO<sub>3</sub> and CaSO<sub>4</sub> compounds.



The presence of the sulfite can be formed if the reaction in Eq. (4.6) further proceeds [34] as:



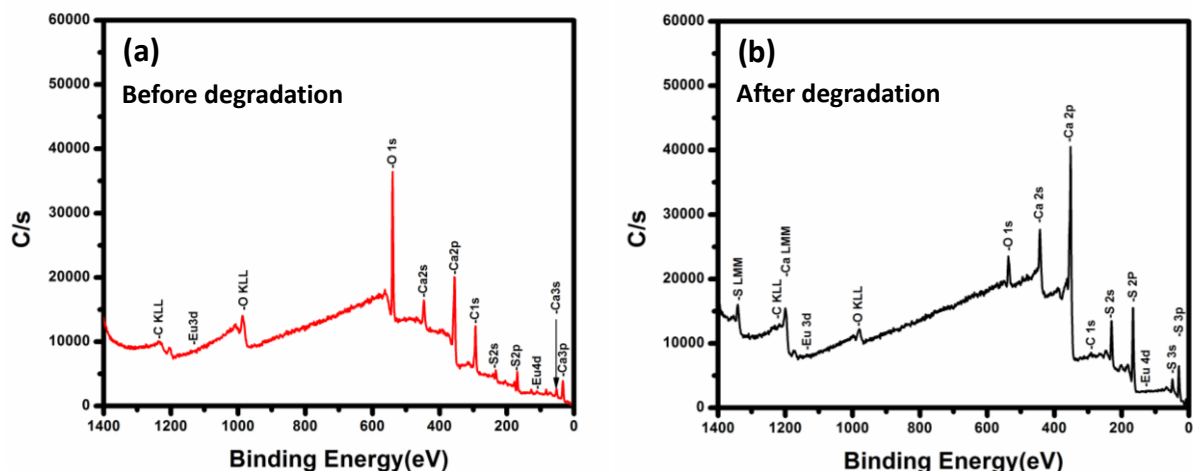


**Figure 4.4:** XPS survey scan spectrum of the undegraded  $\text{CaS:Eu}^{2+}$  (a) before sputtering (b) after sputtering.

Fig.4.5 (a) and (b) show the fitted Ca 2p XPS peaks before and after degradation, respectively. In the Ca 2p XPS spectrum presented, the Ca  $2p_{3/2}$  peaks at 347.0 eV and 347.7 eV are assigned to  $\text{CaSO}_4$  [35] and CaS [36], respectively. The Ca  $2p_{3/2}$  XPS peak at 345.6 eV is assigned to Ca in  $\text{CaSO}_3$  [34]. The Ca  $2p_{1/2}$  peaks are at 350.4, 351.6, and 349.5 eV for Ca in CaS,  $\text{CaSO}_4$ , and in  $\text{CaSO}_3$ , respectively. The energy differences between the  $2p_{3/2}$  and  $2p_{1/2}$  peak positions are in agreement with energy differences reported in Ref. [37].

Two separate peaks are observed before and after degradation for each S 2p spectra shown in Fig.4.6. The S  $2p_{3/2}$  peak at 160.3 eV [37] is attributed to the sulfur in CaS. The S  $2p_{3/2}$  peak at 169.1 eV is from sulfur in  $\text{CaSO}_4$  [35], while that at 167.4 eV is assigned to the S from  $\text{CaSO}_3$  [38]. The S  $2p_{1/2}$  peak positions at 161.4, 168.1 and 170.3 eV are assigned to S in CaS,  $\text{CaSO}_3$ , and  $\text{CaSO}_4$ , respectively. The energy differences between the S  $2p_{3/2}$  and S  $2p_{1/2}$  peaks are in agreement with those given in Ref. [37]. Kumar et al. [34] have also observed two peaks for S 2p at different binding energies.

Fig.4.7 shows the O 1s spectra before degradation and after degradation fitted with two peaks with binding energies at 532.8 and, 531.2 eV that correspond to O in  $\text{CaSO}_4$  [39] and  $\text{CaSO}_3$  [39], respectively. The  $\text{CaSO}_4$  peak increased probably due to stimulated surface chemical reactions.

Table 4.2 gives a summary of identified species in the XPS spectra (peak position and chemical bonding) of CaS:Eu<sup>2+</sup> powder before (B) and after (A) degradation.

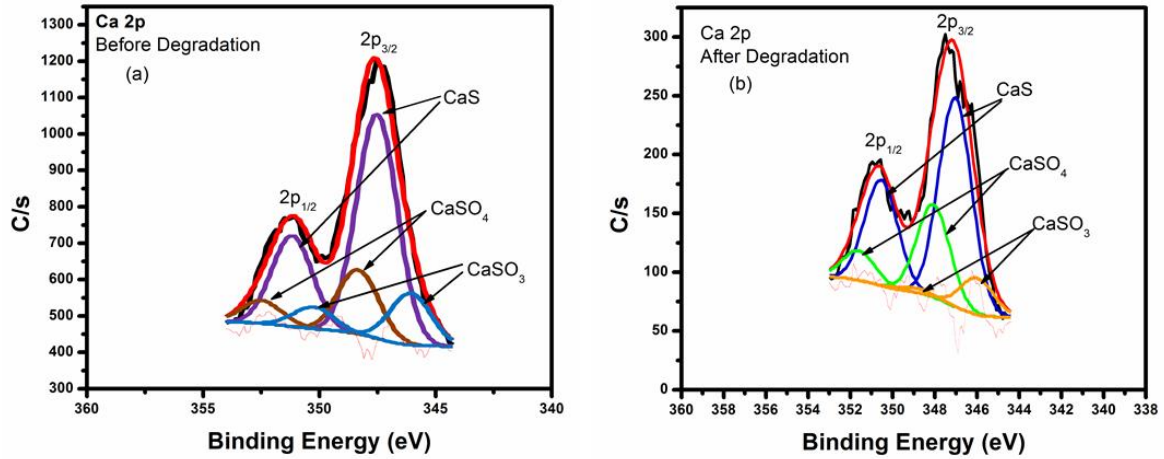


Figure 4.5: XPS Spectra of Ca 2p (a) before and (b) after degradation.

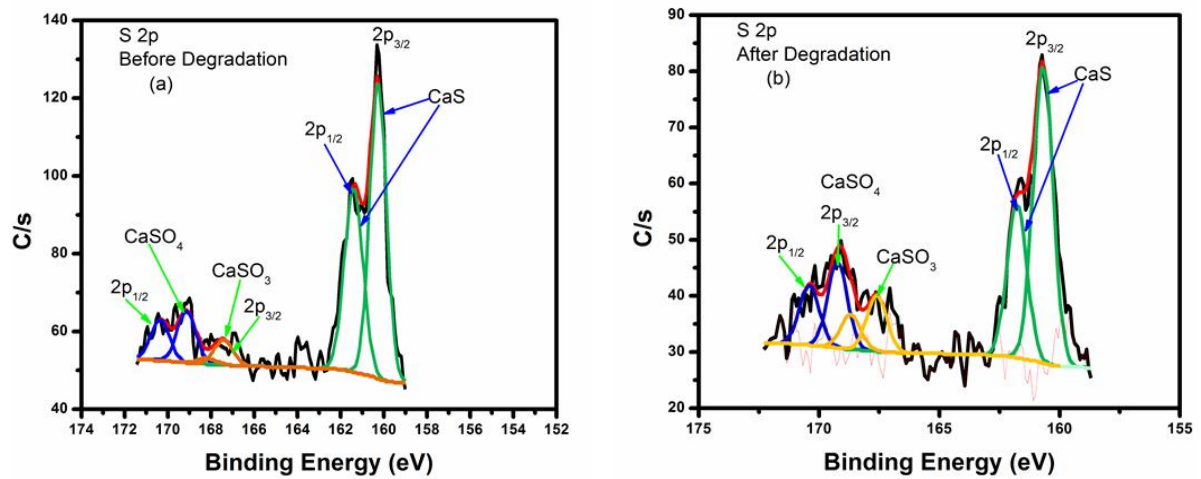
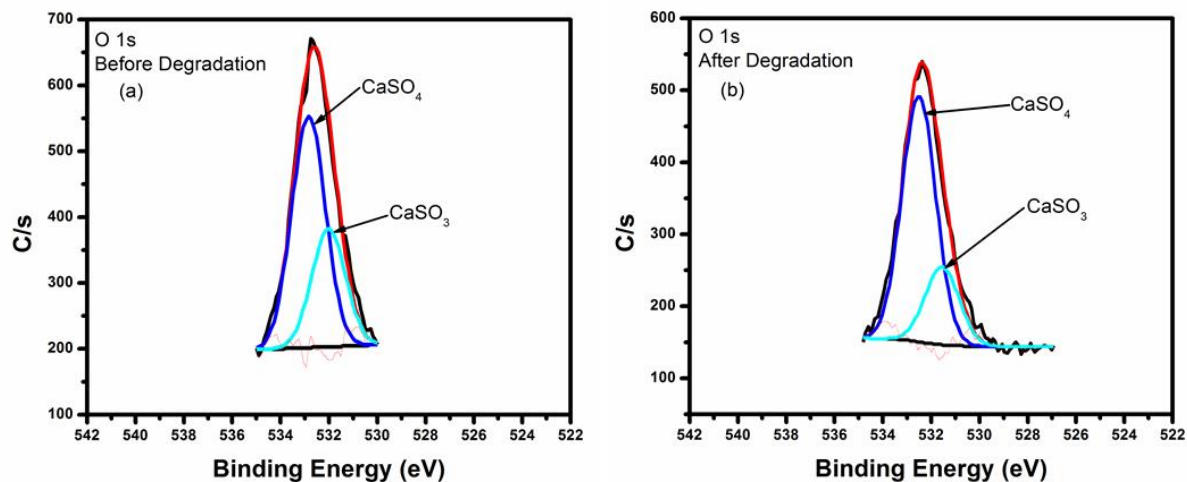


Figure 4.6: XPS spectra of sulfur (S 2p) (a) before and (b) after degradation.



**Figure 4.7:** XPS spectra of O 1s (a) before and (b) after degradation.

**Table 4.2:** XPS peak position, and chemical bonding for CaS:Eu<sup>2+</sup> powder before (B) and after (A) degradation.

Binding energy (eV)						
	Chemical States	Ca 2p <sub>1/2</sub>	Ca 2p <sub>3/2</sub>	S 2p <sub>1/2</sub>	S 2p <sub>3/2</sub>	O 1s
<b>B</b>	<b>CaS</b>	350.4	347.0	161.4	160.3	.....
<b>A</b>		350.4	346.7	161.4	160.3	.....
<b>B</b>	<b>CaSO<sub>4</sub></b>	351.6	347.7	170.3	169.1	532.8
<b>A</b>		351.5	347.8	170.3	169.1	532.5
<b>B</b>	<b>CaSO<sub>3</sub></b>	349.5	345.6	168.1	167.4	531.2
<b>A</b>		349.7	345.7	168.5	167.4	531.5

### 4.3.3. Photoluminescence and Cathodoluminescence Properties of CaS:Eu<sup>2+</sup>

#### 4.3.3.1. The Excitation Spectrum of the Eu<sup>2+</sup> Ion in CaS

Fig. 4.8 shows the energy level diagram and room temperature photoluminescent excitation (PLE) spectrum of the CaS:Eu<sup>2+</sup> commercial powder. The excited  $5d^1$  electronic states of the Eu<sup>2+</sup> ion is split into  $e_g$  and  $t_{2g}$  energy states by the crystal field of the host. As also reported by Park et al. [40], the  $e_g$  and  $t_{2g}$  states are inside and below the conduction band, respectively. To position the conduction band (CB) in the energy diagram, we used an energy band gap of 4.43 eV based as reported previously [8].

The PLE spectrum was recorded when monitoring the emission at 650 nm. The broad excitation band between 200 nm and 320 nm can be associated with Eu<sup>2+</sup>  $4f^7[{}^8S_{7/2}] \rightarrow 4f^6[{}^7F_J]5d^1[e_g]$  and valence-to-conduction band transitions [41], while the excitation band extending from 400-600 nm is ascribed to the  $4f^7[{}^8S_{7/2}] \rightarrow 4f^6[{}^7F_J]5d^1[t_{2g}]$  transitions of Eu<sup>2+</sup> [42]. Both low-energy and high-energy bands show evidence for the “staircase” spectrum. CsCaBr<sub>3</sub>:Eu<sup>2+</sup> investigated by Suta et al. [43] also showed this “staircase” structure for the two excitation bands. The “staircase” structure arises due to the splitting of the  $4f^6$  configuration into seven  ${}^7F_J$  ( $J = 0 \dots 6$ ) states. Their estimated peak energies are given in Table 4.3. The  ${}^7F_0$  on the low-energy band is estimated at 604 nm, which is in good agreement with the value presented in Ref. [24]. The broad band excitation around 331 nm may be due to the presence of trap or defect state within the band gap [44].

#### 4.3.3.2. The Emission Spectra of the Eu<sup>2+</sup> Ion in CaS

The emission was monitored at excitation wavelengths of 247 nm, 331 nm, and 484 nm (Fig. 4.9(a)). For all the excitations, the emitted red light showed wavelength maximum at 650 nm. The conduction band excitation relaxes non-radiatively to the  $4f^6[{}^7F_J]5d^1(e_g)$  states, which in turn relaxes non-radiatively to the  $4f^6[{}^7F_J]5d^1(t_{2g})$  states. It is the dipole-allowed

transitions from the excited  $4f^6[{}^7F_0]5d^1(t_{2g})$  state to the ground state  $4f^7({}^8S_{7/2})$  of the  $\text{Eu}^{2+}$  ions which give rise to the broad emission band centered at 650 nm (Fig. 4.9 (a)). (Note that this sample was measured before exposure to the X-rays for XRD and XPS, and therefore excludes the X-ray effect but not the possible effect of the laser beam). The PL emission spectrum recorded using the 325 nm He-Cd laser as the excitation source is shown in Fig. 4.9 (b). The main emission, a broad band, is centered around 650 nm and is attributed to the emission from the excited state  $4f^65d^1(t_{2g})$ , due to the crystal field splitting of the  $5d^1$  orbitals. The minor peak at 384 nm is attributed to transitions  $4f^6[{}^7F_0]5d^1(t_{2g})$  to  $4f^7({}^8S_{7/2})$  of the  $\text{Eu}^{2+}$  in  $\text{CaSO}_4$ . The  $t_{2g}$  level of  $\text{Eu}^{2+}$  in  $\text{CaSO}_4$  is located around 3.2 eV, while the  $t_{2g}$  band of the  $\text{Eu}^{2+}$  in  $\text{CaS}$  is located around 2.0 eV (see Fig. 4.10). When the  $t_{2g}$  shifts upwards, the  $e_g$  band shifts downwards. In other words, the crystal field in  $\text{Eu}^{2+}$  in  $\text{CaS}$  is stronger than that in  $\text{CaSO}_4$ , and hence the emissions at 650 nm and 384 nm, respectively. Muke et al [45] and Patil et al [46] synthesized  $\text{CaSO}_4:\text{Eu}^{2+}$  and both observed an emission peak at 385 nm, monitored at an excitation of 320 nm. The presence of the emission peak at 384 nm which is assigned to  $\text{Eu}^{2+}$  in  $\text{CaSO}_4$  is consistent with the XPS and XRD data, which indicated that  $\text{CaSO}_4$  is present in the powder. No emission was observed from the parity forbidden  ${}^6P_j$  excited states of the  $4f^7$  ground state. This is because the  $4f^7({}^6P_{7/2}) \rightarrow 4f^7({}^8S_{7/2})$  is normally located around 360 nm (3.4 eV), as reported in Ref. [47], and the crystal field is strong enough to move the lowest  $4f^65d^1$  excited state to below the  ${}^6P_j$  level. Since  $\text{CaS}:\text{Eu}^{2+}$  phosphor exhibits strong absorption at the emission wavelength of a blue LED, it can be used as a wavelength converter under the excitation of the blue LED.



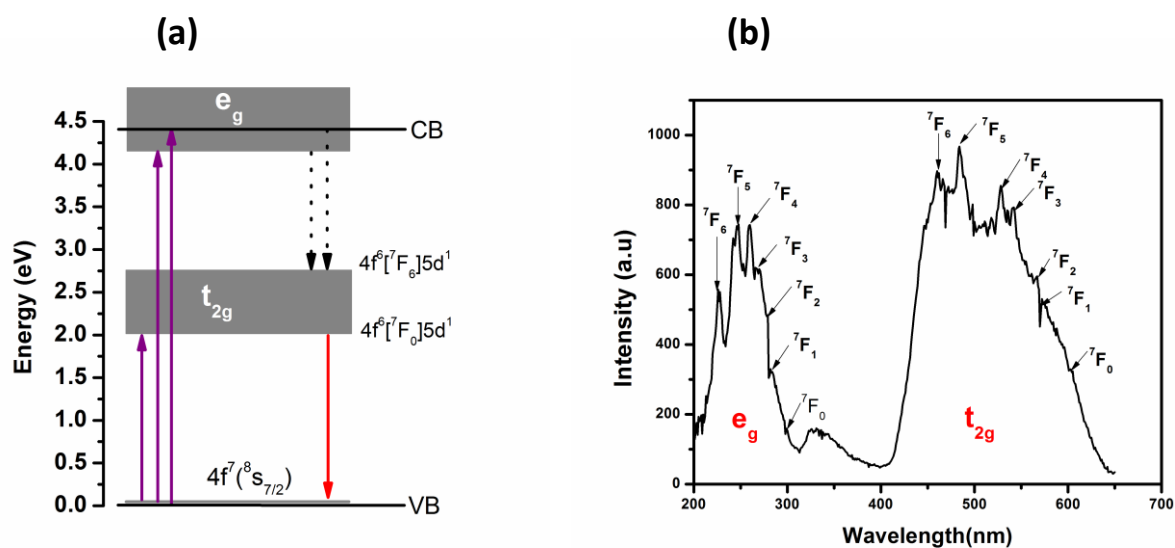


**Figure 4.8:** (a) Energy level diagram for  $\text{Eu}^{2+}$  in CaS. (b) PL excitation spectrum ( $\lambda_{em} = 650\text{nm}$ ) of  $\text{CaS}:\text{Eu}^{2+}$  at room temperature (300 K).

**Table 4.3:** Peak energy values of the  $4f^6(^7F_J)5d^1$  states in  $\text{CaS}:\text{Eu}^{2+}$

$4f^6(^7F_J)5d^1(t_{2g})$			$4f^6(^7F_J)5d^1(e_g)$		
State $^7F_J$	Position (nm)	Energy(eV)	State $^7F_J$	Position (nm)	Energy(eV)
$^7F_0$	604	2.05	$^7F_0$	300	4.13
$^7F_1$	574	2.16	$^7F_1$	282	4.40
$^7F_2$	568	2.18	$^7F_2$	279	4.44
$^7F_3$	541	2.29	$^7F_3$	268	4.63
$^7F_4$	528	2.34	$^7F_4$	260	4.77
$^7F_5$	484	2.56	$^7F_5$	247	5.02
$^7F_6$	460	2.70	$^7F_6$	226	5.49

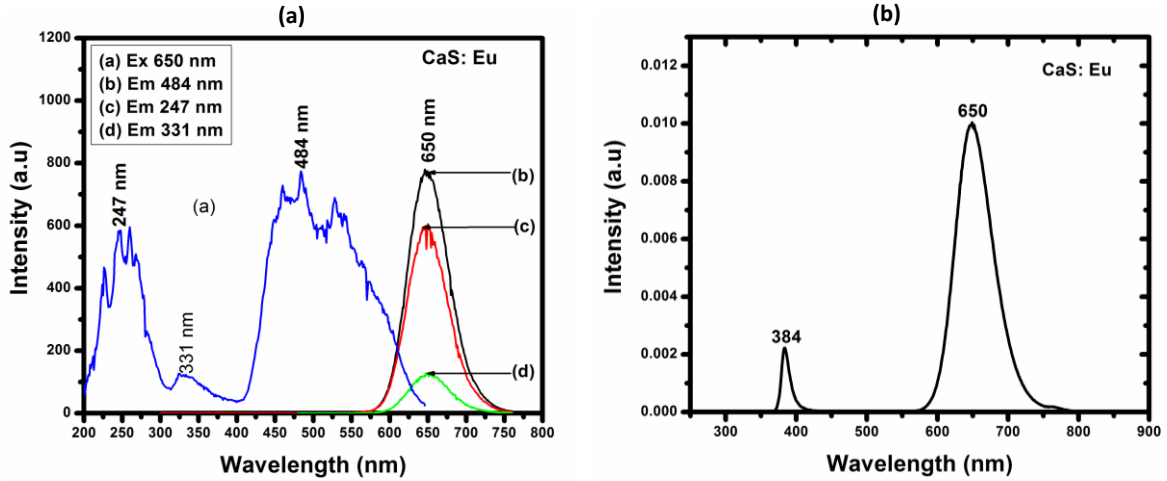


**Figure 4.9:** Graphs showing CaS:Eu<sup>2+</sup> powder: (a) PL excitation and emission spectrum using Cary Eclipse. (b) Emission spectrum using 325 nm He-Cd PL laser.

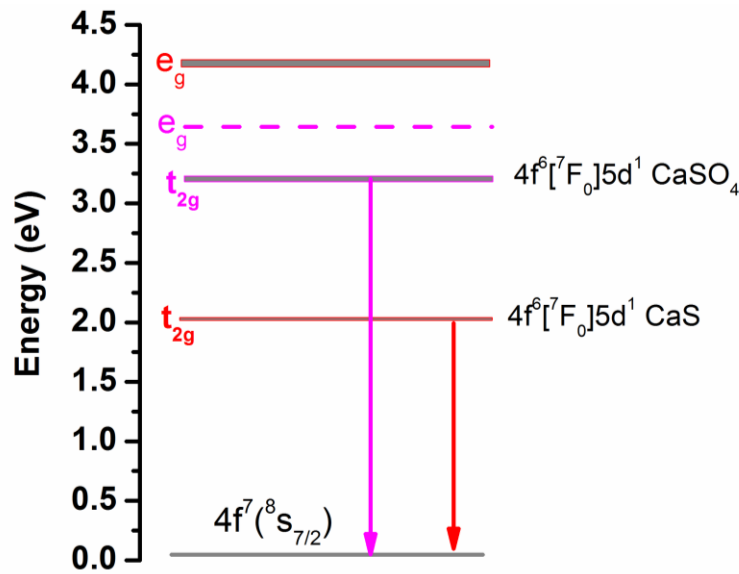


**Figure 4.10:** Energy level diagram for Eu<sup>2+</sup> in CaS and CaSO<sub>4</sub> (impurity in the powder) showing  $4f^6[{}^7F_0]5d^1(t_{2g}) \rightarrow 4f^7(^8S_{7/2})$  transitions, which give rise to the broad band emission.

### 4.3.3.3. AES and APPHs Results

Fig. 4.11 shows the AES spectra before and after degradation with characteristic Auger peaks of S (152 eV), C (273 eV), Ca (294 eV), and O (514 eV). The bombardment of the powder by an electron beam resulted in the decrease of the sulfur and carbon peaks. The slight shift observed in peak energies after degradation is possibly due to surface charging.

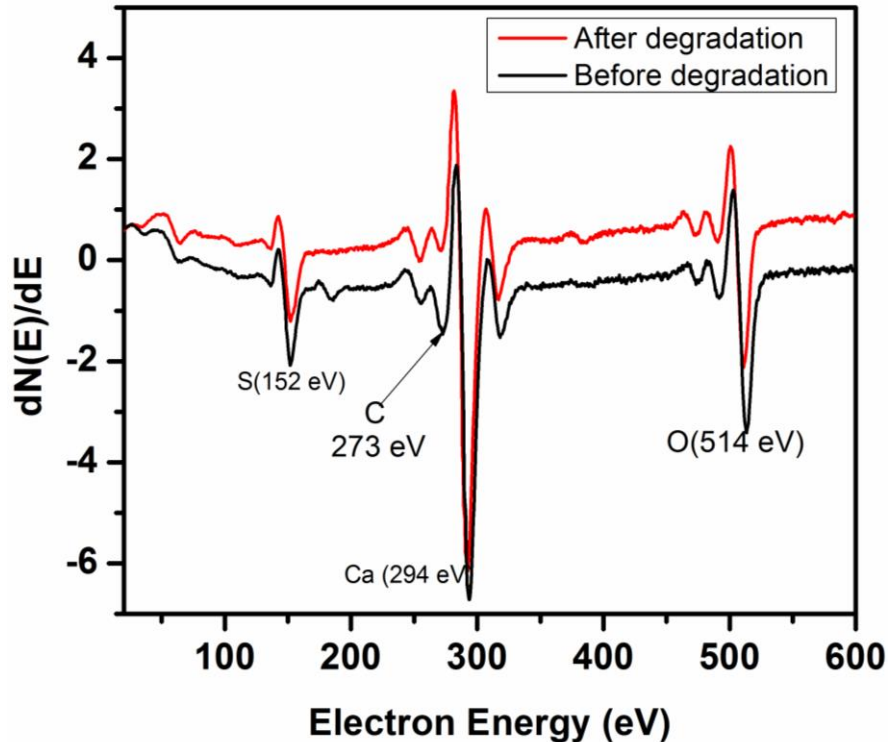


**Figure 4.11:** AES spectra from CaS:Eu<sup>2+</sup> phosphor before and after degradation.

Fig. 4.12 shows the Auger peak-to-peak heights (APPHs) of Ca, S, C, and O and the CL intensity profile as a function of electron dose. Upon exposure to the electron beam, the C APPH immediately started to decrease. The C on the phosphor is present from adventitious atmospheric contamination [18]. At first the S APPH increased due to the removal of the C from the surface, and then started to decrease after an electron dose of about 15 C/cm<sup>2</sup>. Abrams et al. [15] postulated that by the electron beam stimulated surface chemical reactions (ESSCR), the electron beam dissociates adsorbed reactive gas molecules to form reactive

atomic species. These atomic species remove S as volatile  $\text{SO}_x$  or  $\text{H}_2\text{S}$ . The O and Ca APPHs continued to increase as the C was being removed, and then after an electron dose of 150  $\text{C}/\text{cm}^2$  they decreased gradually, stabilizing after an electron dose of 530  $\text{C}/\text{cm}^2$ .

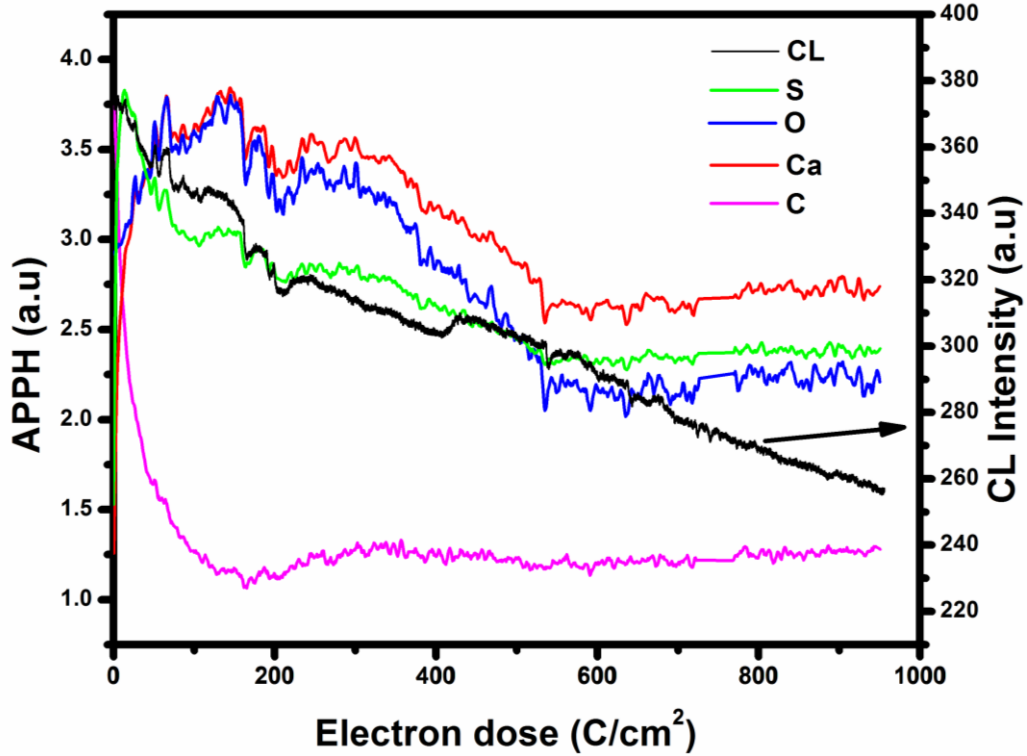


**Figure 4.12:** The relative CL intensity and Auger peak-to-peak heights (APPHs) change with electron dose of the  $\text{CaS}:\text{Eu}^{2+}$  surface during electron bombardment.

In order to minimize the signal fluctuations in the signals evident in Fig. 4.12, the variation of APPH ratios for Ca, S and O (compared to C) were plotted as function of electron dose and the result is shown in Fig. 4.13. As the C is removed from the surface, the APPHs for Ca, O and S initially increase and then start to decrease after an electron dose of 200  $\text{C}/\text{cm}^2$ . The reason for this is most likely due to the formation of the non-luminescent  $\text{CaSO}_4$  layer.

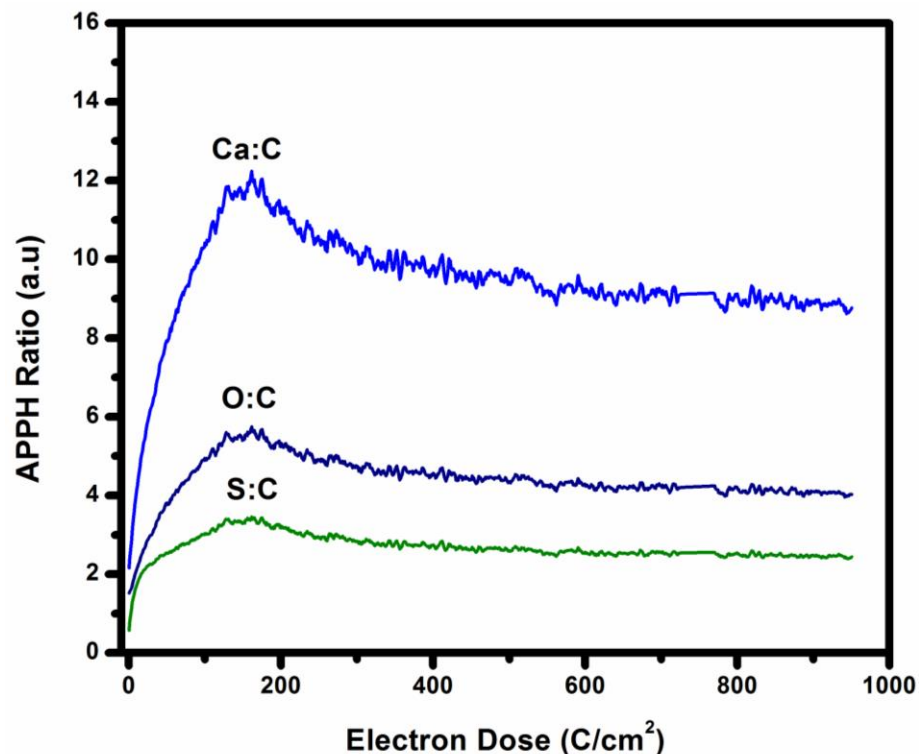


**Figure 4.13:** The variation of Auger peak-to-peak heights (APPHs) ratios of Ca: C, O: C and S: C with electron dose of the CaS:Eu<sup>2+</sup> surface during electron bombardment.

#### 4.3.3.4. CL Results

The CL emission spectra of CaS:Eu<sup>2+</sup> powders before and after 18 hours of degradation are shown in Fig. 4.14. When excited by the electron beam, the powder emitted a red luminescence peaking at around 650 nm. The CL emission intensity was reduced to about 72 % (i.e., reduced by about 28 %) after 18 h of continuous irradiation. This suggests that this material is quite stable under electron irradiation. Electron stimulated surface reactions (ESSCR) leading to a formation of a non-luminescent layer of CaSO<sub>4</sub> on the surface [21, 34] of the CaS could explain the gradual decrease in the CL intensity. Kumar et al. [20] has also proposed that luminescence quenching may be due to the formation of O defects which give rise to electron traps. According to Seager et al. [48] surface charging may also be responsible for CL degradation. The slight shift in AES spectra (Fig.4.11) after electron bombardment is actually an indication that there was surface charging. In the CL process the

electrons that are excited to the conduction band in the depletion layer will experience a repulsive force near the surface and the probability that the electron–hole pair will be swept apart before recombination increases with the consequent loss in CL intensity. The surface charging will also directly alter the CL efficiency if the surface potential becomes large enough to alter the arrival energy of the exciting electrons [49].

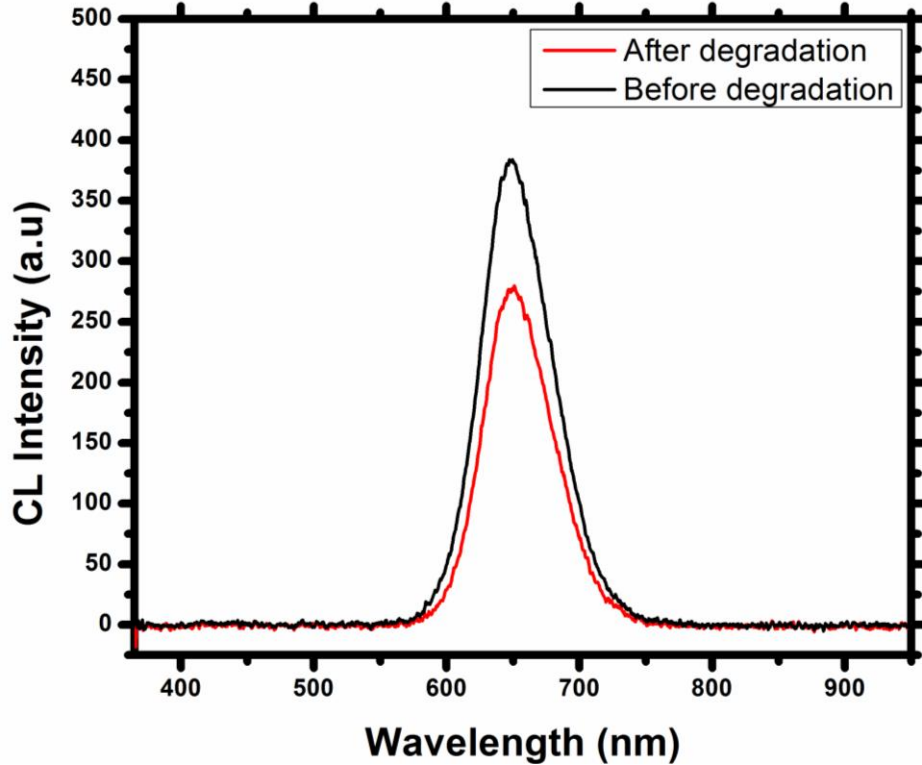


**Figure 4.14:** CL spectra of CaS:Eu<sup>2+</sup> before and after degradation at  $1 \times 10^{-8}$  Torr vacuum.

Fig. 4.15 shows the variations of CL emission intensities of the CaS:Eu<sup>2+</sup> powder with the emission beam current. The electron beam energy was kept constant, at 2 keV while the beam current was varied. The CL intensity increased as the current was increased from 1  $\mu$ A to 13  $\mu$ A, with the rate of change increasing after a beam current of 7  $\mu$ A, as shown in the inset. This implies that the powder does not suffer from saturation of brightness, which is a good property of a FED phosphor [15]. The increase in CL intensity when emission current was increased is attributed to the increase in the current density [50] and the subsequent increase in excited electrons.

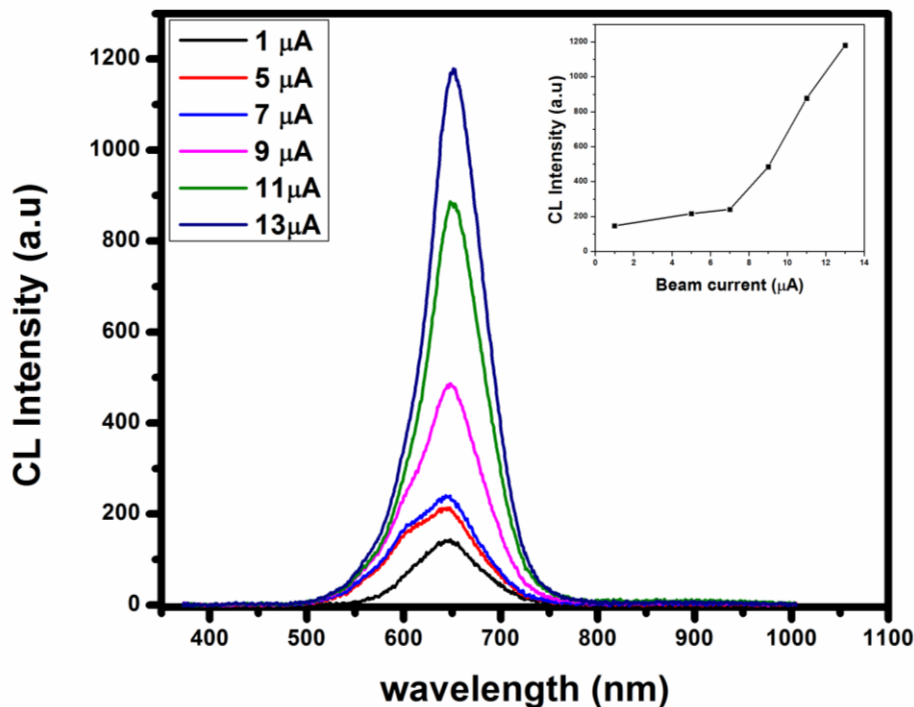


**Figure 4.15:** Variation of CL spectra of the CaS:Eu<sup>2+</sup> powder with different emission current under a constant 2 keV electron-beam excitation in a 1x 10<sup>-8</sup> Torr vacuum.

#### 4.4. Conclusion

The structure and morphology of CaS:Eu<sup>2+</sup> were investigated using XRD, SEM and TEM. The XRD results show that the CaS:Eu<sup>2+</sup> is crystalline with the CaS phase being dominant. From SEM and TEM images, the powder particles are mostly spherical and the size of the particles was in the micrometer range, as confirmed from the TEM data. The average particle size was found to be 3.64 μm. Upon excitation with either the xenon lamp or the 325 nm He-Cd laser, an intense red emission attributed to  $f \rightarrow d$  transitions of Eu<sup>2+</sup> was observed at 650 nm. XRD, XPS, and PL point to the existence of CaSO<sub>4</sub> and a small amount of CaSO<sub>3</sub> in the powder. The CaSO<sub>4</sub> and CaSO<sub>3</sub> may have been formed during synthesis or by reaction of CaS with water vapor, atmospheric O<sub>2</sub> and/or CO<sub>2</sub>. The formation of a CaSO<sub>4</sub> or CaSO<sub>3</sub> layer, surface charging, and possibly formation of O defects upon electron bombardment might collectively be responsible for the CL degradation (of about 28% of the original intensity). An increase in the CL intensity attributed to an increase in beam current density

was observed under beam currents of 1–13  $\mu\text{A}$ . The PL and CL results from this red-emitting phosphor indicate that it is a promising phosphor that can be used as a wavelength converter for white LEDs and is also suitable for FED applications.

## References

1. W. Lehmann, *J. Electrochem. Soc.* **117** (1970) 1389–1393.
2. S. Yang, C. Stoffers, F. Zhang, B. K. Wagner, J. Penczek, S. M. Jacobsen, C. J. Summers, P. N. Yocom, *J. Appl. Phys. Lett.* **72** (1998) 158-160.
3. G. O. Mueller and R. Mueller-Mach, *7th International Display Workshops*, p. 821, Kobe, Japan, 2000.
4. M. Kawanishi, Y. Ono, R. Nakagawa, N. Miura, H. Matsumoto, R. Nakano, *11th Workshop on Inorganic and Organic Electroluminescence and International Conference on the Science and Technology of Emissive Displays and Lighting*, p. 239, Gent, Belgium, 2002.
5. H. Yamamoto, K. Megumi, H. Kasano, *J. Electrochem. Soc.* **134** (1987) 2620-2624.
6. G. L. Marwaha, N. Singh, D. R. Vij, V. K. Mathur, *Mater. Res. Bull.* **14** (1979) 1489-1495.
7. T. Justel, Luminescent Materials for phosphor-converted LEDs. In: *Luminescence: From Theory to Applications*, Cees Ronda (Ed) WILEY-VCH Verlag GmbH & Co. KGaA, Weinheim, (2008).
8. D. Jia, X. Wang, *J. Opt. Mater.* **30** (2007) 375–379.
9. D. Jia, J. Zhu, B. Wu, *J. Electrochem. Soc.* **147** (2000) 3948-3952.
10. A. M. Srivastava, H. A. Comanzo, S. Camardello, S. B. Chaney, M. Aycibin, U. Hapek, *J. Lumin.* **129** (2009) 919–925.
11. A. Meijerink, J. Nuyten, G. Blasse, *J. Lumin.* **44** (1989) 19-31.
12. C. R. Ronda, Emission and Excitation Mechanisms of Phosphors. In: *Luminescence: From Theory to Applications*, Cees Ronda (Ed) WILEY-VCH Verlag GmbH & Co. KGaA, Weinheim, (2008), p. 28.



13. H. C. Swart, L. Oosthuisen, P. H. Holloway, G. L. P. Berning, *Surf. Inter. Anal.* **26** (1998) 337- 342.
14. B. L. Abrahams, W. Roos, P. H. Holloway, H. C. Swart, *Surf. Sci.* **451** (2000) 174-181.
15. B. L. Abrams, W. J. Thomas, J. S. Bang, P. H. Holloway, *Rev. Adv. Mater. Sci.* **5** (2003) 139- 146.
16. W. Lehmann, F. M. Rayan, *J. Electrochem. Soc.* **118** (1971) 477-482.
17. Y. Kojima, T. Toyoma, *J. Alloys Compd.* **475** (2009) 524-528.
18. L. Oosthuizen, H. C. Swart, P. E Viljoen, P. H. Holloway, G. L. P. Berning, *Appl. Surf. Sci.* **120** (1997) 9-14.
19. H. C. Swart, K. T. Hillie *Surf. Interface Anal.* **30** (2000) 383-386.
20. V. Kumar, V. Mishra, M. M. Biggs, I. M. Nagpure, O. M. Ntwaeaborwa, J. J. Terblans, H. C. Swart, *Appl. Surf. Sci.* **256** (2010) 1720-1724.
21. H. C. Swart, J. S. Sebastian, T. A. Trottier, S. L. Jones, P. H. Holloway, *J. Vac. Sci. Technol. A* **14**(3) (1996) 1697-1703.
22. A. Pfahnl, in *Advances in Electron Tube Techniques*, Pergamon, New York, (1961), p. 204.
23. P. H. Holloway, H.C. Swart, O.M. Ntwaeaborwa, *J. Vac. Sci. Technol. A* **31**,050808 (2013) doi.org/10.1116//1.4808467/
24. P. Dorenbos, *J. Lumin.* **104** (2003) 239-260.
25. PHI Multipak™, Version 8.2C, Part number 706570, Software for Complete AES and XPS Data Reduction, Copyright, Ulvac-PHI, Inc., (2007).
26. H. C. Swart, L. Oosthuizen, P. H. Holloway, G. L. P. Berning, *Surf. Interface Anal.*, **26** (1998) 337-342.
27. C. Suryanarayan and M. G. Norton, *X-ray Diffraction: A Practical Approach* (New York: Plenum Press, (1998), p.20.
28. B. D. Cullity, *Elements of X-ray Diffraction*, second ed., Addison-Wesley, Reading, MA, (1956), p.262.
29. J. H. Park, H. L. Park, *J. Appl. Phys.* **73** (Q) (1993)189-204.
30. K. Qui, E. J. Anthony, L. Jia, *Fuel* **80** (2001)549-558.
31. E. J. Anthony, K. Qui, *Energy & Fuels* **17**(2003)363-368.

32. G. Marban, M. Garcia-Calzada, A. B. Fuertes, Chem. Eng. Sci. **54** (1999) 77-90.
33. R. J. Torres-Ordonez, J. P. Longwell, Adel F. Sarofim, Energy & Fuels **3** (1989) 595-603.
34. Vinay Kumar, Varun Mishra, Shreyas S. Pitale, I. M. Nagpure, E. Coetsee, O. M. Ntwaeaborwa, J. J. Terblans, H. C. Swart, J. Appl. Phys. **107** (2010)123533-123536.
35. A. B. Christie, J. Lee, I. Sutherland, J. M. Walls, Appl. Surf. Sci. **15** (1983) 224-237.
36. H. F. Franzen, J. Merrick, M. Umana, A. S. Khan, D. T. Peterson, J. R. McCreary, R. J. Thorn, Electron Spectrosc. Relat. Phenom. **11** (1977) 439-443.
37. J. F. Moulder, W.F. Stickle, P. E. Sobol, K. D. Bomben, *Handbook of X-ray Photoelectron Spectroscopy*, Copyright, Physical Electronics, Inc, (1995), pp. 44-150.
38. R.V. Siriwardane, J. M. Cook, J. Colloid Interface Sci. **104** (1985) 250-207.
39. R. V. Siriwardane, J. M. Cook, J. Colloid. Interface Sci. **114** (1986) 525-535.
40. S. H. Park, S. H. Sohn, K. S. Sohn, Physica B **293** (2000) 187-197.
41. Han Choi, Chang-Hong Kim, Chong-Hong Pyun, J. Solid State Chem. **138** (1998) 149-153.
42. H. Sung, Y. Cho, Y. Huh, Y. R. Do, Bull. Korean Chem. Soc., **28** (8) (2007) 1280-1284.
43. M. Suta, P. Larsen, F. Lavoie-Cardinal, C. Wickleder, J. Lumin. **149** (2014) 35-44
44. V. Kumar, J. Alloys Compd. **492** (2010) L8-L12.
45. A. M. Muke, P. L.Muthal , S. M. Dhopte , S.V. Moharil, J. Lumin. **132** (2012) 342-344.
46. R. R. Patil, P. L. Muthal, S.M. Dhopte, V.K. Kondawar, S.V. Moharil, J. Lumin. **126** (2007)571–574
47. Y. Huang, S. Zhang, S. Kim, Y. M. Yu, H. J. Seob, J. Electrochem. Soc. **159** (2) (2012) J23 - J28.
48. C. H. Seager, W. L. Warren, D. R. Tallant, J. Appl. Phys. **81** (1997) 7994-8001.
49. H. C. Swart, A. P. Greeff, P. H. Holloway, G. L. P. Berning, Appl. Surf. Sci. **140** (1999) 63- 69.
50. A. K. Bedyal, V. Kumar, V. Mishra, S. S. Pitale, E. Coetsee, M. M. Duvenhage, O. M. Ntwaeaborwa, H. C. Swart, J. Mater. Sci. **48** (2013) 3327-3333.

## Chapter 5

### Thermal Quenching, Cathodoluminescence and Thermoluminescence Study of $\text{Eu}^{2+}$ Doped CaS Powder

#### 5.1. Introduction

The  $\text{Eu}^{2+}$  -doped alkaline earth sulfides (e.g. CaS) have attracted the attention of researchers due to their relatively low cost [1] and their potential as phosphors for electroluminescence, cathodoluminescent display [2-4], and LED applications [5, 6]. In white light emitting diode (wLED) applications, the emission from a blue LED is partially converted to red light upon absorption by  $\text{CaS:Eu}^{2+}$ . The position of the broad emission band due to the  $\text{Eu}^{2+}$  ions depends on the centroid shift and the crystal field splitting of the excited  $5d^1$  electronic states of this ion [7]. This splitting is strongly affected by the interaction between impurity ions and the matrix lattice vibrations. Unintended impurities or lattice defects are expected to interfere with these interactions. Energy dispersive X-ray (EDX) analysis is a useful tool for localized elemental analysis. In addition, signals from the same electron beam which yields these characteristic X-rays can be used for scanning electron microscopy (SEM) imaging and cathodoluminescence (CL) mapping. Insight gained from this kind of study would help to select the best synthesis route for producing a given phosphor material in order to come up with particles of the right shape. Recently, Poelman and Smet [8] used CL mapping to study luminescent emission at submicron scale of the powder phosphor  $\text{Ca}_2\text{SiS}_4\text{:Eu}$ . The quest for new sources of white light has led to a great interest for re-engineering well-known hosts or development of new host structures with several merits such as high chemical stability, high luminescent intensity and good thermal quenching for phosphor-converted wLEDs applications when activated by ions such as  $\text{Eu}^{2+}$ . Extensive studies on enhancing the

luminescence and improving the chemical stability of CaS:Eu<sup>2+</sup> have been reported in the literature [2, 5, 9, 10,11].

To avoid saturation at high excitation flux, the converting phosphor in LED application should have a short decay time [12], a requirement easily met in  $d \rightarrow f$  optical transitions of the Eu<sup>2+</sup> ion. However, these transitions can be affected by defects in the host lattice. Therefore, it is important to investigate the presence (or absence) of such defects. Thermoluminescence (TL) is a useful technique in obtaining information about the distribution of defects/traps within the forbidden gap present in a material [13, 14]. Upon thermal stimulation, the intensity of emission from the sample is measured and plotted as a function of temperature. The resulting curve is known as the ‘glow curve’. Several methods have been designed for analyzing glow curves [15, 16]; among them is the initial rise method, which estimates the trap depth by fitting the low-temperature end of a glow peak. In this method, regardless of the order of kinetics, the intensity (I) of the TL emission is proportional to an exponential Boltzmann factor [17] as shown in Eq. (5.1)

$$I \propto \exp\left(\frac{-E_T}{kT}\right) \quad (5.1)$$

Where  $k$  is Boltzmann constant,  $T$  is absolute temperature and  $E_T$  is the activation energy (also called trap depth).

Thermal stability of a phosphor is another important consideration for its application in LEDs [18] because the operating temperature of the LED is always higher than room temperature; therefore the converting phosphor should operate without significant reduction in luminescence efficiency at elevated temperatures [19].

An important thermal parameter for a phosphor is the quenching temperature ( $T_{0.5}$ ) which is defined as the temperature at which the emission intensity has dropped to 50% of the initial intensity. The decay rate of the 5d state can be described using the following expression [20]

$$\Gamma(T) = \Gamma_v + \Gamma_0 \exp\left(\frac{-\Delta E}{k_B T}\right) \quad (5.2)$$

where  $\Gamma_v$  is the radiative decay rate of the 5d state of  $\text{Eu}^{2+}$ ,  $\Gamma_0$  is the attempt rate for thermal quenching,  $k_B$  is Boltzmann's constant, and  $\Delta E$  is the activation energy for thermal quenching [20].

Research on delayed emission in europium doped CaS has mainly been focused on phosphors in which co-dopants were deliberately introduced as defects and which show long afterglow. For example, Jia et al. [21] have investigated trapping processes in  $\text{CaS:Eu}^{2+}$ ,  $\text{Tm}^{3+}$ , and similar investigations have been reported in Refs. [22,23]. Furthermore, Kojima and co-workers [24] have studied the afterglow mechanism and thermoluminescence of  $\text{CaS:Eu}^{2+}$ ,  $\text{Pr}^{3+}$  after irradiation with visible light. Here, we define long afterglow as luminescence that persists from seconds to many hours [25].

In the present work, we report the thermal quenching of luminescence, cathodoluminescence and thermoluminescence studies of europium-doped calcium sulfide, with the aim of determining its suitability in phosphor-converted LED (pc-LED) applications. We determined the fast and slow lifetimes and electron traps responsible for the delayed luminescence of the  $\text{Eu}^{2+}$  in the CaS host lattice. We have used CL mapping to show that the emission from  $\text{Eu}^{2+}$  ions depends on the shape of the phosphor particles. We have conducted kinetic analysis of the experimental TL glow curves using the initial rise and peak shape methods. In addition, we have shown that  $\text{CaS:Eu}^{2+}$  has a relatively low quenching temperature and thus, it is only a suitable material for low-power or remote-phosphor white pc-LEDs.

## 5.2. Experimental

Commercial  $\text{CaS:Eu}^{2+}$  powder phosphor was purchased from Phosphor Technology in the United Kingdom. A Hitachi S-3400N emission scanning electron microscope (SEM), with several attachments was used for surface morphology and elemental analysis. Imaging was obtained by detection of backscattered electrons (BSE). The characteristic X-ray maps were generated using a Noran 7 dry energy dispersive X-ray (EDX) spectrometer from Thermo Scientific. The cathodoluminescence (CL) spectra were captured simultaneously with the X-ray maps, using a ProEM1600 EMCCD camera attached to an Acton SP2300

monochromator (Princeton Instruments), which were used to produce CL surface maps. An electron beam was accelerated using an energy of 20 keV. The vacuum pressure was kept at 30 Pa in order to prevent charge build-up on the sample surface. The photoluminescence emission and excitation spectra were measured using a Edinburgh Instruments FS920 fluorescence spectrometer, which was equipped with a monochromated 450 W Xe lamp as the excitation source. The luminescence quenching studies were carried out by exciting the sample with a blue LED (435 nm). The luminescence was collected by an optical fiber connected to the ProEM1600 EMCCD camera mentioned above. The sample temperature was varied between -50 to 200 °C, in vacuum.

The photoluminescence decay curves were measured using an Andor DH720 ICCD camera connected to a 500 mm monochromator and a 337 nm pulsed nitrogen laser was used to excite the phosphor. The decay curves corresponding to  $\text{Eu}^{2+}$  were measured at 10 K and 300 K using a cryostat (Oxford Instruments Optistat CF) filled with liquid helium. The decay curve corresponding to persistent luminescence was obtained after exciting the phosphor with 1000 lux from a xenon arc lamp for five minutes. Then the decay of luminescence was monitored using a calibrated ILT1700 (International Light Technologies) radiometer in photopic mode.

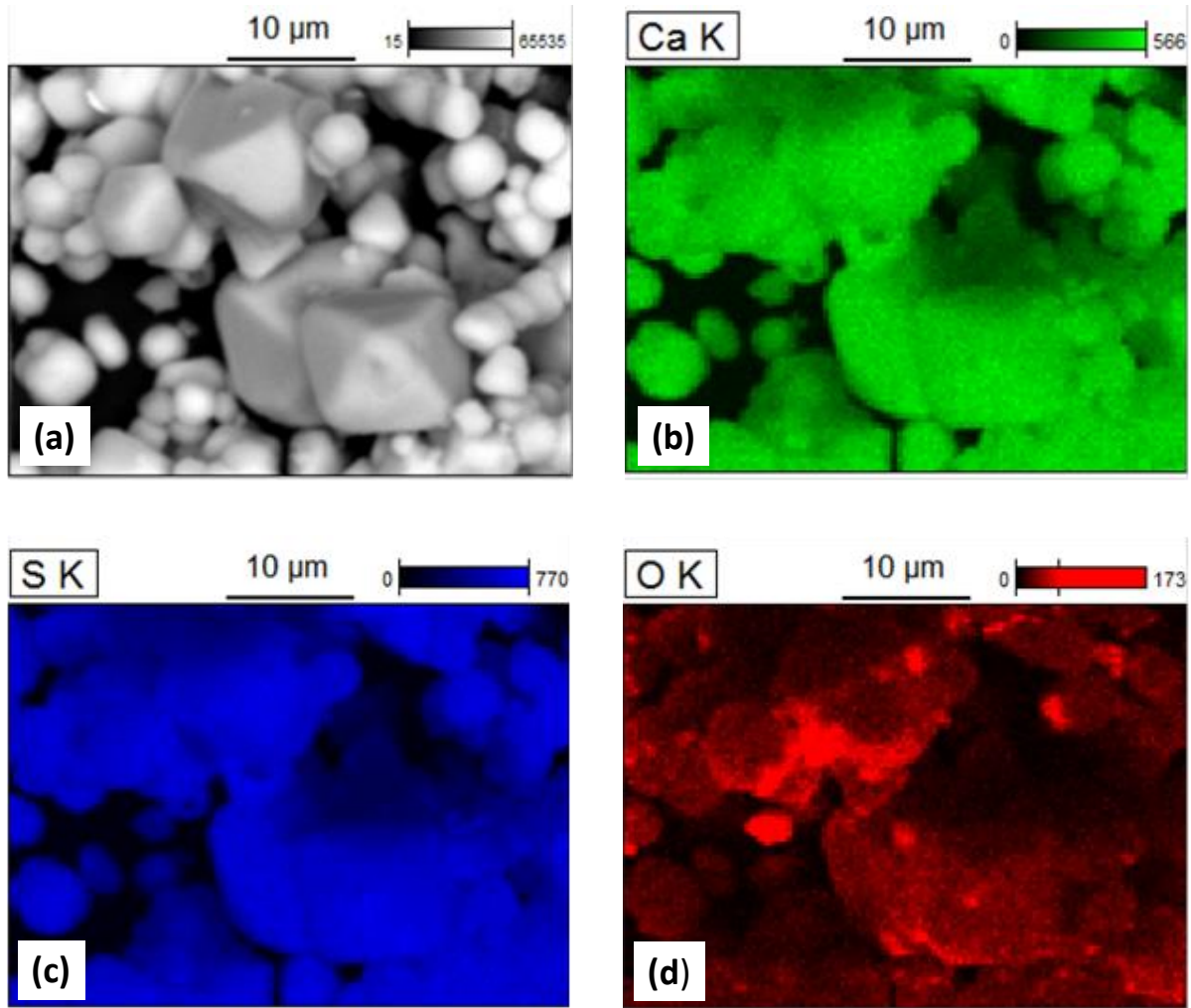
A thermoluminescence reader (Harshaw 3500 TLD Reader) was used to obtain glow curves, by exposing the sample to  $\gamma$ -radiation from a  $^{60}\text{Co}$  source in the dose range of 10 to 50 Gy. Prior to any thermoluminescence measurements, the samples were heated to 300 °C for 1 hour to erase any previously acquired radiation and then cooled to room temperature. Then the glow curves were obtained by first irradiating the sample and then heating it at a uniform rate of 5 °C.s<sup>-1</sup>.

### **5.3. Results and Discussion**

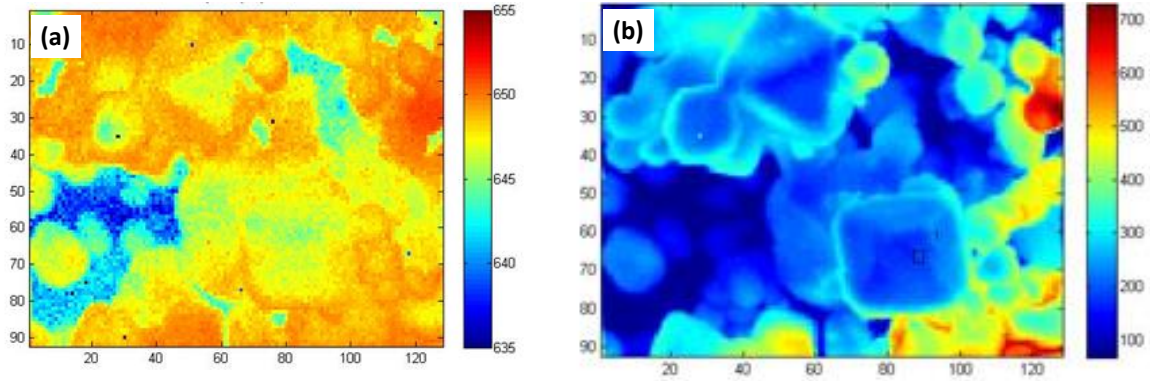
#### **5.3.1. SEM, EDX, CL Images, Cathodoluminescence and Photoluminescence**

Fig.5.1 (a) shows a backscattered secondary electron (BSE) image illustrating the surface morphology, while Fig. 5.1 (b) – (d) are the EDX images of the elements Ca, S and O

respectively, and Fig. 5.2 shows the CL maps of the phosphor powder. The CL maps, backscattered image, and the EDX maps were obtained simultaneously for a given area, with the system operating in spot mode.



**Figure 5.1:** (a) Backscattered electron image and chemical maps for (b) Ca-K, (c) S-K, (d) O-K EDX in false colors.



**Figure 5.2:** CL maps of CaS:Eu<sup>2+</sup> showing (a) emission barycenter in nm and (b) total intensity (arb. units) on the scanned area.

The backscattered electron image of Fig.5.1 (a) shows that the phosphor is made up of spherical and octahedral particles with sizes ranging from 1.6-5  $\mu\text{m}$ , for the spherical and 3-13  $\mu\text{m}$ , for the octahedral particles, respectively. Generally, the spherical particles show better brightness and contrast compared to octahedral particles. The EDX images confirm the presence of the major elements, namely Ca and S from the CaS phosphor and O attributed to a secondary phase (CaSO<sub>4</sub>) as previously reported in Ref. [26]. The EDX images show uniform distribution of both the Ca and S elements on the surface, with O concentrated in certain parts on the defined area. Oxygen appears mostly in the regions with spherical particles and not in the octahedral shaped particles. This is confirmed by the negative image of O in the regions where the octahedral particles are positioned.

The CL maps shown in Fig. 5.2 were produced when the electron beam was swept across the defined area and by collecting a full emission spectrum per position. The integrated CL spectrum is shown in Fig. 5.3 (b). The CL map shows the luminescence intensity variations from one particle to the other, which may be used to determine the distribution of europium ions in the defined area. According to the map, the spherical particles produced more intense CL emission compared to the octahedral particles. This suggests that europium was mostly concentrated on the sites occupied by the spherical particles compared to those occupied by the octahedral particles. It could also be that the octahedral particles suffer from light



trapping inside the particles, due to total internal reflection, whereas the spherical particles offer better chance for the light to escape.

The photoluminescence excitation spectrum was recorded using the emission wavelength of 650 nm, while the emission was monitored at an excitation wavelength of 247 nm (but the phosphor is also excitable at 470 nm). The results are displayed in Fig.5.3 (a). The emission band at 383 nm was not detected when the phosphor was excited with a wavelength of 470 nm. The minor peak at 383 nm and the broad peak at 650 nm are attributed to  $4f^65d^1 \rightarrow 4f^7$  transitions of  $\text{Eu}^{2+}$  in  $\text{CaSO}_4$  and  $\text{CaS}$ , respectively. The fine structure in the excitation spectrum in the region 450-500 nm is an artifact of the measurements. A more detailed explanation on this and the excitation bands is found in our previous work [26].

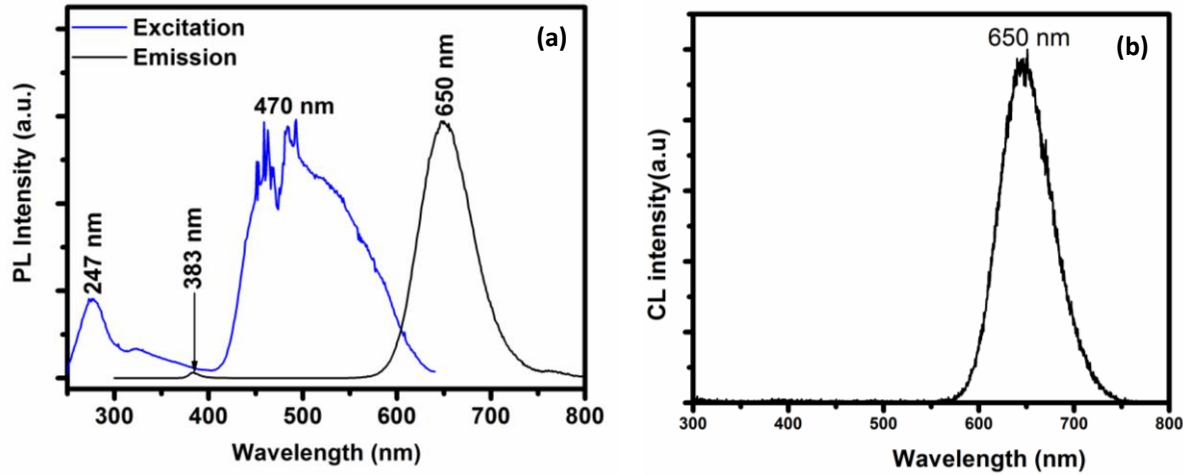


**Figure 5.3:** (a) PL Excitation and emission spectra (b) CL intensity (both at room temperature).

### 5.3.2. Temperature Dependent Decay Times of $\text{CaS:Eu}^{2+}$

Fig. 5.4(a) shows the normalized decay curves of  $\text{CaS:Eu}^{2+}$  powder upon pulsed excitation, measured for the 650 nm emission peak at 10 K and 300 K. The decay characteristics are evaluated based on the decay time calculated using a bi-exponential fit [27]:

$$I = A_1 \exp\left(-\frac{t}{\tau_1}\right) + A_2 \exp\left(-\frac{t}{\tau_2}\right) + C \quad (5.3)$$

where  $I$  is the emission intensity at any time ‘ $t$ ’ after switching off the excitation sources,  $A_1$ ,  $A_2$  and  $C$  are constants, while  $\tau_1$  and  $\tau_2$  are decay constants (also called decay times). The values obtained for  $\tau_1$  and  $\tau_2$  for the CaS:Eu<sup>2+</sup> powder are listed in Table 5.1. The results illustrate that the decay can be described by two decay constants, which both reduce with temperature. The two decay constants are attributed to Eu<sup>2+</sup> ions being in two different environments in the phosphor [28]. The decrease of the decay time with increase of temperature means that non-radiative processes become relevant and is an indication of thermal quenching of the luminescence intensity and a pointer to defects [29, 30].

Next to this microsecond decay, the phosphor also shows some strongly delayed emission. The persistent luminescence decay curve (Fig. 5.4(b)) was measured by exciting the sample for five minutes using a xenon lamp, and then recording the emission for about 800 s. The corresponding time parameters obtained after fitting the curve with a second order exponential decay curve (Eq. 5.3), were  $\tau_1 = 20.6 \pm 0.1$  s and  $\tau_2 = 170.5 \pm 0.7$  s. The electron traps in the phosphor presumably correspond to sulfur vacancies within CaS [31].

**Table 5.1:** Decay times of the luminescence of CaS:Eu<sup>2+</sup> at different temperatures.

Temperature (K)	10		300	
	$\tau_1$	$\tau_2$	$\tau_1$	$\tau_2$
Decay time( $\mu$ s)	0.29 $\pm$ 0.01	0.70 $\pm$ 0.06	0.18 $\pm$ 0.03	0.36 $\pm$ 0.01

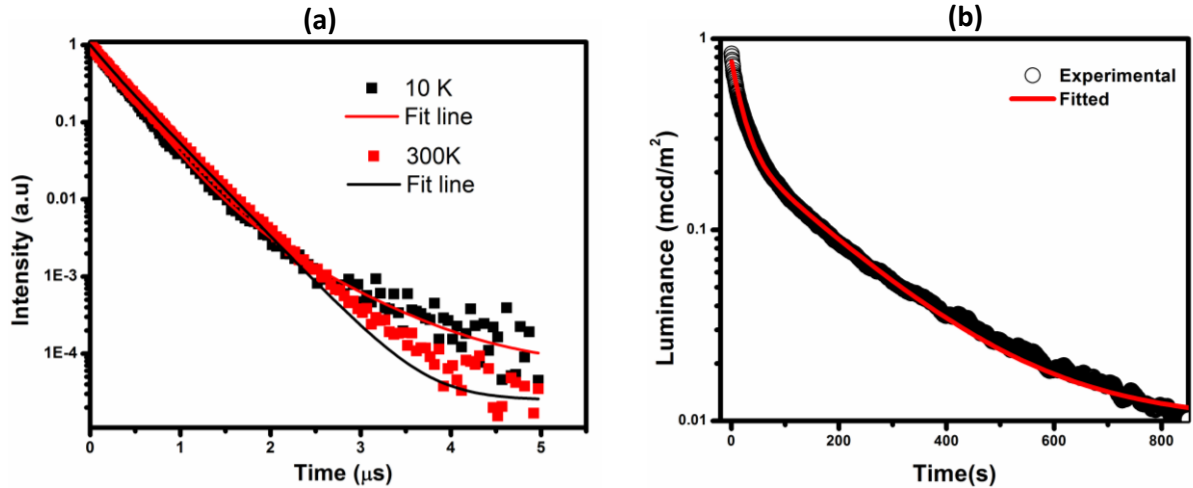


**Figure 5.4:** (a) Luminescence decay curves of CaS:Eu<sup>2+</sup> at 10 K (■) and at 300 K (■). (b) Decay curve of persistent luminescence for the powder measured at room temperature.

### 5.3.3. Thermal Quenching of Luminescence

The integrated intensity spectrum of the CaS:Eu<sup>2+</sup> powder as a function of temperature from -50°C to 200°C is presented in Fig. 5.5 (a). As can be seen in Fig. 5.5 (a), there is a gradual decrease of the luminescent intensity with temperature (between -50°C and 0°C) before a sharp decline after 0°C. At room temperature (27°C), the emission intensity is 51% of the initial intensity. Thus, the CaS:Eu<sup>2+</sup> sample has a relatively low quenching temperature  $T_{0.5}$ , estimated to be 31°C (304 K). This is a relatively low temperature compared to the reported temperature of 475 K [20], a value which was derived from temperature dependent electroluminescence measurements [32]. Yang et al. [33] recently reported a thermal quenching behavior which is more similar to the present results. Interestingly, they observed that small substitution of Ca by Mg and Ga improves the thermal resistance of the luminescence intensity [33].

At -50°C, the emission peak is at 656 nm and gradually shifts towards shorter wavelengths on further increase of temperature until it is at 645 nm at 200°C (as is shown in Fig. 5.5(b)). This shift might be related to a change of symmetry of CaS as a function of temperature. Any

change of the symmetry will affect the crystal field of CaS, and subsequently the 5d-4f emission of this phosphor. A similar change was reported [34] for SrTiO<sub>3</sub> for temperatures lower than 105 K.

The full width at half maximum (FWHM) of the emission bands rises from 58 to 93 nm with increasing temperature between -50°C and 200°C. The variation of the FWHM with temperature is demonstrated in Fig. 5.6 (b) and can be attributed to the occupation of higher vibrational levels [35].

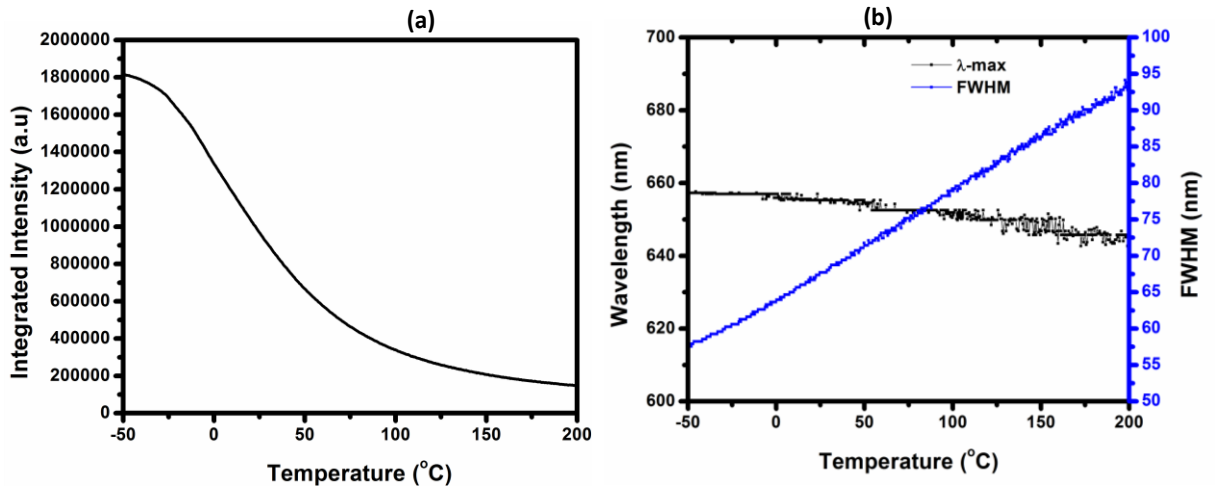


**Figure 5.5:** (a) PL integrated intensity between -50°C and 200°C. (b) Temperature dependence of the FWHM and the peak wavelength of the emission band for the CaS:Eu<sup>2+</sup> powder.

The process of thermal quenching has been explained differently by several workers: For example, Blasse et al. [36, 37] attributed the quenching of 5d → 4f emission in Eu<sup>2+</sup> to a large displacement between the ground and excited states of Eu<sup>2+</sup> in the configuration coordinate diagram, Davolos et al. [38] proposed that thermal activation of an electron from 5d state to conduction band causes the quenching in Ba of the thiogallate, BaGa<sub>2</sub>S<sub>4</sub>. Najafov et al. [39] attributed the thermal quenching in CaGa<sub>2</sub>S<sub>4</sub>:Eu<sup>2+</sup> to thermally excited release of a hole from Eu<sup>2+</sup> to the valence band. Likewise, Chartier et al. [40] proposed a similar model for SrGa<sub>2</sub>S<sub>4</sub>:Eu<sup>2+</sup>. Although Jabbarov and co-workers [30] pointed out that quenching of

luminescence can also be due to energy transfer to impurities, they ruled out this mechanism basing their argument on the fact that increasing the  $\text{Eu}^{2+}$  concentration up to 10% did not show any influence on the quenching activation energy. In an extensive review of several compounds, Dorenbos [20] argued that the idea of thermal quenching due to a large displacement between the ground and excited state in the configuration coordinate diagram is not sufficient to explain quenching of luminescence of  $\text{Eu}^{2+}$  in Ba, Sr, and Ca sites. He demonstrated that the ionization of the 5d electron to conduction band states offers a better explanation to the quenching mechanism. In their investigations of the persistent  $\text{Eu}^{2+}$  luminescence in  $\text{SrAl}_2\text{O}_4:\text{Eu}^{2+}$ ;  $\text{Dy}^{3+}$ , Dorenbos et al. [41, 42] showed that thermal release of a hole to the valence band requires too large an energy and thus cannot be a possible route for persistent luminescence and thermal quenching. In view of the aforementioned, thermal excitation of the 5d electron to conduction band states appears to be an attractive mechanism for thermal quenching of  $5d \rightarrow 4f$  emission in  $\text{CaS}:\text{Eu}^{2+}$ . In fact, our earlier study [26] showed that part of the energy levels of  $\text{Eu}^{2+}$  in CaS are within the conduction band, and hence the delocalization of a 5d electron into the conduction band is possible. The fact that the phosphor used for the study contains an impurity phase, quenching of luminescence due energy transfer to impurities may play a role. The observed thermal quenching of  $\text{CaS}:\text{Eu}^{2+}$  is thus ascribed to energy transfer to impurities (other than the dopant) and to electrons being activated to conduction band states. The fact that the  $\text{CaS}:\text{Eu}$  sample shows persistent luminescence also points to delocalization of an electron from  $\text{Eu}^{2+}$  to an impurity or trap center.

#### **5.3.4. Thermoluminescence Studies**

Thermoluminescence (TL) analysis was used to investigate the deep electron traps within the material. The energy required to stimulate the electrons from the electron traps is used to determine the depth of a given trap [43]. TL glow curves of CaS phosphor were recorded after the  $\text{CaS}:\text{Eu}^{2+}$  was irradiated with gamma rays whose doses were varied from 10 Gy to 50 Gy, with the heating rate fixed at 5 °C/s. The results are presented in Fig. 5.6(a).

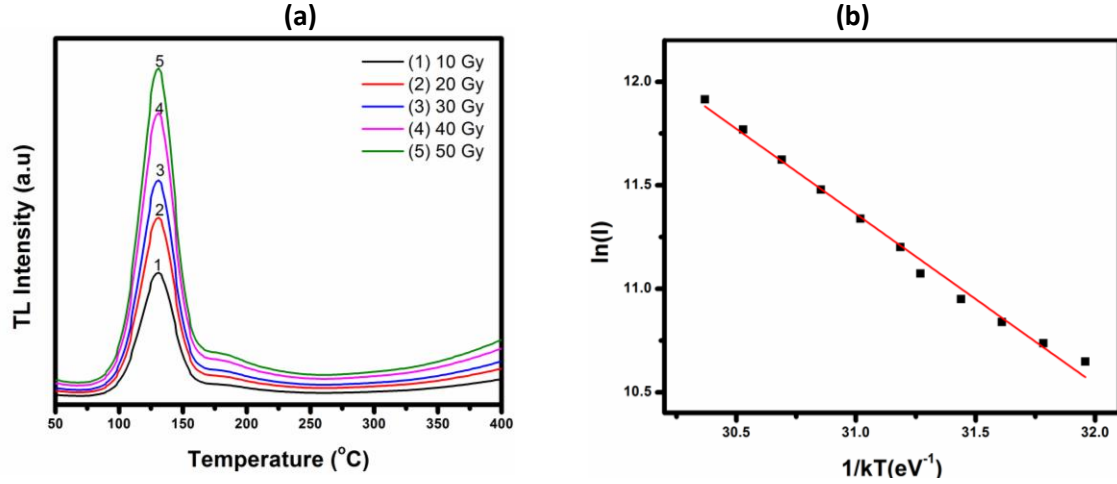


**Figure 5.6:** (a) Thermoluminescence glow curves of CaS:Eu<sup>2+</sup> phosphors after excitation by different doses of 10, 20 30, 40, and 50 Gy, recorded at a heating rate of 5°C/s. (b)The initial rise method used to obtain the activation energy, E. The slope of the linear fit can be used to calculate an approximation of the activation energy of the traps.

The glow curves show a glow peak at around 130°C with the intensity of the glow peaks increasing with  $\gamma$ -dose. There is no shift of the peaks towards lower temperature. This, together with the shape of the peak, is an indication of a first order kinetic glow peak [16]. The rise of intensity with dose indicates that more traps responsible for this glow peak were getting filled leading to those traps releasing charge carriers on thermal stimulation [44].

The initial rise (IR) method was used to determine the activation energy. According to this method, the low temperature tail of a TL glow peak is assumed to be approximately constant, since the dependence of trapped electrons,  $n(T)$  on temperature  $T$  is negligible in that temperature region. By using this assumption of constant  $n(T)$ , the initial rise method (IR) was used on glow curve 1 in Fig. 5.6(a).The activation energy was approximated by modifying Eq. (5.1) as follows:

$$\ln I(T) = -\frac{E}{kT} + \ln C \quad (5.4)$$

where  $I(T)$  is the peak intensity  $I$  at temperature  $T$  in K,  $k$  is Boltzmann constant in eV K<sup>-1</sup>,  $E$  is the activation energy in eV, and  $C$  is a constant. A graph of the plot of  $\ln I$  versus  $1/kT$ , for

the initial part of the data, is presented in Fig. 5.6(b). The activation energy,  $E$ , extracted from the slope of the graph, gives the depth of the trap as  $E = 0.82 \pm 0.02$  eV.

#### 5.4. Conclusion

Elemental analysis of the phosphor clearly shows the presence of O corresponding to the secondary phase ( $\text{CaSO}_4$ ). The powder has a strong absorption in the blue region, showing that a blue LED is a suitable source of excitation for this phosphor. The decay parameters were determined for both  $\text{Eu}^{2+}$  and the electron trapping centers. The sample shows two different decay constants for  $\text{Eu}^{2+}$ , with the decay times decreasing as temperature increased. The different decay constants point to two different environments for the  $\text{Eu}^{2+}$  ions in the CaS host. The decrease in decay time with increase of temperature is ascribed to thermal quenching, which in turn is attributed to energy transfer to impurities and electrons being activated to the conduction band states. The quenching temperature was found to be around  $31^\circ\text{C}$  (304 K). The PL, decay times and thermal quenching of luminescence results indicate that this phosphor is suitable for low-power white pc-LEDs if the thermal quenching profile can be somewhat shifted towards higher temperatures by suppression of impurities or by well-chosen compositional modifications to increase the energy separation between the 5d excited state of the  $\text{Eu}^{2+}$  dopants and the bottom of the conduction band. Thermoluminescence of the gamma- irradiated Eu doped CaS was used to determine the nature of the electron traps. TL intensity was found to increase with  $\gamma$ -dose, with the main TL peak observed at  $130^\circ\text{C}$ . The depth of the trap determined by initial rise method was 0.82 eV.

#### References

1. M. Pham-Thi, J. Alloys Compd. **225**(1995)547-551
2. M. Pham-Thi, G. Ravoux, J. Electrochem. Soc. **138** (1991)1103-1106.
3. M. Ando, Y. A. Ono, J. Appl. Phys. **68** (1990)3578-3583.

4. D. Poelman, R. Vercaemst, R. L. Van Meirhaeghe, W. H. Laflère, F. Cardon, *J. Lumin.* **75** (1997)175-181.
5. C. Guo, D. Huang, Q. Su, *Mater. Sci. Eng. B* **130** (2006) 189-193.
6. M. Nazarov, C. Yoon, *J. Solid State Chem.* **179** (2006) 2529-2533.
7. C. R. Ronda, *Emission and Excitation Mechanisms of Phosphors*. In: *Luminescence: From Theory to Applications*, Cees Ronda (Ed)WILEY-VCH Verlag GmbH & Co. KGaA, Weinheim, (2008), p. 28.
8. D. Poelman, P. F. Smet, *Physica B* **439** (2014)35–40.
9. C. Guo, B. Chu, M. Wu, Q. Su, *J. Lumin.* **105** (2003) 121–126.
10. C. Guo, B. Chu, Q. Su, *Appl. Surf. Sci.* **225** (2004) 198–203.
11. N. Avci, J. Musschoot, P.F. Smet, K. Korthout, A. Avci, C. Detavernier, D. Poelman, *J. Electrochem. Soc.* **156** (2009) J333-J337.
12. T. Justel, *Luminescent materials for phosphor-converted LED*, In: *Luminescence, from Theory to applications*, C. Ronda(ed), Wiley-VCH, Weinheim, 2008 (chap 7 p 184).
13. A. Choubey, S.K. Sharma, S.P. Lochab, D. Kanjilal, *J. Phys. Chem. Solids* **72** (2011) 136-143.
14. Y. Lin, Z. Tang, Z. Zhang, C. Nan, *J. Eur. Ceram. Soc.* **23** (2003) 175-178.
15. R. Chen, S.W.S. Mckeever, *Theory of Thermoluminescence and Related Phenomenon*, World Scientific Press, Singapore, (1997), p.12.
16. V. Pagonis, G. Kitis, C. Furetta, *Numerical and Practical Exercises in Thermoluminescence* Springer Science+Business Media, New York, (2006), p.8.
17. C. Furetta, G. Kitis, *J. Materials Science*, **39** (2004)2277-2294.
18. Yi-Chen Chiu, Chien-Hao Huang, Te-Ju Lee, Wei-Ren Liu, Yao-TsungYeh, Shyue-Ming Jang, Ru-Shi Liu, *Opt. Express* **19** (2011) A331-A339.
19. A. Lakshmanan, R. Satheesh Kumar, V. Sivakumar, P. C. Thomas, M. T Jose, *Indian J. Pure and Appl. Phy.* **49** (2011) 303-307.
20. P. Dorenbos, *J. Phys.: Condens. Matter* **17** (2005) 8103–8111.
21. D. Jia, W. Jia, D. R. Evans, W. M. Dennis, H. Liu, J. Zhu, W. M. Yen, *J. Appl. Phys.* **88** (2000)3402–3407.
22. D. Jia, J. Zhu, B. Wu, *J. Electrochem. Soc.* **147** (2000) 386–389.



23. D. Jia, J. Electrochem. Soc. **153**(2006) H198-H201.
24. Y. Kojima, K. Aoyagi, T. Yasue, J. Lumin. **126** (2007) 319–322.
25. K. Van den Eeckhout, P.F. Smet, D. Poelman, Materials **3**(2010) 2536-2566.
26. R.L. Nyenge, H.C. Swart, O. M. Ntwaeaborwa, Opt. Mater. **40** (2015) 68–75.
27. A. Nag, T.R.N. Kutty, J. Alloys Compd. **354**(2003) 221-231.
28. J. J. Joos, K. W. Meert, A. B. Parmentier, D. Poelman, P. F. Smet, Opt. Mater. **34** (2012) 1902–1907.
29. A.B. Parmentier, P.F. Smet, D. Poelman, Opt. Mater. **33** (2010)141-144.
30. R.B. Jabbarov, C. Chartier, B.G. Tagiev, O.B. Tagiev, N.N. Musayeva, C. Barthou, P. Benalloul, J. Phys. and Chem. of Solids **66** (2005) 1049–1056.
31. P. K. Ghosh, V. Shankar, J. Lumin. **20** (1979) 139-145.
32. M. Ando, Y.A. Ono, J. Cryst. Growth **117** (1992) 969-974.
33. L. Yang, N. Zhang, R. Zhang, B. Wen, H. Li, X. Bian, Mater. Lett. **129** (2014)134-136.
34. P Boutinaud, L Sarakha, E Cavalli, M Bettinelli, P Dorenbos, R Mahiou, J. Phys. D: Appl. Phys. **42** (2009) 045106 (7pp).
35. P.F. Smet, A. B. Parmentier, D. Poelman, J. Electrochem. Soc.**158** (6)(2011) R37-R54.
36. G. Blasse, W. L. Wanmaker, J. W. ter Vrugt, A. Bril, Phil. Res. Rep. **23** (1968)189-200.
37. G. Blasse, B. C. Grabmaier, *Luminescent Materials*, Berlin: Springer, (1994), p 66.
38. M.R. Davolos, A.Garcia, C. Fouassier, P.Hagenmuller, J. Solid State Chem. **83** (1989) 316-323.
39. H. Najafov, A. Kato, H. Toyota, K. Iwai, A. Bayramov, S. Iida, Japan. J. Appl. Phys. **41** (2002)2058-2065.
40. C. Chartier, C. Barthou, P. Benalloul, J.M. Frigerio, J. Lumin.**111**(2005)147-158.
41. P. Dorenbos, Phys. Status Solidi B **242**(2005) R7–R9.
42. P. Dorenbos, J. Electrochem. Soc. **152** (2005)H107-H110.
43. S.W.S. McKeever, *Thermoluminescence of Solids*, Cambridge University Press, New York, (1985), pp 66-74.
44. S. Dutta, S. Som, S.K. Sharma, Physica B **417** (2013) 39-45.

## Chapter 6

### **The Influence of Laser Wavelength on The Structure, Morphology and Photoluminescence Properties of Pulsed Laser Deposited CaS:Eu<sup>2+</sup> Thin Films**

#### **6.1. Introduction**

The red-emitting europium-doped calcium sulfide (CaS:Eu<sup>2+</sup>) is a good candidate for light emitting diode (LED) applications because it has a strong absorption in the blue region that is suitable for blue LED pumping [1]. This phosphor has been investigated in powder and thin film forms, including pulsed laser deposited (PLD) thin films [2-4]. Due to its simplicity and versatility, PLD allows for the growth of thin films of practically any material [5]. In addition, the PLD technique has several attractive features, including stoichiometric transfer of the target material, generation of quality plume of energetic species, and ease of film growth in background pressures ranging from UHV to 100 Pa [6]. The influence of growth parameters such as laser fluence and chamber ambient on the quality of CaS films produced by PLD have been reported [7]. Christoulakis et al. [4] reported the effect of substrate temperature and number of pulses on the morphology and structure of the pulsed laser deposited CaS thin films. Different investigators have used other materials to investigate the nature of the dependence of a material's properties on different laser parameters such as deposition atmosphere [8], chamber pressure [9], pulse duration, and repetition rate [10]. According to Boyd [11], delivery of laser energy at a wavelength strongly absorbed by the target material minimizes energy loss due to thermal diffusion during absorption. However, little, or no attention has been made to investigate the effects of laser wavelength on the properties of PLD thin films of the red-emitting CaS:Eu<sup>2+</sup>.

In this study, we focused on the influence of laser wavelength on the film thickness, structure, morphology, and photoluminescent (PL) properties of PLD grown thin films of CaS:Eu<sup>2+</sup>. Our data demonstrate that our films were generally amorphous and that the

photoluminescence intensity was influenced by the film roughness and thickness. In addition, our AFM data demonstrate that good quality films can be grown using the wavelength of 266 nm, whose laser photon energy is closer to the optical band gap ( $E_g = 4.43$  eV) of CaS. An understanding of the theory of laser-material interaction will help to explain the observed differences in the structure, morphology, and PL properties of the thin films.

### 6.1.1. The Interaction of Laser Radiation and Target: A Theoretical Perspective

A proposed mechanism of the interaction of laser energy and the target is presented in this section. The ablation of target material by pulsed laser can be explained by photothermal, photochemical or non-thermal microscopic mechanism (i.e. intraband absorption, interband transitions and molecular excitation, absorption by collective excitation (excitons, phonons)), and absorption due to impurities and defects [12].

When a laser of intensity  $I$  irradiates a target with a certain index of refraction, a fraction of it is reflected, and a part of the laser energy is absorbed in the target before it exits. According to the principle of conservation of energy, the incident laser energy is the sum of the energies of the reflected laser ( $Re$ ), the absorbed laser ( $Ab$ ) and the transmitted laser ( $Tra$ ), and this can be summarized in Eq. (6.1). By the principle of conservation of energy at the boundary between the two media,

$$Incident\ laser = Re + Ab + Tra \quad (6.1)$$

Inside the target material, the intensity  $I$  of the radiation decays exponentially with the depth  $x$  according to the Beer–Lambert law [13]:

$$I(x) = I(x_0)e^{-\alpha(x-x_0)} \quad (6.2)$$

where  $I(x)$  is the intensity at a point  $x$  below the surface of the target material,  $I(x_0)$  is the intensity at a surface point  $x_0$  and  $\alpha$  is the absorption coefficient, which determines the depth at which light energy of a certain wavelength penetrates the target material. The optical penetration or absorption depth,  $\delta$ , which is the depth at which the intensity of the

transmitted light drops to  $\frac{1}{e}$  of its initial value at the interface has been defined in Ref. [14] as:

$$\delta = \frac{1}{\alpha} \quad (6.3)$$

$\alpha$  is defined in [15] as:

$$\alpha = \frac{4\pi\kappa_a}{\lambda} = \frac{2\omega\kappa_a}{c} = \frac{4\pi n\kappa_0}{\lambda} \quad (6.4)$$

where  $\kappa_a = n\kappa_0$  is the absorption index,  $\kappa_0$  the attenuation index, and  $n$  is the refractive index of the material, respectively. From Eq. (6.3), we can see that a large (at short wavelength) absorption coefficient indicates that the radiation is absorbed near the surface where the radiation enters, and a low value (at long wavelength) means the absorption takes place deeper into the material. Another important parameter that influences the effects of laser-material interactions is the absorptivity of the material for laser radiation. For opaque materials, the absorptivity ( $A$ ) can be expressed as [13]:

$$A = 1 - R \quad (6.5)$$

where  $R$  is the reflectivity of the material. The reflectivity at normal incidence as defined in Ref. [14] is a function of wavelength. Thus, the absorption coefficient, absorptivity, and reflectivity of a material depend on the wavelength of radiation incident on it. Equation (6.4) shows that the absorption coefficient decreases with increase of wavelength and vice versa, while Equation (6.5) indicates that reflectivity increases with wavelength.

The band gap of a material plays an important role in the manner the material absorbs light energy since the absorption depends on the absorption coefficient of the material for a given wavelength of light. In direct-band gap semiconductors, radiation will be absorbed efficiently by thin layers, while for an indirect-band semiconductor (e.g. CaS), a photon as well as a phonon is absorbed, and hence, more energy is required for transition from valence to conduction band [16]. Thus, the probability of absorption is much lower for indirect-band semiconductor due to the involvement of a photon and a phonon [17].

For a photothermal process, the laser beam can be considered as a heat source which induces a temperature rise on the surface and within the bulk of the material. The relevant heat equations and the heat absorption process have been well explained in literature [14, 18]. For a high value of  $\alpha$ , the boiling point of a material is reached faster because the laser energy absorption is confined to the surface region of the target and not spread to a large volume. On the other hand, when the laser energy is absorbed at a larger depth, boiling inside the superheated liquid layer will appear, producing subsurface explosions which will eject a large amount of micron-sized droplets [18]. If the laser wavelength is too long for a given target, then very little absorption of energy takes place, as is illustrated in Fig. 6.1 and observed in the results of sections 6.4.3 and 6.4.4.

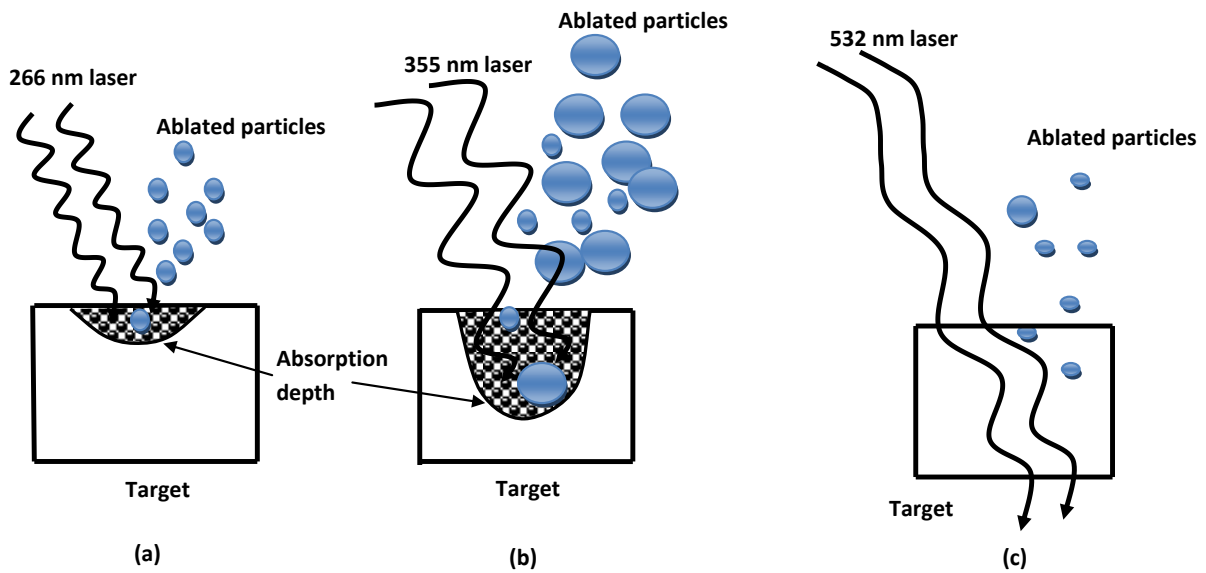


**Figure 6.1:** Schematic illustrations of target absorption: (a) 266 nm laser absorbed near the surface (b) 355 nm laser absorbed deeper into the target, (c) 532 nm laser passing through with little absorption.

## 6.2. Experimental

CaS:Eu<sup>2+</sup> commercial powder phosphor from Phosphor Technology (UK) was pressed without binders to make a pellet (target) for ablation. The pellet was annealed in air at 250°C for 3 h to harden the target and to remove water vapor and other adsorbed volatile

substances. The Si (100) substrates were cleaned by placing them in a beaker containing distilled water, and then transferred into beakers containing acetone and ethanol, successively. The cleaning in acetone and ethanol was carried out in an ultrasonic bath for a period of 15 min. Each piece of substrate was dried using N<sub>2</sub> and stored in plastic packets which were sealed. The deposition chamber of the pulsed laser system was evacuated to a base pressure of  $3.6 \times 10^{-6}$  Torr. The Spectra Physics Quanta-Ray Pro-270 Nd: YAG laser was used to ablate the CaS:Eu<sup>2+</sup> pellet in Ar (10 mTorr) atmosphere. The laser energy, number of pulses and pulse repetition rate were set to 40 mJ (a fluence of  $5.09 \text{ J/cm}^2$ ), 18000 and 10 Hz, respectively. The substrate temperature was fixed at 400° C, and the target distance was kept at 4.5 cm. The fundamental wavelength of the Nd: YAG used for this study is 1064 nm. The frequency-doubled (532 nm), frequency-tripled (355 nm), and frequency-quadrupled (266 nm) harmonics of the Q-switched pulsed Nd: YAG laser were used to provide radiation of different wavelengths. Fig. 6.2 shows photographs of laser plumes formed by the long-wavelength (532 nm), and short-wavelength (266 nm) pulsed laser. The plume formed by the 532-nm wavelength was weak and could hardly be detected by the eye while that formed by the 266-nm wavelength is more intense and could be seen in the normal laboratory lighting.

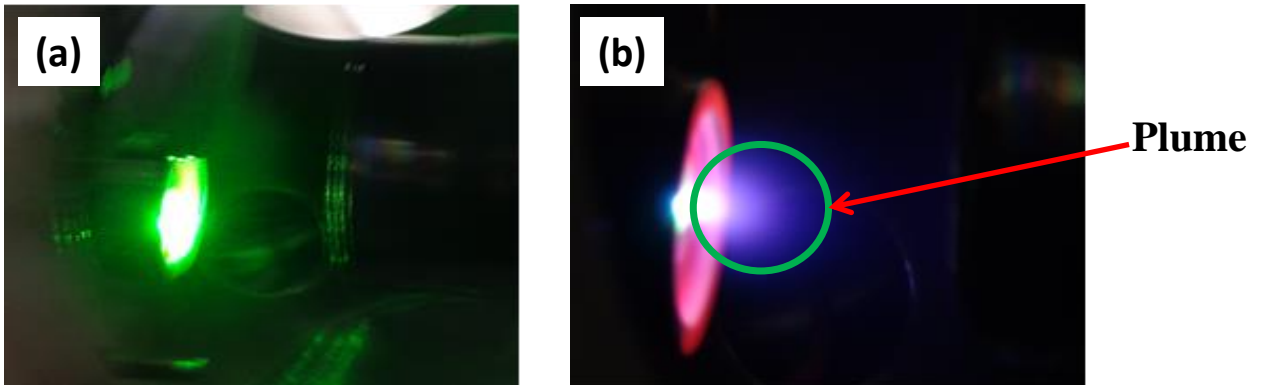


**Figure 6.2:** Formation of a plume by (a) weak plume for the long-wavelength (532 nm), (b) well-defined plume for short-wavelength (266 nm) pulsed laser.

### 6.3. Characterization

X-ray diffraction data were collected using a Bruker AXS D8, with  $\text{CuK}_\alpha$  radiation of wavelength 1.5406 Å. The diffraction patterns were recorded over the range  $15^\circ \leq 2\theta \leq 60^\circ$  with a counting time of 1 s for each step size of  $0.0198461^\circ$ . The chemical composition and thickness of the films were determined using Rutherford Backscattering Spectroscopy (RBS). The RBS spectra were recorded when the films were irradiated with 2 MeV  $^4\text{He}^+$  ions. The scattering angle was fixed at  $165^\circ$  and the detector resolution was 20 keV. The beam current was in the range of 40-50 nA. The chamber pressure was  $3.87 \times 10^{-5}$  mbar at room temperature. Simulation to obtain best-fit curves was performed using SIMNRA [19]. SIMNRA is a Microsoft windows program for the simulation of ion beam analysis energy spectra obtained by Rutherford backscattering, non-Rutherford scattering, elastic recoil detection analysis, and nuclear reaction analysis (NRA) [20]. Information generated from these fits enabled us to determine the film thicknesses. The PL properties of the thin films were measured using a Varian Carry eclipse (model LS 55) spectrophotometer, equipped with a 150-W monochromatized xenon lamp as the excitation source. Surface morphology was analyzed using JEOL JSM-7800F scanning electron microscope (SEM). Particulate sizes for particles on the thin films were determined from the SEM images using the analySIS software. The Oxford instruments energy dispersive X-ray spectroscopy (EDS) was used for composition analysis. The surface morphology and roughness were examined from images captured in the contact mode using a Shimadzu SPM- 9600 Atomic Force Microscopy (AFM).

### 6.4. Results and Discussion

#### 6.4.1. XRD Results

Fig. 6.3 shows the XRD diffraction patterns of  $\text{CaS:Eu}^{2+}$  thin films deposited using different laser wavelengths. The films deposited at 532-nm were amorphous, while crystallinity improved at 266-nm and 355-nm laser, with the films deposited at a laser wavelength of 355 nm showing a narrower peak than films deposited at the laser wavelength of 266 nm. This is

probably due to the large particulate deposited at 355 nm. The thin film deposited at a laser wavelength of 532 nm showed no peak at all. This is probably due to the poor absorption (see Eq. (6.4)) of the 532 nm laser, giving rise to ablated particles which are less energetic. As is seen from Fig. 6.3, diffraction peaks oriented in the (200) plane were obtained for the films deposited at 266 nm and 355 nm. This preferential growth is due to the influence of the Si (100) substrate that is favored by the high mobility of the ablated species [21].

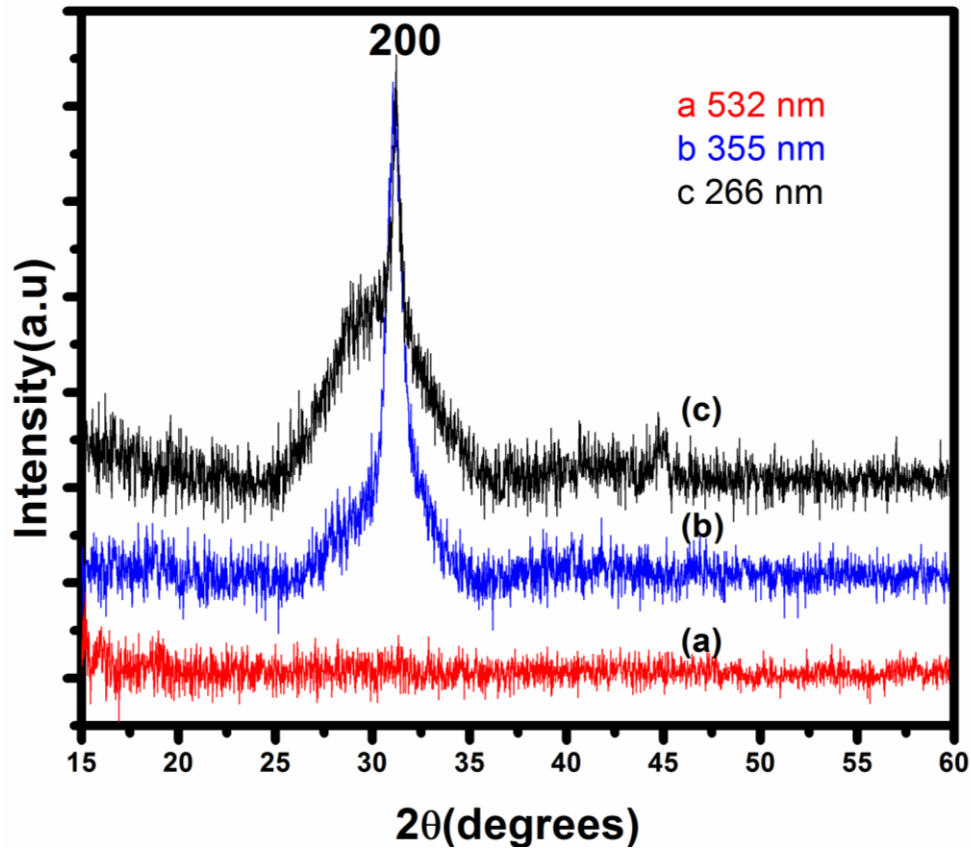


**Figure 6.3:** X-ray diffraction patterns of  $\text{CaS:Eu}^{2+}$  thin films deposited at different laser wavelengths: (a) 532 nm, (b) 355 nm, and (c) 266 nm.

#### 6.4.2. Rutherford Backscattering Results

The RBS spectra, for the films deposited at different laser wavelengths of 266, 355 and 532 nm are shown in Fig. 6.4. The energy peaks for Ca, S and Eu, for all the laser wavelengths



are at ~1.3, ~1.2, and ~1.8 MeV, respectively. The stoichiometry and the thickness of the films are shown in Table 6.1. The peak intensity is a measure of the abundance of each element in the film since the area under each signal is proportional to the total number of atoms for each element in the film [22]. The intensity of the Eu energy peak using the laser wavelength of 532 nm was too weak to be recorded. Although the stoichiometry of the films was comparable to that of the commercial powder (Ca: S; 1:1), there was a slight deficiency of sulfur (noticeable in the 532 nm-film) in the thin films since the films were grown in a non-reactive atmosphere where replacement of lost sulfur is not possible. Films grown in a sulfur rich atmosphere, e.g. in H<sub>2</sub>S have been shown to promote vacancy-free stoichiometry of CaS thin films [23, 24].

The RBS technique detects the number of atoms per unit area in a layer, from which the layer thickness can be determined. The detected energy difference between <sup>4</sup>He<sup>+</sup> ions scattered from the front and the back surface of the film is given by Eq. (6.6) [22]

$$\Delta E = \varepsilon Nt \quad (6.6)$$

where  $\varepsilon$  is the stopping cross section for a given scattering angle,  $N$  is the atomic density of the material, and  $t$  is the thickness of the material. From Eq. (6.6), the thickness of the film is given as follows:

$$t = \frac{\Delta E}{\varepsilon N} \quad (6.7)$$

The thickness  $t$  is in cm if  $E$  is in electron volts,  $\varepsilon$  in electron volts per 10<sup>15</sup> atoms/cm<sup>2</sup>, and  $N$  in atoms/cm<sup>3</sup>. Using the atomic mass unit (a.m.u) of CaS as 72.15, its density as 2.75 g/cm<sup>3</sup>, and the Avogadro's number as 6.02 x 10<sup>23</sup>, the atomic density of CaS was obtained as 2.16 x 10<sup>22</sup> atoms/cm<sup>3</sup>. The values of  $\frac{\Delta E}{\varepsilon}$  were obtained from the simulated data as 325, 350, and 50 x 10<sup>15</sup> atoms/cm<sup>2</sup> for films deposited at laser wavelengths of 266, 355, and 532 nm, respectively. Thus, using Eq. (6.7), the film thicknesses were found to be 150.0, 162.0, and 23.1 nm for deposition at laser wavelengths of 266, 355 and 532 nm, respectively. As explained in section 6.1.1 (see Eqs. (6.3) and (6.4)), the 266-nm laser is absorbed better than

the 355-nm laser and hence formed a smoother film. However, the target is transparent to the 532-nm laser, leading to very little laser energy being absorbed. This could be one of the reasons why the film formed from this deposition is so thin.

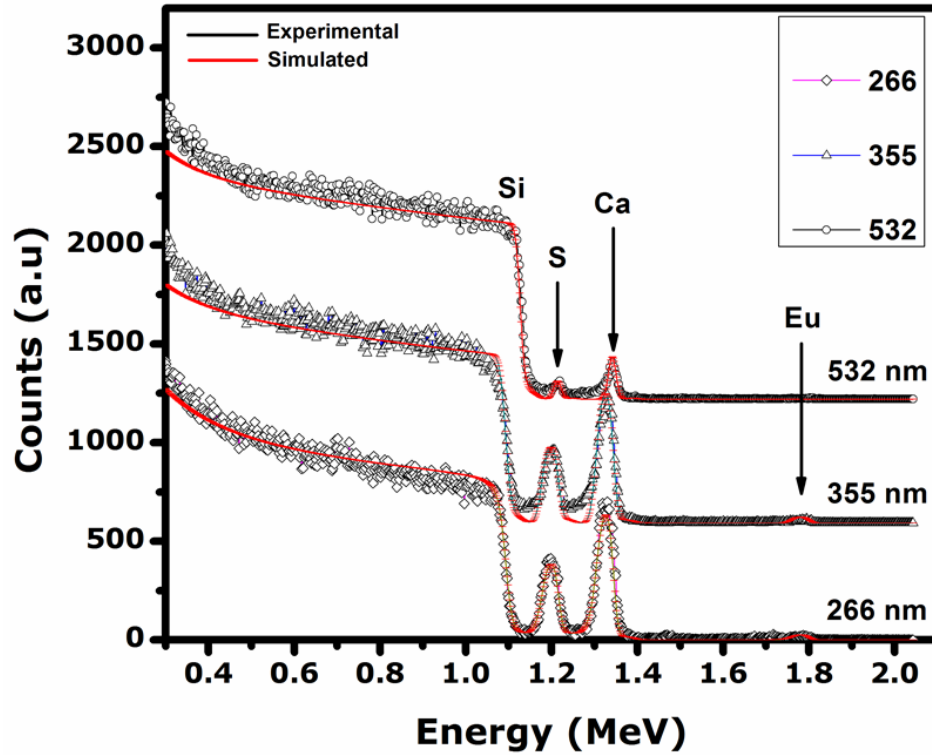


**Figure 6.4:** RBS spectra showing experimental (black) and simulated (red) spectra of the CaS: Eu<sup>2+</sup> thin films deposited at laser wavelengths of 266 nm, 355 nm, and 532 nm.

**Table 6.1:** Stoichiometry (ratios of Ca: S) and thickness of the films deposited at different laser wavelengths.

Laser Wavelength	Thickness ( $\times 10^{15}$ at./cm <sup>2</sup> )	Thickness (nm)	Stoichiometry (at. %)		
			Ca	S	Eu
266	325	150.0	0.515 $\pm$ 0.0087	0.483 $\pm$ 0.0093	0.0021 $\pm$ 0.056
355	350	162.0	0.518 $\pm$ 0.0092	0.481 $\pm$ 0.0099	0.0016 $\pm$ 0.061
532	50	23.1	0.592 $\pm$ 0.02	0.408 $\pm$ 0.029	-

### 6.4.3. AFM, SEM and EDS Results

#### 6.4.3.1. AFM Results

Fig. 6.5 shows the AFM images of the films deposited when using the laser with wavelengths 266, 355 and 532 nm. The deposited films show well-defined spherical grains with root mean square (rms) roughness of 21, 26.7, and 17.9 nm for the 266-, 355-, and 532-nm lasers, respectively.

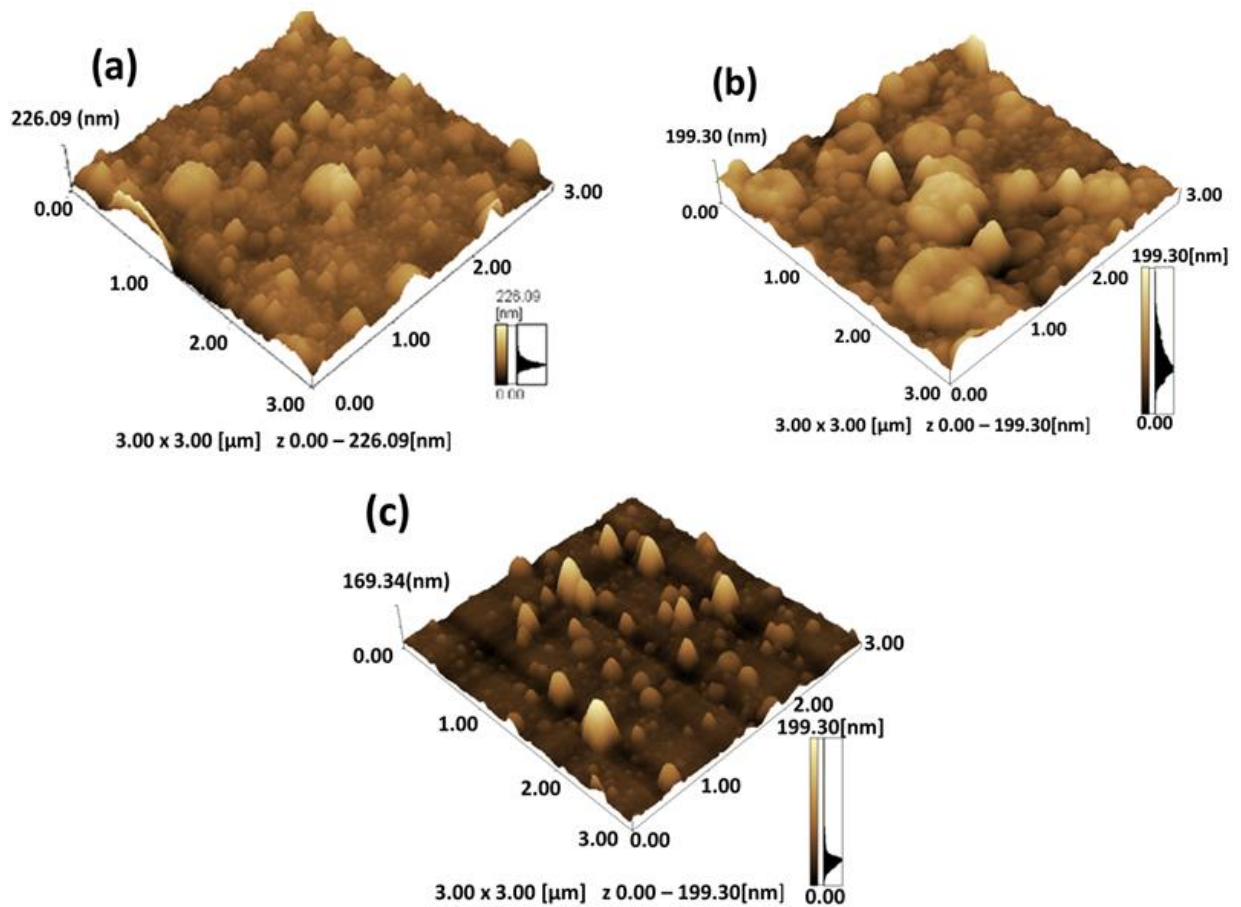


**Figure 6.5:** AFM images of the films deposited using the a) 266 nm, b) 355 nm, and c) 532 nm laser.

The thin film roughness increased as the laser wavelength increased from 266 nm to 355 nm and then decreased as the laser wavelength increased to 532 nm. The increase in the roughness is due to large number of micron-sized particles formed on the 355-nm laser thin film. At laser wavelength of 532 nm, very little ablation took place as shown in Fig. 6.2; therefore, the rate of deposition was greatly reduced, hence the reduced roughness.

#### **6.4.3.2. SEM and EDS Results**

Fig. 6.6 presents the SEM photographs showing the surface morphology of the films deposited using the 266-, 355-, and 532-nm wavelengths of the Nd: YAG laser. The particles were spherically-shaped, with sizes ranging from 0.05 to 0.7  $\mu\text{m}$ , 0.08 to 0.9  $\mu\text{m}$ , and 0.06 to 0.7  $\mu\text{m}$  for laser wavelengths 266, 355, and 532 nm, respectively. All the film surfaces consist of bigger and smaller spherical particles. Bigger particles were formed when smaller particles agglomerated together. The particulate size and density increased as the laser wavelength changed from 266 to 355 nm, and then decreased as the laser wavelength was changed to 532 nm.

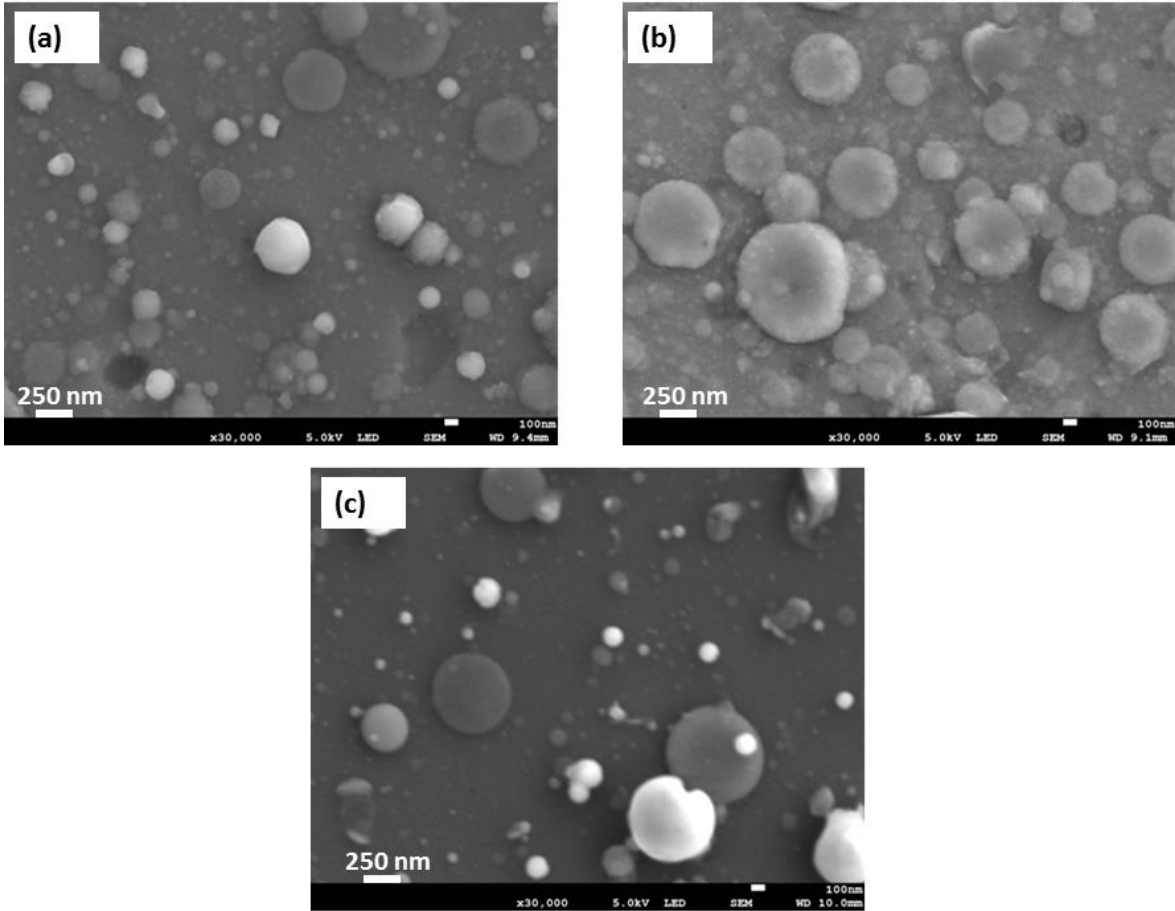


**Figure 6.6:** SEM photographs of films deposited at different laser wavelengths; (a) 266 nm, (b) 355 nm and 532 nm.

The observed differences in the morphology for different laser wavelengths are ascribed to different optical absorption coefficients of CaS at 266, 355, and 532 nm. In the case of the laser irradiation at 355 nm, because of the high optical penetration as shown by Eq. (6.3), the superheating effect appeared deeper in the target, producing subsurface explosion, hence the large particulate. Laser radiation at wavelength of 532 nm was barely absorbed; more of it being reflected and hence the relatively smoother surface. The 266-nm laser was absorbed near the surface, hence the medium sized particles.

The EDS spectra for the film deposited using a laser wavelength of 532 nm is shown in Fig. 6.7. The results confirm the presence of all the main elements (i.e., Ca and S) of the

CaS:Eu<sup>2+</sup> thin films. Similar EDS spectra were recorded from the other two films. Due to the relatively low concentration of Eu<sup>2+</sup> ions in the films, its signal could not be detected. The silicon (Si) is from the Si (100) substrate, while the oxygen (O) is probably a contaminant coming from the environment. Spectrum 7 (S7) and spectrum 5 (S5) in the inset (middle) show the positions where EDS analysis was performed. The legend shows bar graphs of the weight % of the elements at positions S5 and S7. The weight % of Ca at S5 is about 35% while that of S at the same position is about 20%. The weight% at position S7 for both Ca and S is less than 5%. Thus, the brighter region contains more Ca, which has a higher backscatter coefficient [25]. There is relatively more S in the darker particles. Our results are in good agreement with work reported in Ref. [26].

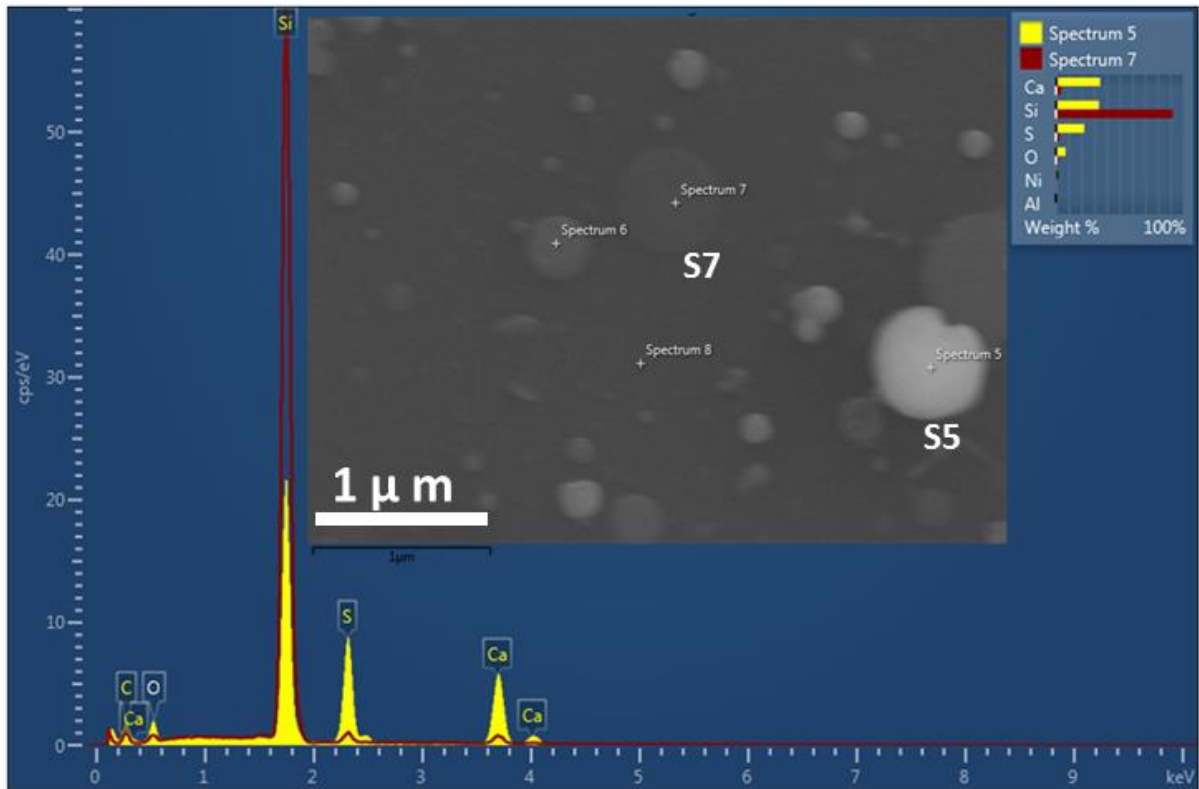


**Figure 6.7:** EDS spectra of CaS:Eu<sup>2+</sup> PLD thin films deposited at laser wavelengths of 532 nm. EDS was performed in positions S5 and S7 (inset).

#### 6.4.4. Photoluminescence Results

The emission and excitation spectra were recorded when monitoring the emission at 650 nm and the respective absorptions were observed in the wavelength ranges of 200 to 600 nm at room temperature. Samples were excited at 470 nm and the respective emissions observed in the wavelength ranges 500 to 800 nm at room temperature. Fig.6.8 shows the PL excitation and emission spectra of the films deposited using the 266-, 355-, and 532-nm laser wavelengths. The excited  $5d^1$  electronic states of the  $\text{Eu}^{2+}$  ion is split into  $e_g$  and  $t_{2g}$  energy states by the crystal field of the host. As has been reported by Park et al. [27], the  $e_g$  and  $t_{2g}$  states are inside and below the conduction band, respectively. Therefore, the broad excitation band between 200 nm and 320 nm is a mixture of  $\text{Eu}^{2+}$   $4f^7[{}^8S_{7/2}] \rightarrow 4f^6[{}^7F_J]5d^1[e_g]$  and valence-to-conduction band transitions [28], while the excitation band extending from 400-600 nm is ascribed to the  $4f^7[{}^8S_{7/2}] \rightarrow 4f^6[{}^7F_J]5d^1[t_{2g}]$  transitions of  $\text{Eu}^{2+}$  [29]. It therefore follows that a blue-emitting LED would be a good source of excitation for this phosphor. The emission peak observed at 650 nm (Fig. 6.8 (b)) is attributed to the dipole-allowed transitions from the excited  $4f^6[{}^7F_0]5d^1(t_{2g})$  state to the ground state  $4f^7({}^8S_{7/2})$  of the  $\text{Eu}^{2+}$  ions. The 355-nm laser-produced films showed a higher PL intensity than those formed using the 266-nm lasers. The higher PL intensity observed for the longer wavelength (355 nm) laser film is attributed to the larger particulates on the film. However, it should be noted that this improved PL intensity is a trade off with formation of large particulate which is the major drawback of PLD-grown thin films. The PL intensity reduced dramatically at a laser wavelength of 532 nm compared to the intensity at 355 nm, and this observation can be explained as follows. As shown by Eq. (6.3) and (6.4) (section 6.1.1), the absorption of the laser by the material decreased with an increase in wavelength, therefore at higher wavelength, absorption is less significant. At a laser wavelength of 532 nm, it was observed that the plume was very small, and there was huge light being reflected (Fig. 6.2). On the other extreme, the 266-nm laser was absorbed better and formed a beautiful plume. This implies that very little ablation took place for the 532-nm laser, and this could explain why

the PL emission is very low for that wavelength. These observations fit well into Eq. (6.5) and are in agreement with Bauerle [15], Dohotre and Harimkar [30] who have shown that the reflectivity of materials increases with wavelength. In other words, we can say that, when reflectivity decreases, a larger part of a laser is absorbed.

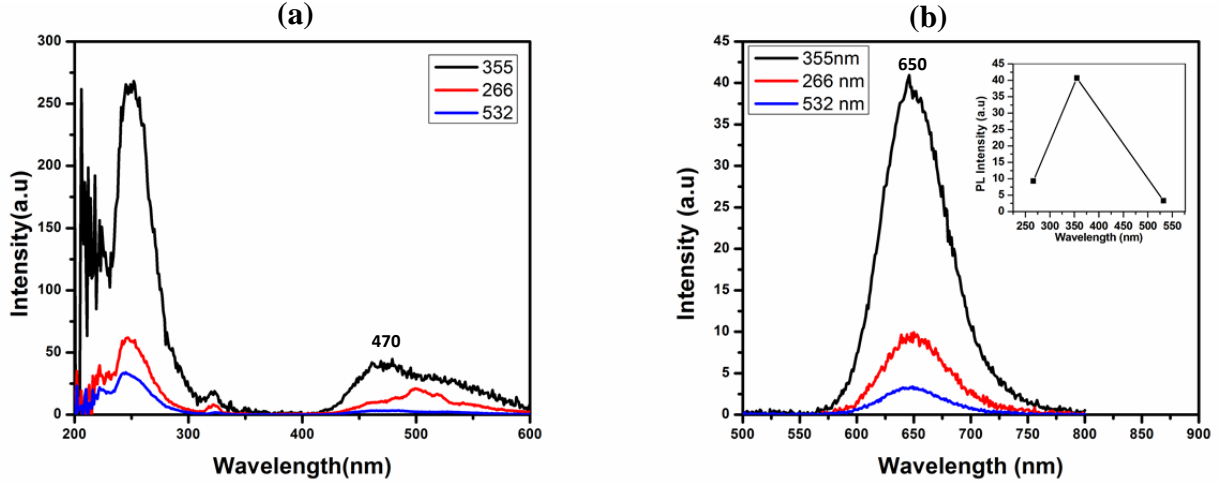


**Figure 6.8:** PL (a) Excitation and (b) Emission spectra at laser wavelength 266, 355, and 532 nm and inset, variation of PL intensity with wavelength.

## 6.5. Conclusion

CaS:Eu<sup>2+</sup> thin films were successfully deposited on Si (100) substrates by the pulsed laser deposition technique. The XRD data confirmed that the films were generally amorphous, except for a sharp diffraction peak oriented in the (200) plane observed from the films deposited at 266 and 355 nm. The film deposited at the wavelength of 532 nm was found to be thinner than those deposited at the wavelengths of 266 and 355 nm, and this was attributed to the poorly absorbed laser energy due to the target being transparent to the 532-nm laser wavelength. The highest PL intensity was observed from the film deposited at the wavelength of 355 nm, and the least intensity was observed from the film deposited at the wavelength of 532 nm. This was attributed to the fact that the film deposited at 355 nm was rougher and thicker than that deposited at 266 and 532 nm. Generally, the surface quality of the film deposited at 266 nm was better than that of the films deposited at 355 (formation of



particulate) and 532 nm. Therefore, we can safely conclude that the laser wavelengths of 355 and 532 nm whose laser photon energies are less than the optical band gap of CaS:Eu<sup>2+</sup> are not suitable for the deposition of thin films for this target. Finally, due to its good absorption around 470 nm, CaS:Eu<sup>2+</sup> is a good candidate for phosphor-converted LED applications using a blue LED as a source of excitation.

## References

1. D. Jia, X. Wang, *Opt. Mater.* **30** (2007) 375-379.
2. C. Guo, D. Huang, Q. Su, *Mater. Sci. Eng. B.* **130** (2006) 189-193.
3. J. E. Van Hackee, P. F. Smet, K. De Keyser, D. Poelman, *J. Electrochem. Soc.* **154** (9) (2006) J278-J282.
4. S. Christoulakis, M. Suche, N. Katsarakis, E. Koudoumas, *Appl. Surf. Sci.* **253** (2007) 8169-8173.
5. E. Gyorgy, I. N. Mihailescu, M. Kompitsas, A. Giannoudako, *Thin Solid Films* **446** (2004) 178-183.
6. D.P. Norton, *Mater. Sci. Eng. R.* **43** (2004) 139-247.
7. R.R. Biggers, J.G. Jones, I. Maartense, J. D. Busbee, D. Dempsey, D. Liptak, D. Lubbers, C. Varanasi, D. Mast, *Eng. Appl. Artif. Intell.* **11** (1998) 627-635.
8. P.D. Nsimama, O.M. Ntwaeaborwa, H.C. Swart, *J. Lumin.* **131** (2011) 119-125.
9. J.J. Dolo, O.M. Ntwaeaborwa, J.J. Terblans, E. Coetsee, B.F. Dejene, M. M. Biggs, H.C. Swart, *Appl. Phys. A.* **101** (2010) 655-659.
10. H.S. Kwok, P. Mattocks, L. Shi, X.W. Wang, S. Witanachchi, Q.Y. Ying, J.P. Zheng, D.T. Shaw, *Appl. Phys. Lett.* **52** (1998) 1825-1827.
11. I. W. Boyd, *Ceram. Int.* **22** (5) (1996) 429-434.
12. Y. A. Il'insky, L.V. Keldysh, *Electromagnetic Response of Material Media*; Plenum Press: New York, 1994; p250.
13. W.M. Steen, *Laser Materials Processing*; Springer: London, 1991; pp81- 89.

14. M.S. Brown, C.B. Arnold, Fundamentals of Laser-Material Interaction. In: *Laser Precision Microfabrication*, Koji Sugioka, Michel Meunier', Alberto Piqué (Editors) Springer-Verlag: Berlin Heidelberg, 2010; pp. 91-120.
15. D. Bauerle, *Laser Processing and Chemistry*; Springer-Verlag: Berlin Heidelberg, 2011; p20.
16. A. Kitai, *Principles of Solar Cells, LEDs and Diodes: the role of the PN junction*; John Wiley & Sons, Ltd: West Sussex, 2011; pp162-164.
17. A. Goetzberger, Knobloch, B. Voss, *Crystalline Silicon Solar Cells*; John Wiley & Sons, Inc.: New York, 1998; pp 30-34.
18. V. Craciun, D. Craciun, Appl. Surf. Sci. **138** (1999) 218-223.
19. M. Mayer, *SIMNRA User's Guide, Report IPP 9/113*, Max-Planck-Institut für Plasmaphysik: Garching, Germany, 1997; pp 4-47.
20. M. Meyer, Nucl. Instrum. Methods Phys. Res. B. **332**(2014)176-180.
21. K.T. Hillie, C. Curren, H.C. Swart, Appl. Surf. Sci. **177** (2001)73-77.
22. W. Chu, J. Mayer, M.A. Nicolet, *Backscattering spectrometry*; Academic press, Inc.: San Diego, California, 1978; pp 90-94.
23. J. B. Francisco, *PhD Dissertation*: The Temple University, 2009.
24. D. Poelman , R. Vercaemst, R.L. Van Meirhaeghe, W. H. Laflere, F. Cardon, J. Lumin. **75**(1997)175-181.
25. J. I. Goldstein, D. Newbury, D.C. Joy, C.E. Lyman, P. Echlin, E. Lifshin, L. Sawyer, J. R. Michael, *Scanning electron Microscopy and X-ray Microanalysis*; Kluwer Academic/Plenum Publishers: New York, 2003; p142.
26. P.P. Mokoena, M. Gohain, B.C.B. Bezuidenhoudt, H.C. Swart, O. M. Ntwaeaborwa, O. M. J. Lumin. **155** (2014) 288-292.
27. S.H. Park, S.H. Sohn, K.S. Sohn, Physica B. **293** (2000)187-197.
28. H. Choi, C. Kim, C. Pyun, J. Solid State Chem. **138** (1998)149-153.
29. H. Sung, Y. Cho, Y. Huh, Y. Do, Bull. Korean Chem. Soc. **28** (8) (2008) 1280-1284.
30. N.B. Dahotre, S. Harimakar, *Laser Fabrication and Machining of Materials*; Springer Science + Business Media, LLC: New York, 2008; p 36.

## Chapter 7

### TOF SIMS Analysis, Structure and Photoluminescence Properties of Pulsed Laser Deposited CaS:Eu<sup>2+</sup> Thin Films

#### 7.1. Introduction

Phosphor materials prepared by doping alkaline-earth sulfides with rare-earth (RE) ions have found practical applications such as display panels [1,2], cathode ray tubes [3,4], thermoluminescence (TL) dosimeters [5,6], optical storage devices [2,7] and light emitting diodes (LEDs) [12]. Alkali earth sulfide phosphors such as divalent europium (Eu<sup>2+</sup>) doped calcium sulfide (CaS:Eu<sup>2+</sup>) and strontium sulfide (SrS:Eu<sup>2+</sup>) are good materials for blue pumped three-band phosphor-converted white LEDs since both phosphors have strong absorption in the blue region [8, 9]. Phosphors can be used as bulk powders or thin films. In general, thin film phosphors have several advantages over bulk powders, such as higher lateral resolutions from smaller grains, increased thermal stability, more uniform density, reduced outgassing and better adhesion to solid substrates [10, 11]. Various properties of CaS:Eu<sup>2+</sup> in powder form have been reported extensively [8, 12, 13, 14], while thin film forms of this material deposited using different techniques such atomic layer deposition [15] and electron beam evaporation [16] have also been investigated. In recent years, the pulsed laser deposition (PLD) technique has gained popularity due to its ability to transfer the material stoichiometry from a multi-component ablation target to a growing film [17-19]. In order to get films with the desired properties using the PLD technique, different deposition parameters need to be optimized. Examples of such parameters are partial pressure [20], laser fluence [21], substrate temperature [22], pulse duration [23], etc. Growing thin films in a specific gas environment has influence on the expansion of the laser-produced plasma. For instance it may modify the kinetic energy and may also induce compositional changes on the deposited films [24]. The crystalline structure, morphology, photoluminescence and

compositional changes were analyzed by X-ray diffractometer (XRD), atomic force microscopy (AFM) and scanning electron microscopy (SEM), photoluminescent spectrophotometry, energy dispersive X-ray spectroscopy (EDS) and time-of-flight secondary ion mass spectrometry (TOF SIMS), respectively. TOF-SIMS is an effective technique for the detection of impurities/dopants in the host material in the ppm range [25]. The TOF-SIMS instrument in both static and dynamic mode was used to observe the chemical information in Eu<sup>2+</sup>-doped CaS PLD thin films.

This study aims at evaluating photoluminescent properties, the morphology, and composition, of CaS:Eu<sup>2+</sup> thin films prepared by the pulsed laser deposition technique. We report the influence of Ar, O<sub>2</sub>, and vacuum atmospheres on the structure, surface morphology and photoluminescence properties of the deposited thin films. Our data demonstrates that the thickness/roughness and the PL intensity of the films depend on the atmosphere in which the films were grown. In addition, our data indicate that the dopant exists in two oxidation states, due to oxidation of Eu<sup>2+</sup> to Eu<sup>3+</sup>.

## 7.2. Experimental

CaS:Eu<sup>2+</sup> commercial powder phosphor from Phosphor Technology (UK) was pressed without binders to make a pellet (target) for ablation. The pellet was annealed in air at 250 °C for 3 h to harden and remove water vapor and other volatile adsorbed substances. The Si (100) substrates were placed in a beaker containing ethanol and cleaned using an ultrasonic bath for a period of 15 minutes. Each piece of substrate was dried using N<sub>2</sub> and stored in plastic packets which were sealed. The deposition chamber of the pulsed laser system was first evacuated to a base pressure of 3.6 x 10<sup>-6</sup> Torr. The Spectra Physics Quanta-Ray Pro-270 266 nm Nd: YAG laser was used to ablate the phosphor pellet in a vacuum, Ar (5 mTorr), and O<sub>2</sub> (5 mTorr) atmospheres. The laser fluence, number of pulses and repetition rate were set to 5.09 J/cm<sup>2</sup>, 18000 and 10 Hz, respectively. The substrate temperature was fixed at 200 °C, and the target distance was fixed at 4.5 cm.

### 7.3. Characterization Methods

The JEOL JSM-7800F field emission scanning electron microscope (FE-SEM), operated at 3.0 kV was used to analyze the surface morphology. The Oxford instruments AzTEC energy dispersive X-ray spectroscopy (EDS) was used for composition analysis. The surface morphology and roughness were examined from images captured in contact mode using the Shimadzu SPM- 9600 Atomic Force Microscopy (AFM). X-ray diffraction data were collected using a Bruker AXS D8 ADVANCE X-ray diffractometer (XRD), with  $\text{CuK}_\alpha$  radiation of wavelength 1.5406 Å, operated at 40 kV and 40 mA. Diffraction patterns were recorded over the range  $15^\circ \leq 2\theta \leq 50^\circ$  with a counting time of 1 s for each step size of  $0.0037^\circ$ . Photoluminescent (PL) properties of the thin films were measured using a Varian Carry eclipse (model LS 55) spectrophotometer at room temperature with a monochromatized 150 W xenon flash lamp as the source of excitation. The TOF-SIMS measurements were performed using an IONTOF TOF-SIMS5 ion mass spectrometer. The mass spectra and images of the thin films both in positive and negative secondary ion polarities were acquired using a pulsed 30 kV  $\text{Bi}^+$  primary beam ion gun with a pulse repetition rate of 10 kHz. The beam had a spot diameter of 5  $\mu\text{m}$  in spectroscopy mode and 200 nm in imaging mode, an ion current of  $\sim 1$  pA and 0.25 pA in spectroscopy and imaging modes, respectively. For the acquisition of depth profiles, the  $\text{O}_2^+$  sputter gun operated at 1kV,  $\sim 250$  nA was used in both spectroscopy and imaging positive modes. To acquire depth profiles in negative mode the  $\text{Cs}^+$  sputter gun operated at 2 kV and  $\sim 130$  nA was employed. The sputter raster was  $300 \times 300 \mu\text{m}^2$  and the area that was analyzed was  $100 \times 100 \mu\text{m}^2$ .

## 7.4. Results and Discussion

### 7.4.1. XRD Results

The XRD patterns for the as-deposited thin films are shown in Fig.7.1. There were no diffraction peaks from the film prepared in  $\text{O}_2$  atmosphere meaning that the film was completely amorphous. As can be seen from Fig. 7.8 (c), films formed in an oxygen atmosphere contain sizeable amounts of  $\text{CaO}^+$  and  $\text{CaOH}^+$  ions, suggesting phases of these

materials are inherently present in the films. These impurities can exert an effect by binding to a crystal surface, thus possibly preventing or disturbing further crystal growth on that particular face [25]. This may explain why films grown in oxygen atmosphere show much poorer degree of crystallinity compared to the other environments. The films prepared in argon and vacuum showed broad (200) preferred-orientation peak. The formation of a peak for these films suggests a degree of crystallinity for the films prepared in vacuum and argon atmosphere. Christoulakis et al. [11] has also reported the formation of amorphous or polycrystalline PLD thin films of CaS:Eu, Sm prepared in an inert atmosphere (helium).

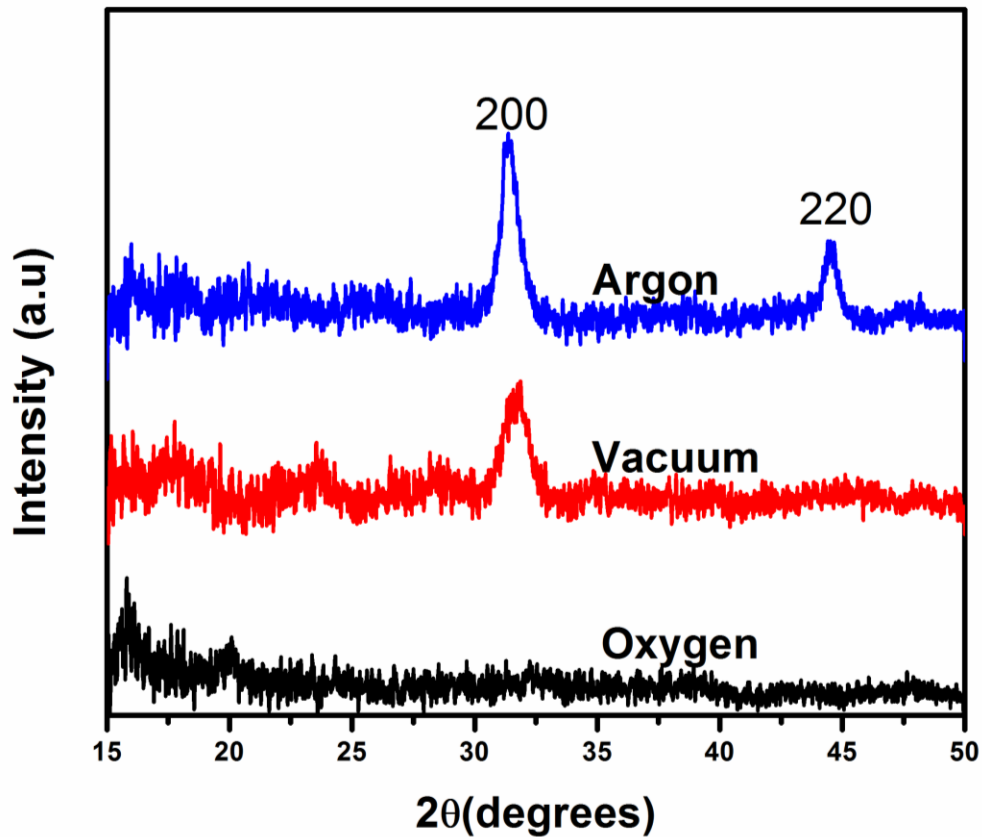


**Figure 7.1:** The XRD spectra of the CaS:Eu<sup>2+</sup> thin films deposited in different atmospheres.

## 7.4.2. AFM and SEM Results

### 7.4.2.1. AFM Results

Fig. 7.2 shows  $10 \times 10 \mu\text{m}^2$  AFM images of the thin films deposited in different atmospheres, with mostly spherically shaped grains of varying sizes, non-homogeneously spread over the surfaces. The root mean square (RMS) roughness is 65 nm, 26 nm for films deposited in Ar, and vacuum atmospheres, respectively. Fig. 7.2 (c) shows the image of the film deposited in oxygen, with a roughness of 61 nm. The film deposited in vacuum is smoother possibly because the deposited film is bombarded by the fast moving plume particles which cause re-sputtering of the surface. The oxygen and argon molecules slow down the plume particles, allowing for better nucleation and growth [26]. Argon molecules are heavier than those of oxygen, implying that they slow plume particles more than oxygen molecules. Indeed, nucleation in an argon atmosphere may even start before the particles reach the substrate. This explains why the film prepared in argon is the roughest.

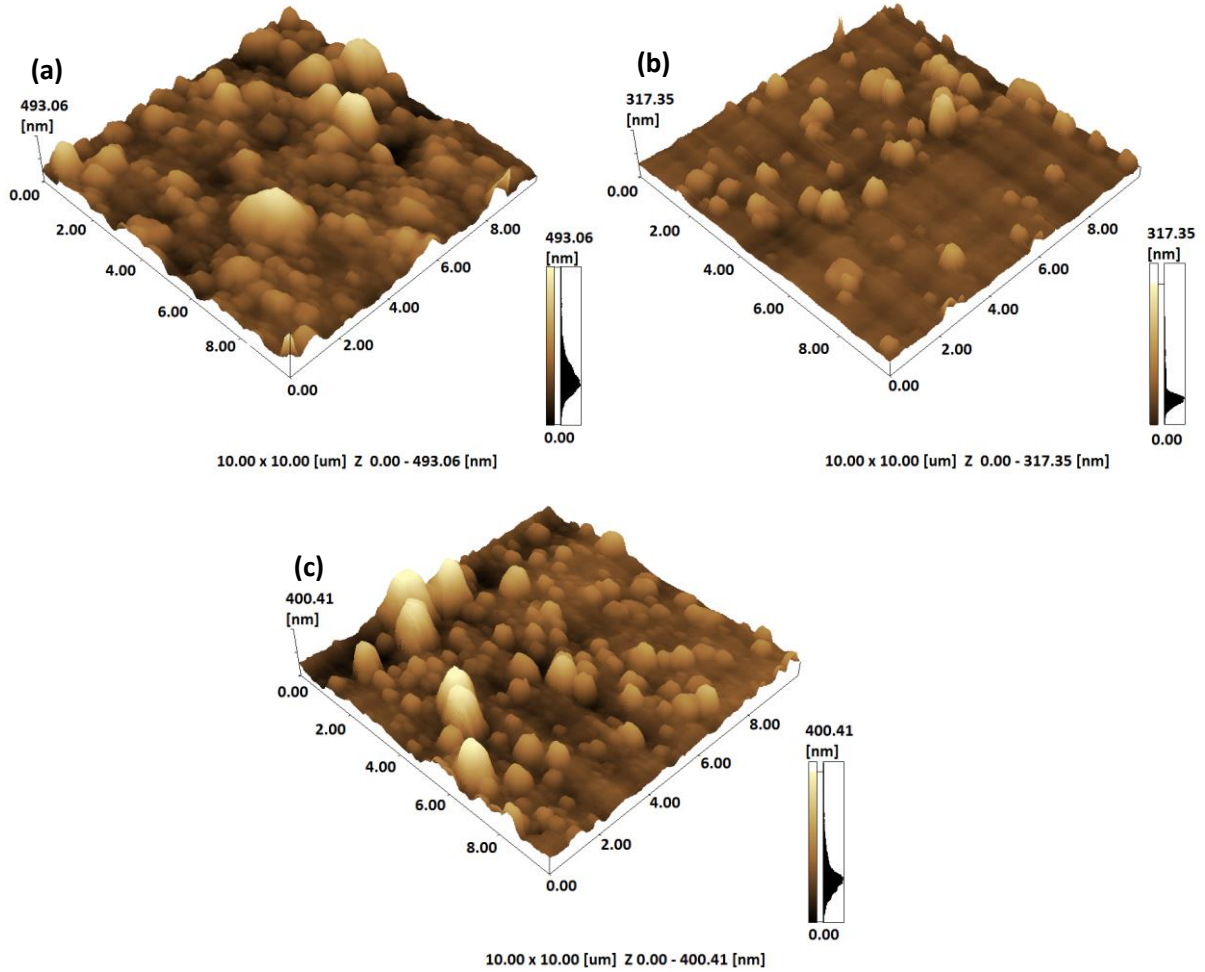


**Figure 7.2:** The AFM images of the PLD CaS:Eu<sup>2+</sup> thin films in a) Ar, b) vacuum, and c) O<sub>2</sub> atmospheres.

#### 7.4.2.2. SEM and EDS Results

The surface morphology of the films deposited in different atmospheres is shown in Fig. 7.3. The images show that the films consisted of large and small spherical particles. The large particles show evidence of agglomeration. The film prepared in argon (Fig. (7.3a)) shows larger particulate and that prepared in oxygen shows medium-sized particles while that prepared in a vacuum (Fig. (7.3b)) is clearly relatively smoother than films grown in



argon/oxygen atmospheres. This is in agreement with the results obtained in section 7.4.2.1 for AFM images.

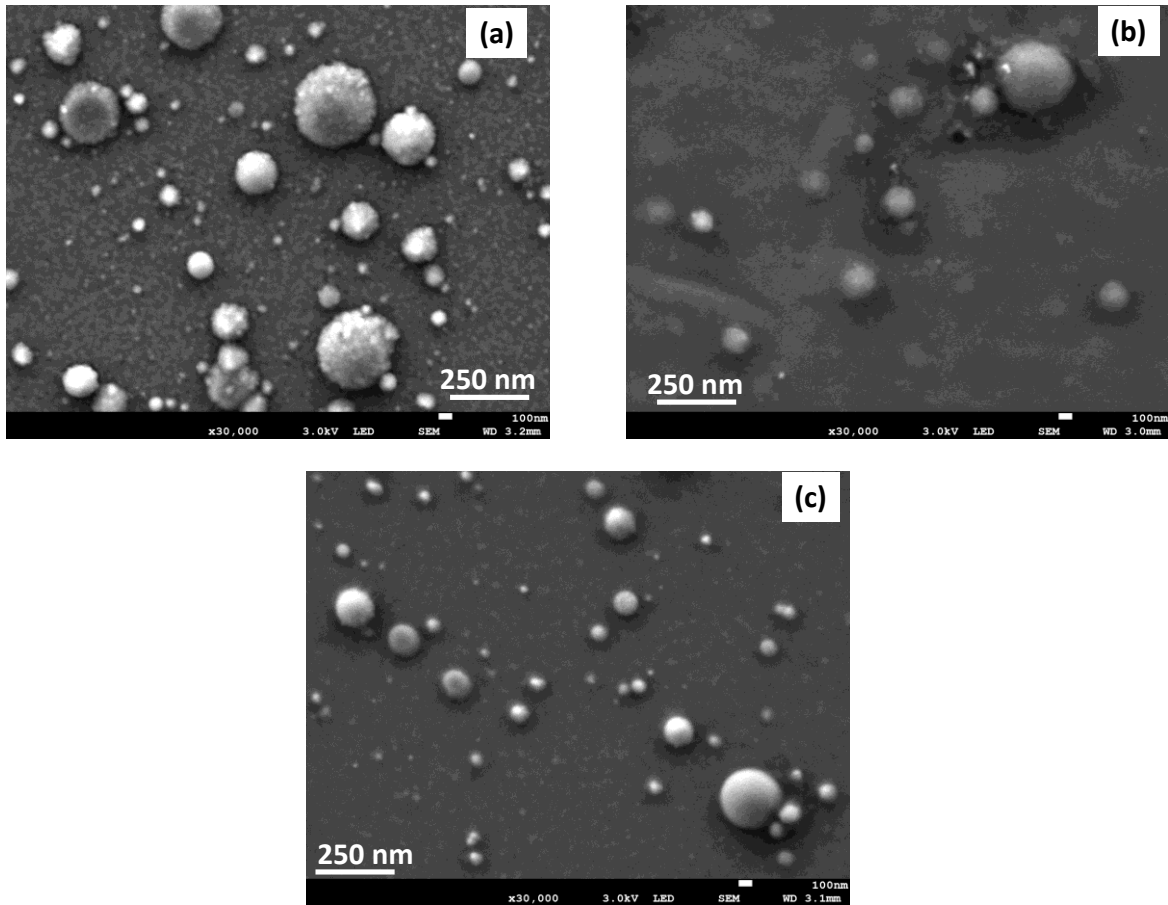


**Figure 7.3:** SEM images of films deposited in different atmospheres (a) argon (b) vacuum and (c) oxygen.

The EDS spectrum for the films deposited in an argon atmosphere is shown in Fig. 7.4. The results confirm the presence of Ca and S, which are the principal elements in the film. In addition, carbon (C), oxygen (O), and silicon (Si) were also detected. Aluminium (Al) is detected in even much lower concentrations. The O is likely a contamination from the environment or during preparation of the powder, while the carbon is likely coming from the atmospheric hydrocarbons. The Si signal is from the Si (100) substrate, while the Al could be incidental impurity during the handling of the films. EDS analysis was performed on a

particle labeled spectrum 3 (S3) and on the flat area labeled spectrum 4 (S4) on the SEM image in the inset of Fig.7.4. The weight % of Ca at S3 is about 50% while that of S at the same position is about 30%. At position S4, the weight % for Ca and S is 45% and 32%, respectively. Thus, region S3 which is brighter than region S4 has more Ca than S. Region S4, a relatively smoother region, has more Si than S3, while S4 has more O than S3. Region S3 is thicker than region S4 owing to the drop-like deposit found in S3. This explains why the EDS signal S4 is higher than that found at S3. Table 7.1 shows the approximate % by weight and atomic % of the main elements in the analyzed regions. Thus, the brighter region contains more Ca, which has a higher atomic number than S, and hence a higher backscatter coefficient [27]. The higher count rates of oxygen were also observed in the TOF SIMS spectrum (Fig.7.9) as is discussed in section 7.4.4.

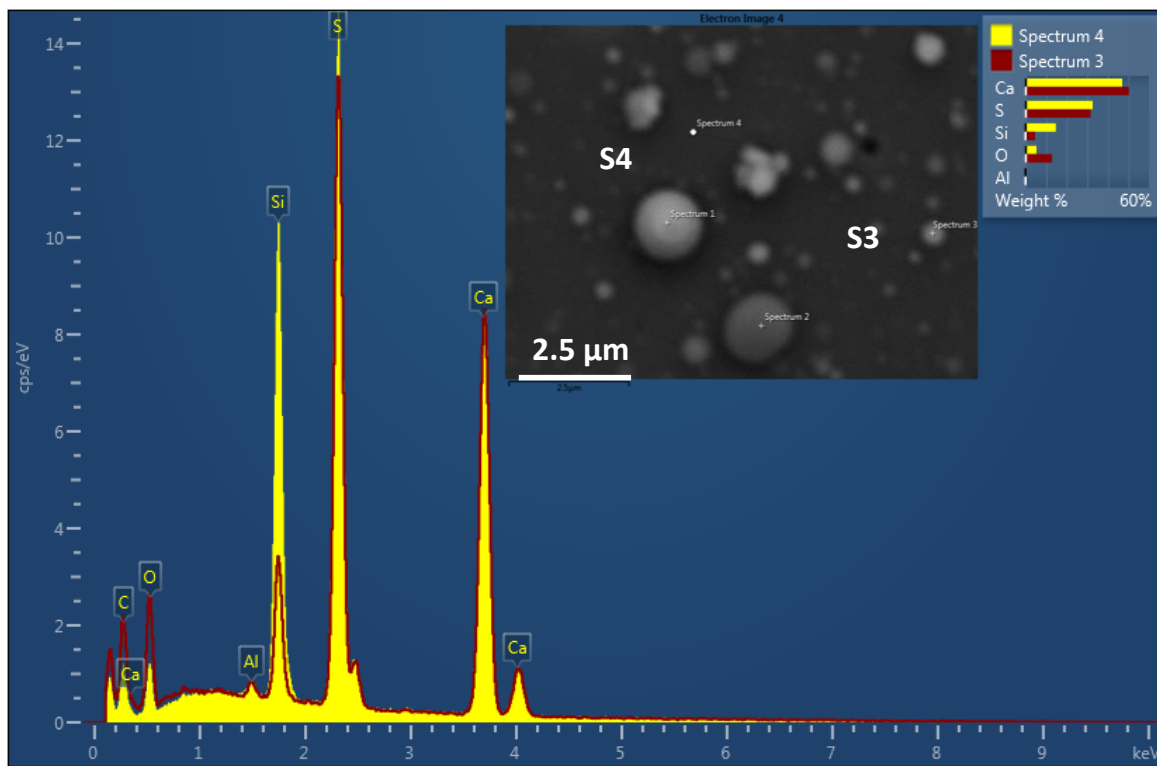


**Figure 7.4:** EDS spectra of CaS:Eu<sup>2+</sup> PLD thin films deposited in an argon atmosphere. EDS was performed in positions S3 and S4 (inset).

**Table 7.1:** Approximate elemental concentration by % weight and % atomic in regions S3 and S4 (see Fig. 7.4)

Element/Region	S3		S4	
	Wt%	At%	Wt%	At%
Ca	50	40	45	38
S	30	30	32	34
O	12	24	5	10
Si	5	6	15	18

### 7.4.3. Photoluminescence Results

The PL excitation and emission spectra of CaS:Eu<sup>2+</sup> thin films deposited at different atmospheres are shown in Fig.7.5. The excitation spectra in Fig. 7.5(a) were recorded when monitoring the emission at 650 nm and it shows two excitation peaks with maxima at 250 and 470 nm. The peak at 250 nm is assigned to the band-to-band transition of the CaS host material and the peak at 470 nm is assigned to the  $f \rightarrow d$  transition of Eu<sup>2+</sup> [28]. The samples were excited at 250 nm and then at 470 nm. In our previous study [29] we demonstrated that, irrespective of the excitation wavelength, the emission peak for CaS:Eu<sup>2+</sup> was always around 650 nm. In the present study, however, the PL spectra exhibit mixed emission from Eu<sup>2+</sup> and Eu<sup>3+</sup> when the films were excited at the wavelength of 250 nm as shown in Fig 7.5 (b). The broad emission band attributed to the transitions from the excited  $4f^6[{}^7F_0]5d^1(t_{2g})$  state to the ground state  $4f^7({}^8S_{7/2})$  of the Eu<sup>2+</sup> ions is located at 650 nm and the narrow emission band attributed to the  ${}^5D_0 \rightarrow {}^7F_2$  transitions of Eu<sup>3+</sup> is located at 618 nm. This result indicates that there was energy transfer from the host to Eu<sup>2+</sup>/Eu<sup>3+</sup> resulting in radiative emission. A more detailed analysis of the transitions of Eu<sup>2+</sup> in CaS can be found in our previous work in Ref. [29]. The film grown in argon showed the greatest PL intensity (for the Eu<sup>2+</sup> emission) at 650 nm followed by that grown in O<sub>2</sub>, and the least intensity was recorded from the film prepared in vacuum. The higher PL intensities from the films deposited in oxygen and argon atmospheres can be ascribed to the film's relatively rougher surfaces as observed from the AFM pictures in Fig. 7.2 and SEM images of Fig. 7.3. The fact

that the films prepared in oxygen were amorphous, and yet showed better intensity than films grown in a vacuum, makes it reasonable to conclude that the roughness played a greater role in the PL intensity than the crystallinity. Rough surfaces can also increase the intensity of the light emission from the surface by limiting the chances of light piping by total internal reflection at the film-substrate interface. It has been reported in the literature [30-33] that light trapping due to internal reflection from smooth surface is reduced as the surface becomes progressively rougher. This is in agreement with the roughness data calculated from the AFM images. The narrow band peak at 618 nm is very small for the films deposited in argon and vacuum and it is relatively large in the film prepared in O<sub>2</sub> atmosphere due to increased conversion of Eu<sup>2+</sup> to Eu<sup>3+</sup> in the presence of O<sub>2</sub>. For further confirmation of the mixed Eu<sup>3+</sup>/Eu<sup>2+</sup> luminescence, the PL emission spectrum of the film deposited in O<sub>2</sub> is deconvoluted into two Gaussian peaks labeled 3 and 4 as shown in Fig 7.6. Peak 3 is the narrow band PL emission (618 nm) due to the  $f \rightarrow f$  transition of Eu<sup>3+</sup> and peak 4 is the broad emission band due to the  $f \rightarrow d$  transitions of Eu<sup>2+</sup>. Fig. 7.7 shows the PL emission spectra of the films excited at the wavelength of 470 nm. Unlike the spectra in Fig 7.5(b), these spectra do not show mixed luminescence. Only the broad emission band with the maximum at 650 nm assigned to the  $4f^65d^1 \rightarrow 4f^7$  transitions of Eu<sup>2+</sup> is displayed. The narrow band emission peak associated with the  $^5D_0 \rightarrow ^7F_2$  transitions of Eu<sup>3+</sup> [34] at 618 nm is suppressed even on the film prepared in O<sub>2</sub> atmosphere. This result indicates that for the excitation at 470 nm, Eu<sup>2+</sup> ions are selectively excited. Consistent with the PL emission data in Fig 7.5 (b), the film prepared in argon atmosphere exhibited the highest PL intensity, followed by that prepared in O<sub>2</sub> atmosphere and the least intensity was observed from the film prepared in vacuum.

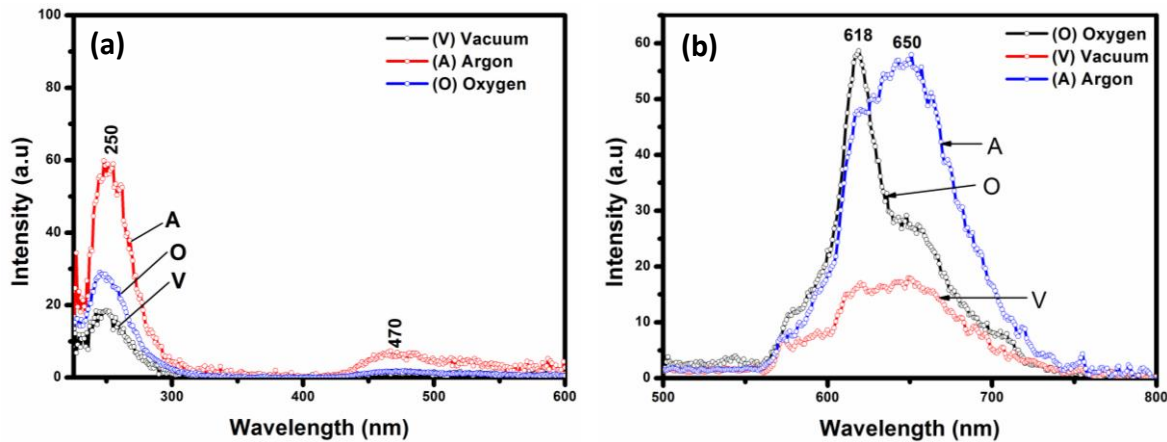


**Figure 7.5:** PL (a) excitation spectra and (b) the emission spectra of the CaS:Eu<sup>2+</sup> thin films deposited in different atmospheres.

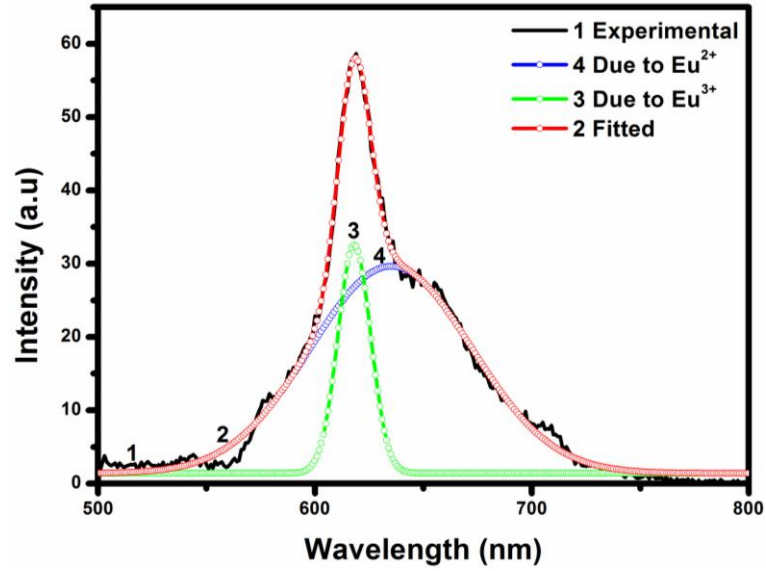


**Figure 7.6:** Deconvoluted PL emission ( $\lambda_{exc} = 250 \text{ nm}$ ) spectrum of the film prepared in  $\text{O}_2$  atmosphere.

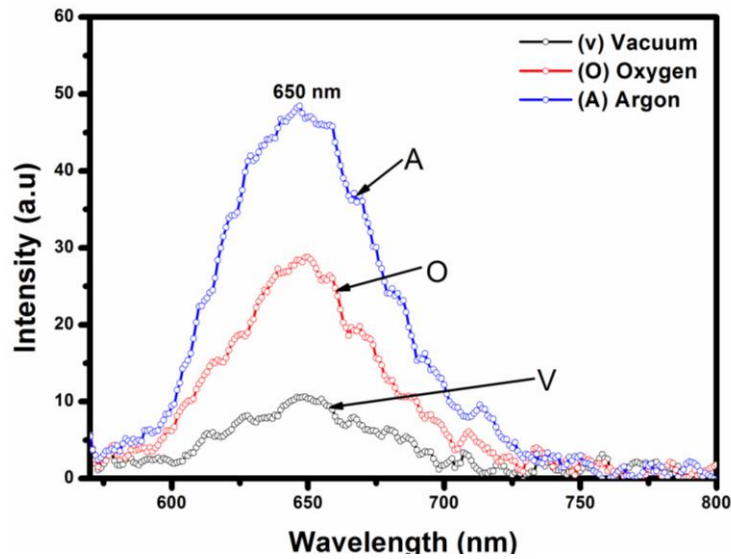


**Figure 7.7:** PL emission spectra ( $\lambda_{exc} = 470 \text{ nm}$ ) for the film deposited in different atmospheres.

#### 7.4.4. TOF-SIMS Analysis

Fig. 7.8 (a), 7.8 (b), and 7.8 (c) show the depth profiles of the thin films deposited in vacuum, argon and oxygen, respectively recorded in the positive polarity mode. As can be seen from

the depth profiles, the ions detected in the positive mode for the film deposited in vacuum are  $\text{Si}^+$ ,  $\text{Ca}^+$ ,  $\text{CaO}^+$ ,  $\text{CaOH}^+$ , and  $\text{CaH}^+$ . Environmental O, moisture, and hydrocarbons probably lead to the formation of  $\text{CaO}^+$ ,  $\text{CaH}^+$ , and  $\text{CaOH}^+$ , respectively. The tail of the  $\text{Si}^+$  profile into the  $\text{Ca}^+$  layer suggests that Si diffuses into that layer. The inverse is also true for  $\text{Ca}^+$ . In a study [35] using a similar set up, the same phenomenon of apparent diffusion was observed, but a different explanation was offered which they referred to as TOF SIMS induced artificial topographic effects. This topographical effect may be the reason why the interface in the film prepared in oxygen atmosphere is narrower. It could be that there was a big particle and an exposed substrate in the vicinity of the point where the etching beam was focused.

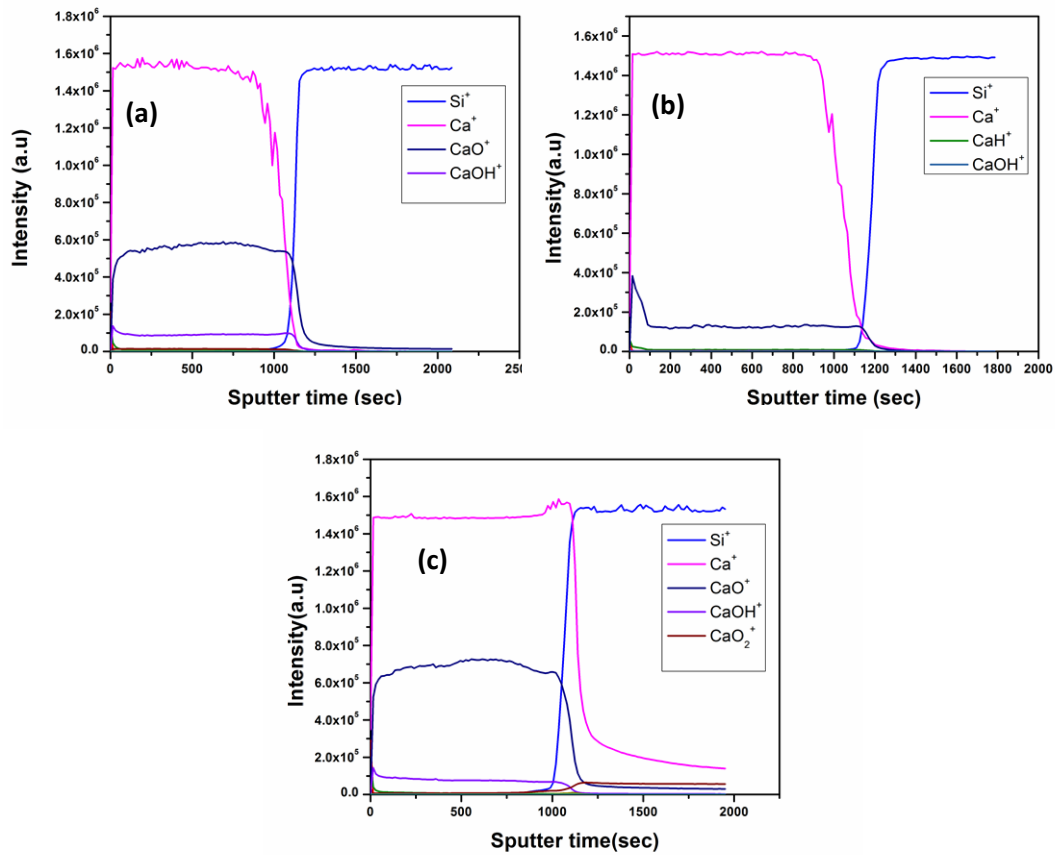


**Figure 7.8:** TOF-SIMS depth profile of a  $\text{CaS:Eu}^{2+}$  PLD thin film (on a Si (100) substrate) in positive spectroscopy mode deposited in a) a vacuum, b) an argon atmosphere, and c) an oxygen atmosphere.

Fig. 7.9 (a-c) is the TOF-SIMS spectra of the films deposited in argon, oxygen and vacuum, respectively showing the atomic and molecular ionic species. The spectra were recorded in the negative polarity mode. The ions detected were  $C^-$ ,  $O^-$ ,  $Si^-$ ,  $S^-$ ,  $SiO^-$ , and  $CaS^-$  located at  $m/z = 12.14, 16.05, 27.98, 31.88, 44.14,$  and  $71.99$ , respectively, as shown in Fig. 7.9 (a-c). The  $C^-$  is probably coming from atmospheric hydrocarbons while  $O^-$  probably comes from the environment and the  $Si^-$  is from the substrate. The high count rate for oxygen observed in Fig. 7.9 (c) is due to the fact that the film was deposited in oxygen-rich atmosphere.

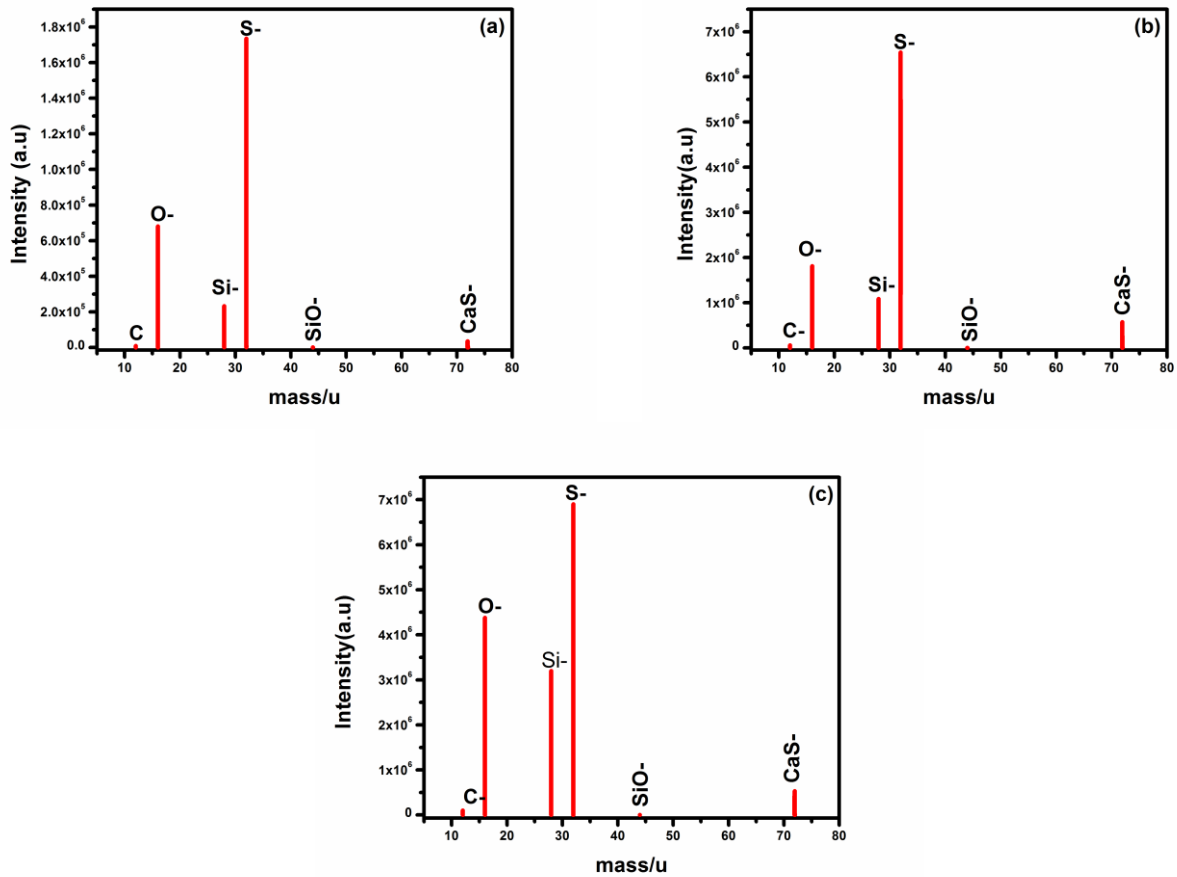


**Figure 7.9:** TOF-SIMS spectra of  $CaS:Eu^{2+}$  PLD thin films obtained in a) argon, b) vacuum, c) oxygen and grown on Si (100) substrates.

## 7.5. Conclusion

The pulsed laser deposition technique was used to grow CaS:Eu<sup>2+</sup> thin films on Si (100) substrates in different atmospheres. The thin films prepared in an oxygen atmosphere were amorphous while those prepared in vacuum and argon atmosphere showed a degree of crystallinity. The emission detected at around 650 nm for all the films was attributed to  $4f^6 5d^1 \rightarrow 4f^7$  transitions of Eu<sup>2+</sup> ion. An emission at around 618 nm was observed, and was attributed to  $^5D_0 \rightarrow ^7F_2$  transitions in Eu<sup>3+</sup>, probably formed by oxidation of Eu<sup>2+</sup>. Results from the TOF SIMs study show that all the films contain oxygen although the film prepared in oxygen contain more oxygen. Thin films grown in an argon atmosphere were rougher than those grown in oxygen and vacuum atmospheres, while the smoothest films were grown in a vacuum atmosphere; consequently the best PL intensity was obtained for films deposited in an argon atmosphere. From these results we conclude that for the atmospheres used for this study, it would be best to prepare the thin films in an argon atmosphere. It is however, necessary to consider optimizing other deposition parameters such as laser pulse deposition rate, fluence and deposition time, in order to get even better PL intensity from the films.

## References

1. K. Onisiwa, Y. Abe, K. Tamura, T. Nakayama, M. Hanazomo, Y. A. Ono, J. Electrochem. Soc. **138** (1991) 599-601.
2. R. S. Crandall, Appl. Phys. Lett. **50** (1987)551-553.
3. H. Kasano, K. Megumi, H. Yamamoto, J. Electrochem. Soc. **131**(1984)1953-1960.
4. T. Suzuki, H. Yamamoto, K. Megumi, O. Kanahisa, Y. Morita, N. Watanabe, Y. Uehara, J. Electrochem. Soc. **134**(1987) 2620-2624.
5. G. I. Marwaha, N. Singh, D. R. Vij, V. K. Mathur, Mater. Res. Bull. **14** (1979)1489-1495.
6. M. A. S. Sweet, J. Rennie, Nucl. Instrum. Meth. A **283** (1989) 330-334.
7. L. H. Robins, J. A. Tuchman, Phys. Rev. B **57** (1998) 12094-12103.
8. D. Jia, X. Wang, Opt. Mater. **30** (2007) 375-379.
9. Y. Hu, W. Zhuang, H. Ye, S. Zhang, Y. Fang, X. Huang. J. Lumin. **111** (2005) 139-145.



10. D. P. Norton, Mater. Sci. Eng. R. **43** (2004) 139-247.
11. S. Christoulakis, M. Suche, N. Katsarikis, E. Koudoumas, Appl. Surf. Sci. **253** (2007) 8169- 8173.
12. H. Sung, Y. Cho, Y. Huh, Y. R. Do, Bull. Korean Chem. Soc. **28** (2007)1280-1284.
13. C. Guo, D. Huang, Q. Su, Mater. Sci. Eng. B **130** (2006) 189-193.
14. M. Nazarov, C. Yuon, J. Solid State Chem. **179** (2006) 2529-2533.
15. S. Dey, S. Y. Yun, Appl. Surf. Sci. **143** (1999) 191-200.
16. R. Vercaemst, D. Poelman, R. L. Van Meirhaeghe, L. Fiermans, W. H. Laflere, F. Cardon, J. Lumin. **63** (1995) 19-30.
17. G. A. Hirata, O. A. Lopez, L. E. Shea, J. Y. Yi, T. Cheeks, J. McKittrick, J. Siqueiros, M. Avalos-Borja, A. Esparza, C. Falcony, J. Vac. Sci. Technol. A **14** (1996) 1694-1696.
18. M. S. Hegde, J. Indian Acad. Sci. **113**(2001) 445 - 458.
19. C. B. Arnold, M. J. Aziz, Appl. Phys. A **69** (1999) S23-S27.
20. T. Haugan , P. N. Barnes, L. Brunke, I. Maartense, J. Murphy, Physica C **397** (2003) 47- 57.
21. L. Fang, M. Shen, J. Cryst. Growth **310** (2008) 3470-3473.
22. M. Suche , S. Christoulakis, , N. Katsarikis, E. Koudoumas, Appl. Surf. Sci. **253** (2007) 8141- 8145.
23. L.V. Zhigilei, B. J. Garrison, Appl. Phys. A **69** (1999) S75- S80.
24. J. Gonzalo, R. Gomez San Roman, J. Perrière. C.N. Afonso, R. Perez Casero, Appl. Phys. A **66** (1998) 487-491.
25. B. R. Chakraborty, D. Haranath, H. Chander, S. Hellway, S. Damach, H.F. Arlinghaus, Nanotechnology **16** (2005) 1006-1015.
26. P. D. Nsimama, O. M. Ntwaeabrwa, H. C. Swart, J. Lumin. **131** (2011) 119-125.
27. J. I. Goldstein, D. Newbury, D. C. Joy, C. E Lyman, P. Echlin, E. Lifshin, L. Sawyer, J. R. Michael, *Scanning electron Microscopy and X-ray Microanalysis*, Kluwer Academic/Plenum Publishers, New York, 2003.
28. H. Choi, C. Kim, C. Pyun, J. Solid State Chem. **138** (1998) 149-153.
29. R. L. Nyenge, H.C. Swart, O. M. Ntwaeaborwa, Opt. Mater. **40** (2015) 68-75.
30. S. L. Jones, D. Kumar, R. K Singh, P. H. Holloway, Appl. Phys. Lett. **71** (3) (1997) 404.
31. S. J. Lee, Jpn. J. Appl. Phys. **37**(1998) 509-516.

32. I. Schnitzer, E. Yablonovitch, Appl. Phys. Lett. **63** (16) (1993) 2174-2176.
33. K. G. Cho, D. Kumar, Z. Chen, P. H. Hollaway, R. K. Singh, in: F.R.Libsch, B.Chalamala, R.Friend, T.Jackson ,H.Ohshima (Eds),Flat Panel Displays and Sensors:Principles, Materials and processes, 1999,MRS Symposium proceeds,Vol. 558, 1999 (spring meeting).
34. S. K. K. Shaat, H.C. Swart, O. M. Ntwaeaborwa, J. Electron Spectros. Relat. Phenom. **197** (2014) 72-79.
35. A. Yousif, R.M. Jafer, J. J. Terblans, O. M. Ntwaeaborwa, M. M. Duvenhage, V.Kumar, H. C. Swart, Appl. Surf. Sci. **313** (2014) 524-531.

## Chapter 8

### **The Influence of the Number of Pulses and Post-deposition Annealing on the Morphology and Photoluminescence Properties of CaS:Eu<sup>2+</sup> Pulsed Laser Deposited Thin Films**

#### **8.1. Introduction**

The bulk europium-doped calcium sulfide (CaS:Eu<sup>2+</sup>) has an intense red emission at around 650 nm and has found applications in cathode ray tubes [1], optical storage devices [2] and light emitting diodes [3]. Due to their high efficiency, compactness, long operational lifetime, low power consumptions, and environmental friendly characteristics [4], light emitting diodes (LED) are increasingly gaining popularity as sources of white light. Red-emitting alkali earth sulfide phosphors, such as CaS:Eu<sup>2+</sup> is a good candidate for three-band phosphor-converted white LEDs since this phosphor has a strong absorption in the blue region [5- 7]. Most of the reported works on CaS:Eu<sup>2+</sup> are on powder samples. However, thin films have several advantages over powders, which include higher lateral resolution from smaller grains, better thermal stability, reduced outgassing, and better adhesion to the solid surface [8]. At present, a variety of deposition techniques such as atomic layer epitaxy (ALE) [9], Pechini sol-gel deposition [10], chemical vapour deposition (CVD) [11], and pulsed laser deposition (PLD) [12] have been used for growing thin films. Among these techniques, the PLD has stood out as one of the most suitable techniques for growing thin films for it has unique advantages such stoichiometric transfer of the target material and excellent surface morphology [13]. The fundamental properties of PLD thin films, depends on several parameters, which include substrate temperature, laser fluence, repetition rate, the deposition atmosphere, and number of pulses. Nsimama et al. [14], in their study of laser ablated SrAl<sub>2</sub>O<sub>4</sub>:Eu<sup>2+</sup>:Dy<sup>3+</sup> reported that the roughness increased with an increase in the number of pulses.

In this study, we investigated the influence of the number of pulses on the structure, particle morphology and photoluminescence (PL) properties of CaS:Eu<sup>2+</sup> thin films grown by the PLD technique. The effect of annealing on PL emission intensity was also investigated. Our results show that the PL intensity is dependent on the roughness of the films and the roughness was shown to increase with the number of pulses. It was necessary to anneal the films in order to improve the emission, indeed the PL intensity increased dramatically for the films annealed at 800°C.

## 8.2. Experimental

CaS:Eu<sup>2+</sup> commercial powder phosphor from Phosphor Technology (UK) was pressed without binders to make a pellet (target) for ablation. The pellet was annealed in air at 250°C for 3 h to harden and remove water vapor and other volatile adsorbed substances. The substrates were placed in a beaker containing ethanol and cleaned using an ultrasonic bath for a period of 15 min. Each piece of substrate was dried using N<sub>2</sub> and stored in plastic packets which were sealed. The deposition chamber of the pulsed laser system was evacuated to a base pressure of  $4.6 \times 10^{-6}$  mbar.

The Spectra Physics Quanta-Ray Pro-270 266 nm Nd: YAG laser was used to ablate the pellet in an Argon atmosphere. The laser energy and repetition rate were set to 45 mJ (a fluence of  $5.73 \text{ Jcm}^{-2}$ ) and 10 Hz, respectively. The substrate temperature was maintained at 200°C, and the target distance was set at 4.5 cm. Ablation of the target was first performed on a dummy substrate for approximately 3 minutes in order to clean off any possible contamination that might otherwise be at the surface of the target. After this process, the dummy was rotated out of the way and the deposition done on the substrate. The films were deposited in an argon atmosphere, with the deposition pressure fixed at 10 mTorr, and the number of pulses as 18000, 12000 and 6000.

The morphology of the films was studied using a Scanning Electron Microscope (SEM), and the atomic force microscopy (AFM). The Shimadzu Superscan SSX-550 system was used to capture the SEM images, employing secondary electrons (SE) as the source of signal. The SEM was set to an accelerating voltage of 5.00 kV, a probe diameter of 1.8 nm, and a working distance (WD) of 12 mm. AFM was done using the Shimadzu SPM- 9600 in contact

mode. X-ray diffraction data was collected using a Bruker AXS D8, with  $\text{CuK}_\alpha$  radiation of wavelength  $1.5406 \text{ \AA}$ , operated at 40 kV and 40 mA. Diffraction patterns were recorded over the range  $15^\circ \leq 2\theta \leq 50^\circ$  with a counting time of 1 s for each step size of  $0.0037^\circ$ .

PL properties of the thin films were measured using a Cary Eclipse (model LS 55) spectrophotometer at room temperature using a mono-chromatized xenon flash lamp as the excitation source. The 18000-pulses films were annealed in an  $\text{H}_2$ /argon atmosphere. The annealing was carried out for a period of 2 hours. The PL emission of the samples was monitored at 470 nm while the excitation was monitored at 650 nm. The PMT voltage was set at 1000 V, while the slit widths were set to 20 nm and 10 nm, respectively for as prepared and annealed films.

### **8.3. Results and Discussion**

#### **8.3.1. XRD Results**

Fig. 8.1 shows the XRD graphs of the as-deposited thin films deposited at different number of pulses. The film deposited using the least number of pulses (6000) is amorphous with a broad peak having a maximum at  $2\theta = 31.6^\circ$ , while the films deposited at 18000- and 12000-pulses were crystalline with diffraction peaks along the (200) and (220) directions.

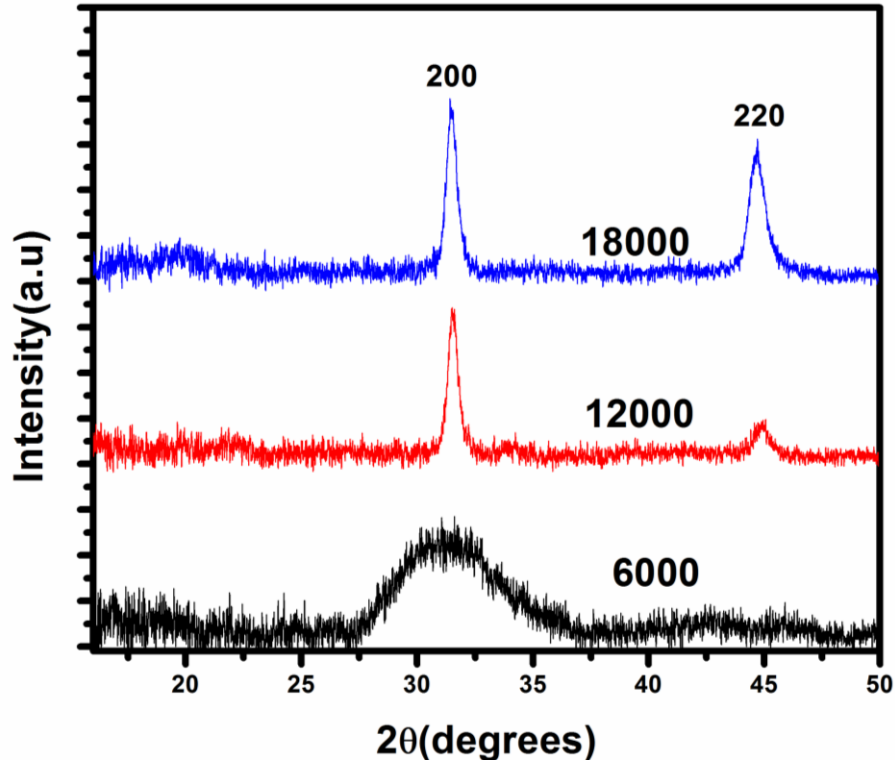


**Figure 8.1:** XRD diffractograms of the CaS:Eu<sup>2+</sup> thin films deposited at 18000, 12000 and 6000 pulses.

The XRD data of Fig.8.1 also shows that the preferred orientation was along the (200) plane. This is probably due to the fact that the (200) plane of CaS has the lowest surface energy [15]. It could also be due to the influence of the Si (100) substrate that is favoured by the high mobility of the ablated species [16]. The fact that the (200) was also prominent in the target material implies that there was a good lattice match. As the number of pulses increased, the (220) plane started to appear, indicating a decreasing substrate influence following an increase in the film thickness. The broadening of the (200) peak at (Fig.8.1), was used for the estimation of the crystallite size ( $D$ ), using Scherer's formula [17, 18]:

$$D = \frac{k\lambda}{\beta \cos\theta} \quad (8.1)$$

where  $\beta$  is the FWHM of the peak in radians, and  $k$  is a factor which is usually set as 0.89, and  $\lambda$  is the X-ray radiation wavelength (0.154056 nm for this study) and  $\theta$  is the peak

position, also known as Bragg angle. The estimated sizes (excluding for 6000 pulses) are shown in Table 8.1.

**Table 8.1:** Variation of crystal size with number of pulses

<b>Number of pulses</b>	<b>FWHM(<math>^{\circ}</math>)</b>	<b>D(nm)</b>
<b>12000</b>	0.55	14.94
<b>18000</b>	0.51	15.88

As seen from Fig.8.2, new peaks developed at around  $2\theta = 32^{\circ}$  upon annealing at temperatures  $400^{\circ}\text{C}$  and  $600^{\circ}\text{C}$ . Other smaller peaks observed at around  $2\theta = 46.80$  and  $47.60$ . These extra peaks are attributed to the substrate. The peak at  $2\theta = 32^{\circ}$  become very small for annealing temperature  $800^{\circ}\text{C}$ , suggesting less contribution from the substrate. The most likely reason for this is that the substrate is completely covered by the film for this sample. From the XRD spectra (Fig.8.2), it is also observed that the peaks became narrower, suggesting that there was an improvement in crystallinity with an increase in annealing temperature. Using peak (200) the estimated crystallite sizes as calculated using Eq.8.1 are shown in Table 8.2.

**Table 8.2:** Change of crystallite size with annealing temperature.

<b>Annealing temp (<math>^{\circ}\text{C}</math>)</b>	<b>FWHM(<math>^{\circ}</math>)</b>	<b>D(nm)</b>
<b>400</b>	0.33	24.72
<b>600</b>	0.31	25.92
<b>800</b>	0.24	34.55

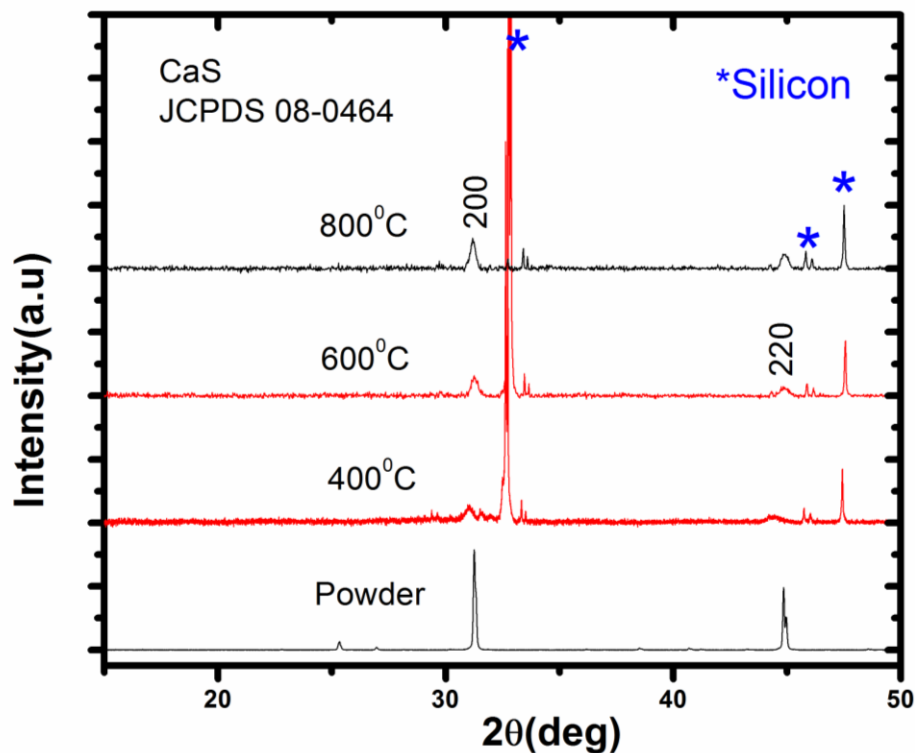


**Figure 8.2:** XRD spectra for annealed CaS:Eu<sup>2+</sup> thin films.

### 8.3.2. AFM and SEM Results

#### 8.3.2.1. AFM Results

Fig.8.3 shows the AFM images of 500 x 500 nm<sup>2</sup> for the films deposited at a) 18000, b) 12000, and c) 6000 pulses. The surface root mean square (rms) roughness is 6.5 nm, 2.7 nm and 1.9 nm for 18000, 12000, and 6000 pulses, respectively. The sample deposited at 18000 pulses (Fig. 8.3(a)) gave large spherical particles, while the sample deposited at 6000 showed relatively smaller particles. Similar observations were reported in Ref. [19]. The variation of surface roughness with number of pulses for the films is shown in Fig. 8.3 (d). From this figure, we concluded that the surface roughness increased when depositing at a higher number of pulses (a thicker layer is expected with an increase in the number of pulses). These results are in agreement with the results reported in Ref. [14].



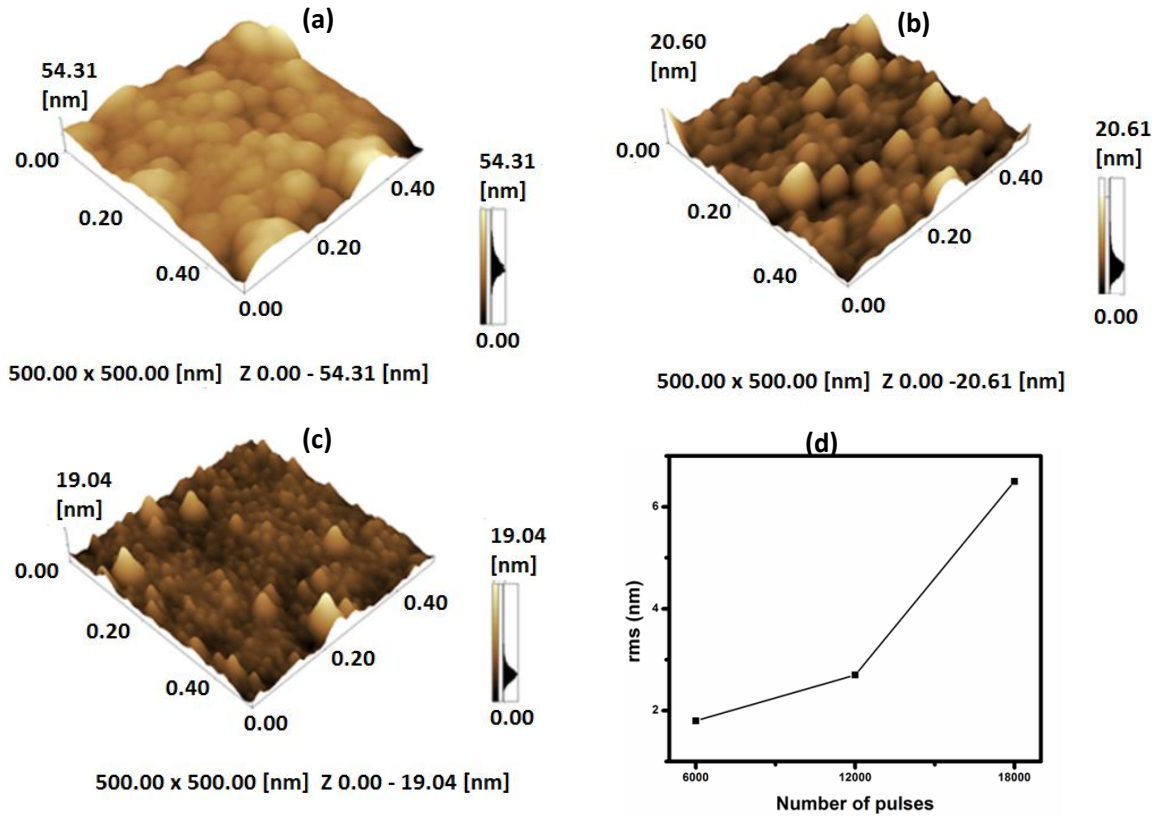


**Figure 8.3:** AFM images of PLD CaS:Eu<sup>2+</sup> thin films deposited at a) 18000, b) 12000, c) 6000 pulses, and (d) the variation of CaS:Eu<sup>2+</sup> thin films rms roughness with number of pulses.

Fig.8.4 shows the AFM pictures of the films annealed at 400°C, 600°C, and 800°C. The RMS roughness values were 18.55 nm, 19.55 nm, and 22.84 nm, for films annealed at 400°C, 600°C, and 800°C, respectively, clearly showing an increase of roughness with an increase of annealing temperature. This is most likely due to an increase in particle size for higher temperatures increase the mobility of particles which in turn encourages nucleation into bigger particles.

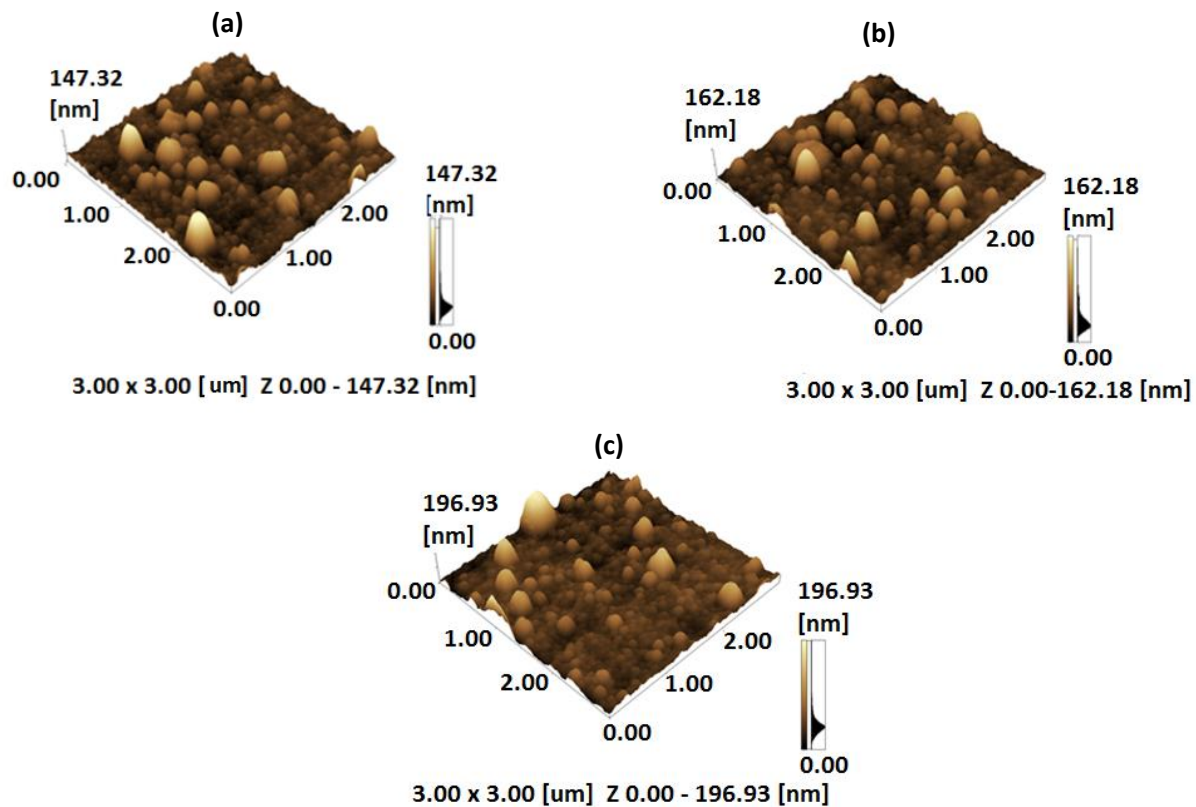


**Figure 8.4:** AFM pictures for thin films annealed at, (a) 400°C, (b) 600°C, and 800°C in H<sub>2</sub>/Ar atmosphere.

### 8.3.2.2. SEM Results

Fig.8.5 shows the SEM images of the surface morphology for films deposited at a) 18000, b) 12000, and 6000 pulses.

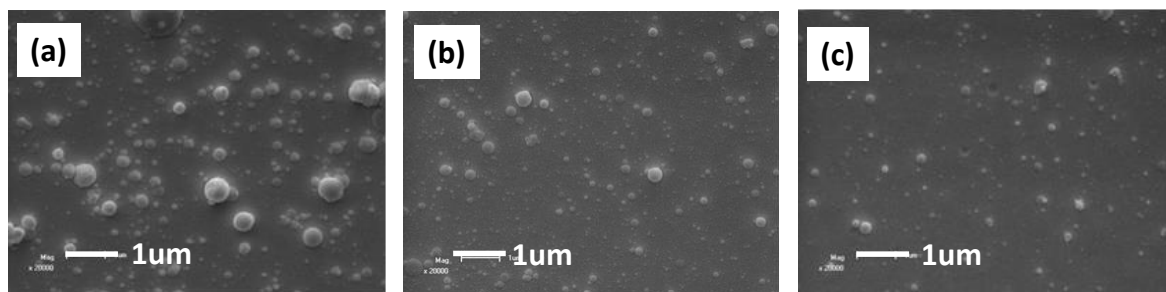


**Figure 8.5:** The SEM images of CaS:Eu<sup>2+</sup> films deposited at (a) 18000, (b) 12000, and (c) 6000 pulses.

The surfaces for all the films are covered by spherically-shaped particles which were not uniformly distributed, and varying in sizes. Clearly, the 18000 pulses film was very rough while the one formed at 6000 pulses was the smoothest. This is due to the higher number of particulates at a larger number of pulses and fewer particles growing at a smaller number of pulses.

Fig.8.6 shows the SEM (at magnification of 16000) photographs of the films annealed at 400°C, 600°C, and 800°C. It can be seen that there was an increase in the size and density of the particulates.

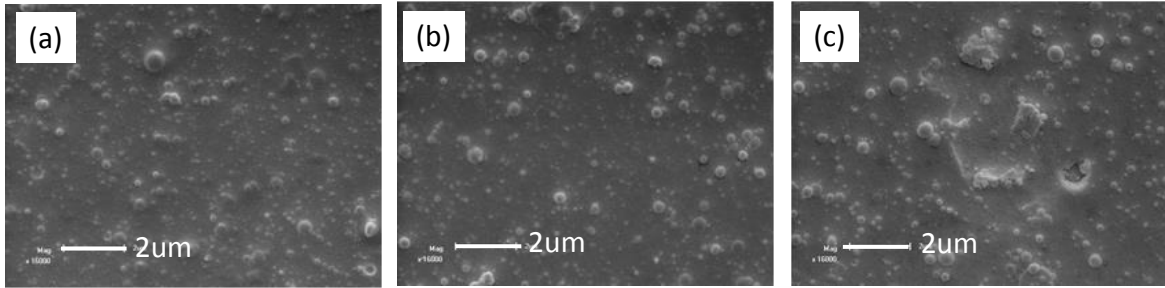
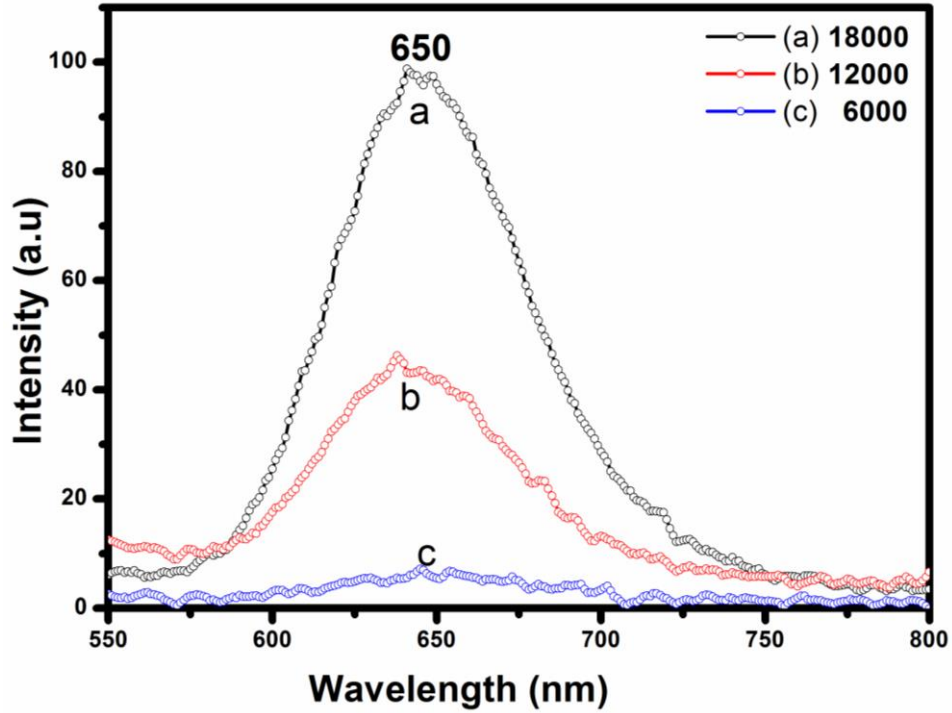


**Figure 8.6:** SEM images for thin films annealed at, (a) 400°C, (b) 600°C, and (c) 800°C.

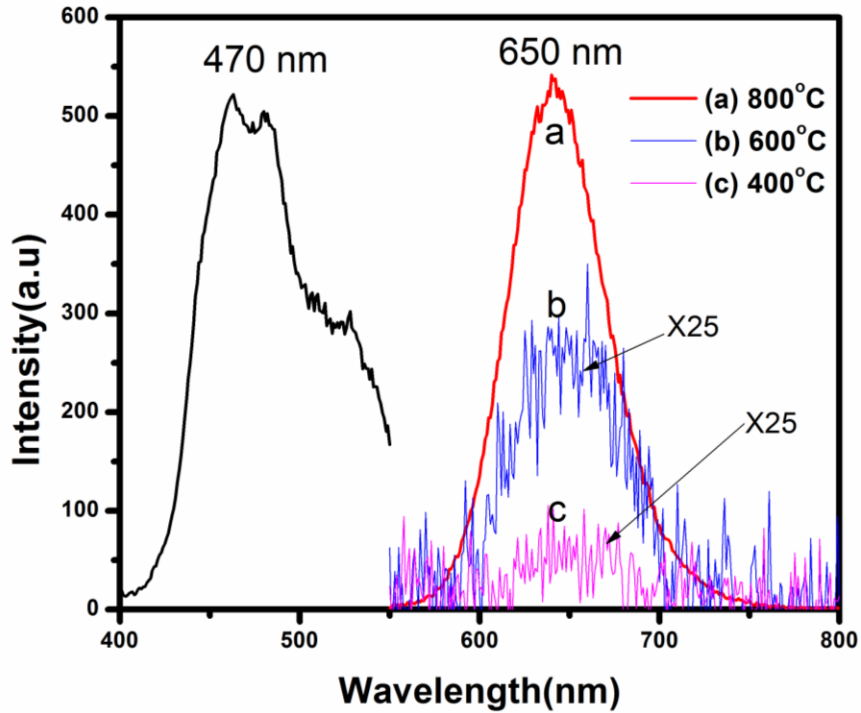
#### 8.4. Photoluminescence Results

Fig.8.7 shows the PL emission spectra of the CaS:Eu<sup>2+</sup> thin films deposited at 18000, 12000, and 6000 pulses in an argon atmosphere. All the samples were excited at 470 nm. The emission peak observed at 650 nm is attributed to  $4f^65d^1 \rightarrow 4f^7$  transitions of Eu<sup>2+</sup> [20]. The highest intensity from Eu<sup>2+</sup> was observed from the thin film deposited at 18000 pulses, and the least intensity was from the film deposited at 6000 pulses. The improvement in PL intensity is probably brought about by reduced internal reflections caused by rougher (and hence thicker) surfaces of the films. The increase in particulate size, as observed from SEM photographs and Table 8.1, and hence an increase in roughness also contributed to increase in PL intensity at higher number of pulses. Thus, the PL intensity strongly depends on the morphology and rms roughness of the films.

Fig. 8.8 shows the excitation (only for the 800°C-film) and emission spectra of the 18000-pulses samples annealed at 400°C, 600°C, and 800°C in a H<sub>2</sub>/Ar. The emission for films annealed at 400°C and 600°C was too weak and had to be magnified by 25. The PL intensity of the film increased tremendously after annealing at 800°C. This increase in PL intensity is attributed to improvement in crystallinity of the films upon annealing as observed in the XRD results in Fig.8.2.



**Figure 8.7:** Emission spectra for PLD CaS:Eu<sup>2+</sup> thin films at different number of pulses.



**Figure 8.8:** PL results for the 18000-pulses CaS:Eu<sup>2+</sup> thin films annealed at 400°C, 600°C, and 800°C in a H<sub>2</sub>/Ar atmosphere.

### 8.5. Conclusion

We demonstrated that the pulsed laser deposition technique is suitable for the growth of europium-doped calcium sulfide thin films on Si (100) substrates. From the AFM and SEM results, we established that samples deposited at a higher number of pulses were rougher than those deposited at lower pulses. The XRD results showed that the as-prepared films have poor crystallinity, with the (200) peak being a preferred orientation for all the samples. The PL emission at 650 nm is attributed to the  $4f^65d^1 \rightarrow 4f^7$  of Eu<sup>2+</sup> ions. PL intensity increased with increase in the number of pulses, and post-deposition annealing greatly improved the intensity. The best emission intensity was obtained from the film annealed at 800°C. The improved PL intensity from the film prepared using the highest number of pulses (18000) is attributed to the increased surface roughness and layer thickness, while that recorded upon annealing is attributed to improved crystallinity.

## References

1. H. Kasano, K. Megumi, H. Yamamoto, J. Electrochem. Soc. **131**(1984)1953-1960.
2. L. H. Robins, J. A. Tuchman, Phys. Rev. B **57** (1998) 12094-12003.
3. H. Sung, Y. Cho, Y. Huh, Y. R. Do, Bull. Korean Chem. Soc. **28** (2007)1280-1284.
4. [www.nobelprize.org/nobel\\_prizes/physics/laureates/2014/advanced-physicsprize2014.pdf](http://www.nobelprize.org/nobel_prizes/physics/laureates/2014/advanced-physicsprize2014.pdf), accessed on 7/10/2014
5. D. Jia, X. Wang, Opt.Mater. **30** (2007) 375-379.
6. C. Guo, D. Huang, Q. Su, Mater. Sci. Eng. B **130** (2006) 189-193.
7. Y. Hu, W. Zhuang, H. Ye, S. Zhang, Y. Fang, X. Huang, J. Lumin. **111** (2005) 139-145.
8. J. S. Base, K. S. Shim, S. B. Kim, J. H. Jeong, S. S. Yi, J. C. Park, J. Cryst. Growth **264** (2004) 290-296.
9. J. Ihanus, M. Ritala, M. Leskela, T. Prohaska, R. Resch, G. Friedbacher, M. Grasserbauer Appl. Surf. Sci. **120** (1997) 43-50.
10. Y. Wu, R. Fan, P. Yang, Nano letters **2** (2002) 83-86.
11. P.Y. Jia, J. Lin, X.M. Han, M. Yu, Thin Solid Films **483** (2005) 122-129.
12. D. P. Norton, Mat. Sc. and Eng. R **43** (2004) 139-247.
13. A. Mesaros-Hristen, O. Alm, E. Jeane, P. Boman, Thin Solid Films **516** (2004) 304.
14. P. D. Nsimama, O. M. Ntwaeaborwa, E. Coetsee, H. C. Swart, Physica B **404** (2009) 4489–4492.
15. H. Yoshiyama, S. Tanaka, Y. Mikami, S. Ohshio, J. Nishiura, H. Kawakami, H. Kobayashi, J. Cryst. Growth **86** (1988) 56-60.
16. K.T. Hillie, C. Curren, H. C. Swart, Appl. Surf. Sc. **177** (2001) 73-77.
17. B. D. Cullity, *Elements of X-ray Diffraction*, second ed., Addison-Wesley, Reading, MA, 1956, p. 99.
18. P. H. Klug, L.E. Alexandar, *X-ray Diffraction Procedures for Polycrystalline and Amorphous Materials*, Wiley, New York, 1974.
19. S. Christoulakis, M. Suche, N. Katsarakis, E. Koudoumas, Appl. Surf. Sci. **253** (2007) 8169- 8173.
20. R. L. Nyenge, H.C. Swart, O. M. Ntwaeaborwa, Opt. Mater. **40** (2015) 68-75.

## Chapter 9

### **Influence of Substrate Temperature and Deposition Pressure on the Pulsed Laser Deposited Thin Films of CaS:Eu<sup>2+</sup> Phosphors**

#### **9.1. Introduction**

There is a growing interest in rare-earth-doped alkaline earth sulfides such as CaS:Eu<sup>2+</sup> (red-emitting) and CaS:Ce<sup>3+</sup> (green-emitting) as candidates for down conversion of blue light for phosphor-converted white LEDs (pc-WLEDs). This is so because both of these phosphors strongly absorb the blue light emitted by a blue LED [1] to emit red and green, respectively. Europium doped calcium sulfide has been studied by a substantial number of workers for its application in cathode ray tubes [2, 3] and pc LEDs [1, 4, 5]. The development of a WLED as a source of light is important because LEDs have a high durability and low energy consumption when compared to other light sources, such as incandescent and fluorescent lamps. Thus, the LED as a source of light promises to overtake, if not displace and make obsolete our current sources of light energy. As opposed to the traditional powder phosphors, thin films offer the benefits of a reduction of material wastage, and better adhesion to solid substrates [6, 7]. A variety of thin film growth techniques have been developed, including, spray pyrolysis, sputtering, metal organic chemical vapor deposition (MOCVD), pulsed laser deposition (PLD) [18], and Dey et al. [19] has grown CaS thin films using the atomic layer deposition (ALD) technique. Among these methods, PLD has emerged as one of the most popular techniques, offering a number of advantages over other techniques, which include, but not limited to, congruent transfer of target materials, versatility, flexibility, and relatively low substrate temperature [8]. Nsimama and co-workers [9] showed that the structure and other properties of SrAl<sub>2</sub>O<sub>4</sub>:Eu<sup>2+</sup>, Dy<sup>3+</sup> thin films during a PLD process are affected by such parameters as number of laser pulses, while [11] showed that wavelength of the laser radiation is important for the growth of CaS:Eu<sup>2+</sup>. Substrate temperature and deposition

pressure, which have a strong bearing on the kinetics of particles on the surface of the growing film and thus have an influence on the quality of the thin film.

In this study, we report the growth, and characterization of CaS:Eu<sup>2+</sup> thin films deposited on Si (111) substrates in an argon atmosphere for deposition pressure in the range 40-350 mTorr, and the substrate temperature varying from 200°C to 650°C. The subsequent influence of substrate temperature and deposition pressure on the growth rate is evaluated. Photoluminescence properties were investigated and evaluated for possible applications in pc-white LED technologies.

## 9.2. Experimental

CaS:Eu<sup>2+</sup>, a commercial powder, obtained from Phosphor Technology (UK) was used in this study. To make the target for ablation, the powder was cold-pressed without binders using a custom made target holder [10]. The target was annealed in air at 250 °C for a 3-hour period to harden and remove adventitious water-containing species and other volatile adsorbed substances. Thin films of CaS:Eu<sup>2+</sup> were grown on Si (111) substrates using the Spectra Physics Quanta-Ray Pro-270 Nd: YAG laser operated in the 266 nm wavelength mode. Subsequently, the substrates were prepared and cleaned using the procedure outlined elsewhere [11] in greater detail. The deposition chamber had been evacuated to base pressure of  $5.7 \times 10^{-5}$  mbar before backfilling with the Ar gas at a pressure of  $5.33 \times 10^{-2}$  mbar (40 mTorr). The laser energy, number of pulses and pulse repetition rate were fixed at 40 mJ (a fluence of  $5.09 \text{ J/cm}^2$ ), 18000 and 10 Hz, respectively. The substrate temperature was in the range 200°C- 650°C, argon gas deposition pressure was varied from 40 mTorr to 350 mTorr, while the target was kept at 4.5 cm from the non-rotating substrate holder.

## 9.3. Characterization

The crystalline nature and phase composition of the thin films was investigated using a Bruker AXS D8 ADVANCE X-ray diffractometer (XRD), operated at 40 kV and 40 mA, with a CuK<sub>α</sub> radiation of wavelength 1.5406 Å. Diffraction patterns were recorded in the  $2\theta$



range of 15° to 50°, with a counting time of 1 s for each step size of 0.0037°. The Shimadzu SPM-9600 atomic force microscopy (AFM) operated in the contact mode was used to observe the surface morphology and roughness of the thin films. Photoluminescent (PL) spectra measurements of the thin films were carried out using a Varian Carry eclipse (model LS 55) spectrophotometer at room temperature with a monochromatized 150 W xenon flash lamp as the source of excitation. The PMT voltage was set to 600 V, while the emission and excitation slit widths were both 10 nm.

## 9.4. Results and Discussion

### 9.4.1. XRD Results

Fig.9.1 (i) shows the XRD patterns of the films deposited on Si (111) at substrate temperature ranging from 200°C to 650°C. The peaks marked S are from the substrate, while those marked with an asterisk\* are suspected to come from CaSO<sub>4</sub>, as we showed in an earlier study [12]. For all deposition temperatures, the films exhibited a (200) texture, while the (111) texture increased as the substrate temperature was increased from 200°C to 400°C, then gradually decreased as the substrate temperature rose to 550°C, and eventually disappeared at substrate temperature of 650°C. Also, as the (200) preferred orientation became more pronounced, the (220) orientation became more diminished. From these observations, it implies that as the substrate temperature increased, and crystallinity improved, the preferred orientation of the films became (200). The (200) peak (Fig.9.1 (i)), was used for the estimation of the crystallite size (D), using Scherer's formula [13, 14]:

$$D = \frac{k\lambda}{\beta \cos\theta} \quad (9.1)$$

where  $\beta$  is the FWHM of the peak in radians, and  $k$  is a factor which is usually set as 0.89, and  $\lambda$  is the X-ray radiation wavelength (0.154056 nm) and  $\theta$  is Bragg's angle. The estimated sizes are shown in Table 9.1.

**Table 9.1** Variation of crystallite size with substrate temperature

Sub Temp	2 $\theta$ ( $^{\circ}$ )	FWHM( $^{\circ}$ )	D(nm)
200	31.321	0.3149	25.92
400	31.382	0.2519	32.41
550	31.394	0.2204	37.04
650	31.373	0.2047	39.88

As can be seen from Table 9.1, and Fig. 9.1(ii), the full width at half maximum (FWHM) of the (200) peak decreased as the substrate temperature was increased, resulting to a corresponding increase of the crystallite size.

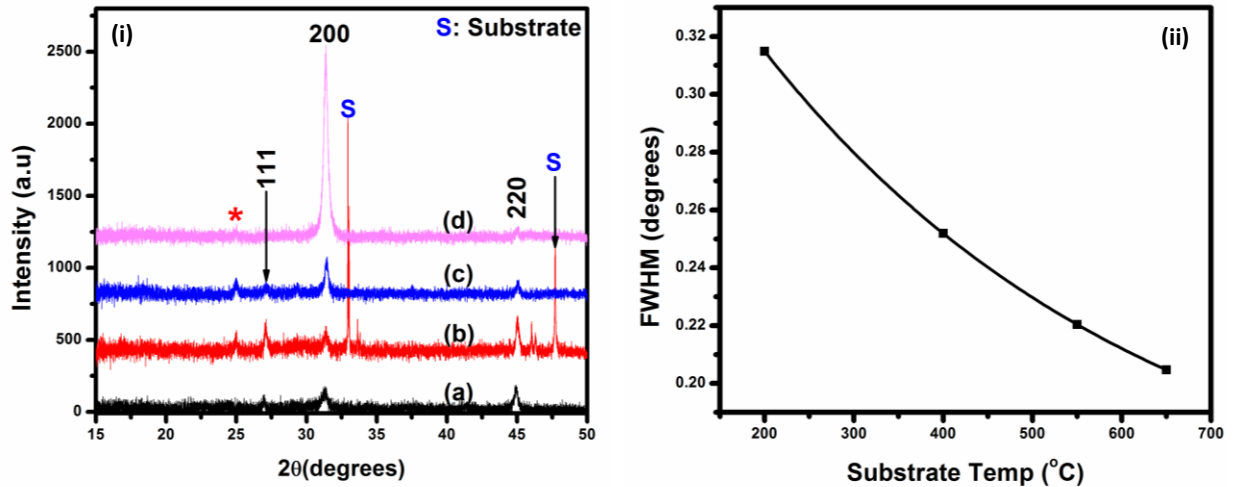


**Figure 9.1:** (i) X-ray diffraction patterns for CaS:Eu<sup>2+</sup> films deposited at various temperatures: (a) 200°C, (b) 400°C, (c) 550°C, (d) 650°C. (ii) Variation of FWHM of (200) peak with substrate temperature.

The X-ray diffraction patterns of the films deposited on Si (111) at deposition pressure ranging from 40 mTorr to 350 mTorr are shown in Fig. 9.2. Preferential growth of films on the (111) plane is more pronounced than on the (220) plane. The (200) plane is clearly visible

for films deposited at pressures of 80 and 160 mTorr. The reason for this is most likely differences in surface energies of these planes [15]. The fact the preferred plane is affected by pressure suggests existence of compressive stress in the film plane.

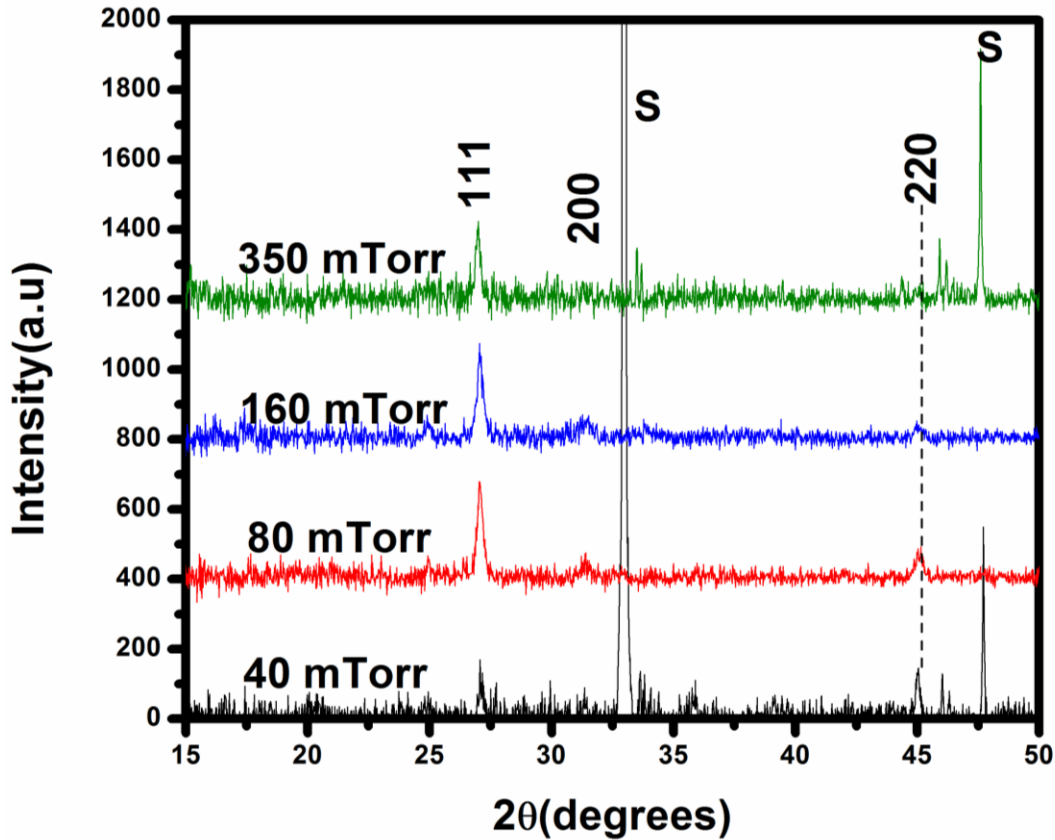


**Figure 9.2:** XRD patterns for films deposited at different argon pressures. S is due to the substrate.

#### 9.4.2. AFM Results

Fig.9.3 presents 3-dimensional AFM images for films deposited on the silicon substrate for different substrate temperatures. The images show well defined spherically shaped grains that are uniformly distributed over the surface with root mean square (RMS) roughness of 12 nm, 21 nm, 22 nm, and 24 nm, for films deposited at substrate temperatures of 200°C, 400°C,

550°C, and 650°C, respectively. The increased roughness with temperature rise is attributed to a higher rate of particle growth at higher temperatures [16].

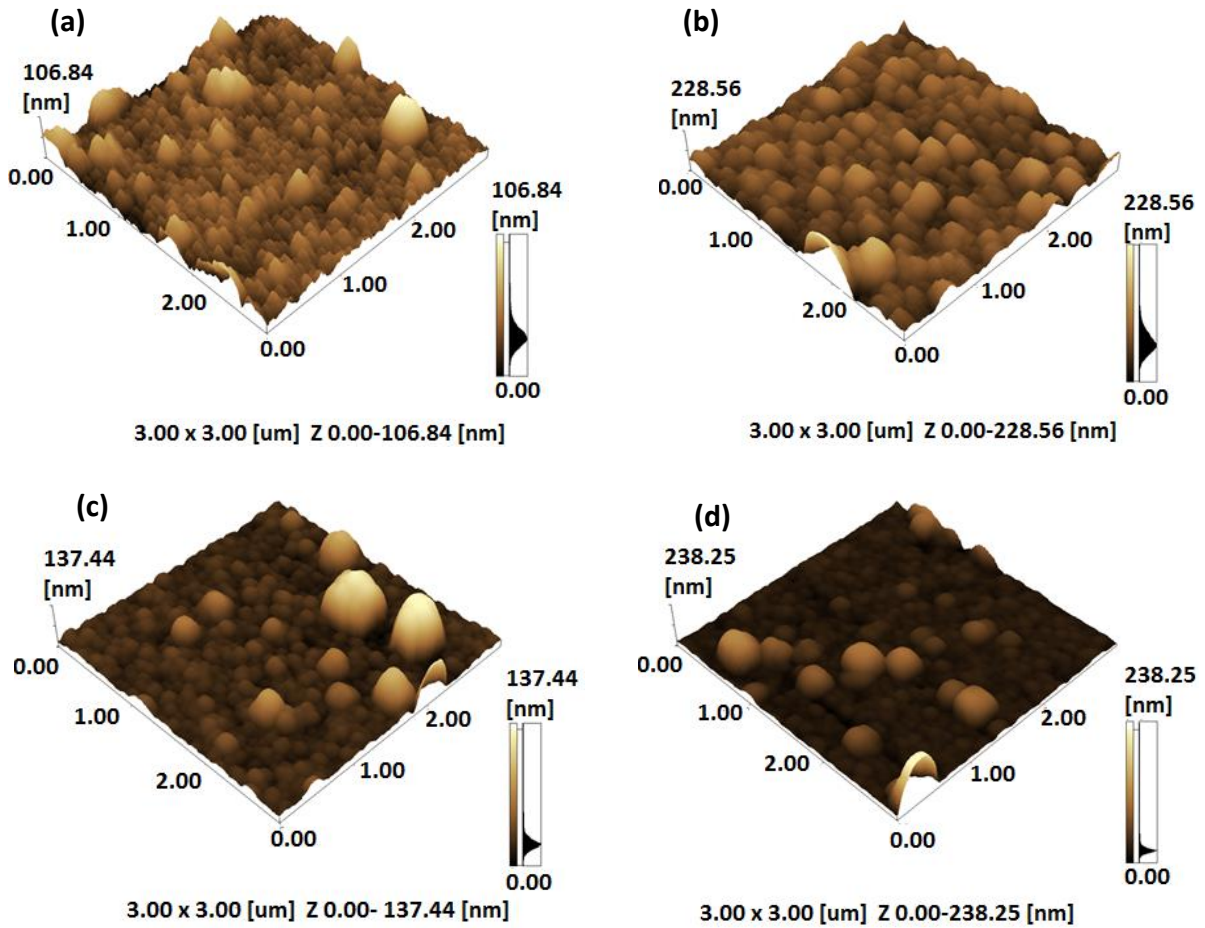


**Figure 9.3:** AFM images for CaS:Eu<sup>2+</sup> for substrate temperatures of (a) 200°C, (b) 400°C, (c) 550°C, and (d) 650°C.

Fig. 9.4 shows AFM images with root mean square (RMS) roughness of 21 nm, 26 nm, 12 nm, and 10 nm, for deposition pressures of 40 mTorr, 80 mTorr, 160 mTorr and 350 mTorr, respectively. As the argon pressure increased from 40 mTorr to 80 mTorr, the surface roughness increased from 21 to 26 nm, and then decreased to 10 nm, as the pressure was increased to 350 mTorr. The change in growth rate as the pressure increases explains why the

surface roughness initially increases as the pressure is increased and then starts to decrease with further increase of deposition pressure (see subsection 9.4.3).

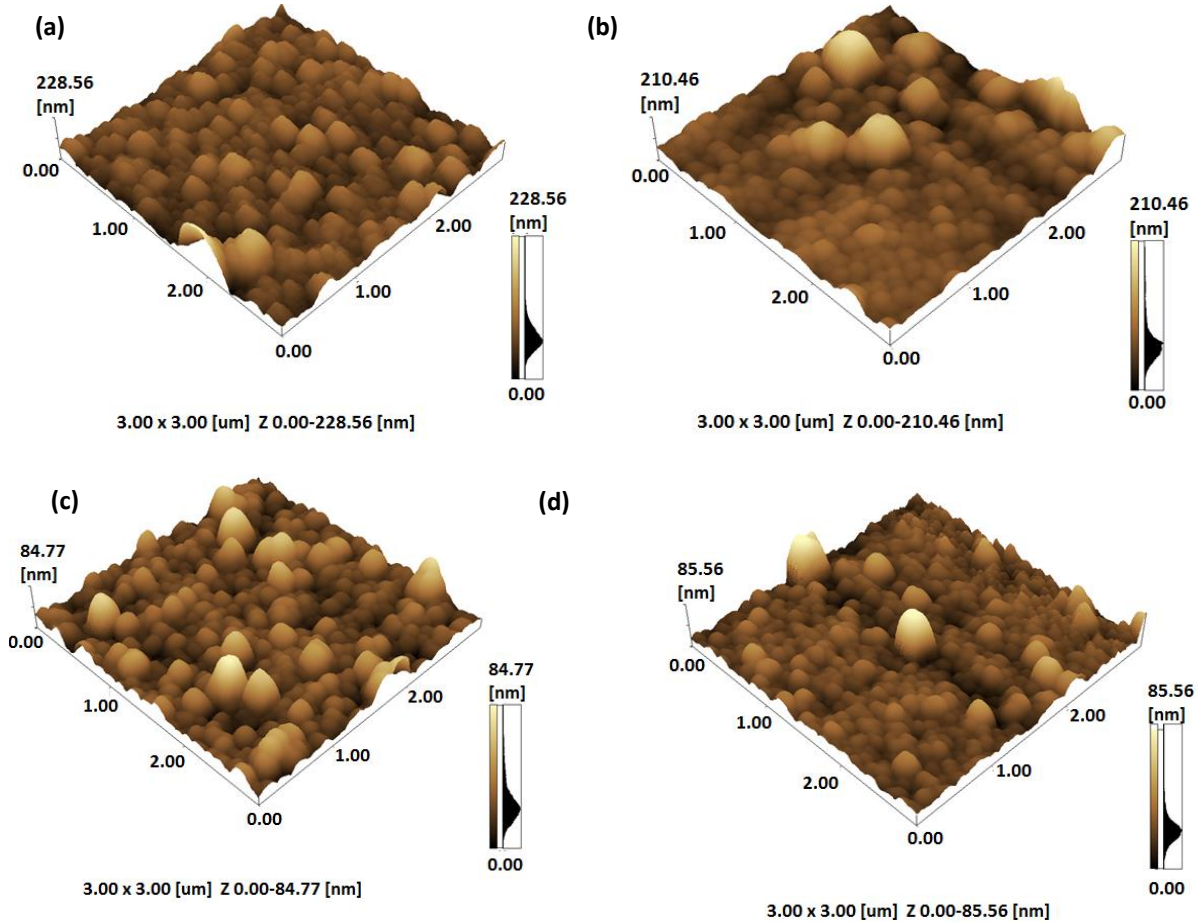


**Fig. 9.4:** AFM images of CaS:Eu<sup>2+</sup> thin films deposited in argon pressure of (a) 40 mTorr, (b) 80 mTorr, (c) 160 mTorr, (d) 350 mTorr.

### 9.4.3. Photoluminescence Results

Samples were excited at 470 nm and the respective emissions observed in the wavelength ranges 500 to 800 nm at room temperature. The effects of substrate temperature on the photoluminescence excitation (PLE) and PL intensity of the thin films are shown in Fig. 9.5. As can be seen from Fig. 9.5 (b), increasing the substrate temperature increased the intensity of the emission spectrum. The PL was very weak for films grown at 200°C, while the PL intensity was much higher for films grown at a substrate temperature of 650°C. The increase

in the PL emission intensity can be attributed to both grain growth (minimizing grain-boundary area) and a reduction of disorder around the  $\text{Eu}^{2+}$  in the lattice [17]. Grain boundaries have been reported [18] as non-luminescent or luminescent-quenching regions. Jones et al. [19] attributed the increase in PL intensity with temperature to increased optical scattering induced by rough surfaces. The grain growth is consistent with the observation that the roughness of the films increase with increase in substrate temperature (see section 9.4.2).

The broad emission peak observed at around 650 nm is attributed to the dipole-allowed transitions from the excited  $4f^6[{}^7F_0]5d^1(t_{2g})$  state to the ground state  $4f^7({}^8S_{7/2})$  of the  $\text{Eu}^{2+}$  ions, while the source of the excitation bands is as previously reported [12].

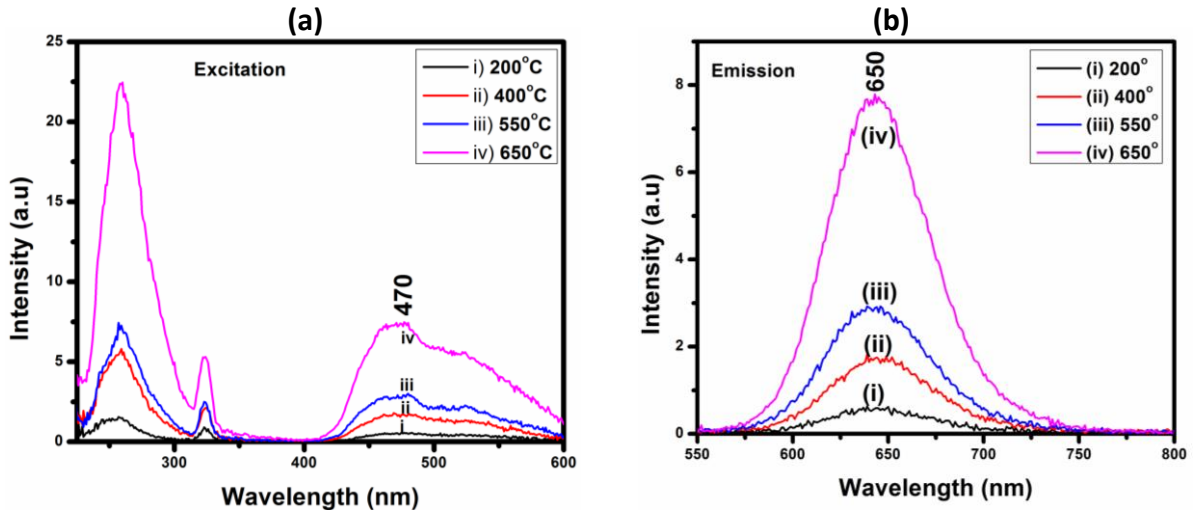


**Figure 9.5:** (a) The excitation and (b) emission spectra for  $\text{CaS:Eu}^{2+}$  PLD thin films at various substrate temperatures; (i)  $200^\circ\text{C}$ , (ii)  $400^\circ\text{C}$ , (iii)  $550^\circ\text{C}$ , (iv)  $650^\circ\text{C}$ .

The variation of the PL intensity with argon deposition pressure is presented in Fig. 9.6. The PL intensity increased as the pressure was increased from 40 mTorr to 80 mTorr, and then a sharp decrease of PL intensity upon increasing the pressure further. The initial increase in PL intensity with increase of pressure from 40 mTorr to 80 mTorr can be explained if we take into account the behavior of ablated particles in a PLD process. The collision between ions in the plasma and the molecules of the background gas reduces the kinetic energy of the ions, and thus the plasma plume is less damaging to the already formed film, this encourages an

increase in the growth rate [21], hence the increase in PL intensity. However, if the gas pressure is too high, the velocities of various species in the laser-generated plume will further be slowed down due to the collisions with the gas molecules, and thus the surface activation of the species will be hampered [22], giving rise to a lower growth rate, and hence the observed reduction in PL intensity for argon pressure greater than 80 mTorr. In [19] it was reported that an increase of deposition pressure for  $Y_2O_3:Eu$  thin films led to an increase in PL intensity, however, unlike us; only two different pressures were considered.

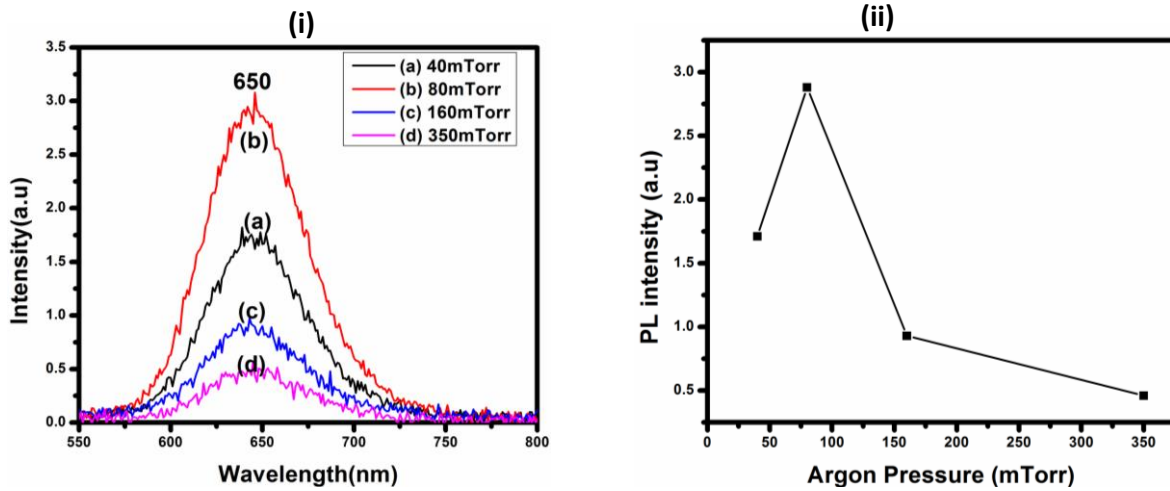


**Figure 9.6:** Variation of (i) PL intensity and (ii) PL peak with chamber deposition pressure.

## 9.5. Conclusion

Thin films of europium (II)-doped calcium sulfide were PLD deposited onto silicon (111) substrates held at temperatures range 200°C-650°C, and argon background pressure in the range 40 mT-350 mTorr. As the substrate temperature was increased from 200°C to 650°C PL intensity improved, indeed there was a sharp increase in PL intensity at substrate temperature of 650°C. As is indicated by XRD FWHM of the (200) peak, higher substrate temperatures resulted in better crystallinity. The PL intensity increased with deposition pressure up to 80 mTorr, while it decreased for pressures above this, thus, the optimal deposition pressure is 80 mTorr.

## References

1. D. Jia, X. Wang, *Opt. Mater.* **30** (2007) 375-397.
2. H. Kasano, K. Megumi, H. Yamamoto, *J. Electrochem. Soc.* **131** (1984) 1953-1960.
3. H. Yamamoto, K. Megumi, H. Kasano, *J. Electrochem. Soc.* **134** (1987) 2620-2624.
4. C. Guo, D. Huang, Q. Su, *Mater. Sci. Eng. B* **130** (2006) 189-193.
5. Mihail Nazarov, Chulsoo Yoon J. *Solid State Chem.* **179** (2006) 2529–2533.
6. D. P. Norton, *Mater. Sci. Eng. R.* **43** (2004) 139-247.
7. S. Christoulakis, M. Suche, N. Katsarikis, E. Koudoumas, *Appl. Surf. Sci.* **253** (2007) 8169- 8173.
8. L. Fang, M. Shen, *J. Cryst. Growth* **310** (2008) 3470– 3473.
9. P.D. Nsimama, O.M. Ntwaeaborwa, E. Coetsee, H.C. Swart, *Physica B* **404** (2009) 4489–4492.
10. A. Yousif, H. C. Swart, O. M. Ntwaeaborwa, E. Coetsee, *Appl. Surf. Sci.* **270** (2013) 331-339.
11. R.L. Nyenge, P.T. Sechogela, H.C. Swart, O.M. Ntwaeaborwa, *J. Mod. Opt.* **62** (2015) 1102-1109, DOI:10.1080/09500340.2015.1020898.
12. R. L. Nyenge, H. C. Swart, O.M. Ntwaeaborwa, *Opt. Mater.* **40** (2015) 68–75.
13. B. D. Cullity, *Elements of X-ray Diffraction*, second ed., Addison-Wesley, Reading, MA, 1956, p. 99.
14. P. H. Klug, L.E. Alexandar, *X-ray Diffraction Procedures for Polycrystalline and Amorphous Materials*, Wiley, New York, 1974.
15. J. G. Che, C. T. Chan, W-E. Jian, T. C. Leung, *Phys. Rev. B*, **57**(1998)1875-1880.
16. O. M. Ntwaeaborwa, P. D. Nsimama, J.T. Abiade, E. Coetsee, H. C. Swart, *Physica B* **404** (2009) 4436–4439.
17. J. McKittrick, C. F. Bacalski, G. A. Hirata, K. M. Hubbard, S. G. Pattillo, K. V. Salazar, M. Trkula, *J. Am. Ceram. Soc.*, **83** (5) (2000) 1241–46.
18. L. E. Shea, J. McKittrick, M. L. F. Phillips, *J. Electrochem. Soc.*, **145** (11) (1998)3165–3170.



19. S. L. Jones, D. Kumar, K.-G. Cho, R. Singh, P. H. Holloway, *Displays* **19** (1999) 151–167.
20. S. Dey, Sun Jin Yun, *Appl. Surf. Sci.* **143** (1999) 191–200.
21. K.T. Hillie, C. Curren, H. C. Swart, *Appl. Surf. Sci.* **177** (2001) 73-77.
22. H. Kim, Transparent Conducting Oxide Films, In: *Pulsed Laser Deposition of Thin Films: Applications-Led Growth of Functional Materials*, Edited by Robert Eason, 2007 John Wiley & Sons, Inc. pp 243-244.

## Chapter 10

### Summary and Suggestions for Future Work

#### 10.1. Thesis Summary

This thesis divided into two sections reports on: the photoluminescence, cathodoluminescence degradation, XPS analysis, thermoluminescence, and temperature dependence investigation of the CaS:Eu<sup>2+</sup> powder. In the second section, the luminescent properties of the pulsed laser deposited thin films prepared from the powder obtained from Phosphor Technology (UK) are investigated.

For morphological and topographical analysis, the SEM and AFM were employed. The PL data were obtained using the He-Cd 325-nm laser and the Cary Eclipse fluorescence spectrometer. The structure of the powder and films was determined using the X-ray diffractometer. The CL data were collected using the CL system connected to the AES system. The elemental composition analysis of the powder was carried out using the XPS, AES, and EDS. While the same for the thin films were done using the RBS and EDS. The RBS was also used to determine the thickness of the films. An Edinburg instruments FS920 fluorescence spectrometer equipped with a cryostat filled with liquid nitrogen was used to record low temperature measurements. The thermoluminescence data for samples exposed to  $\gamma$ -radiation from <sup>60</sup>Co source were obtained using a Harshaw thermoluminescence Reader (Harshaw 3500 TLD Reader). The Spectra Physics Quanta-Ray Pro-270 Nd: YAG laser was used to ablate the phosphor pellet to form thin films under different conditions, such as different laser wavelength, working atmosphere, number of pulses, deposition pressure and substrate temperature. The IONTOF TOF-SIMS5 ion mass spectrometer in both static and dynamic mode was used to observe the chemical information in Eu<sup>2+</sup> doped CaS PLD thin films prepared in different atmospheres.

The PLE spectra consisted of two broad bands while the emission spectra consisted of one broad band. The excitation band between 200 nm and 320 nm is associated with  $\text{Eu}^{2+}$   $4f^7[{}^8S_{7/2}] \rightarrow 4f^6[{}^7F_J]5d^1[e_g]$  and valence-to-conduction band transitions, while the excitation band extending from 400-600 nm is ascribed to the  $4f^7[{}^8S_{7/2}] \rightarrow 4f^6[{}^7F_J]5d^1[t_{2g}]$  transitions of  $\text{Eu}^{2+}$ . The red emission observed at 650 nm was attributed to the transitions from the excited  $4f^6[{}^7F_0]5d^1(t_{2g})$  state to the ground state  $4f^7({}^8S_{7/2})$  of the  $\text{Eu}^{2+}$  ions. XRD, XPS, and PL point to the existence of  $\text{CaSO}_4$  and a small amount of  $\text{CaSO}_3$  in the powder. The  $\text{CaSO}_4$  and  $\text{CaSO}_3$  may have been formed during synthesis or by reaction of  $\text{CaS}$  with water vapor, atmospheric  $\text{O}_2$  and/or  $\text{CO}_2$ . The formation of a  $\text{CaSO}_4$  or  $\text{CaSO}_3$  layer, surface charging, and possibly formation of O defects upon electron bombardment might collectively be responsible for the CL degradation. An increase in the CL intensity attributed to an increase in beam current density was observed under beam currents of 1–13  $\mu\text{A}$ .

The decrease in decay time with increase of temperature is attributed to thermal quenching, which is due to electrons being activated to the conduction band. Thermoluminescence of the gamma- irradiated Eu doped  $\text{CaS}$  was used to determine the nature of the electron traps. TL intensity was found to increase with  $\gamma$ -dose, with the main TL peak observed at 130°C. The depth of the trap determined by initial rise method was 0.82 eV. The quenching temperature was found to be around 304 K. The PL, decay times and thermal quenching of luminescence results indicate that this phosphor is suitable for low-power white pc-LEDs.

The phosphor target was ablated using Nd: YAG laser whose wavelength was either 266 nm, 355 nm or 532 nm. The thickness of the thin film was determined by RBS and was found to depend on the laser wavelength used for ablation. The film deposited at the wavelength of 532 nm was found to be thinner than those deposited at the wavelengths of 266 and 355 nm, and this was attributed to the poorly absorbed laser energy due to the target being transparent to the 532-nm laser wavelength. The highest photoluminescent emission intensity at around 650 nm was observed from the film deposited at the wavelength of 355 nm, and the least intensity was observed from the film deposited at the wavelength of 532 nm. This was

attributed to the fact that the film deposited at 355 nm was rougher than that deposited at 266 and 532 nm. Thus, the best wavelength for depositing PLD thin films of CaS:Eu<sup>2+</sup> was found to be 266 nm. Although the stoichiometry of the films was comparable to that of the commercial powder (Ca: S; 1:1), there was a slight deficiency of sulfur, noticeable in the 532-nm film.

The thin films prepared in an oxygen atmosphere were amorphous while those prepared in vacuum and argon atmosphere showed a slight degree of crystallinity. An emission at around 618 nm was observed, and was attributed to  $D_0 \rightarrow {}^7F_2$  transitions in Eu<sup>3+</sup>, probably formed by oxidation of Eu<sup>2+</sup>. Results from TOF SIMS study show that all the films contain oxygen although the film prepared in oxygen contains more oxygen. Thin films grown in an argon atmosphere were rougher than those grown in oxygen and vacuum atmospheres, while the smoothest films were grown in a vacuum atmosphere; consequently the best PL intensity was obtained for films deposited in an argon atmosphere.

PL intensity increased with increase in the number of pulses, and post-deposition annealing greatly improved the intensity. The best emission intensity was obtained from the film annealed at 800°C. The improved PL intensity from the film prepared using the highest number of pulses (18000) is attributed to the increased surface roughness and layer thickness, while that recorded upon annealing is attributed to improved crystallinity. The PL intensity also increased with deposition pressure up to 80 mT, and then decreased for pressures above this, thus, the optimal deposition pressure is 80 mT. As the substrate temperature was increased from 200°C to 650°C, PL intensity improved showing a sharp increase in PL intensity at substrate temperature of 650°C.

## 10.2. Recommendations for Future Work

The work presented in this thesis is not exhaustive and suggests future research is still necessary in order to gain more fundamental understanding of this sulfide-based phosphor. For instance, it is not very clear where the CaSO<sub>4</sub> found in the powder came from; is it an impurity or was it dependent on the source of excitation? More work on thermoluminescence studies should be done using another source of radiation, for example, UV or blue light and also investigate the effect of different heating rates. This could help in

determining whether the thermoluminescence in  $\text{CaS:Eu}^{2+}$  is dependent on the type of radiation.

The laser wavelengths at our disposal were 266 nm, 355 nm, 532 nm, and 1064 nm. Since CaS is a wide band material, we recommend that a laser of a wavelength shorter than 266 nm should be used for ablation and the quality of the films thereof investigated. Preparing or annealing the thin films in a sulfur-rich atmosphere should be explored. This is important because the present study was carried out in both inert and oxygen atmospheres.

A study should be done to find out the effect of exposing the thin films to moist air or oxygen. Then a suitable coating material to prevent films from absorbing atmospheric water should be found.

It is important to construct a LED device based on  $\text{CaS:Eu}^{2+}$  in form of powder and thin films and test its performance under different operating conditions. This will help sort out any technological challenges.

## Appendix A: Publications and Conferences/Workshops

### (a) Publications

1. R.L. Nyenge, H.C. Swart, O.M. Ntwaeaborwa, *Luminescent properties, intensity degradation and X-ray photoelectron spectroscopy analysis of CaS:Eu<sup>2+</sup> powder*, Opt. Mater. **40** (2015) 68–75.
2. R.L. Nyenge, P.T. Sechogela, H.C. Swart, O.M. Ntwaeaborwa, *The influence of laser wavelength on the structure, morphology and photoluminescence properties of pulsed laser deposited CaS:Eu<sup>2+</sup> thin films*, J. Mod. Opt. **62** (2015) 1102-1109, DOI: 10.1080/09500340.2015.1020898.
3. R. L. Nyenge, S.K.K. Shaat, L.L. Noto, P.P. Mokoena, H. C. Swart, O. M. Ntwaeaborwa, *TOF SIMS Analysis, Structure and Photoluminescence Properties of Pulsed Laser Deposited CaS:Eu<sup>2+</sup> thin films*, J. Lumin. **167** (2015) 172-178.
4. R.L. Nyenge, H.C. Swart, O.M. Ntwaeaborwa, *Influence of Substrate Temperature and Deposition pressure on Pulsed laser deposited thin films of CaS:Eu<sup>2+</sup> phosphors*, Physica B doi.org/10.1016/j.physb.2015.08.046 .
5. R. L. Nyenge, H. C. Swart, O. M. Ntwaeaborwa, *The influence of the number of pulses and post annealing on the morphology and photoluminescence properties of CaS:Eu<sup>2+</sup> pulsed laser deposited thin films*, conference proceedings, 60<sup>th</sup> Annual Conference of the South African Institute of Physics.
6. R.L. Nyenge, H.C. Swart, D. Poelman, P. F. Smet , L.I.D.J. Martin, L.L. Noto, S. Som, O.M. Ntwaeaborwa, *Thermal quenching, cathodoluminescence and thermoluminescence study of Eu<sup>2+</sup> doped CaS powder*, submitted to J. Alloys Compd. on 18/09/2015.

## **(b) Presentations in Conferences/Workshops**

1. R. L. Nyenge, in attendance, the 58<sup>th</sup> annual conference of South African Institute of Physics (SAIP), 8-12<sup>th</sup> July, 2013, Richards Bay Campus, University of Zululand.
2. R. L. Nyenge, P.T. Sechogela, H. C. Swart, O. M. Ntwaeaborwa, “The influence of laser wavelength on the structure, morphology and photoluminescence properties of pulsed laser deposited CaS:Eu<sup>2+</sup> thin films”, ALC femto second Laser Workshop, 18-20 NOV 2014, University of Stellenbosch, South Africa.
3. R. L. Nyenge, S.K.K. Shaat, L. L. Noto, P. P. Mokoena, H.C. Swart, O.M. Ntwaeaborwa, “TOF SIMS Analysis, structure and photoluminescence properties of pulsed laser deposited CaS:Eu<sup>2+</sup> thin films”, 6<sup>th</sup> South African Conference on Photonic Materials, 5 - 7 May 2015, Mabula Game Lodge, Limpompo, South Africa.
4. R.L. Nyenge, H. C. Swart, O. M. Ntwaeaborwa, “The influence of the number of pulses and post annealing on the morphology and photoluminescence properties of CaS:Eu<sup>2+</sup> pulsed laser deposition thin films”, 60<sup>th</sup> Annual Conference of the South African Institute of Physics, 29 June – 3 July 2015, Port Elizabeth, South Africa.
5. R.L. Nyenge, H.C. Swart, O.M. Ntwaeaborwa, “Cathodoluminescent and Photoluminescent Properties of Pulsed Laser Deposited Thin Film Phosphors”, International Conference on Laser Ablation 31 August - 4 September 2015, Cairns, Queensland, Australia.